N73-13777

NASA TECHNICAL NOTE

NASA TN D-6971

NASA TN D-6971

TESTS OF A MIXED COMPRESSION AXISYMMETRIC INLET WITH LARGE TRANSONIC MASS FLOW AT MACH NUMBERS 0.6 TO 2.65

by Donald B. Smeltzer and Norman E. Sorensen
Ames Research Center
Moffett Field, Calif. 94035

NATIONAL AERONAUTICS AND SPACE ADMINISTRATION • WASHINGTON, D. C. • DECEMBER 1972

1. Report No. NASA TN D–6971	2. Government Accession No.	3. Recipient's Catalog No.
4. Title and Subtitle TESTS OF A MIXED COMPRESSION AXISYMMETRIC INLET WITH LARGE TRANSONIC MASS FLOW AT MACH NUMBERS 0.6 TO 2.65		5. Report Date December 1972 6. Performing Organization Code
7. Author(s) Donald B. Smeltzer and Norman E. Sorensen		8. Performing Organization Report No. A-4231
9. Performing Organization Name and Address NASA Ames Research Center Moffett Field, Calif. 94035		10. Work Unit No. 764-74-01-06-00-21 11. Contract or Grant No.
12. Sponsoring Agency Name and Address National Aeronautics and Space Administration Washington, D. C., 20546		13. Type of Report and Period Covered Technical Note 14. Sponsoring Agency Code

15. Supplementary Notes

16. Abstract

A 38.8-cm (15.28-in.) capture diameter model of a mixed-compression axisymmetric inlet system with a translating cowl was designed and tested. The internal contours, designed for Mach number 2.65, provided a throat area of 59 percent of the capture area when the cowl was retracted for transonic operation. Other model features included a boundary-layer removal system, vortex generators, an engine airflow bypass system, cowl support struts, and rotating rakes at the engine face. All tunnel testing was conducted at a tunnel total pressure of about 1 atm (a unit Reynolds number of about 8.53×10^6/m at Mach number 2.65) at angles of attack from 0° to 4°.

The following results were obtained: Total-pressure recovery and distortion at the engine face as a function of bleed mass-flow ratio, the effect of bleed and vortex generator configurations on pressure recovery and distortion, inlet tolerance to unstart due to changes in angle of attack or Mach number, surface pressure distributions, boundary-layer profiles, and transonic additive drag. At Mach number 2.65 and with the best bleed configurations, maximum total pressure recovery at the engine face ranged from 91 to 94.5 percent with bleed mass-flow ratios from 4 to 9 percent, respectively, and total-pressure distortion was less than 10 percent. At off-design supersonic Mach numbers above 1.70, maximum total-pressure recoveries and corresponding bleed mass flows were about the same as at Mach number 2.65, with about 10 to 15 percent distortion. In the transonic Mach number range, total pressure recovery was high (above 96 percent) and distortion was low (less than 15 percent) only when the inlet mass-flow ratio was reduced 0.02 to 0.06 from the maximum theoretical value (0.590 at Mach number 1.0).

17. Key Words (Suggested by Author(s)) Propulsion Airbreathing Inlet Internal flow		18. Distribution Statement Unclassified – Unlimited	
19. Security Classif. (of this report) Unclassified	20. Security Classif. (of this page) Unclassified	21. No. of Pages 188	22. Price* $3.00

* For sale by the National Technical Information Service, Springfield, Virginia 22151

SYMBOLS

A	area
A_c	capture area
A_{min}	minimum duct area normal to the average local flow
A_x	local duct area normal to the inlet centerline
b	local dimension for vortex generators or bleed hole spacing
C_{D_a}	additive drag coefficient based on A_c
CR	contraction ratio $\frac{A_c}{A_{min}}$
D	capture diameter 38.8 cm (15.28 in.)
d	local diameter
h	height of boundary-layer probe from surface
M	Mach number
m	mass flow
m_∞	free-stream mass flow based on A_c
p	static pressure
p_p	pitot pressure
p_t	total pressure
Δp_{t_2}	total-pressure-distortion parameter, $\frac{p_{t_{2}\,max} - p_{t_{2}\,min}}{\bar{p}_{t_2}}$
R	capture radius
$\frac{r}{R}$	ratio of centerbody radius to capture radius
$\frac{r'}{R}$	ratio of cowl radius to capture radius
$\frac{x}{R}$	ratio of axial distance measured from the tip of the centerbody to capture radius
$x_{A_c/A_{min}}$	distance from the centerbody tip to the throat on the centerbody surface

x_c	axial distance measured from the cowl lip
$x_{c A_c/A_{min}}$	distance from the cowl lip to the throat on the cowl surface
$\frac{x_{lip}}{R}$	axial distance from centerbody tip to cowl lip divided by capture radius
α	inlet angle of attack, deg
α_u	angle of attack for incipient unstart, deg
θ	circumferential position (0° is at top of inlet)
θ_2	circumferential position of rotating engine face rake assembly

Subscripts

∞	free stream
o	inlet lip (theoretical)
i	inlet lip
ι	local
1	throat
2	engine face
bl	total bleed
bl_{1-4}	bleed through the individual zones
bp	bypass
e	conditions at exit
max	maximum
min	minimum
st	strut

Superscript

$\overline{(\ )}$	average value

NOTE: The designations for bleed and vortex generator configurations are explained by figures 7 and 8, respectively.

TESTS OF A MIXED COMPRESSION AXISYMMETRIC INLET WITH LARGE TRANSONIC MASS FLOW AT MACH NUMBERS 0.6 TO 2.65

Donald B. Smeltzer and Norman E. Sorensen

Ames Research Center

SUMMARY

The internal performance is presented for a large-scale model of a mixed-compression axisymmetric inlet with a translating cowl for the Mach number range 0.6 to 2.65, angles of attack from 0° to 4°, and a constant total pressure of about 1 atm (a unit Reynolds number of about 8.53×10^6/m at Mach number 2.65). The model capture diameter was about 38.8 cm (15.28 in.) and the length from the cowl lip to the engine face was 2.2 capture diameters. Other features were the following: a boundary-layer removal system, vortex generators, an engine airflow bypass system, and cowl support struts.

The supersonic diffuser was designed for Mach number 2.65 by the method of characteristics with constraints on the contours that gave 59 percent of the capture area at the throat when the cowl was retracted for transonic operation. The design of the subsonic diffuser prevented reduction of this high transonic area ratio and provided contours that avoided flow separation.

Various bleed and vortex generator configurations were investigated at Mach number 2.65. With the best combinations, maximum total-pressure recovery at the engine face was about 91 to 94.5 percent with bleed mass-flow ratios from 4 to 9 percent, respectively, and total-pressure distortion was less than 10 percent. At off-design supersonic Mach numbers above 1.70, maximum total-pressure recovery and corresponding bleed mass-flow ratio were about the same as at Mach number 2.65, but with distortion generally higher (10 to 15 percent). At transonic Mach numbers, total-pressure recovery was high (above 96 percent) and distortion was low (less than 15 percent) only when the mass-flow ratio was reduced about 0.02 to 0.06 from the theoretical maximum (0.590 to Mach number 1.0). To achieve this performance it was necessary to change the bleed and vortex generator configuration as the Mach number was reduced. As the cowl was translated for off-design operation, the throat moved downstream on the centerbody; consequently, the performance was best when the centerbody throat bleed was moved downstream to the vicinity of the throat. At the higher Mach numbers $M_\infty \geq 2.4$), the performance was best with vortex generators on both cowl and centerbody. However, because of the throat movement, they entered the supersonic diffuser as the cowl was translated and, consequently, the performance was best without vortex generators at Mach number 2.3 to 0.6.

INTRODUCTION

Supersonic aircraft require inlet systems capable of efficient operation over a wide Mach number range. The results of inlet investigations reported in references 1 through 4 showed that mixed-compression axisymmetric inlet systems could meet this requirement. However, these inlets provided relatively low transonic airflow, which may not match the flow requirements of some turbojet engines, severely reducing the propulsion system thrust. This reduced thrust coupled with inherently high transonic aerodynamic drag would lead to low acceleration and high fuel consumption. A primary objective of this investigation was to alleviate this condition by designing an inlet for considerably higher transonic airflow than the previous inlets.

The design Mach number was 2.65. The prinicipal design goals were to provide high perfomance potential throughout the Mach number range with internal contours that provided high airflow for transonic operation—and with a short length to minimize the inlet weight. Many aspects of the design were based on previous experience (refs. 1-4); these are discussed in following sections.

The experimental investigation was conducted with a quarter-scale model in the Ames Unitary Plan Wind Tunnels. Figure 1 is a photograph of the model mounted in one of these wind tunnels. The test Mach number range was 0.6 to 2.65 and the total pressure was constant at about 1 atm (a unit Reynolds number of about 8.53×10^6/m at Mach number 2.65). Total-pressure recovery and distortion at the engine face were measured as a function of bleed and/or engine face mass-flow ratio. Measurements were also made of bypass mass-flow ratio, inlet sensitivity to unstart (caused by changes in angle of attack or Mach number), internal surface pressure distributions, boundary-layer profiles, and pressures to calculate transonic additive drag.

MODEL AND INSTRUMENTATION

Sketches of the model and instrumentation are shown in figure 2, the coordinates of the internal surfaces are given in table 1, and the coordinates of the struts (upstream of the engine face) are given in table 2.

The model had a capture diameter of about 38.8 cm (15.28 in.) and was considered to be about quarter scale. The model components that were remotely controlled during testing were a translating cowl (for internal area variations), a translating sleeve and fixed plug (for control of the terminal shock wave position), exits for each bleed zone and the bypass duct, and rotating rakes at the engine face.

There were two sets of struts (fig. 2(a)): one located just upstream of the engine face (these struts would normally be used for centerbody bleed removal and cowl support but not on this model), and one downstream of the engine face (these struts provided ducting for the centerbody bleed and support for the cowl). In addition, there were four separate bleed zones and a bypass slot (fig. 2(b)). The bleed zones were isolated to reduce recirculation of the flow from the higher to lower pressure regions. There were fairings for the bleed and bypass exits to ensure low back pressures (fig. 2(a)). Finally, there were two locations for vortex generators on the centerbody and one on the cowl (fig. 2(b)). The centerbody locations were used one at a time.

Instrumentation, consisting of total and static pressure rakes and static pressure orifices, was used to measure the internal performance. Rakes, spaced on an area weighted basis (fig. 2(c)), were used to measure the total-pressure recovery at the engine face (fig. 2(b)) at x/R = 6.8. Pressures for the computation of the main duct mass flow were measured by six static pressure rakes, each consisting of two tubes spaced on an area-weighted basis near the main duct exit (fig. 2(a) at x/R = 15.807). Total pressure rakes were used for measurements in the boundary layer (fig. 2 (b)). A 10-tube total-pressure rake at the inlet throat measured pressures used in evaluating the performance of the supersonic diffuser (fig. 2(b)). Measurements from static- and total-pressure rakes in the centerbody bleed ducts were used to compute the centerbody bleed mass flow (fig.2(b)). Four rakes, each consisting of five total and three static pressure tubes, were spaced 90° apart at the station of maximum centerbody diameter. Measurements from these tubes were used to compute the transonic mass flow.

Static-pressure orifices, located longitudinally along the top inner surfaces of the cowl and centerbody, extended to the engine-face station (fig. 2(b)). Static-pressure orifices, located longitudinally on the side of one strut near both walls, extended from the strut leading edge to the engine face. Orifices were located circumferentially in each bleed and the bypass plenum chambers. Measurements from these orifices were used to calculate the cowl bleed and bypass mass flows, and all bleed and bypass plenum chamber pressure recoveries.

DESIGN

General Considerations

Design goals, successful for previous inlet systems (refs. 1-4), were used for the present design. These include high performance throughout the Mach number range, minimum inlet length (weight), and low inlet drag. An additional goal, not used previously, was a large throat area for transonic operation.

The internal contours were considered appropriate for an operational inlet system. However, other components such as bleed and bypass plenums and exits, and external contours were adopted from a previous wind tunnel model and were not representative of operational hardware. Design details of the important inlet-system components follow.

Supersonic Diffuser

The major design goal was to achieve isentropic compression and a uniform throat Mach number of 1.25 at the design Mach number of 2.65, with contours that gave the largest possible throat area when the cowl was retracted for transonic operation. An additional goal was to provide a stability margin[1] with a controlled expansion to about Mach number 1.4 downstream of the throat. Based on previous experience, if these goals were achieved, there would be high performance throughout the Mach number range.

---

[1] A resistance to unstart from a sudden decrease in engine airflow demand which drives the terminal shock wave upstream.

The maximum possible area ratio for transonic operation and the corresponding necessary critical dimension (r_{max}/R and r'_{min}/R) were calculated with the method developed in appendix A. A sample calculation is included in the appendix.

The contours were designed with the aid of the method of characteristics; the computer program used is described in reference 5. Figure 3 shows the computed results at the design Mach number of 2.65, including the flow field mesh, static pressure and Mach number distributions on the cowl and centerbody surfaces, total-pressure recovery and Mach number distributions across the throat, and the axial locations and values of local surface slopes used in the computer input. The design goals were closely met: the inviscid total-pressure recovery was 0.9997 and Mach number was about 1.25 across the throat ($x/R \simeq 4.22$); the flow expanded to about Mach number 1.40 downstream of the throat ($x/R \simeq 4.50$); the throat area (A_{min}/A_c) was 0.595 with the cowl retracted to $x_{lip}/R = 3.663$ (at this point the maximum cowl and centerbody diameters are axially alined).

The procedure for developing these contours is discussed in detail in the following paragraphs. Special criteria, successful for previous designs, were used for starting points in developing the contours: (1) a small initial cone angle with its corresponding small flow deflection angle through the bow shock for high performance (essentially no shock loss) and low spillage drag during off-design operation, (2) a small initial internal cowl angle for high performance and low external drag, (3) the cowl lip just downstream of the bow shock to eliminate spillage for operation at the design Mach number, and (4) an inflection point on the centerbody near the axial location of the shock wave impingement from the cowl lip at the design Mach number. Previous experience also gave some insight into the rates of change of surface slope with distance that would not require "relatively large" boundary layer bleed to control separation. (The computer program used a linear rate of change of surface slope with distance between input points.)

With initial estimates for these criteria, the remainder of the "trial" contours were calculated so that the critical dimensions of maximum centerbody radius (r_{max}) and minimum cowl radius (r'_{min}) were equal to the computed values and located as shown in the appendix. The flow field was computed by the method of characteristics, and the solution was "checked" for performance at the throat. (The parameters checked included Mach number, pressure recovery, rates of compression, local expansion regions, etc.) Many iterations of this "trial and check" procedure were required to develop the final contours, although they are not the only contours that would give the indicated performance.

Because of compromises necessary for the high internal performance, the final critical dimensions were not ideal. That is, the critical centerbody dimension (r_{max}/R) was slightly upstream and the critical cowl dimension (r'_{min}/R) was slightly downstream of the throat (fig. 3). In addition, these ratios were slightly larger and slightly smaller, respectively, than their optimum calculated values. With these deviations from the ideal, the throat area for transonic operation was slightly less than theoretically possible. However, this was partially compensated for by the initial positive cowl angle (1.5°), which increased the minimum area ratio from that with a straight (0°) cowl. (This positive angle could result in a larger external cowl angle and perhaps higher cowl drag.)

The final contours included no boundary-layer compensation, because previous experience indicated that a boundary-layer-removal system would closely compensate for displacement effects.

However, in conjunction with the present investigation, experiments were conducted with a cowl modified to partially account for the boundary-layer displacement thickness. The results, presented in appendix B, are considered inconclusive.

Cowl Support Struts

Table 2 includes a sketch of the cowl support struts and their coordinates. Three struts were used, instead of the usual four, because of the possibility of a weight reduction. The struts were sized to accommodate the expected centerbody boundary layer bleed. However, they were not used as bleed ducts on this model. At the design Mach number, the expected bleed was 3 percent of the capture mass flow at a pressure recovery of 20 percent and Mach number of 0.25. This pressure recovery and Mach number were considered conservative estimates and were based on the work reported in references 1 through 3. A sharp leading edge was used for the struts because of the high duct Mach numbers during transonic operation ($M \simeq 0.7$ at the leading edge); the blunt trailing edge mated with engine guide vanes. The leading edge of each strut was a straight line inclined to the inlet centerline (fig. 2(b)); the resulting long cowl template provided additional cowl support although the struts were not load-carrying members on this model.

Subsonic Diffuser

Some of the subsonic diffusers previously designed (refs. 1-4) showed evidence of flow separation, which was traced to regions where the rates of change of surface slope with distance were relatively large. Therefore, the choices for the present design were limited to contours with smaller rates of slope change than those where flow separation had previously been detected. With this contour limitation, the principle objective was to find contours such that the large throat area for transonic operation ($A_{min}/A_C = 0.595$ with $x_{lip}/R = 3.663$) included in the design of the supersonic diffuser would not be followed by a smaller area further downstream.

The design procedure was first to select centerbody contours with about the maximum rate of change of slope and cowl contours with smaller rates. A position for the cowl for transonic operation was noted where there would be no downstream throat. The cowl was then placed in the design position ($x_{lip}/R = 2.325$) to make minor contour adjustments so that there was a continuing increase in area with distance. Then, the centerbody templates of the struts were located at the intersection of the contoured portion of the centerbody and the support tube ($x/R = 5.65$) to avoid a surface discontinuity; the leading edge of the cowl template was located upstream at the point where nearly the maximum "acceptable" changes to the cowl surface were required to compensate for the strut area. This maintained the continuous increase in area with distance. Finally, the engine face was located just downstream from the base of the struts. The diameter at the engine face was sized to mate with engines currently under study and provided Mach numbers ranging from 0.27 to 0.51 for free-stream Mach numbers between 2.65 and 1.0, respectively.

After numerous compromises, made at various steps during the above procedure, the final integrated design was accomplished. It was considered to be about as short as possible—2.2 capture diameters measured from the cowl lip to the engine face. The resulting area distributions (fig. 4) show that the final translation distance for operation through the Mach number range increased from 0.67 capture diameters ($x_{lip}/R = 2.325$ to 3.663 based on the supersonic diffuser contours) to

0.78 capture diameters (x_{lip}/R = 2.325 to 3.880). However, the corresponding throat area (A_{min}/A_c) decreased only from 0.595 to 0.590.

With these contours, the throat was not stationary on the cowl or centerbody as the cowl lip was retracted (fig. 5). On the centerbody (lower curve), it moved steadily downstream until, near the transonic operating position ($x_{lip}/R = 3.75$), it moved rapidly upstream to the vicinity of the maximum diameter. On the cowl (upper curve), the throat moved slowly upstream and near the transonic operating position ($x_{lip}/R = 3.70$), it moved rapidly to the vicinity of the lip. These combined characteristics provided the variation in inlet contraction ratio shown in figure 6.

Bleed System

The total extent of bleed holes in all zones is shown in figure 2(b). Bleed zones 1 and 2 were located on the cowl and centerbody, respectively, in regions of high pressure gradient, and were expected to prevent flow separation in the supersonic diffuser. These zones were drilled with holes with a diameter to capture radius ratio of 0.0125, in a pattern that provided an overall uniform porosity of 40 percent. Bleed zones 3 and 4 were located (based on previous experience) in the throat region on the cowl and centerbody, respectively, to provide a variation in mass flow as the terminal shock wave moved in the throat. Since throat bleed was assumed necessary at all supersonic Mach numbers, a large expanse of holes was provided in zone 4 (centerbody). However, in an operational inlet system with a translating centerbody, only a small portion of this zone would be open at a fixed centerbody position. This could be accomplished by compartmenting this zone and, with the use of a sliding valve, closing or opening successive compartments as the throat moved downstream on the centerbody. For this inlet model, the hole pattern in all bleed zones was altered wtih a plastic resin material; the method used to derive the final bleed patterns is described in the next major section. Bleed plenum chambers, ducts, and exits, as they would be an operational inlet system, were not used on this model (see model description).

Bypass System

The bypass system supplies air for several purposes: inlet-engine matching, secondary air requirements, and auxiliary air for takeoff. The bypass slot, sized for an expected takeoff air requirement, was located upstream of the engine face in a region of nearly constant static pressure, thereby lessening the possibility of flow distortion and recirculation. The rounded lips of the slot were designed to accommodate takeoff doors and a secondary airflow system, although these (as well as operational bypass plenum chambers and exits) were not provided on this model (see model description).

Vortex Generators

Vortex generators were necessary to avoid high total-pressure distortion at the engine face which, from previous subsonic diffuser experience, occurs with rapidly diverging surfaces. They were located downstream of the throat bleed at the design Mach number to induce the mixing action where the boundary layer was relatively thin (fig. 2(b)). However, vortex generators at this location on the centerbody would be in the supersonic flow field with relatively little cowl translation and will cause performance penalties. Therefore, an alternative location was also chosen farther downstream (fig. 2(b)), at which the vortex generators enter the supersonic flow field at a lower Mach number and hence, the penalties might be less.

The height of the vortex generators was greater than that previously used so that material could be removed during testing if smaller generators were needed. At the alternate (downstream) location on the centerbody, the height was greater, because this location was considerably downstream of the throat bleed at the higher free-stream Mach numbers, and therefore the boundary layer would be thicker. The spacing between adjacent generators was chosen for uniformly mixed flow at the engine face. Other design details were based on the work in reference 6.

TEST PROCEDURE

Tests were conducted in the 8- by 7-, 9- by 7-, and 11- by 11-ft test sections of the Ames Unitary Plan wind tunnels. Data were obtained over the transonic and supersonic Mach number ranges 0.6 to 1.1 and 1.55 to 2.65, respectively. Most testing was done at 0° angle of attack, although, some data were recorded at angles up to 4°.

Supersonic Test

At Mach number 2.65, the hole pattern in each bleed zone was varied, and each variation was tested at different contraction ratios (positions of the cowl lip). The data were recorded using the exit plug to change the position of the terminal shock wave. In this way, many overall bleed configurations were found where the performance was high. Three configurations (A, C, and B-1), representative of the available range of tradeoffs of bleed versus pressure recovery, were selected for more detailed investigation. Configurations A and C (fig. 7(a)), with relatively high and low bleed flow, respectively, were tested only at Mach numbers 2.65 and 2.60. Configuration B-1 and its variations (fig. 7(b)) were tested at Mach numbers 2.65 to 1.55. Each variation was tested over a range of Mach numbers to find the Mach number for the highest performance in terms of bleed versus pressure recovery.

At 0° angle of attack and with zero bypass, the supercritical performance was measured for various contraction ratios (positions of the cowl lip) at each Mach number. At selected points on the performance curves of pressure recovery versus mass flow, the performance was measured (fixed inlet geometry) as the angle of attack or Mach number was changed, and the total pressure variation at the engine face was measured with the rotating rakes. In addition, at the contraction ratio for the best supercritical performance, performance was measured with various fixed bypass exit areas.

Many of the measurements just described were made with various vortex generator configurations. All configurations with vortex generators had them in the forward location on the centerbody as shown in figure 2(b), except configuration D where they were at the alternate location. The alignment and spacing of all configurations is shown in figure 8. No single configuration was tested at all Mach numbers.

The combinations of bleed and vortex generator configurations and the Mach numbers where they were tested are shown in table 3. The results reported are considered fairly representative of all data and, hence, data from all of these combinations are not presented.

Transonic Test

At transonic Mach numbers, the bleed and bypass exits were always closed. Data were recorded with and without vortex generators, at 0° angle of attack for several positions of the cowl lip, and at other angles for the position where the largest mass flow was measured. In addition, variations in total pressure at the engine face were measured with the rotating rakes for a few conditions.

MEASUREMENT TECHNIQUES AND ACCURACY

The estimated accuracy of the primary parameters is given below.

Parameter	Accuracy
$\bar{p}_t/p_{t_\infty}$	±0.005
$m_{bl_{1-4}}/m_\infty$	± .003
m_{bp}/m_∞	± .02
α	± .10°
p/p_∞	± .2
M_∞	± .005
m_i/m_∞	± .02 ($\alpha = 0°$ to $2°$)[a] (transonic tests)
m_2/m_∞	± .02 ($\alpha = 0°$ to $2°$)[a] (supersonic tests)

[a] At angles of attack larger than 2°, mass-flow ratio (m_2/m_∞ and m_i/m_∞) may be in error by ±0.050 or more because of increased flow nonuniformity.

The measurement techniques and accuracies of all parameters except mass-flow ratio have been well established from many tests at the Ames Unitary Plan wind tunnels. For mass-flow ratio, however, the calibration procedure was not "conventional," and the accuracies, although confirmed from previous tests (refs. 1-3), are not as well established. For this reason, the technique for calibrating the mass-flow measurements is described in detail.

For supersonic Mach numbers, the mass-flow ratio entering the inlet is shown in figure 9 as a function of the cowl lip position (x_{lip}/R). These results were calculated with a modified form of the computer program described in reference 5. They are quite accurate when the cowl lip is near the bow shock (m_0/m_∞ near 1.0), and since mass-flow ratios were calibrated under these conditions, there was an accurate quantity for comparison.

Mass-flow ratio at the engine face (m_2/m_∞) was computed from static-pressure measurements near the main duct exit, a choked main-duct exit area, and a calibration factor, which corrected the computed ratio so it was equal to the entering mass-flow ratio (m_0/m_∞) less an estimated bleed mass-flow ratio (about 0.10 (m_0/m_∞) at critical pressure recovery). Even though the mass flow

(m_2/m_∞) thus computed was in error, the increments were assumed to be quite accurate. These increments were used to calibrate the bleed mass flows.

The cowl bleed mass-flow ratios (zones 1 and 3) were computed with plenum chamber pressures and known choked exit areas, and the centerbody flows (zones 2 and 4) with static and total pressures in the bleed ducts. In turn, each bleed exit was closed and the main duct pressure was raised to a near-critical condition by reducing the flow through the other bleed zones, closing the plug at the main duct exit, and increasing the inlet contraction ratio. Then the exit of the bleed to be calibrated was opened incrementally and the mass flow was computed and corrected with a calibration factor to make it equal to the increments in the main duct mass flow $(\Delta m_2/m_\infty)$. Small additional corrections were required because as each bleed exit was opened, the bleed flow through the other zones changed. Errors caused by these corrections were eliminated by iterating many calibrations over a range of variables (such as bleed configuration, contraction ratio, exit plug position). Bleed calibration factors were determined only at Mach number 2.65 and were used at other supersonic Mach numbers because the bleed mass flow was small (3 percent or less for each zone).

After the bleed mass flows were calibrated, a correction was made to the calibration factor for the mass flow at the engine face so that the computed mass flow (m_2/m_∞) plus the total bleed mass flow (m_{bl}/m_∞) equaled the entering mass flow (m_o/m_∞). This correction was small because the measured and originally estimated bleed mass flows were quite close. However, it was found that this calibration factor was influenced by the total pressure distortion at the engine face, and hence measurements of mass flow at the engine face (m_2/m_∞) were less accurate than bleed mass flow.

Bypass mass-flow ratio (m_{bp}/m_∞) was computed with plenum chamber pressures and a known choked exit area. The calibration procedure was identical to that for bleed mass flow. Because the bypass mass flow was large, however, the flow was calibrated at all supersonic Mach numbers with accuracies about equal to that for the mass flow at the engine face.

Bleed and bypass mass flows were calibrated only at 0° angle of attack, but are probably as valid at small angles (up to 2°). At larger angles, flow asymmetry could cause circumferential circulation in the plenum chambers, which could reduce the accuracy of the calibrations.

At transonic Mach numbers (0.6-1.1), the mass flow entering the inlet (m_i/m_∞) was computed from the average of static and total pressures, measured across the duct at the station of maximum centerbody diameter. No calibration factor was applied to the computed results. The measurements from these rakes, the measured pressures on the centerbody, and an estimated friction drag term were used to compute the additive drag (ref. 7).

RESULTS AND DISCUSSION

The principal performance parameters considered in this investigation are engine-face pressure recovery and distortion. At supersonic speeds these parameters generally are presented as functions of bleed mass-flow ratio (m_{bl}/m_∞), because inlet system efficiency involves the trade of pressure recovery for bleed drag. For this reason the more common function, engine-face mass-flow ratio m_2/m_∞, is not used but can be calculated by merely subtracting the bleed mass-flow ratio from the theoretical capture mass-flow ratio (fig. 9). At transonic speeds the principal parameters are presented as functions of throat mass-flow ratio (m_l/m_∞) because it is more accurate. Note, however, that $m_l/m_o = m_2/m_\infty$ because the bleed and bypass exits were closed. All results are presented in figures 10 through 60; table 4 is an index to the figures.

The discussion of results is divided into four parts: development of the bleed configurations at Mach number 2.65, data for three bleed configurations at Mach numbers 2.65 and 2.60 (because the inlet Mach number may vary slightly, depending on the location of the inlet on the vehicle, results at Mach numbers slightly less than design are equally important), limited results at lower supersonic Mach numbers, and transonic results.

Bleed Configuration Development at Mach Number 2.65

The objective was to develop bleed configurations that permitted both started inlet operation at the design position of the cowl lip with surface-pressure distributions approximating the inviscid theoretical values. Operation at the design position is important, since under these conditions the bow shock wave intersects the cowl lip, thereby eliminating spillage drag. Matching of the theoretical and experimental pressure distributions was considered important for high internal performance and acceptable tolerance to transient disturbances (i.e., changes in angle of attack or Mach number that occur before an inlet control system can respond with changes in geometry).

Theoretical and experimental static-pressure distributions are shown in figure 10, and corresponding pitot pressure profiles at various cowl and centerbody stations, including the throat, are shown in figure 11 for four bleed configurations. Note the different locations for bleed zones 1 and 2 shown in figure 10. The throat bleeds (zones 3 and 4) were not changed during this portion of the bleed development. Results with bleed zones 1 and 2 concentrated upstream of shock wave impingements on the cowl and centerbody, respectively, are shown in figures 10(a) and 11(a). These initial bleed locations were chosen because similar locations were adequate for the inlets reported in references 1 through 3. However, with bleed at these locations, the inlet unstarted near the position of the cowl lip (contraction ratio) indicated on figure 10(a) and, therefore, could not be contracted to the design position ($x_{lip}/R = 2.325$). Theoretically, the inviscid characteristics lines between the limits labeled 1 and 2 (see sketch, fig. 10(a)), which originate on the cowl between $x/R = 2.364$ and 3.234, coalesce on the cowl between $x/R = 4.02$ and 4.08. In the actual flow, this coalescence was stronger due to boundary-layer displacement effects. In fact, coalescence was so strong it caused a severe adverse pressure gradient with subsonic flow between $x/R = 4.0$ and 4.1, and hence more contraction probably caused separation and the inlet unstarted. In addition, with bleed at these locations, there was nonuniform compression in the throat ($x/R \simeq 4.25$) as shown by the static pressure variation, and very poor inlet tolerance to transient disturbances (changes in angle of attack of less than 1° unstarted the inlet). However, with these bleed locations there was a satisfactory pitot pressure profile in the throat (fig. 11(a)). The low pressure near the cowl may represent a high Mach number, which is consistent with the low cowl surface static pressure in the throat or a relatively thick cowl boundary layer when compared to that on the centerbody.

When the centerbody bleed in the supersonic diffuser (zone 2) was moved upstream (as far as possible on this model), the inlet remained started with the cowl at the design position ($x_{lip}/R = 2.325$). The resulting surface pressure distributions and pitot pressure profiles are shown in figures 10(b) and the lower half of 11(a), respectively. With this location for bleed zone 2, there was still a severe adverse pressure gradient on the cowl ($x/R \simeq 4.0$) and, in addition, there was a severe gradient on the centerbody ($x/R \simeq 4.0$). Also the tolerance to transient disturbances was about the same as for the previous configuration while the compression in the throat ($x/R \simeq 4.22$) was somewhat more uniform. However, unlike the previous configuration, the performance at the throat was relatively poor, as evidenced by the low pitot pressures (fig. 11(a)). This probably occurred because of fairly strong shock waves resulting from excessive coalescence. In addition, there was considerable flow asymmetry in the throat, as evidenced by the different pitot pressure readings from the throat rake (near the centerbody) and the centerbody boundary layer rake at $x/R = 4.222$, which were located 180° apart.

When the bleed on the cowl surface (zone 1) was distributed over a wider area with the centerbody bleed (zone 2) the same as in the previous configuration, the adverse pressure gradients on both cowl and centerbody were greatly reduced, and the regions of subsonic flow were eliminated (fig. 10(c)). In addition, the tolerance to transient disturbances increased–the inlet remained started at angle of attack up to 2°. However, at the inlet throat ($x/R \simeq 4.22$), the compression was still nonuniform. The corresponding pitot pressures are shown in figure 11(b). Measured pressures were in substantial agreement with theory across most of the throat. As with the previous configurations, the boundary layer in the throat was relatively thicker on the cowl than on the centerbody.

When the bleed was distributed for both zones 1 and 2 (fig. 10(d)), the pressure gradients were reduced further. Moreover, the measured pressures were in better agreement with theoretical predictions, the compression in the throat $x/R \simeq 4.22$) was more uniform, and the inlet tolerance to transient disturbances was increased (up to 2.5° angle of attack without unstarting). However, the pitot pressure and throat profiles were not substantially different than those for the previous configuration (fig. 10(c)). Also, there was still some flow asymmetry in the throat near the centerbody.

Bleed flow rates for the configurations just discussed were excessive (10-15 percent at critical pressure recovery, i.e., just before the inlet unstarts) and, therefore, are not presented. However, the total bleed was somewhat less for the distributed pattern (fig. 10(d)) than it was for the others (fig. 10(a)-10(c)). To reduce the bleed flow while maintaining high performance at the engine face, many additional distributed patterns were investigated and the throat bleed (zones 3 and 4) was changed. Three of these configurations, representative of the available range of performances in terms of bleed versus pressure recovery, were selected for more extensive investigation. (These configurations, A, B-1, and C, are shown in fig. 7.) With bleed configuration A, both maximum pressure recovery and corresponding bleed flow were high (configurations with higher bleed rates did not significantly increase the maximum pressure recovery); with configuration B-1, maximum pressure recovery and the corresponding bleed flow were slightly lower; and with configuration C, maximum pressure recovery was somewhat lower still and the corresponding bleed flow was about the lowest that allowed started inlet operation near the design contraction ratio.

Theoretical and experimental surface pressure distributions and throat profiles are shown in figure 12 for bleed configuration A (highest total bleed flow but the best agreement with inviscid predictions). The hole pattern in the supersonic diffuser (zones 1 and 2) was similar to that shown in figure 10(d) (except for the gap in bleed zone 2). In the throat (zones 3 and 4), the bleed was concentrated near the minimum area. Near the cowl and centerbody surfaces, the pitot pressures in the throat were somewhat less than those for the configuration shown in figure 10(d). However, they were in substantial agreement with theory across most of the throat.

Performance at $M_\infty = 2.65$ and 2.60

Supercritical performance– At Mach number 2.65, the performance with the three bleed configurations was determined for various positions of the cowl lip–that is, contraction ratios. These results are shown in figures 13(a) through (c). With configurations A and B-1, the inlet remained started at the smallest value of cowl lip position (largest contraction ratio) possible with this model and therefore could be operated at design conditions ($x_{lip}/R = 2.325$). With configuration C, however the inlet unstarted near the smallest value of cowl lip position ($x_{lip}/R = 2.365$) indicated on figure 13(c) because of the low bleed, and thus could not be operated at design conditions ($x_{lip}/R = 2.325$) as a started inlet.

For all configurations, the distortion was considered low (≤ 10 percent) over the useful supercritical operating range. However, for configuration C, this range was small because, with the low bleed rates, the inlet unstarted before the terminal shock wave moved into the throat.

Tolerance to transients and stability margin– For most results, maximum and critical pressure recovery coincided; that is, maximum pressure recovery occurred just before the inlet unstarted. However, the inlet cannot normally operate at this point because it would unstart if a very small transient disturbance occurred (disturbances occurring so suddenly that the control system would have no time to respond with changes in geometry, such as opening the bypass and/or increasing the throat area). Therefore, the performance at supercritical conditions is of paramount importance. Possible operating points, where an acceptable stability margin is available for some missions, are indicated by the filled-in symbols in figure 13(a) through (c). At these points, the inlet unstarted at the angles of attack or Mach numbers shown in the tables. For instance, with bleed configuration A and the inlet operating at the design point–$x_{lip}/R = 2.325$ and 0° angle of attack–the angle of attack could change to 2° before the inlet unstarted. Although these values may not represent the tolerance to sudden changes, because the changes could only be made slowly, they do indicate possible incremental improvements as the cowl lip is retracted (reduced contraction ratio).

The choice of a supercritical operating point also provides an unstart stability margin. For example, for the point just discussed the pressure recovery and bleed mass-flow ratio can increase by 0.038 and 0.026, respectively, before the inlet unstarts. This means that the corrected weight flow demanded by an engine could decrease by 0.06 to 0.07 without unstarting the inlet.[2] If the inlet was operated at a higher pressure recovery and bleed mass flow than indicated by the filled symbols, the stability margin would decrease, and conversely, if operated at lower recovery and bleed, the stability margin would increase. However, the tolerance to a change in angle of attack or Mach number would not necessarily increase with the operating point at a lower pressure recovery.

With configuration B-1, the characteristics are quite similar to those with A although the transient tolerance and stability margin are less. With configuration C, however, these parameters are quite small. Thus, bleed configurations A and B-1 could provide sufficient stability margin and tolerance to transient disturbances for some missions with the "natural" characteristics of the inlet

---

[2] The change in corrected weight flow is approximately the sum of the increase in bleed and pressure recovery.

system, whereas with configuration C, some auxiliary device would probably be required to avoid unstart. All stability margins and transient tolerances apply only singly; two or more simultaneous disturbances would reduce the indicated values.

Similar data for Mach number 2.60 are shown in figures 14(a) through (c). For started operation at this Mach number, the cowl lip was retracted slightly (decreased contraction ratio), therefore there was some spillage. However, pressure recovery, distortion, bleed mass flow, and stability margin were about the same as at Mach number 2.65. The tolerance to transients was also about the same as at Mach number 2.65, although these data are shown only for configuration B-1.

Cowl bleed back pressure– For the results shown in figure 13 ($M_\infty = 2.65$), the bleed plenum exit areas were such that the pressure ratio across the bleed holes indicated choked conditions. Similar results, with smaller cowl plenum exit areas (bleed holes not choked), are shown in figure 15 for bleed configuration A. (The data indicated by the circles are repeated from fig. 13). At a constant pressure recovery, bleed mass flow decreased significantly for all reduced cowl exit area combinations (curves represented by all symbols except circles). However, the inlet tolerance to changes in angle of attack also decreased when operating at the points represented by the filled symbols. These points represent a slightly different stability margin for each configuration; for an identical margin, the differences in unstart angle of attack might be less, but pressure recovery would be lower.

Performance with changes in angle of attack or Mach number– The limits of transient disturbances that could occur without unstarting the inlet were discussed previously. In addition, when these disturbances do occur, pressure recovery must not decrease nor distortion increase significantly. The changes in pressure recovery, distortion, and bleed mass flow that occurred when the angle of attack or Mach number was changed are shown in figure 16(a) and (b). At 0° angle of attack, the data are the filled-in symbol data from figures 13 and 14. In general, as the Mach number was decreased, pressure recovery and bleed mass flow increased because the terminal shock wave moved upstream, while distortion decreased. As the angle of attack was changed, pressure recovery decreased while distortion and bleed mass flow increased. However, neither angle of attack nor Mach number changes caused large performance penalties.

Distortion– The total pressure distortion shown in figure 16 was calculated with the rakes at the engine face located between the support struts (see fig. 2(c)). Distortion is more accurately determined from detailed surveys with the rotating rakes. Circumferential total pressure profiles, from which the distortion parameter (Δp_{t_2}) can be calculated, are plotted at various radial distances from the inlet centerline in figure 17 for bleed configuration A and for conditions corresponding to the chosen operating point (filled triangles in fig. 13(a)). Profiles are shown for 0° angle of attack and for positive and negative angles near those where the inlet unstarted. The pressures at 60°, 180°, and 300° were measured with three rakes behind the support struts; these pressures are considered static since they were the same as the local surface static pressures. The filled symbols indicate pressures used to calculate the listed pressure recovery and distortion. Distortion calculated by considering all pressures (excluding statics behind the struts) would be about 1 to 2 percent higher, and pressure recovery similarly computed would be about the same as the listed values.

At 0° angle of attack, the pressures were relatively low near the cowl surface ($r/R = 0.837 - 0.954$), but were consistent with the low performance of the supersonic diffuser near the cowl surface noted earlier. Furthermore, there were total-pressure gradients near one side of each strut from $r/R = 0.623$ to 0.954. The reason for these gradients is not known. Without the gradients, circumferential distortion would be very low and most of the distortion would be radial.

Profiles are shown at both positive and negative angles of attack (figs. 17(b) and (c)) because the support struts were asymmetric in the angle-of-attack plane. At both positive and negative angles, circumferential distortion was higher than at 0°. Moreover, at both positive and negative angles, there were regions of separated flow near the cowl surface. (The flow is considered to be separated when the total and static pressures are equal.)

Static pressure distributions– Static pressure distributions, recorded as the terminal shock wave moves upstream, may reveal unnecessary compression or expansion regions, which reduce the compression efficiency and the effectiveness of the bleed system. Typical distributions, with sketches of the cowl and centerbody geometry alined with these distributions, are shown in figure 18 for Mach numbers 2.65 and 2.60.

At both Mach numbers the inlet remained started with the terminal shock wave well upstream of the throat. (The terminal shock was located where $p/p_\infty \simeq 10$ to 12.) Moreover, the terminal shock wave feeds farther upstream through the boundary layer. These shock wave phenomena give a greater change in bleed mass flow and hence a greater stability margin than would be expected from inviscid considerations.

In the subsonic diffuser, the flow expands smoothly on the centerbody to the engine face except for the sudden drop at $x/R \simeq 4.7$, which is probably caused by the vortex generators, although there is no comparable drop on the cowl. However, on the cowl, the flow compresses locally at $x/R \simeq 5.9$. Since the contours were designed for a continuous area expansion, the reason for these local compressions is not understood.

Static-pressure distributions at angle of attack must be considered in control system design. Cowl static-pressure distributions, with the inlet operating supercritically, are shown in figure 19 for 0° and ±1.3°, corresponding to leeward and windward pressures, respectively. At angle of attack, the leeward pressure gradient in the supersonic diffuser increased and the windward gradient decreased. At the same time, the terminal shock wave moved slightly downstream on the leeward and upstream on the windward side. As a consequence, this flow asymmetry would require that flow sensors be located at multiple circumferential positions.

Changes in static-pressure distributions as the Mach number decreases must also be considered for control system design. Figure 20 shows centerbody static-pressure distributions as the Mach number was decreased from 2.65 to 2.58. For small decreases in Mach number, the terminal shock wave was nearly stationary ($p/p_\infty \simeq 10\text{-}12$). However, near the Mach number where the inlet unstarted ($M_\infty = 2.58$), the terminal shock wave moved upstream, resulting in a small region of subsonic flow upstream of the throat.

Bleed mass flow and pressure recovery– The mass flows and corresponding pressure recoveries in the plenum chambers for the individual bleed zones are required to determine the drag of the bleed system. These quantities are shown in figures 21 through 24 and correspond to the supercritical performance shown in figures 13 and 14. In general, the change in total bleed flow results from changes in all zones as shown in figures 21 and 22 for Mach numbers 2.65 and 2.60, respectively. As the terminal shock wave moved upstream, changes first occurred in zones 3 and 4 (throat bleed), and as the shock wave moved further upstream changes occurred in zones 1 and 2 (supersonic diffuser bleed). The advantage of changes in bleed in all zones is a larger stability margin compared to a system where only the throat bleed changes. The corresponding plenum chamber pressure recoveries are shown in figures 23 and 24 for Mach numbers 2.65 and 2.60, respectively. These pressures would be considerably higher, with no reduction in the measured mass flows, if the bleed exit areas were reduced so that the pressure ratio across the holes at critical conditions was just sufficient to choke the flow through the holes. The data in figures 23 and 24 show that if the inlet is operated supercritically, the bleed plenum chamber pressure recovery will be reduced considerably. That is, for critical (maximum) conditions (fig. 23(a)) the plenum recovery for bleed zone 3 was about 35 percent; if the pressure recovery at the engine face was reduced, say to 91 percent to satisfy stability margin requirements, the plenum recovery would be only about 20 percent, considerably less than would be possible with no control margin requirement.

The effect of reduced cowl bleed plenum exit areas on the supercritical performance is shown in figure 15 and was discussed previously. The individual cowl bleed mass flows and plenum chamber pressure recoveries corresponding to these results are shown in figure 25. (The unstart angles of attack shown in figure 15 are repeated.) In some cases, the plenum pressure recovery was increased at critical conditions without reducing the mass flow. For instance, compare the curves indicated by the circles and right triangles for zone 1; at critical conditions, the plenum recovery was increased 0.04 while the mass flow remained nearly the same. However, many more combinations of exit areas would have to be investigated to find those that gave the highest plenum recovery while maintaining the required inlet performance.

Bypass– The previous discussion considered only results with the bypass exit closed. At the design Mach number, the bypass serves several purposes: to provide small mass flows for engine cooling requirements, to provide matching of the inlet-engine airflow, and to remove large mass flows in the event of a serious engine malfunction. Therefore, high pressure recovery and low distortion at the engine face, over a large range of bypass mass flows is important. Figures 26 and 27 show the inlet performance, as a function of mass flow at the engine face, for various bypass exit area ratios. As was the case with zero bypass, pressure recovery was high and distortion was low over a range of supercritical operation for all bypass exit area ratios. A natural consequence of operation with bypass is that the stability margin increased (change in mass flow plus pressure recovery from operating to critical conditions). This occurs because, in addition to changes in bleed and pressure recovery, there were changes in bypass as the terminal shock wave moved upstream.

The bypass mass flow and plenum chamber pressure recovery are required to calculate bypass drag. These quantities are shown in figures 28 and 29 for the supercritical performance data just discussed. At a constant total pressure recovery, the bypass plenum recovery is nearly constant for mass flows of about 15 percent or less, and decreased for larger mass flows.

Angle of attack– The previous discussion of performance at angle of attack was confined to small angles where no change in the geometry at or near design conditions was required for started operation. At larger angles, the contraction ratio must be reduced (x_{lip}/R increased) for started operation. When operating under these conditions, an engine can tolerate rather low inlet pressure recovery although the engine performance is reduced, but to avoid compressor stall it is important that distortion not be excessive.

Circumferential total pressure profiles are shown in figure 30 for ±4° angle of attack. At both angles, pressure recovery was considered acceptable while distortion was considered high. (Sustained engine operation with this distortion could cause thrust loss and/or stall.) However, for this cowl lip position ($x_{lip}/R = 2.981$), the centerbody bleed was well upstream of the throat; on an operational inlet system, the centerbody bleed would remain near the throat as the centerbody was extended, and hence the angle of attack performance might improve.

Vortex generators– For the performance discussed above, vortex generators were located on the cowl and upstream on the centerbody (configuration AA). At this centerbody position they entered the supersonic flow field when the cowl was translated for off-design operation and thus were expected to cause performance penalties. For this reason, the performance was measured for other configurations with smaller generators that might reduce the disturbance in the supersonic flow field (configuration CC), with the centerbody generators moved downstream to enter the supersonic stream at a lower Mach number where penalties might be less (configuration DA), and without vortex generators if no configuration with them was acceptable at lower Mach numbers (configuration 00). The performance with these configurations is shown in figures 31 and 32. Pressure recovery was about constant for all configurations with vortex generators, but distortion was low (<10 percent) over the useful supercritical operation range only with AA. Without vortex generators (fig. 31 (a)), the supercritical pressure recovery at a constant bleed mass flow decreased 1 to 2 percent and the corresponding distortion was considerably higher than with AA. This high distortion was caused by separation on the cowl shown by the radial total pressure profiles in figure 33. At maximum pressure recovery, there is no separation without vortex generators, and therefore the generators reduce distortion only moderately. However, at supercritical conditions ($\bar{p}_{t_2}/p_{t_\infty} \approx 0.91$,), the flow is separated on the cowl without vortex generators; thus distortion is considerably lower with generators.

Off-Design Supersonic Performance

Operation at off-design supersonic Mach numbers ($M_\infty = 2.65$ to 1.55) required translation of the cowl, and, as this was done, the throat moved downstream on the centerbody. This throat movement required alteration of both the centerbody bleed hole pattern and vortex generator configuration for good performance. However, because these alterations were made manually, only a limited number were investigated, and hence the best configurations were not necessarily found.

Maximum performance– Because performance penalties were found when the vortex generators entered the supersonic flow field as the cowl was retracted, they were removed for much of the investigation. The maximum pressure recovery and corresponding distortion and bleed mass flow that resulted with the vortex generators removed are shown in figure 34. In the bleed configuration key shown in figure 34, the numbers 1 through 4 indicate centerbody throat bleed moved progressively downstream (see fig. 7(b)). In addition, the designation B'indicates additional holes opened in zone 2. Each configuration was tested over a range sufficient to find the Mach number for the highest performance. The Mach number for maximum pressure recovery decreased as the bleed in zone 4 was moved downstream. Because of the low surface pressures, bleed mass flow was relatively low for configuration B'-4, which could explain the relatively low pressure recovery and high distortion.

Supercritical performance– Supercritical performance, corresponding to the maximum performance in figure 34, is shown in figure 35 for Mach numbers from 2.56 to 2.0. As at the design Mach number, maximum and critical pressure recovery coincide. That is, maximum pressure recovery occurred just before the inlet unstarted for all configurations. However, the bleed configuration that gave the highest critical pressure recovery at each Mach number did not necessarily give the best supercritical performance. For instance, at Mach number 2.50 (fig. 35(b)), the critical pressure recovery was highest with bleed configuration B-2 while at supercritical conditions, say 6 percent bleed, the best performance was with configuration B-1. At critical conditions for most configurations, distortion was 10 percent or less, while supercritically it increased significantly.

Vortex generators– A number of vortex generator configurations were investigated in an attempt to reduce the high distortion at supercritical conditions without vortex generators. These results are shown in figures 36 through 44. (Figure 8 gives a key to the vortex generator configurations.) The basic configuration denoted AA was tested at Mach numbers 2.65 and 2.60. The other configurations, tested at lower Mach numbers, involved a variation in circumferential spacing (configuration B), height (configuration C), or axial location on the centerbody (configuration D). Although no single configuration was tested at all Mach numbers, some conclusions about their relative merits can be drawn. The lowest distortion and best operating point (bleed versus pressure recovery at supercritical conditions) was obtained with a relatively dense spacing of vortex generators located just downstream of the throat on both cowl and centerbody (configuration CC, figs. 36(b), 37(b), and 38(b)). However, when this or any other configuration with vortex generators on the centerbody entered the supersonic flow field, distortion was high and pressure recovery relatively low (e.g., figs. 42(b), 43, and 44). With vortex generators on the cowl only (configurations OA, OB, and OC), distortion and pressure recovery were generally about the same or slightly lower than without vortex generators (e.g., figs. 37(c), 38(c), 39, 40, . . .). Overall, this investigation showed that the best overall performance throughout the Mach number range was obtained without vortex generators (configuration 00).

The relative effectiveness of the various vortex generators configurations is shown in figure 45 by radial total pressure profiles from a typical rake at the engine face. These profiles show that vortex generators have effects that depend on the shape of the profile without vortex generators. When this profile is relatively "full" near either wall (e.g., fig. 45(c) or (d) near the cowl), vortex generators on that surface reduce pressure recovery considerably. When the profile without vortex generators is not "full" near a wall (e.g., fig. 45(a) or (b) near the centerbody for the point labeled "supercritical"), vortex generators can reduce distortion and can increase pressure recovery. When the profile without vortex generators is moderately "full" (e.g., fig. 45(a) at maximum pressure recovery) near either wall, vortex generators reduce distortion and pressure recovery only slightly. From these results, it was expected that vortex generators downstream on the centerbody would have reduced the distortion at Mach number 2.10 (fig. 45(c)), because they were in the subsonic diffuser. This was not the case, however–perhaps because they were too high (fig. 8). With centerbody generators in the supersonic diffuser (fig. 45(d)), distortion was considerably higher and pressure recovery considerably lower than without vortex generators, although there was no evidence of separation for either configuration.

Circumferential variations in total pressure are more important than radial because of the relatively greater sensitivity of engines to the former. Circumferential variations are shown at Mach number 2.56 in figure 46(a), (b), and (c) for configuration 00, for configuration BB, and for configuration CC, respectively. Pressures at 60°, 180°, and 300° are considered to be static, as previously noted in the design point data. Without vortex generators, the variation in pressure at a fixed radius was small. Therefore, the indicated distortion ($\Delta p_{t_2} = 0.152$) was mostly radial. However, the flow was almost completely separated (static and total pressure equal) near the centerbody ($r/R = 0.429$ and 0.534), and there were extensive regions of low pressure between the struts at $r/R = 0.623$, 0.701, and 0.773.

With vortex generator configuration BB or CC, the pressures were randomly distributed at each radius, but circumferential distortion was generally low. The decrease in indicated distortion ($\Delta p_{t_2} = 0.144$ and 0.128 for configurations BB and CC, respectively) was due to an increase in the minimum measured pressure and a decrease in the maximum. With configuration BB, the region of separated flow was small ($r/R = 0.429$ near 300° strut) and with CC, separation was eliminated. In addition, unlike the profiles without vortex generators, there was considerable flow asymmetry at most radii for both configurations. Because of this asymmetry, it is concluded that even though configuration CC gave the best inlet operating point (lowest bleed and distortion at a constant pressure recovery), the mixing induced by the vortex generators was incomplete, hence performance might be improved considerably with other vortex generator configurations.

Circumferential total-pressure profiles for Mach numbers 2.10 and 1.75 are shown in figure 47 for configurations B′-3 and B′-4, respectively, and vortex generator configuration 00; these combinations gave the highest pressure recovery and lowest distortion at these Mach numbers. The profiles are for supercritical operation at Mach number 2.10 and for critical at Mach number 1.75 because the inlet was self-starting (i.e., no change in geometry was required to restart the inlet). At Mach number 2.10 (fig. 47(a)), the profiles are similar to those without vortex generators at Mach number 2.56 (fig. 46(a)). That is, there were regions of low pressure between the struts at $r/R = 0.429$ to 0.773. However, at Mach number 2.10, the flow was not separated at radii near the centerbody as it was at Mach number 2.56. Thus, the circumferential distortion was quite low, and the indicated distortion ($\Delta p_{t_2} = 0.114$) was mainly radial. At Mach number 1.75, the profiles are much like those at Mach number 2.10, except for regions of low pressure near the top of the duct. These low pressure regions meant that circumferential distortion was somewhat higher than at Mach number 2.10.

Transient performance– As at the design Mach number, the inlet must remain started with acceptable pressure recovery and distortion when transient disturbances are encountered. The effects of angle of attack on the principle performance parameters with the inlet started are shown in figure 48. At all Mach numbers, angles slightly larger than those shown unstarted the inlet, except Mach number 1.75, where the inlet was self-starting and data were recorded at angles where the terminal shock wave was external. At all Mach numbers, pressure recovery decreased and the corresponding distortion and bleed mass flow increased with changes in angle of attack from zero. The asymmetry of these changes at positive and negative angles could be caused by the asymmetry of the struts.

Static pressure distributions– At off-design conditions, static pressure distributions are important for the same reasons discussed in the section dealing with design Mach number static pressure distributions. Centerbody static pressure distributions at 0° angle of attack are shown in figure 49 as the terminal shock wave moved upstream. At Mach number 2.56 (fig. 49(a)) the compression is nearly continuous upstream of the terminal shock wave. (The terminal shock wave is located in the region where the pressures indicate slightly supersonic to slightly subsonic flow

$p/p_\infty \simeq 9$ to 11 at Mach number 2.56.) At the lower bleed flows, the slight expansion at $x/R \simeq 4.25$ could be caused by bleed zone 4. However, at Mach numbers 2.00 and 1.75 (fig. 49(b) and (c), respectively), there are extensive expansion regions upstream of the terminal shock wave (e.g., $x/R \simeq 4.25$-4.55, fig. 49(b)). Without these expansions, the compression could be accomplished within a shorter length. In addition, at all Mach numbers, the inlet remained started with the terminal shock wave upstream of the geometric throat. This increased the change in throat bleed, and hence increased the inlet stability margin. At all Mach numbers, bleed zone 2 was located near the initial adverse pressure gradient on the centerbody, which may account for the relatively good performance throughout the Mach number range.

Static pressure distributions at angle of attack must also be considered at off-design conditions for reasons previously discussed. Centerbody static-pressure distributions at angle of attack are shown in figure 50 for four off-design supersonic Mach numbers. (The pressures at positive and negative angles are on the leeward and windward sides, respectively.) In the supersonic diffuser, the pressure rise generally moved upstream and downstream on the leeward and windward sides, respectively, although at each Mach number the gradient remained about the same. (At Mach number 1.75, the terminal shock wave was external at positive angle of attack.) However, the movement of the terminal shock wave was inconsistent with changing angle of attack. At Mach number 2.56, its movement was not clearly defined ($p/p_\infty \simeq 9$ to 11); at Mach number 2.50, it moved upstream and downstream on the windward and leeward sides, respectively ($p/p_\infty \simeq 4.5$ to 5.5). At Mach number 1.75, the terminal shock wave moved far upstream ($p/p_\infty \simeq 2.5$ to 3.0) because the inlet was unstarted.

Static-pressure distributions for a single bleed configuration at each Mach number were shown in figures 49 and 50. Distributions for different bleed configurations at a constant Mach number can be important for control system analysis. Results from three bleed configurations are shown in figure 51 for Mach number 2.41 and 0° angle of attack as the terminal shock wave moved upstream. The compression was not particularly efficient for any configuration, since there were expansion regions or plateaus ($x/R \simeq 4.2$ to 4.6) upstream of the terminal shock wave ($p/p_\infty \simeq 7$ to 9). However, the pressure distributions probably are most favorable with the throat bleed upstream (fig. 51(a)), because there was no subsonic flow upstream of the pressure rise through the terminal shock wave ($p/p_\infty \simeq 7$ to 9). This configuration also had the lowest supercritical bleed flow (0.05 at 91-percent pressure recovery) and the largest change in bleed from this point to critical conditions; hence, it had the largest stability margin.

Bleed mass flow and pressure recovery— Calculation of bleed drag requires the mass flows and corresponding plenum chamber pressure recoveries for each zone. The mass flows are shown in figure 52 for the Mach number range 2.56 to 1.75. The bleed exit areas were not changed from those at Mach number 2.65 because variable exits will probably not be part of an operational system. At the higher Mach numbers ($M_\infty \geq 2.41$), where the centerbody bleed was concentrated for good performance, the mass flow changed through all zones as the terminal shock wave moved upstream. At the lower Mach numbers ($M_\infty \leq 2.30$), where the centerbody throat bleed was moved downstream for good performance, the mass flow through zone 2 did not change. In addition, the change in mass flow through zone 1 decreased. These effects reduced the change in total bleed flow from supercritical to critical conditions and hence, reduced the inlet stability margin from that at the higher Mach numbers.

The bleed plenum chamber pressure recoveries, corresponding to the mass flows just discussed, are shown in figure 53. As at the design Mach number, these recoveries were somewhat low (see design Mach number discussion), and they show that operation of the inlet at less than maximum pressure recovery, thereby providing some stability margin, decreases the operating bleed plenum chamber pressure recovery considerably. For instance, at Mach number 2.56 (fig. 53(a)), if operation at 91-percent pressure recovery is needed for the required stability margin, bleed zone 1 will provide about 0.20 plenum chamber pressure recovery (0.10 less than the highest measured value).

Bypass– The previous discussion considered only results with the bypass exit closed. However, small bypass mass flows are generally required for inlet-engine matching at off-design supersonic Mach numbers; in addition, large mass flows might be required for matching in the event of an engine malfunction. Therefore, good inlet performance is important for a wide range of bypass mass flows. The inlet performance with bypass, as a function of the mass-flow ratio at the engine face, is shown in figure 54 for the Mach number range 2.30 to 1.75. At a constant pressure recovery, the bypass mass-flow ratio is the increment between any curve with bypass and the curve for zero bypass. Maximum (critical) pressure recovery was nearly constant at each Mach number for small bypass mass flows ($A_{bp_e}/A_c \leq 0.081$) and decreased for large mass flows. The corresponding distortion generally increased with increased bypass. At a constant supercritical pressure recovery (e.g., 91 percent), distortion was generally constant for all bypass mass flows.

Operation with bypass will increase the inlet drag. The momentum drag penalty can be calculated with the bypass mass flows and plenum chamber pressure recoveries shown in figure 55, although it was not done in this investigation. However, the data show that the plenum chamber pressure recovery increased with increased mass flow (at a constant pressure recovery) and thus increased the available momentum. This occurred mainly because a greater percentage of the high energy core flow was removed as the mass flow increased.

Transonic Performance

To deliver the high mass-flow ratio provided in the design to the engine face, all transonic testing was done with the bleed exits closed. In addition, because vortex generators were found to cause performance penalties, most data were obtained without them.

The performance at 0° angle of attack without vortex generators is shown in figure 56. Of the indicated positions of the cowl lip, the highest theoretical mass-flow ratio (noted on each figure) occurred with $x_{lip}/R = 3.881$: with $x_{lip}/R = 4.088$, the cowl lip was at the station of maximum centerbody diameter. Mass-flow ratios as high as the theoretical maximums were not measured at any Mach number. However, the blockage of the rakes for measuring mass flow was about 1 percent of the throat area. Since no correction was made for this blockage, the inlet may actually have captured nearly the maximum theoretical mass-flow ratio.

When operating at maximum mass-flow ratio, distortion is high and the pressure recovery relatively low, and therefore, an actual inlet would probably have to operate at a reduced mass-flow ratio. If operation was restricted by some arbitrary distortion limit, say 15 percent, the mass-flow ratio would be about 0.57 at Mach number 1.0, and about 0.64 at Mach number 0.6, or 0.02 and 0.06 less than the theoretical maximums, respectively. In addition, as the mass-flow ratio decreased, the additive drag increased because of increased spillage, which theoretically is offset by lip suction. However, lip suction was not measured experimentally.

A comparison of the transonic performance with and without vortex generators is shown in figure 57 for the cowl lip position with the largest mass-flow ratio $x_{lip}/R = 3.881$. At reduced mass-flow ratios, vortex generators decreased distortion slightly and were somewhat more effective at the higher Mach numbers. However, at higher mass-flow ratios, where the inlet would normally operate, there was little or no change in distortion with vortex generators. In addition, vortex generators reduced the pressure recovery, but at maximum mass flow the curves do tend to converge.

As for supersonic Mach numbers, pressure recovery and distortion must be acceptably high and low, respectively, at angle of attack. These parameters are shown in figure 58 for angles of attack up to 8°. Since mass-flow ratio could not be measured accurately at angle of attack because of flow asymmetry, it was assumed constant at the values measured at 0°. For this reason, the mass-flow ratios at 5° and 8° angle of attack are questionable. As the angle of attack was increased, pressure recovery decreased and distortion increased, and these effects increased with increasing Mach number.

The transonic distortion data previously shown were with the rakes at the engine face in a fixed position ($\theta_2 = 0°$). Total pressure profiles at constant radii, plotted from many circumferential measurements from the rotating rakes, are shown in figures 59 and 60 for Mach numbers 0.8 and 1.0. (Again, pressures at 60°, 180°, and 300° are considered static.) If all pressures (except those behind the struts) were used in computing distortion, it would be higher than indicated on each figure. For example, at Mach number 1.0 and 0° angle of attack (fig. 60(a)), the indicated distortion is 0.123; using all pressures it is 0.193 and is relatively constant at all angles of attack. However, the number of low-pressure regions increased with increasing angle of attack. With either method of calculation, the distortion at both Mach numbers was higher at 5° than at 8° angle of attack.

CONCLUDING REMARKS

A large-scale model of an axisymmetric inlet system, designed for isentropic compression supersonically and a large mass-flow ratio transonically, was tested. The effect of bleed and vortex generator configuration, bypass, angle of attack, etc., on the internal performance was measured.

There was good performance throughout the supersonic Mach number range only when the bleed and vortex generator configurations were changed. The inlet throat was nearly stationary relative to the cowl (i.e., it moved downstream relative to the centerbody) as the cowl was retracted for off-design operation. Thus, the performance was good throughout the supersonic Mach number range only when the centerbody throat bleed was moved downstream. In general, however, the performance was best when this bleed was upstream of the geometric throat. At the higher supersonic Mach numbers (2.41 to 2.65), the performance was best with a relatively dense spacing of vortex generators just downstream of the throat. At the lower supersonic Mach numbers (1.55 to 2.30), however, the vortex generators were in the supersonic flow field because the throat moved downstream on the centerbody as the cowl was translated, and therefore the performance was better without vortex generators.

At transonic Mach numbers (0.6 to 1.1), the bleed exits were closed so that the high mass flow included in the design would be delivered to the engine face. In addition, as at the lower supersonic Mach numbers, the performance was better transonically without vortex generators.

With the best bleed and vortex generator configurations, the following results were obtained:

1. With moderate boundary layer bleed in the supersonic diffuser ($m_{bl}/m_\infty \simeq 0.02$ to 0.035 in zones 1 and 2), distributed on the cowl and centerbody in the regions of adverse pressure gradient, measurements indicated that most of the flow at the inlet throat had been compressed isentropically at all supersonic Mach numbers (1.55 to 2.65).

2. With bleed in the throat region, total-pressure recovery at the engine face and bleed mass-flow ratio increased as the terminal shock wave moved upstream, thus providing an inlet stability margin to unstart at all Mach numbers.

3. At supersonic Mach numbers 2.65 and 2.60, maximum total-pressure recovery at the engine face was greater than 94 percent with a corresponding bleed mass-flow ratio of approximately 0.08 and a corresponding total pressure distortion of less than 10 percent. At lower supersonic Mach numbers (1.55 to 2.56), maximum total pressure recovery was in the range of 92 to 96 percent with bleed mass flow ratios from 0.045 to about 0.09. For these Mach numbers, corresponding distortion was about 10 to 15 percent.

4. At transonic Mach numbers (0.6 to 1.1), total pressure recovery at the engine face ranged from 90 to 93 percent and the corresponding total pressure distortion from 20 to 30 percent when the inlet was operated at maximum mass-flow ratio ($m_i/m_\infty = 0.59$ for $M = 1.0$). However, when the mass-flow ratio was reduced by 0.02 to 0.06 for Mach numbers 1.1 to 0.60 respectively, pressure recovery increased to about 96 percent and distortion decreased to about 15 percent.

5. If operated at Mach number 2.65 and 0° angle of attack, with a stability margin of about 0.07, the inlet remained started without changing geometry at angles of attack up to about 2.5° with bleed distributed in the supersonic diffuser; with bleed concentrated in a relatively small region, the inlet unstarted at about 1°.

Ames Research Center
National Aeronautics and Space Administration
Moffett Field, Calif., 94035, April 1972

APPENDIX A

ESTIMATION OF THE MAXIMUM TRANSONIC MASS-FLOW RATIO OF AN AXISYMMETRIC-SUPERSONIC INLET WITH A TRANSLATING CENTERBODY

For axisymmetric supersonic inlets that achieve the required area variations for operation throughout the Mach number range by extending the centerbody, equations for calculating the highest transonic mass-flow ratio that could be included in the design, and the internal dimensions necessary for this result, can be derived from geometric considerations at the design Mach number and at Mach number 1.0. The sketch shows the internal dimensions that must be considered in the derivation. (Note the centerbody has been split to show the geometry at both Mach numbers.)

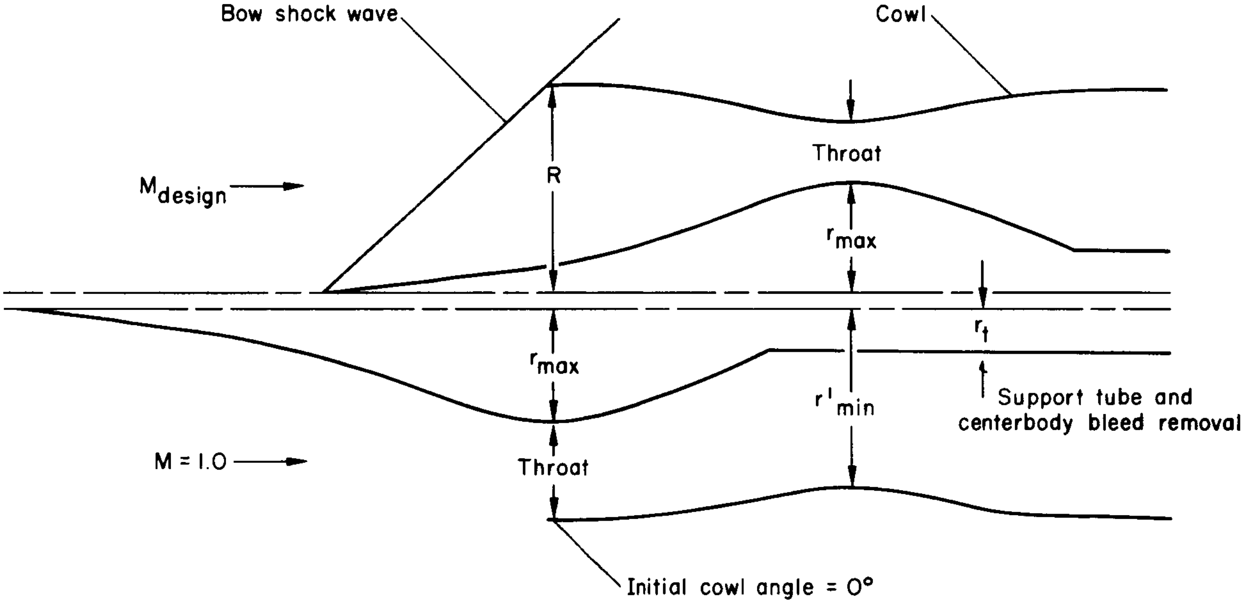

Two geometric considerations are necessary for the derivation: (1) at the design Mach numbers, the critical dimensions (r_{max}, r'_{min}) must be longitudinally alined and the inlet throat must be located at that station; and (2) for transonic operation, the contouring of the centerbody must terminate upstream so that the critical cowl dimension (r'_{min}) is longitudinally alined with the centerbody support tube (r_t).

At the design Mach number, the inlet contraction ratio (C) is defined by:

$$\frac{(A/A_*)_{M_{design}}}{(A/A_*)_{M_{throat}}} \frac{P_{t_{throat}}}{P_{t_\infty}} = C \frac{R^2}{r'^2_{min} - r^2_{max}} \tag{A1}$$

At Mach number 1.0, the throat area ratio is defined by:

$$\left(\frac{A_o}{A_c}\right)_{M=1.0} = 1 - \left(\frac{r_{max}}{R}\right)^2 = K\left[\left(\frac{r'_{min}}{R}\right)^2 - \left(\frac{r_t}{R}\right)^2\right] \tag{A2}$$

A constant K (<1) is introduced so that the area downstream, at the location of the minimum cowl radius (r'_{min}), does not become the throat due to boundary layer growth.

A simultaneous solution of equations ((A1) and (A2)) eliminates r'_{min}, and the resulting equation, when substituted in the left side of equation (A2) and rearranged, gives the equation for the transonic area ratio:

$$\left(\frac{A_o}{A_c}\right)_{M=1.0} = \frac{K}{K+1}\left[\frac{C+1}{C} - \left(\frac{r_t}{R_c}\right)^2\right]$$

The contraction ratio (C) is calculated from the desired flow conditions in the throat at the design Mach number. The support tube area ratio (r_t/R_c) is usually sized from the anticipated centerbody boundary-layer bleed mass flow, pressure recovery, and Mach number; data are available for the Mach number range 2.5 to 3.5 (refs. 1-3), so that these quantities can be estimated. The constant K that allows for transonic boundary layer is not so easily determined. However, if the support tube radius is oversized by say 4 percent, the transonic mass-flow ratio will be decreased by only 2 percent (K appears as $K/(K+1)$ in the formula). After these quantities are specified and the transonic area ratio calculated, the critical dimensions (r_{max}, r'_{min}) required for this result can be calculated from equation (A2).

Large rates of change of surface slope with distance must be avoided and off-design area distributions must be considered. However, any reduction in the transonic area ratio can be somewhat compensated with a positive initial cowl angle as was used for the present design. The following quantities were used in the calculations for the present design:

$C = 2.90$* *(Calculated from $M_{design} = 2.65$, $M_{throat} = 1.25$, $\frac{p_{throat}}{p_{t_\infty}} = 1.0$)

$K = 0.97$

$\frac{r_t}{R} = 0.36$

The calculated and actual design values of the transonic area ratio and critical dimensions are compared in the table below.

	Calculated	Actual design
A_o/A_c	0.598	0.5956
r_{max}/R	.633	.6481
r'_{min}/R	.864	.8645
Initial cowl angle	0°	1.5°

APPENDIX B

EFFECT OF CHANGING THE COWL CONTOUR TO ACCOUNT FOR THE BOUNDARY-LAYER DISPLACEMENT THICKNESS

At Mach number 2.65 the experimental surface pressures and gradients in the supersonic diffuser were greater than predicted by inviscid theory. This was attributed to the effects of boundary-layer displacement thickness. In an attempt to obtain better agreement between the inviscid theoretical and experimental distributions, the cowl was modified to compensate for the boundary-layer displacement thickness which was calculated with the aid of the computer program of reference 8, as shown in figure 61. Also shown are the regions for laminar, transitional, and turbulent boundary layers, and the location and thickness of material actually removed from the cowl. (The location for the start of transition was a required program input. For the centerbody, this was based on sublimation studies and for the cowl, on data from ref. 9 for flat plates.) Full compensation was not carried through all the way to the throat to avoid changing the contraction ratio, and thereby maintain comparable tunnel shock wave losses. Instead, the compensated contour was faired from $x/R = 2.950$ into the uncompensated contour at $x/R = 3.800$. No compensation was included in the centerbody contours because of model structural considerations.

The effect of the compensation on the pressure distributions on the cowl and centerbody are shown in figure 62. Some differences in the measured pressure distributions are seen, but the agreement with the inviscid theory is considered unimproved.

The effect of the compensation on the performance at the engine face is shown in figure 63. Pressure recovery as a function of bleed mass-flow ratio was approximately the same for both contours; the corresponding distortion was higher and the unstart angle of attack was slightly lower for the compensated contour. The differences in pressure recovery and distortion were attributed principally to the difference in vortex generator length (fig. 8) while the change in α_u was attributed to unfavorable differences in pressure distribution in the supersonic diffuser.

The effect on performance of adding boundary-layer compensation to the centerbody is not known. It is believed, however, that small additional changes in the contour would have small effects on the engine-face performance so long as the contraction ratio is not changed.

REFERENCES

1. Sorensen, Norman E.; and Smeltzer, Donald B.: Investigation of a Large-Scale Mixed Compression Axisymmetric Inlet System Capable of High Performance at Mach Numbers 0.6 to 3.0. NASA TM X-1507, 1968.

2. Smeltzer, Donald B.; and Sorensen, Norman E.: Investigation of a Nearly Isentropic Mixed-Compression Axisymmetric Inlet System at Mach Numbers 0.6 to 3.2. NASA TN D-4557, 1968.

3. Smeltzer, Donald B.; and Sorensen, Norman E.: Investigation of a Mixed-Compression Axisymmetric Inlet System at Mach Numbers 0.6 to 3.5. NASA TN D-6078, 1970.

4. Cubbison, Robert W.; Meleason, Edward T.; and Johnson, David F.: Effects of Porous Bleed in a High Performance Axisymmetric Mixed-Compression Inlet at Mach 2.5. NASA TM X-1692, 1968.

5. Sorensen, Virginia L.: Computer Program for Calculating Flow Fields in Supersonic Inlets. NASA TN D-2897, 1965.

6. Taylor, H. D.: Summary Report on Vortex Generators. UAC Research Department R-05280-9, 1950.

7. Sibulkin, Mervin: Theoretical and Experimental Investigation of Additive Drag. NACA Rep. 1187, 1954.

8. Maslowe, S. A.; Benson, John L.: Computer Program for the Design and Analysis of Hypersonic Inlets. NASA CR 114344, 1964.

9. Hopkins, Edward J.; Jillie, Don W.; and Sorensen, Virginia L.: Charts for Estimating Boundary-Layer Transition on Flat Plates. NASA TN D-5846, 1970.

TABLE 1. – INLET COORDINATES

Centerbody

$\frac{X}{R}$	$\frac{r}{R}$
0	0
Straight taper	
2.560	0.4055
2.650	0.4202
2.750	0.4367
2.850	0.4540
2.950	0.4721
3.050	0.4907
3.150	0.5103
3.250	0.5301
3.350	0.5509
3.450	0.5721
3.550	0.5940
3.650	0.6140
3.700	0.6218
3.750	0.6278
3.800	0.6329
3.850	0.6370
3.900	0.6407
3.950	0.6437

$\frac{X}{R}$	$\frac{r}{R}$	
4.000	0.6460	
4.050	0.6477	
4.088	0.6481	← $\frac{r_{max}}{R}$
4.125	0.6477	
4.175	0.6461	
4.225	0.6437	
4.300	0.6381	
4.400	0.6285	
Straight taper		
4.750	0.5916	
4.850	0.5793	
4.950	0.5640	
5.050	0.5468	
5.150	0.5289	
5.250	0.5066	
5.350	0.4807	
5.400	0.4640	
5.450	0.4430	
Straight taper		
5.650	0.3600	
Straight line		
8.565	0.3600	

Cowl

$\frac{X_c}{R}$	$\frac{r'}{R}$
0	1.000
Straight taper	
0.175	1.0046
0.250	1.0062
0.325	1.0073
0.375	1.0077
0.425	1.0078
0.500	1.0074
0.575	1.0062
0.650	1.0042
0.725	1.0011
0.800	0.9972
0.875	0.9921
0.950	0.9862
1.025	0.9792
1.100	0.9712
1.175	0.9622
1.250	0.9520
1.350	0.9379
1.450	0.9235
1.550	0.9093
1.650	0.8949
1.700	0.8875

	$\frac{X_c}{R}$	$\frac{r'}{R}$	
	1.750	0.8806	
	1.800	0.8758	
	1.833	0.8738	
	Straight taper		
	2.000	0.8662	
	2.025	0.8652	
	2.050	0.8647	
	2.075	0.8645	← $\frac{r'_{min}}{R}$
	Straight line		
	2.175	0.8645	
	2.275	0.8655	
	2.475	0.8700	
	2.675	0.8760	
	2.875	0.8821	
	3.075	0.8905	
	3.175	0.9001	
	3.375	0.9295	
	3.575	0.9582	
	3.675	0.9675	
	3.775	0.9733	
	3.875	0.9766	
	3.975	0.9784	
	4.165	0.9800	
	Straight line		
Engine face →	4.475	0.9800	

TABLE 2. – STRUT COORDINATES

$\frac{x_{st}}{R}$	Centerbody template $\frac{y_{st}}{R}$	Cowl template $\frac{y_{st}}{R}$
0	0.0458	0.0458
0.10	0.0620	0.0620
0.20	0.0783	0.0783
0.30	0.0899	0.0899
0.40	0.0965	0.0965
0.50	0.0997	0.0997
0.60	0.0999	0.0999
0.70	0.0955	0.0988
0.80	0.0884	0.0967
0.90	0.0760	0.0931
1.00	0.0552	0.0885
1.10	0.0190	0.0830
1.142	0	——
1.20	——	0.0751
1.30	——	0.0649
1.40	——	0.0510
1.50	——	0.0285
1.592	——	0

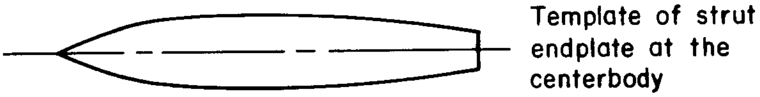

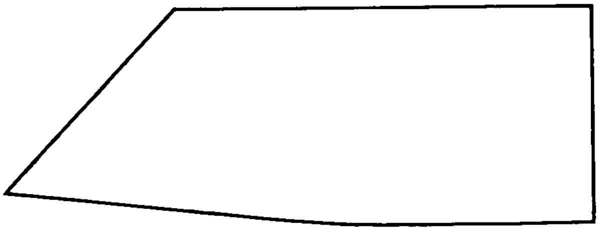

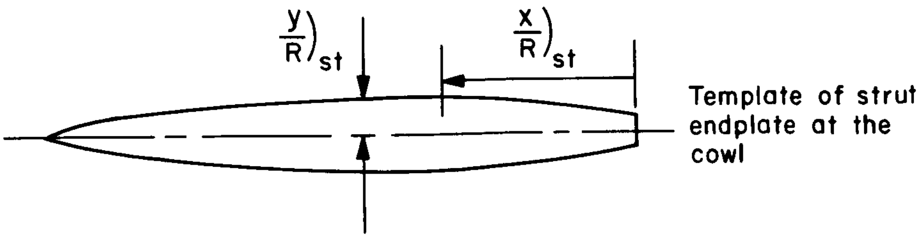

TABLE 3. – MACH NUMBERS, BLEED, AND VORTEX GENERATOR CONFIGURATIONS

Bl'd, Pat'n / M_∞	A	C	B–1	B–4	B′–1	B′–2	B′–3	B′–4
2.65	AA,CC, OO	AA	AA, DA	—	—	—	—	—
2.60	AA	AA	AA, DA	—	—	—	—	—
2.56	—	—	BB,BO,OO	—	BO, CO, CC,OO	—	—	—
2.50	—	—	AA, BB, BO, OO	—	BO, CO, CC, OO	OO	OB,DB,OO	—
2.41	—	—	BB, BO,OO	—	BO, CO, CC, OO	OO	OB,DB,OO	—
2.30	—	—	BB, OO	—	—	OO	OB, DB,OO	—
2.25	—	—	AA	—	—	—	DB	—
2.20	—	—	—	—	—	OO	OB,DB,OO	—
2.15	—	—	—	—	—	—	DB	—
2.10	—	—	—	—	—	OO	OB,DB,OO	—
2.05	—	—	—	OA	—	—	DB	OA,OO
2.00	—	—	AA	OA	—	—	OB, DB, OO	OA,OB,OC BB,CC,OO
1.95	—	—	—	OA	—	—	—	OA,OO
1.90	—	—	—	OA	—	—	—	OA,OB,OC BB,CC,OO
1.85	—	—	—	OA	—	—	—	OA,OO
1.80	—	—	—	—	—	—	—	OO
1.75	—	—	AA	—	—	—	—	OB, OC BB,CC,OO
1.70	—	—	—	—	—	—	—	OB,OO
1.55	—	—	AA	—	—	—	—	OC

TABLE 4. – INDEX TO FIGURES

Figure	Description
1	Model photograph
2	Model geometry
3	Design flow field
4	Area distributions
5	Throat location
6	Contraction ratio
7	Bleed patterns
8	Vortex generator configurations
9	Theoretical mass flow
10	Bleed development, $M_\infty = 2.65$
11	Pitot pressure profiles, $M_\infty = 2.65$
12-33	Design performance, M_∞ 2.65 and 2.60
12	Supersonic diffuser performance, $M_\infty = 2.65$
13	Supercritical performance, various x_{lip}/R, $M_\infty = 2.65$
14	Supercritical performance, various x_{lip}/R, $M_\infty = 2.60$
15	Supercritical performance, various bleed back pressures, $M_\infty = 2.65$
16	Transient disturbance performance, $M_\infty = 2.65$ and 2.60
17	Distortion at angle of attack, $M_\infty = 2.65$
18	Static-pressure distributions, $M_\infty = 2.65$ and 2.60
19	Static-pressure distributions at angle of attack, $M_\infty = 2.65$
20	Effect of Mach number on static-pressure distributions
21	Individual bleed zone flow, $M_\infty = 2.65$
22	Individual bleed zone flow, $M_\infty - 2.60$
23	Individual bleed plenum pressures, $M_\infty = 2.65$
24	Individual bleed plenum pressures, $M_\infty = 2.60$
25	Effect of back pressure on the cowl bleed flows, $M_\infty = 2.65$
26	Supercritical performance with bypass, $M_\infty = 2.65$
27	Supercritical performance with bypass, $M_\infty = 2.60$
28	Bypass mass flow and plenum pressures, $M_\infty = 2.65$
29	Bypass mass flow and plenum pressures, $M_\infty = 2.60$
30	Distortion at angle of attack, $M_\infty = 2.65$
31	Supercritical performance, various vortex generator configurations, $M_\infty = 2.65$
32	Supercritical performance, various vortex generator configurations, $M_\infty = 2.60$
33	Radial distortion, various vortex generator configurations, $M_\infty = 2.65$
34-55	Off-design performance, $M_\infty = 2.65$-1.55
34	Maximum performance with various bleed patterns
35	Supercritical performance with various bleed patterns
36-44	Supercritical performance with various vortex generator configurations
45	Radial distortion profiles
46-47	Circumferential distortion profiles
48	Transient angle of attack performance
49-51	Centerbody static pressure distributions
52	Supercritical bleed flow, individual zones
53	Bleed plenum chamber pressure recovery, individual zones
54	Supercritical performance with bypass

TABLE 4. – INDEX TO FIGURES – Concluded

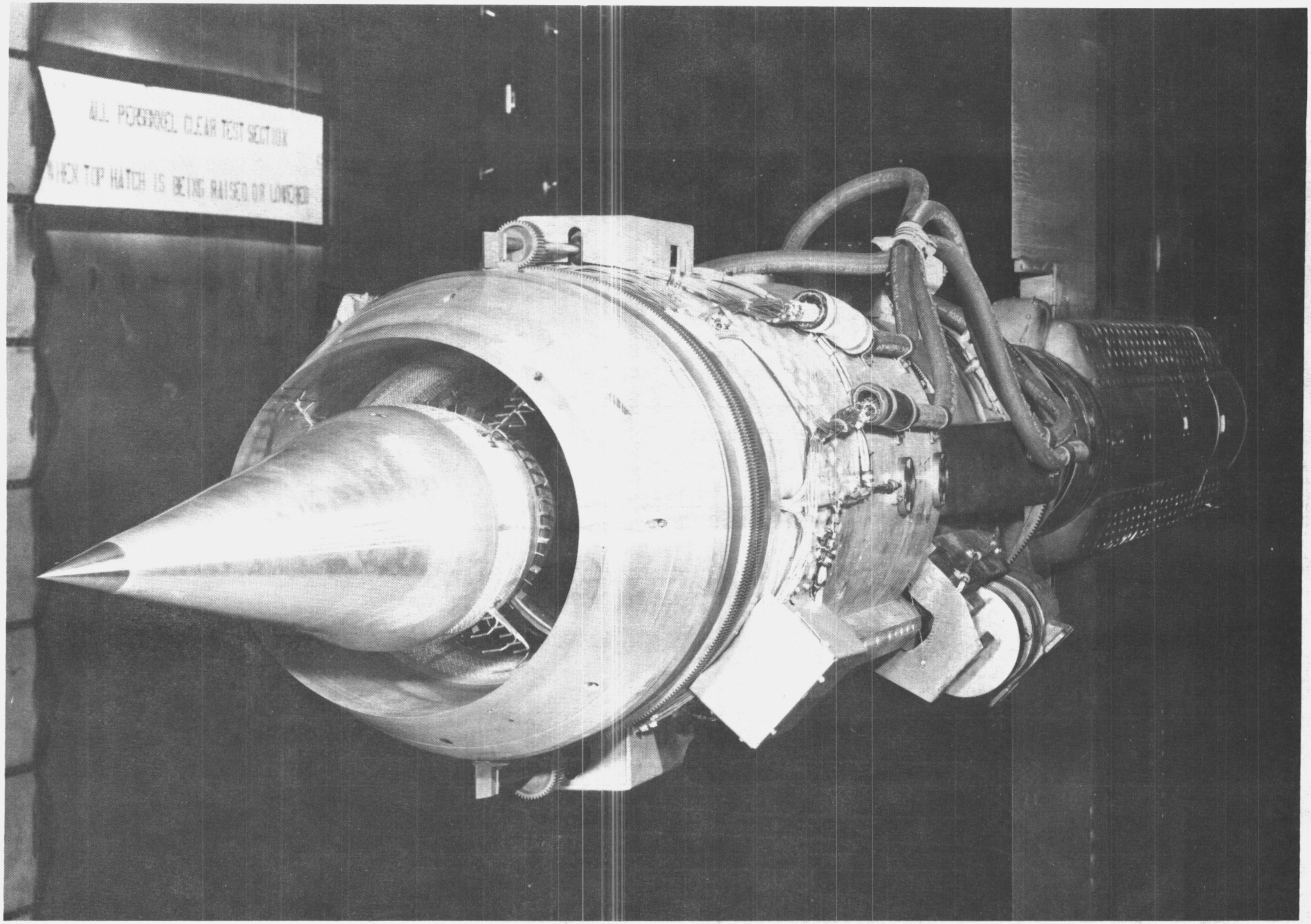

Figure 1. – Model mounted in transonic wind tunnel.

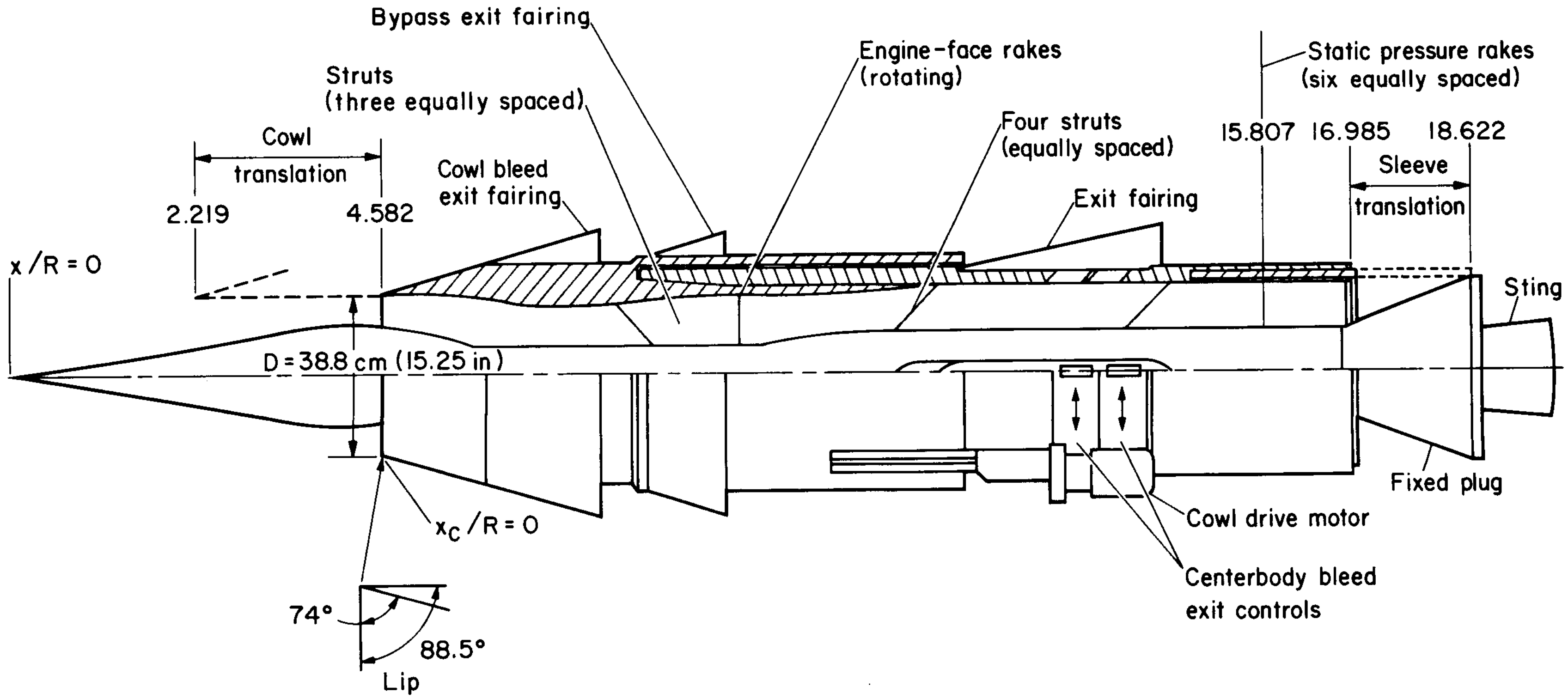

(a) Overall model.

Figure 2. – Model schematic.

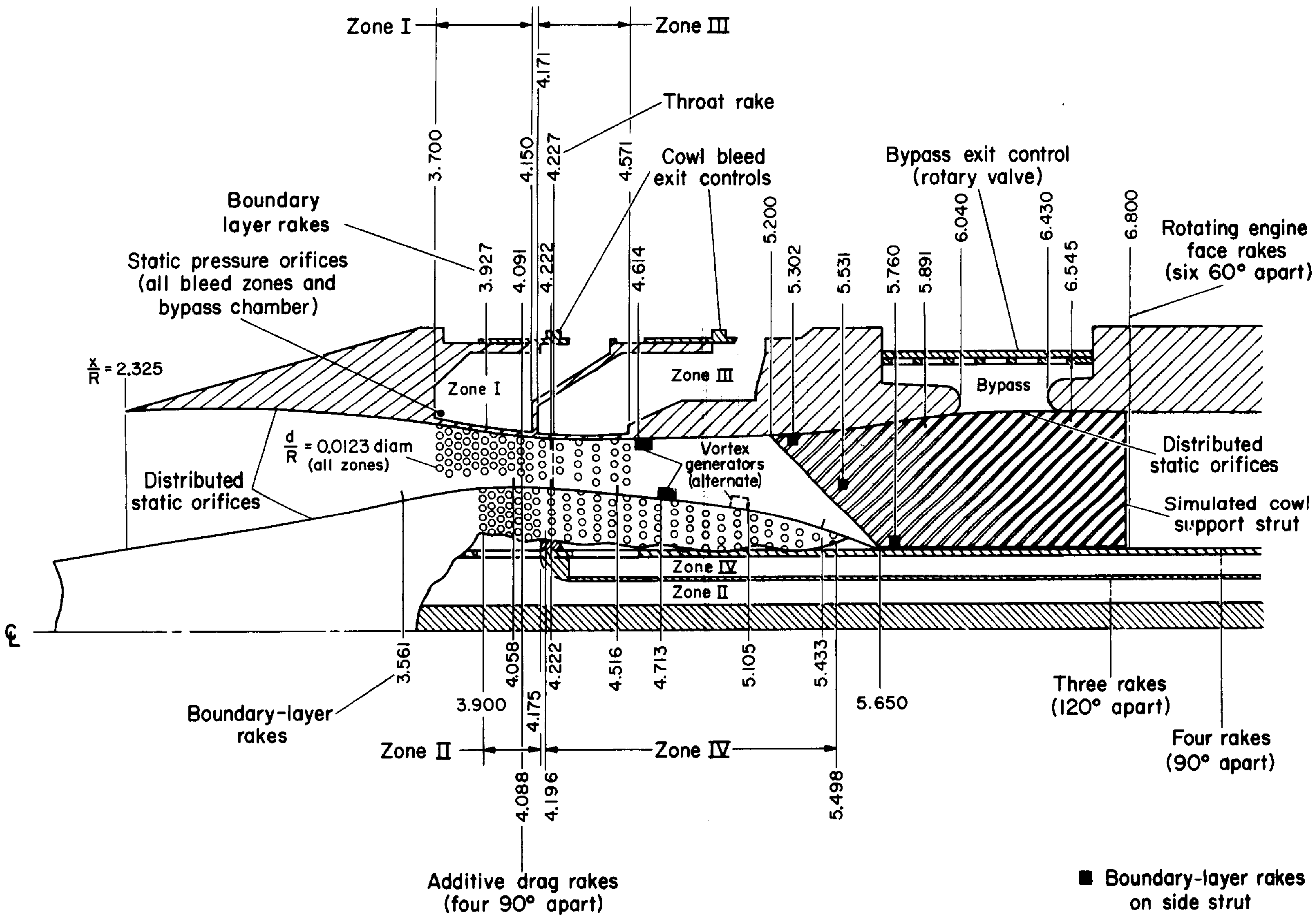

(b) Instrumentation, bleed, and bypass configurations.

Figure 2. – Continued.

The position of the rotating engine-face rake assembly is designated by θ_2 with the 0° position as shown below.

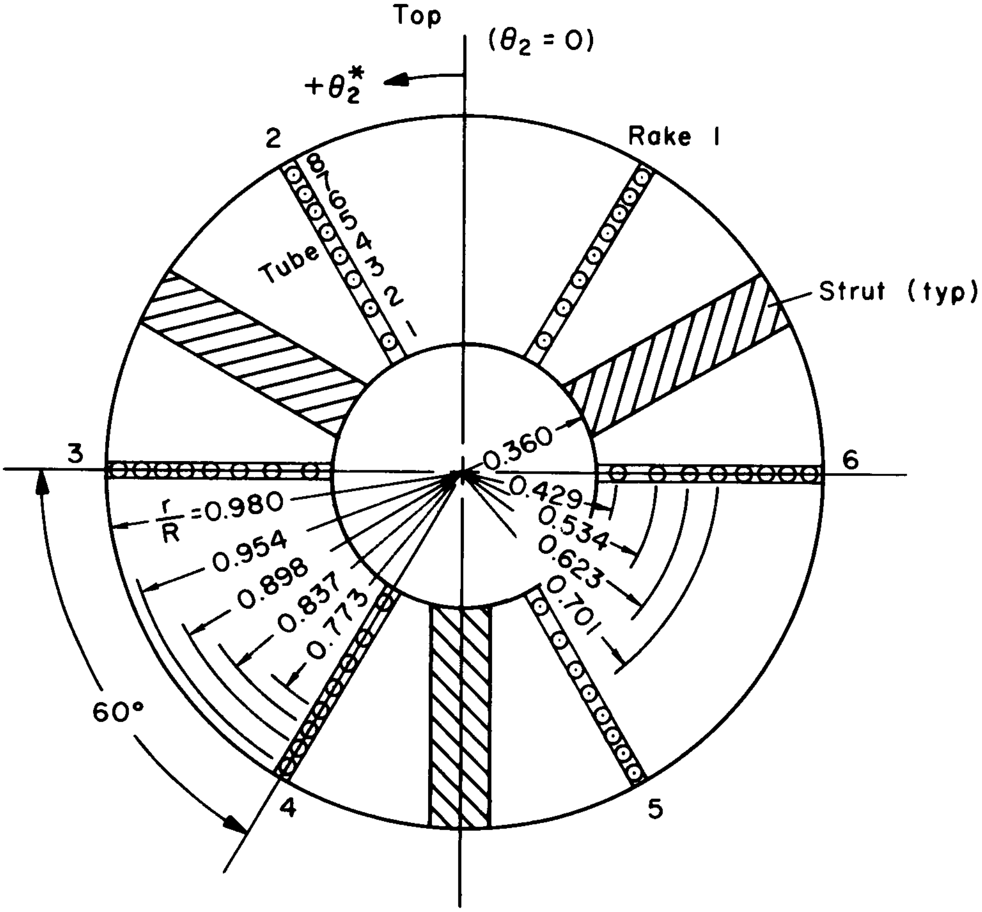

(c) Engine-face tube locations (looking downstream).

Figure 2. – Concluded.

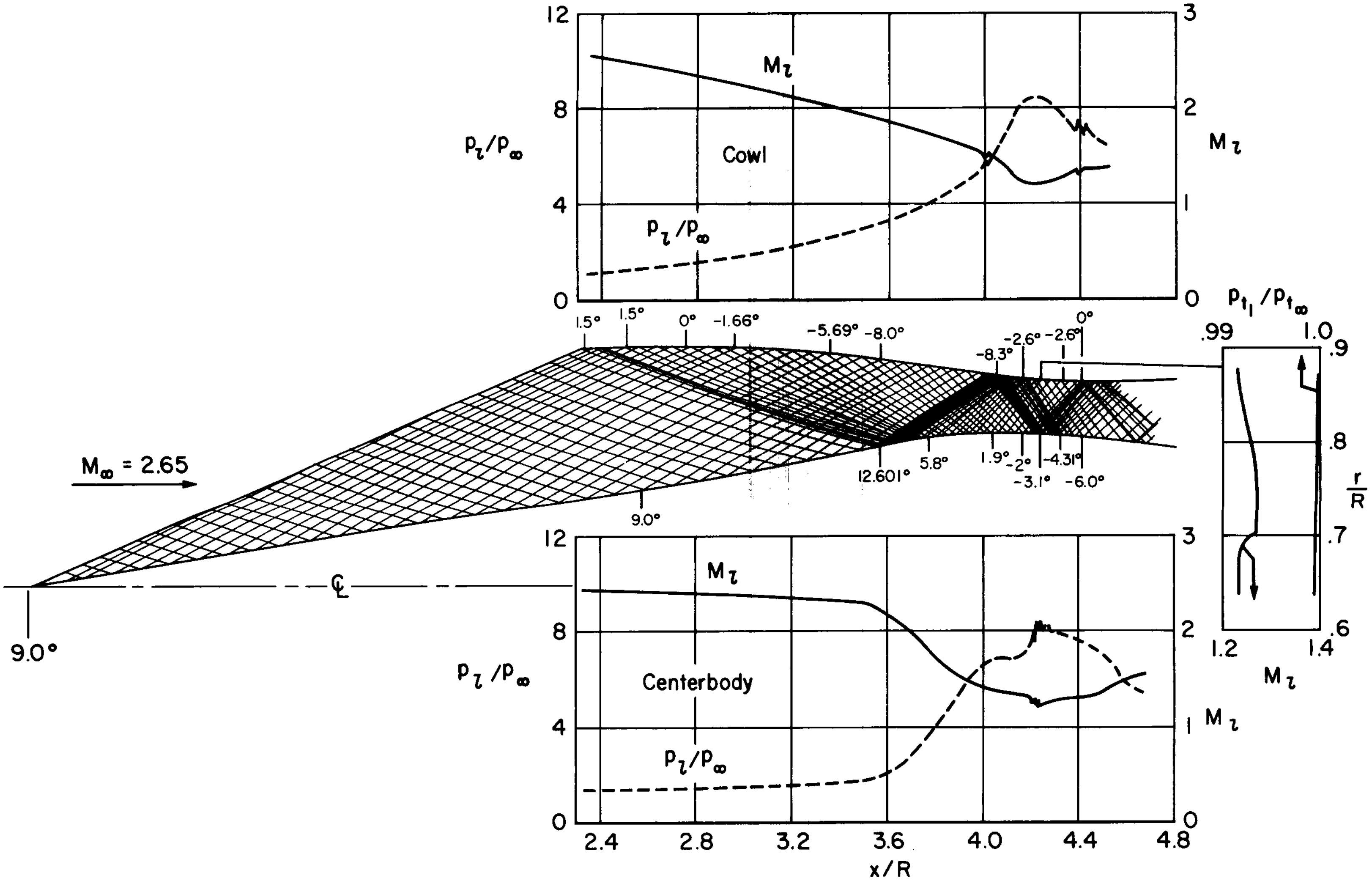

Figure 3. – Design theoretical flow field.

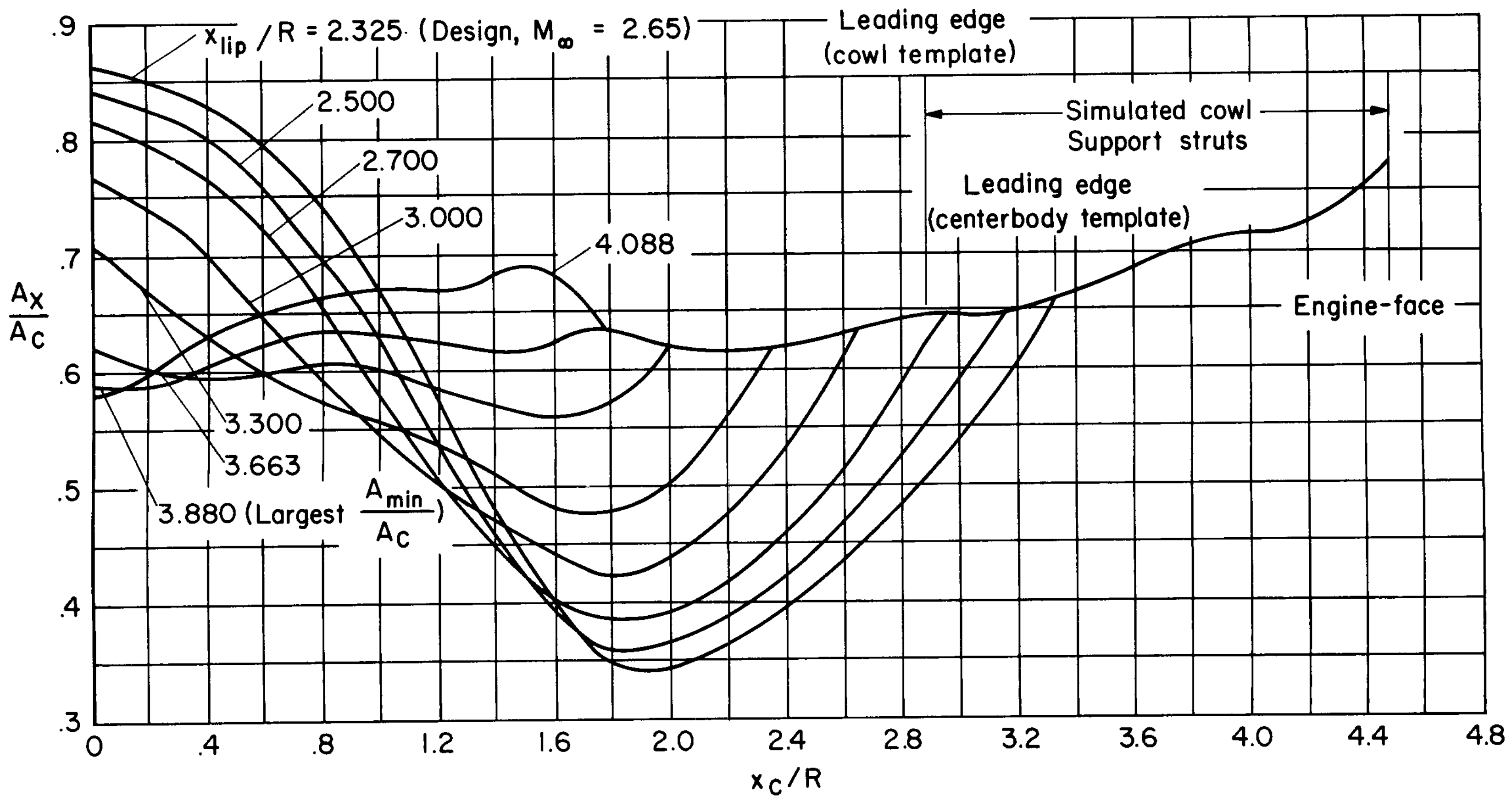

Figure 4. – Diffuser area distributions at various cowl positions.

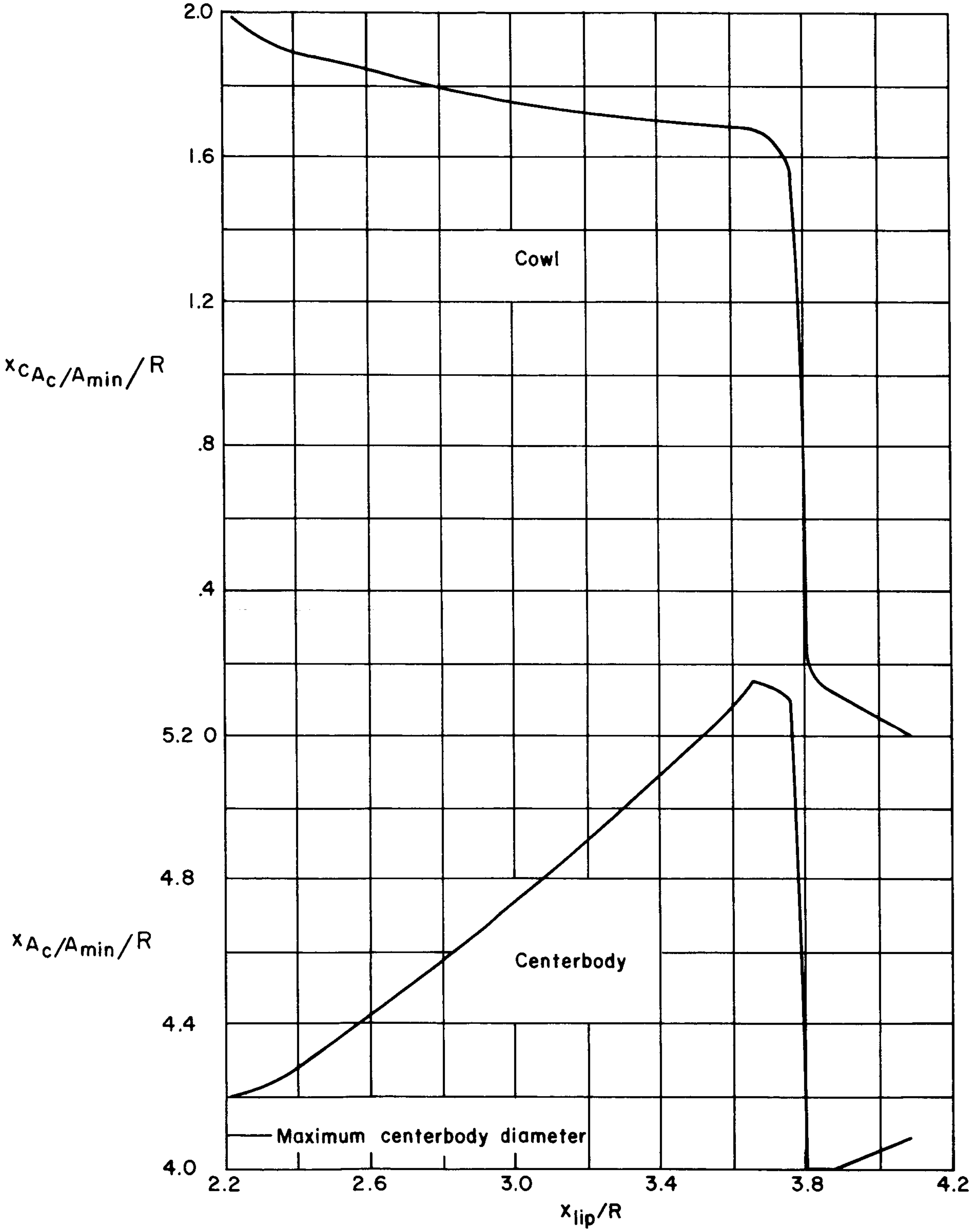

Figure 5. – Variation in inlet throat location with changing cowl position.

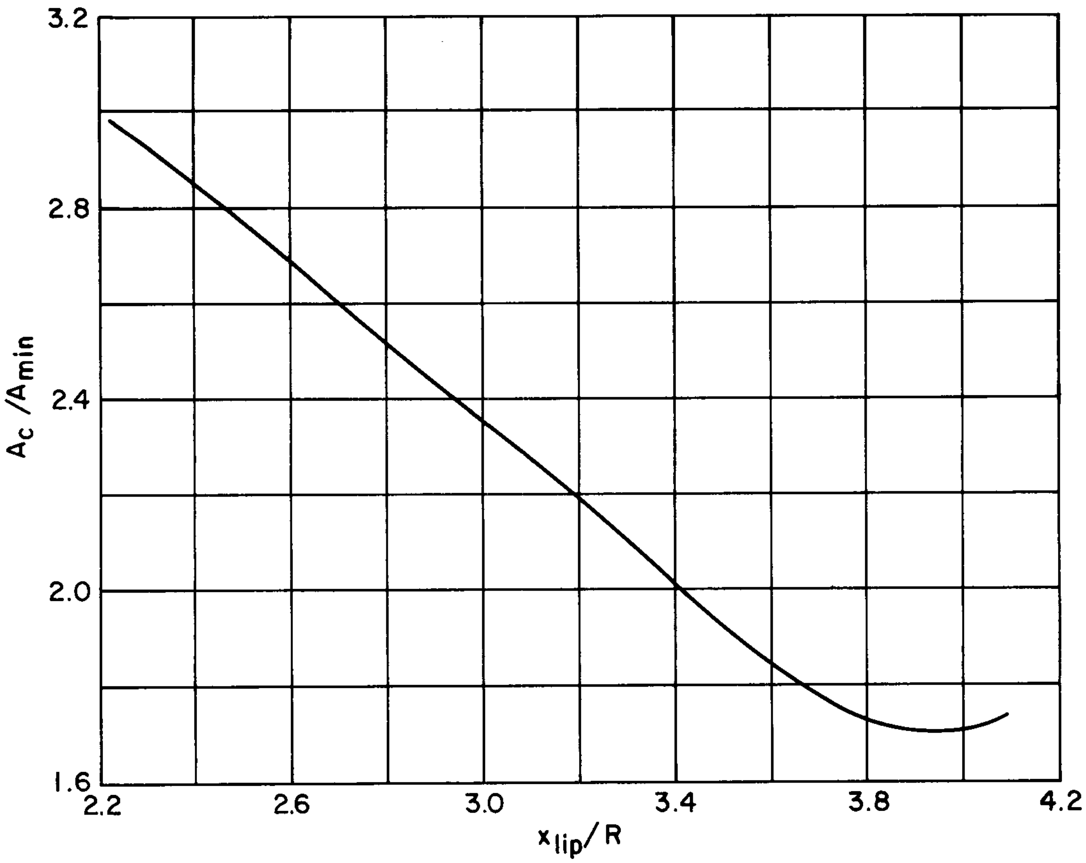

Figure 6. – Variation in inlet contraction ratio with changing cowl position.

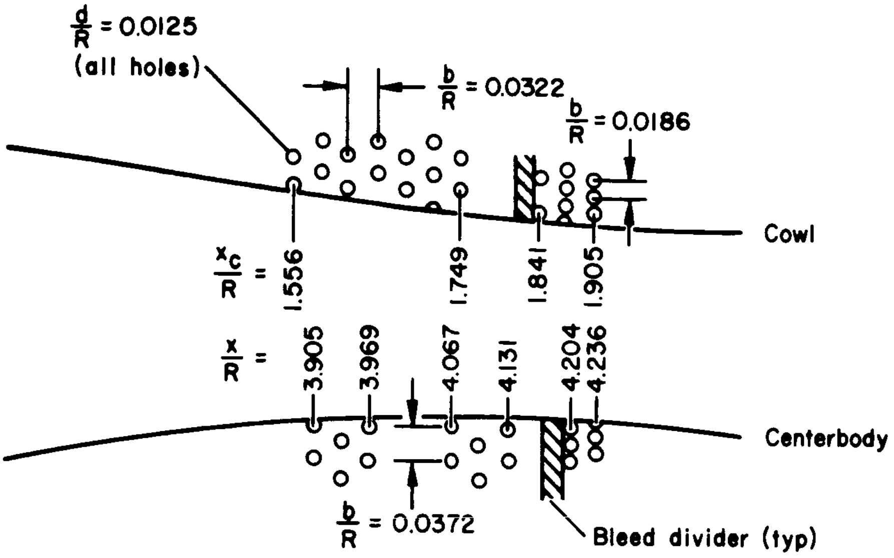

Bleed configuration A

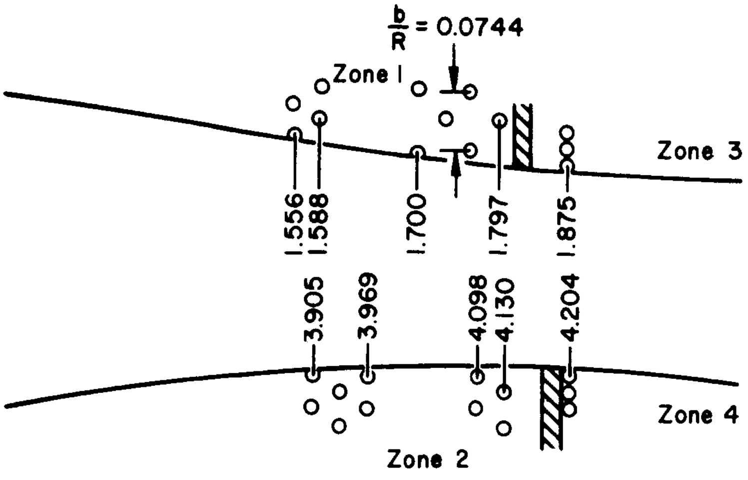

Bleed configuration C

(a) $M_\infty = 2.65$ and 2.60

Figure 7. – Bleed configurations.

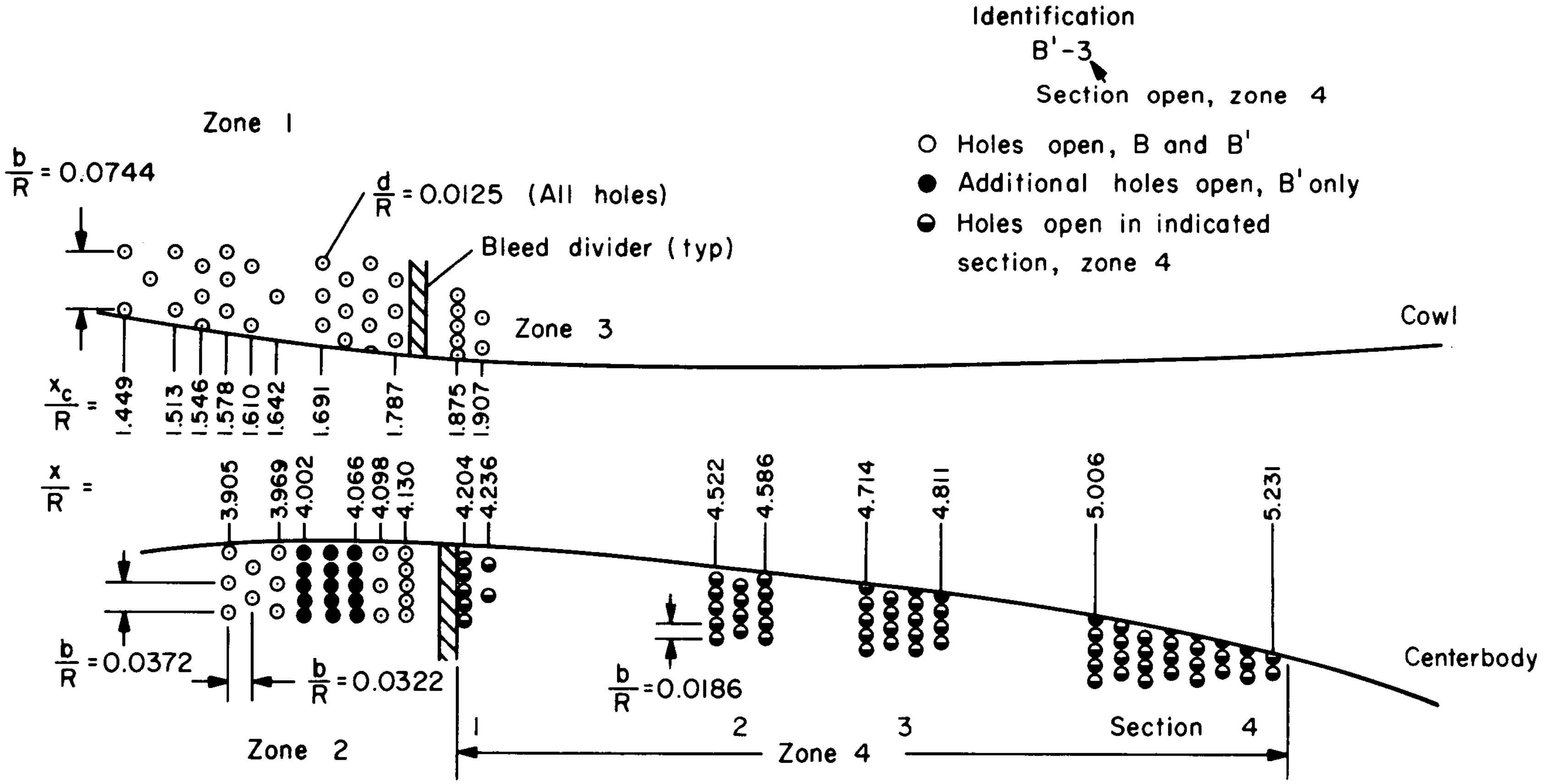

Bleed configurations B and B', sections 1 - 4

(b) $M_\infty = 1.55$ to 2.65

Figure 7. – Concluded.

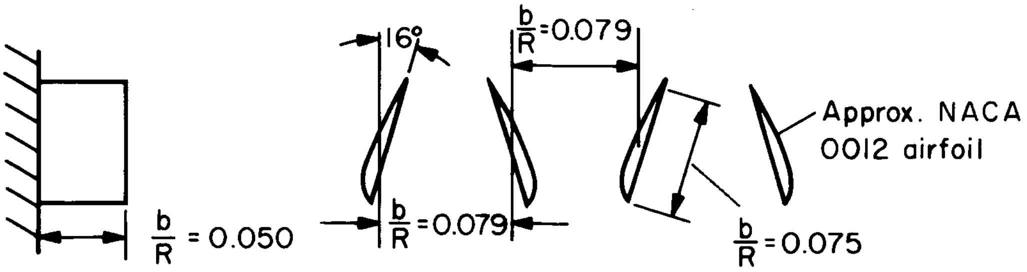

a) Configuration A

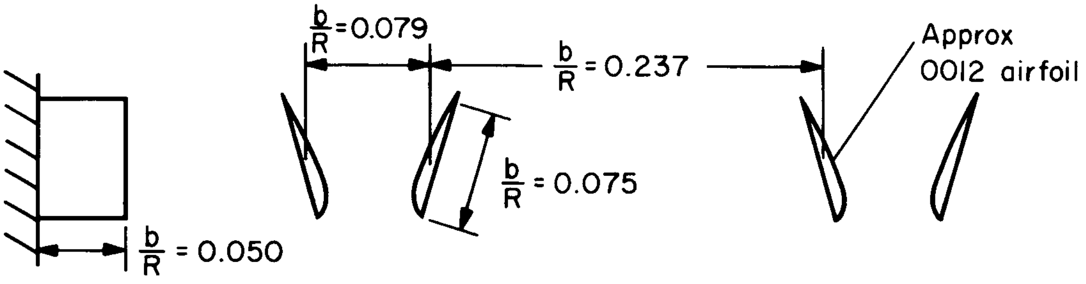

b) Configuration B

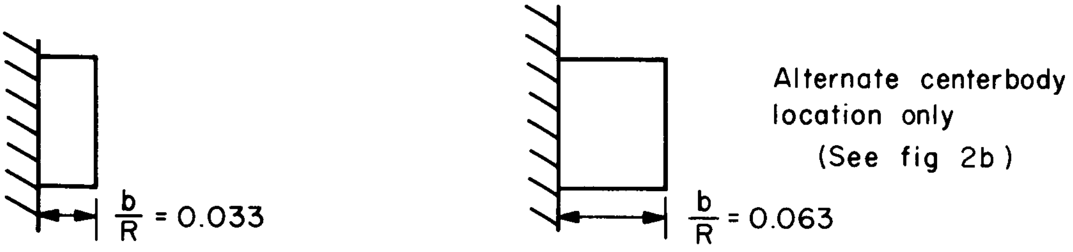

c) Configuration C
(Spacing same as A)

d) Configuration D
(Spacing same as A)

e) Configuration O
(No vortex generators)

Identification

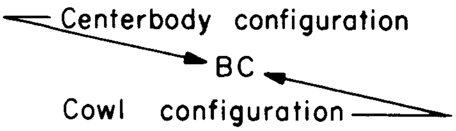

Figure 8. – Vortex generator configurations.

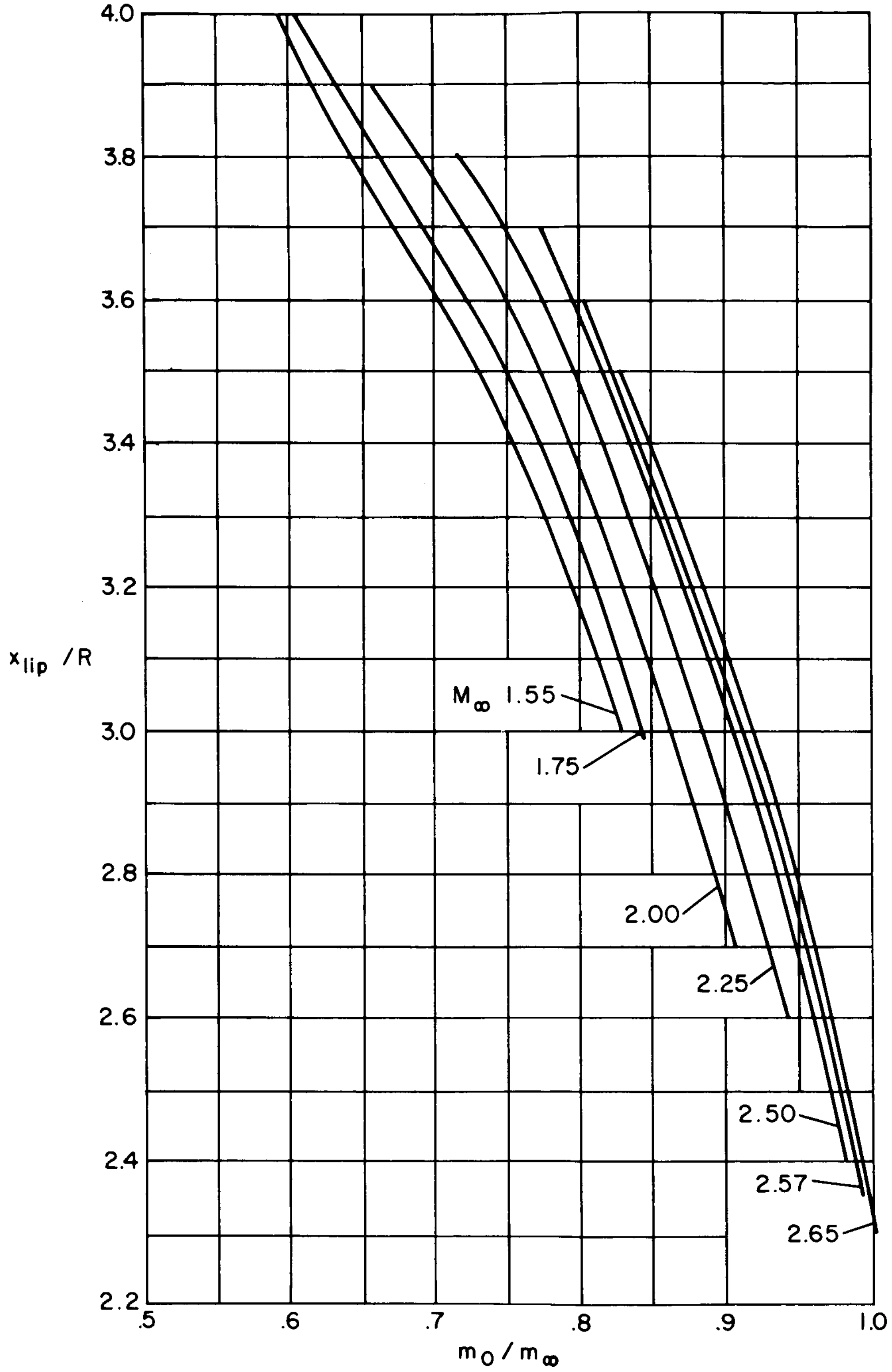

Figure 9. – Inlet theoretical mass-flow ratio, $\alpha = 0°$

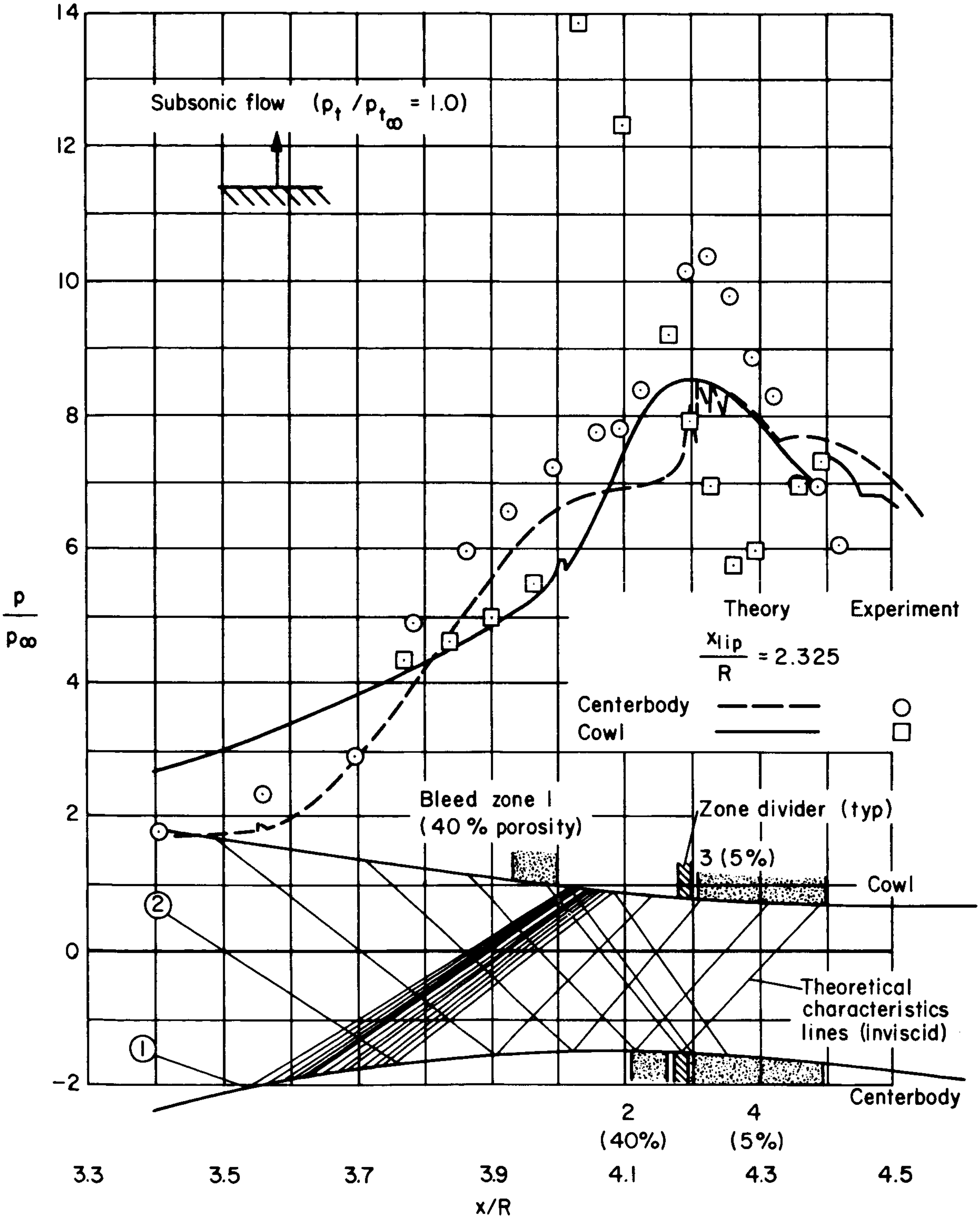

(a) $x_{lip}/R = 2.364, CR = 2.870$

Figure 10. – Static-pressure distributions in the supersonic diffuser with various bleed configurations; $M_\infty = 2.65, \alpha = 0°$.

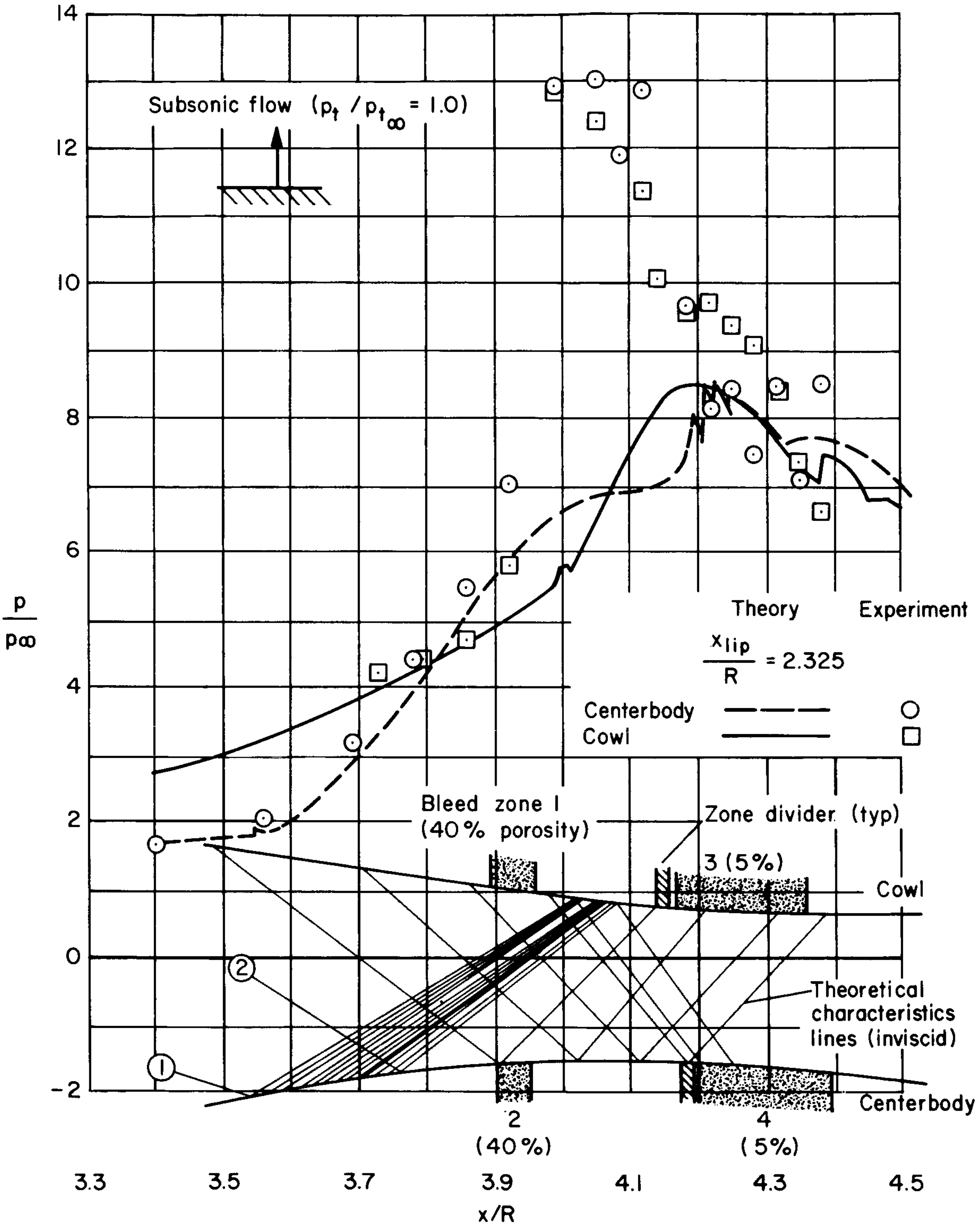

(b) $x_{lip}/R = 2.325$, $CR = 2.900$

Figure 10. – Continued.

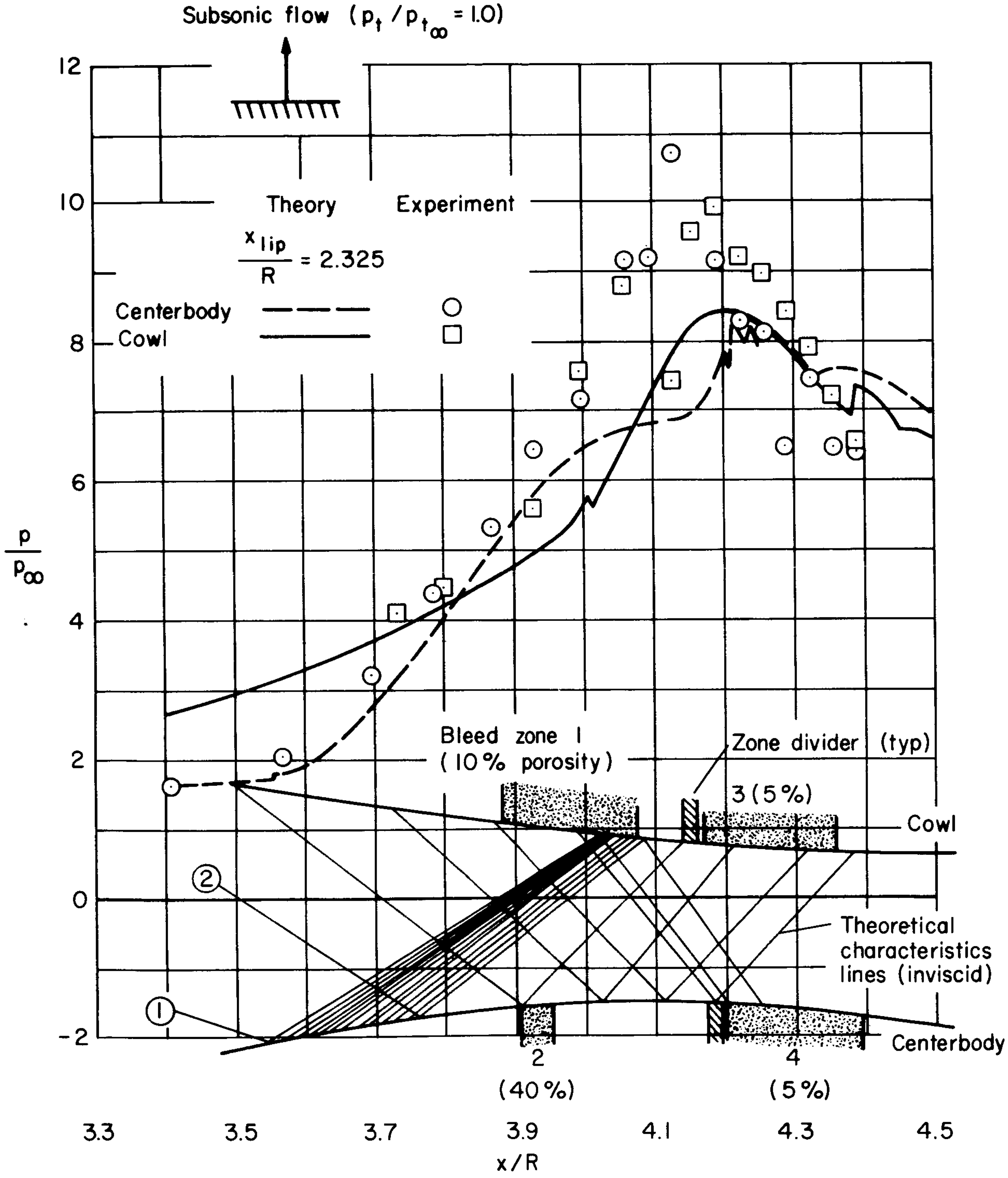

(c) $x_{lip}/R = 2.325, CR = 2.900$

Figure 10. – Continued.

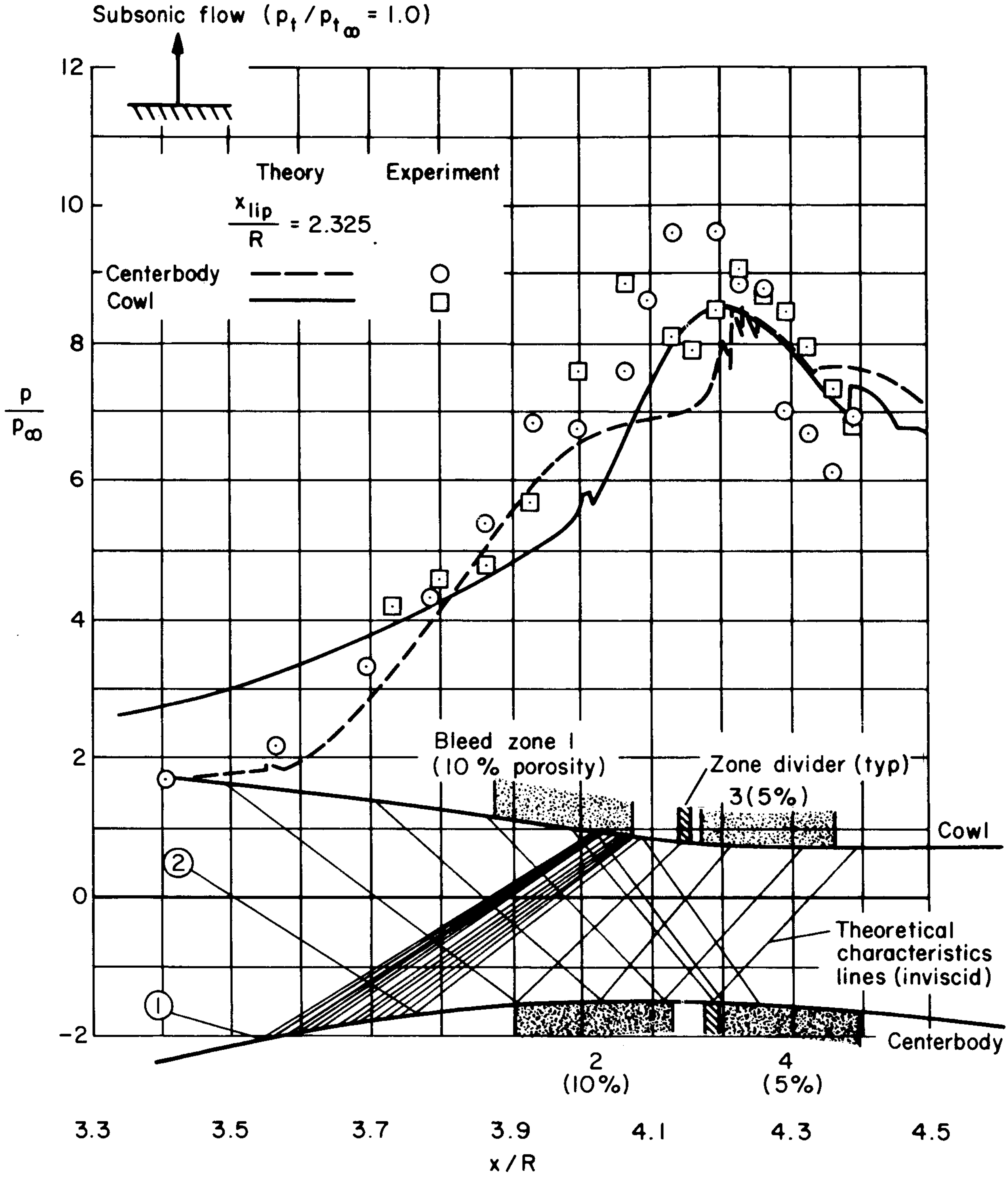

(d) x_{lip}/R = 2.325, CR = 2.900

Figure 10. – Concluded.

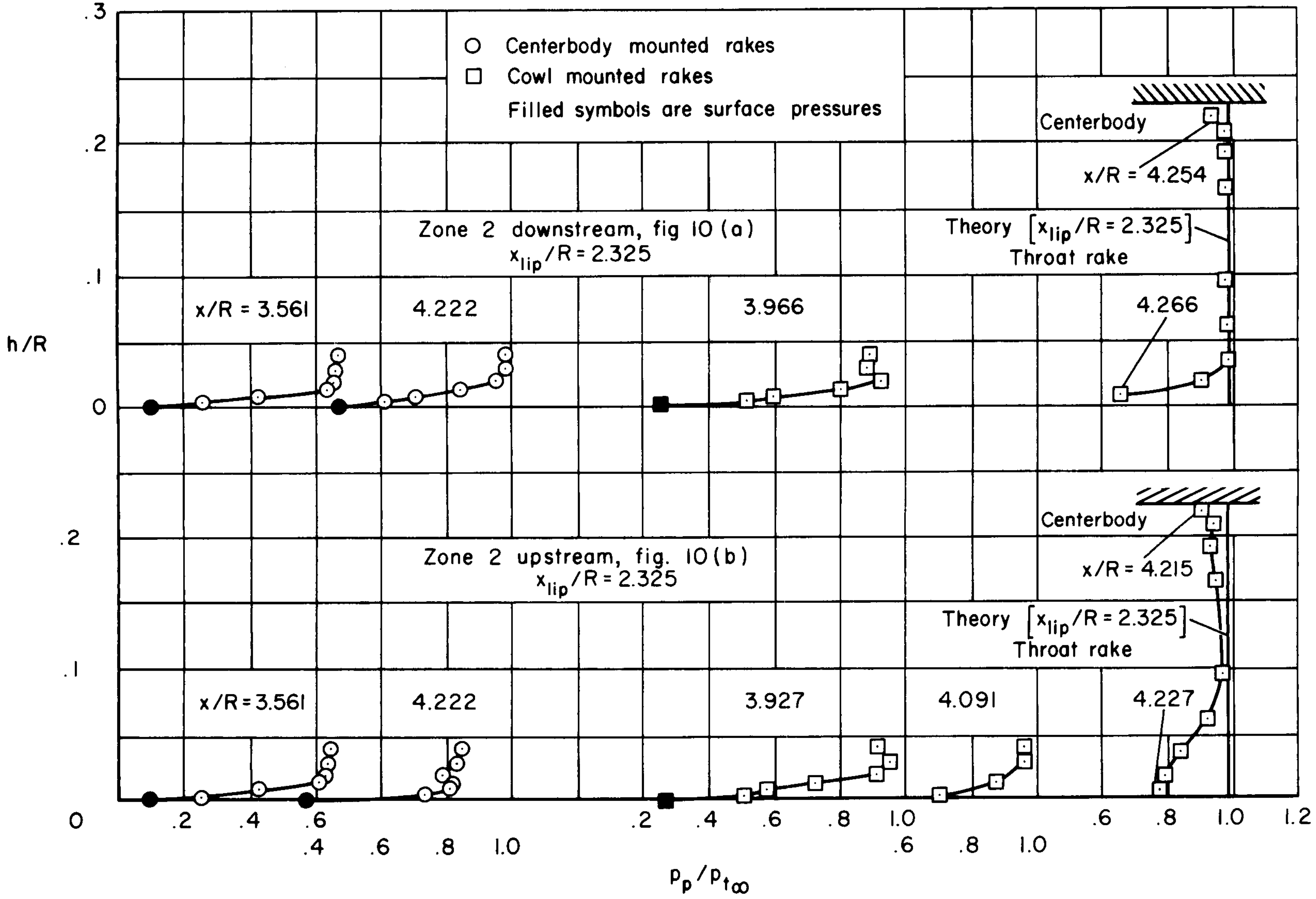

(a) Concentrated bleed configurations.

Figure 11. – Pitot-pressure profiles.

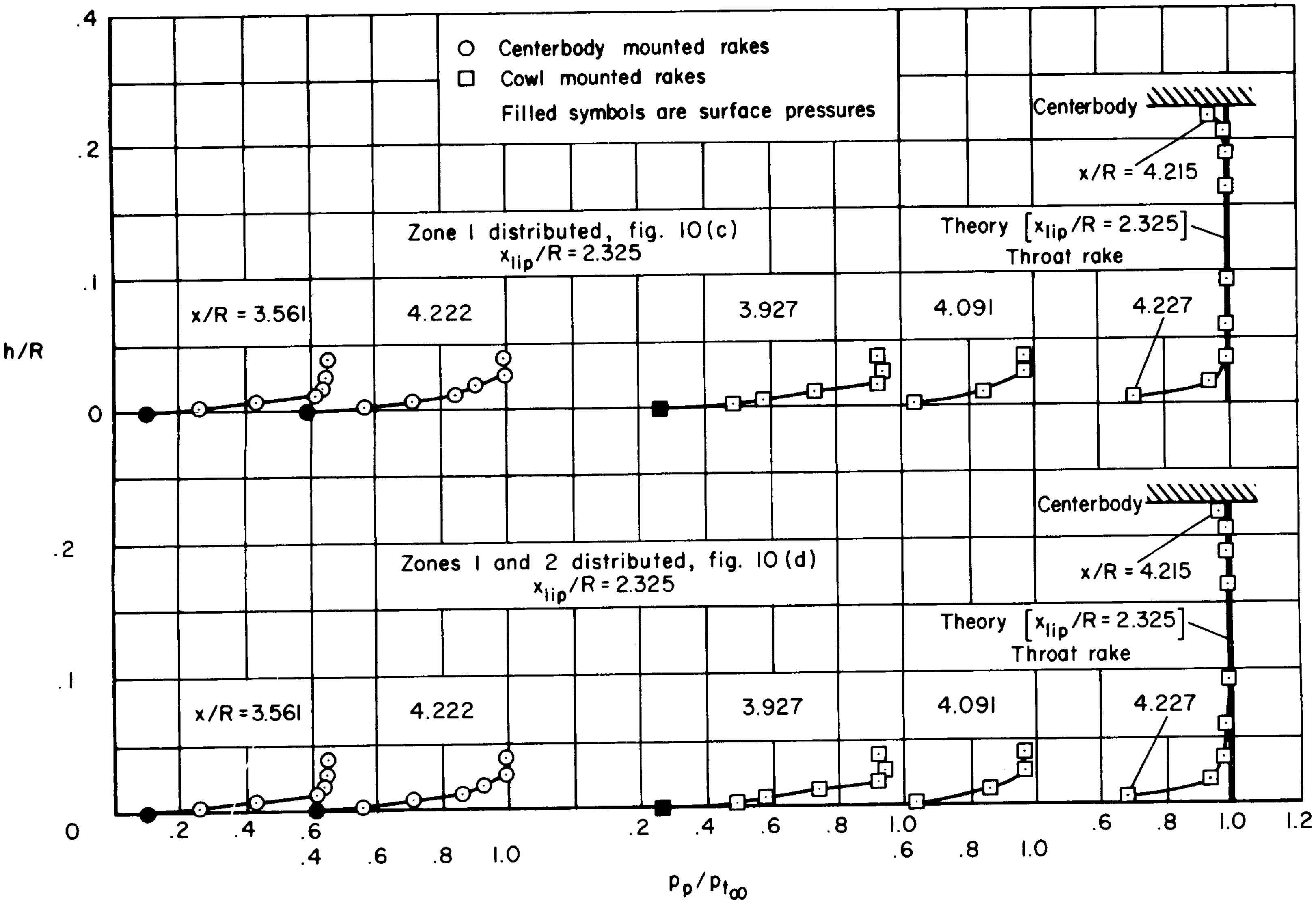

(b) Distributed bleed patterns.

Figure 11. – Concluded.

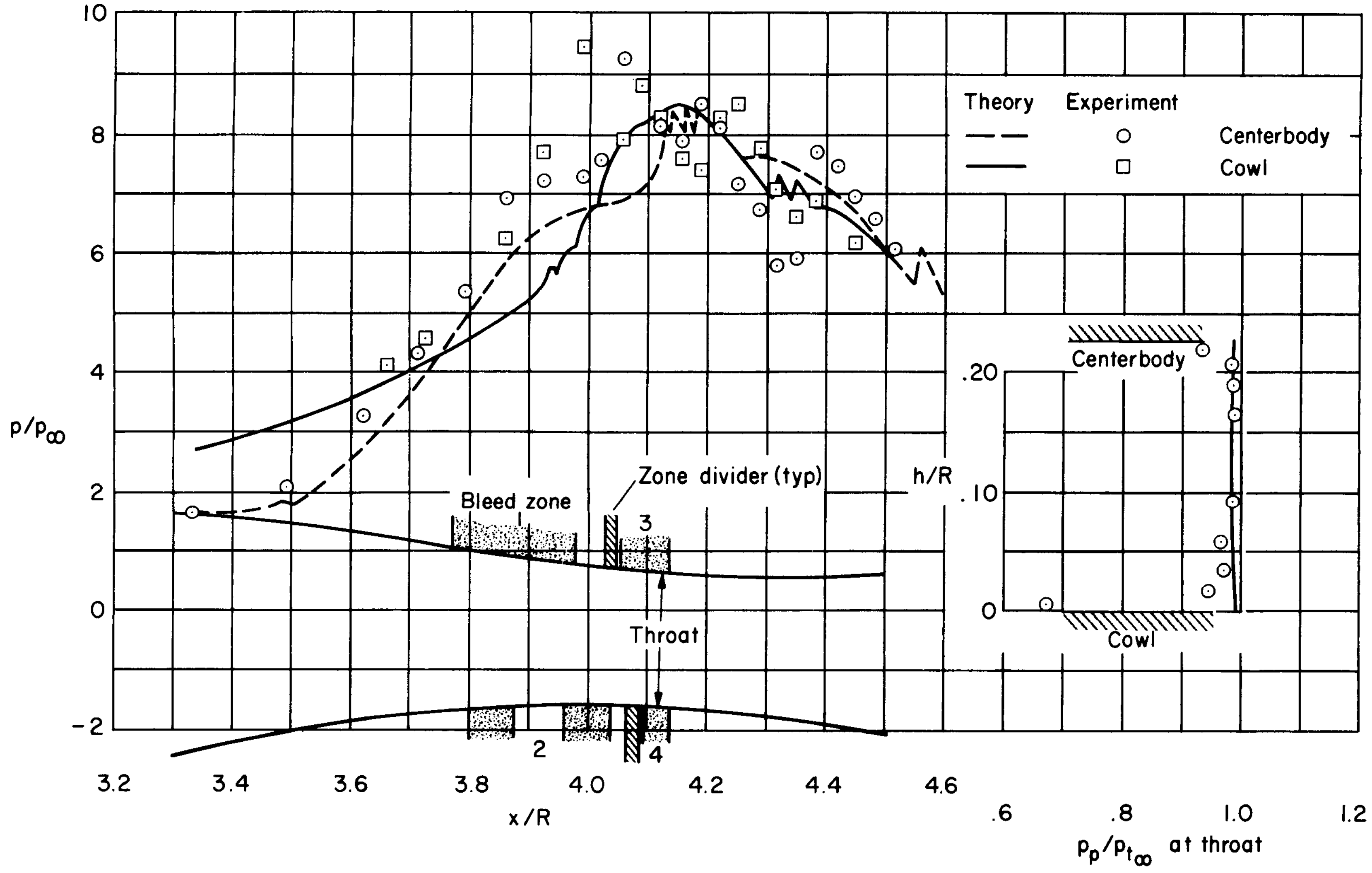

Figure 12. – Theoretical and experimental performance of the supersonic diffuser; $M_\infty = 2.65$, bleed configuration A, $x_{lip}/R = 2.325$, $\alpha = 0°$, $m_{bp}/m_\infty = 0$, $\theta_2 = 0°$.

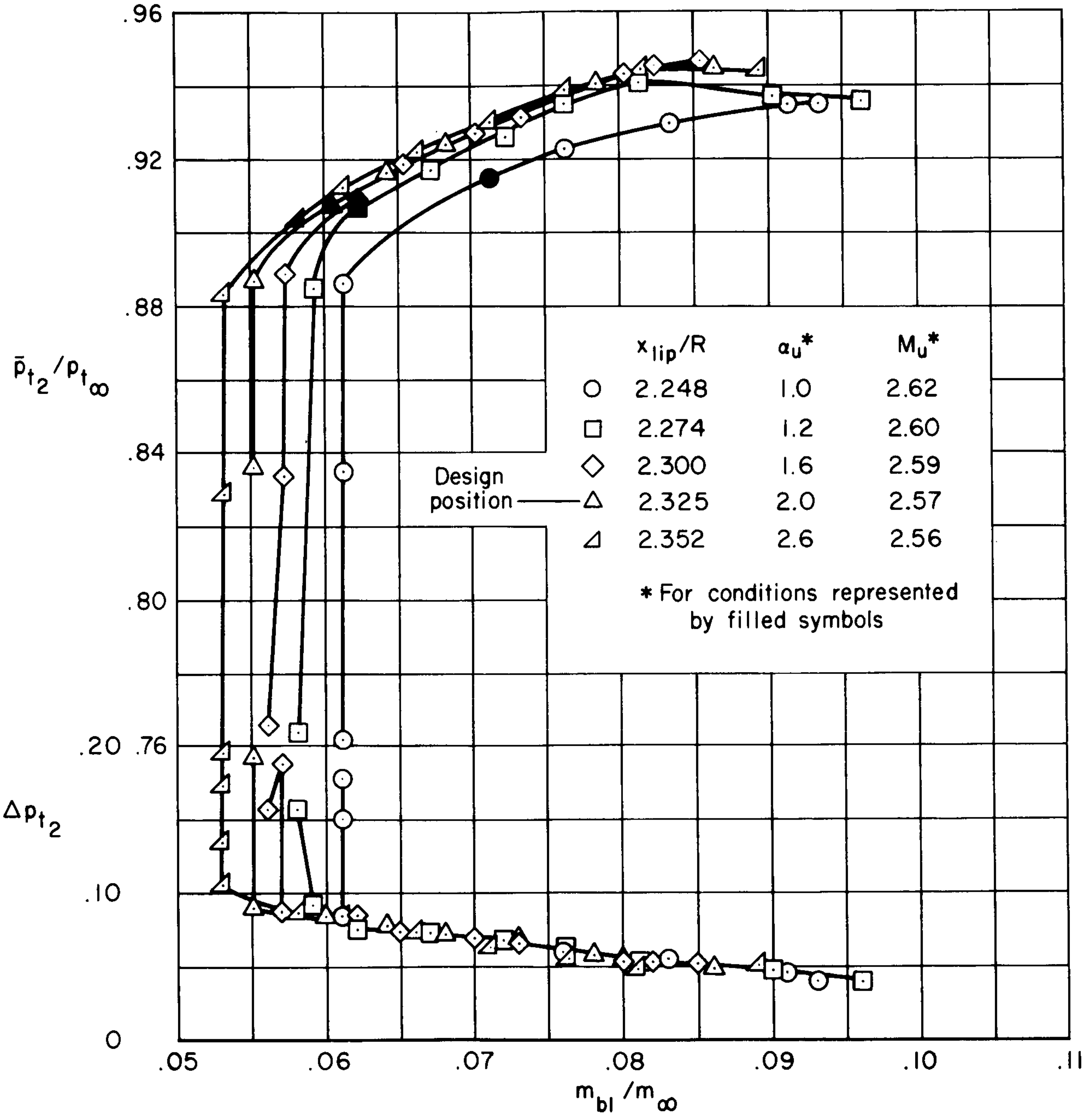

(a) Bleed configuration A.

Figure 13. – Supercritical performance for various positions of the cowl lip; $M_\infty = 2.65$, $\alpha = 0°$, $m_{bp}/m_\infty = 0$, $\theta_2 = 0°$, vortex generator configuration AA.

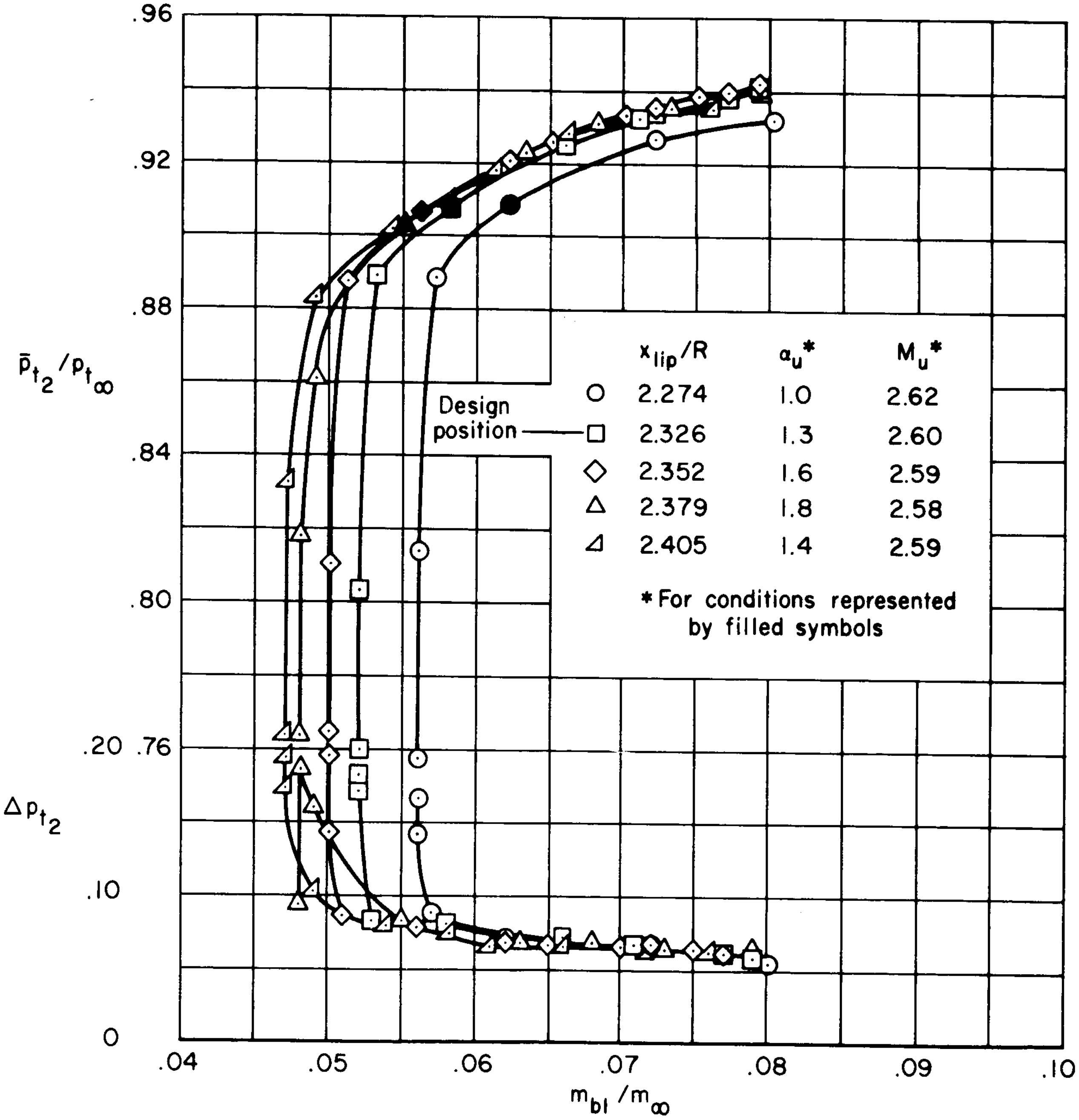

(b) Bleed configuration B-1.

Figure 13. – Continued.

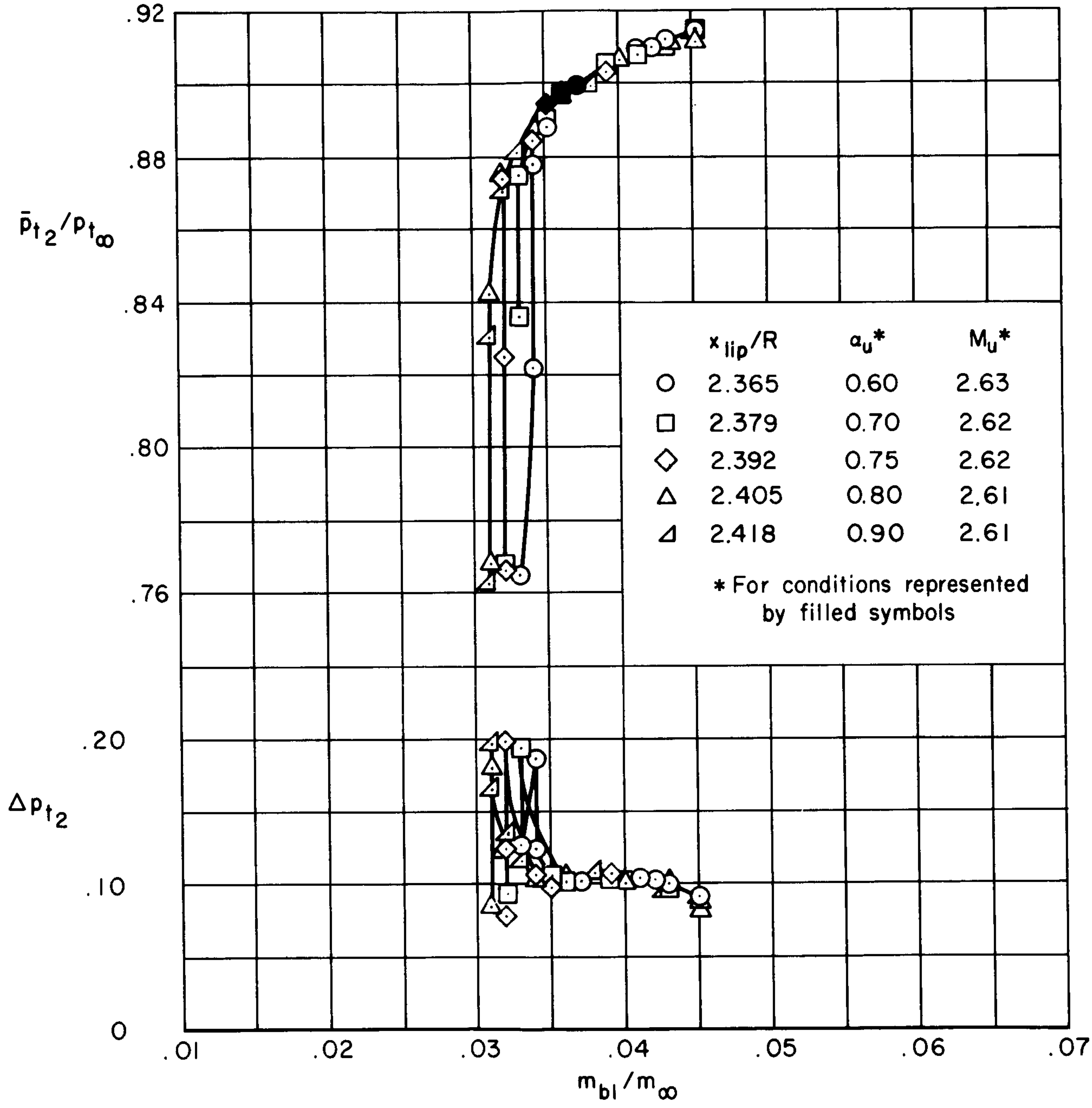

(c) Bleed configuration C.

Figure 13. – Concluded.

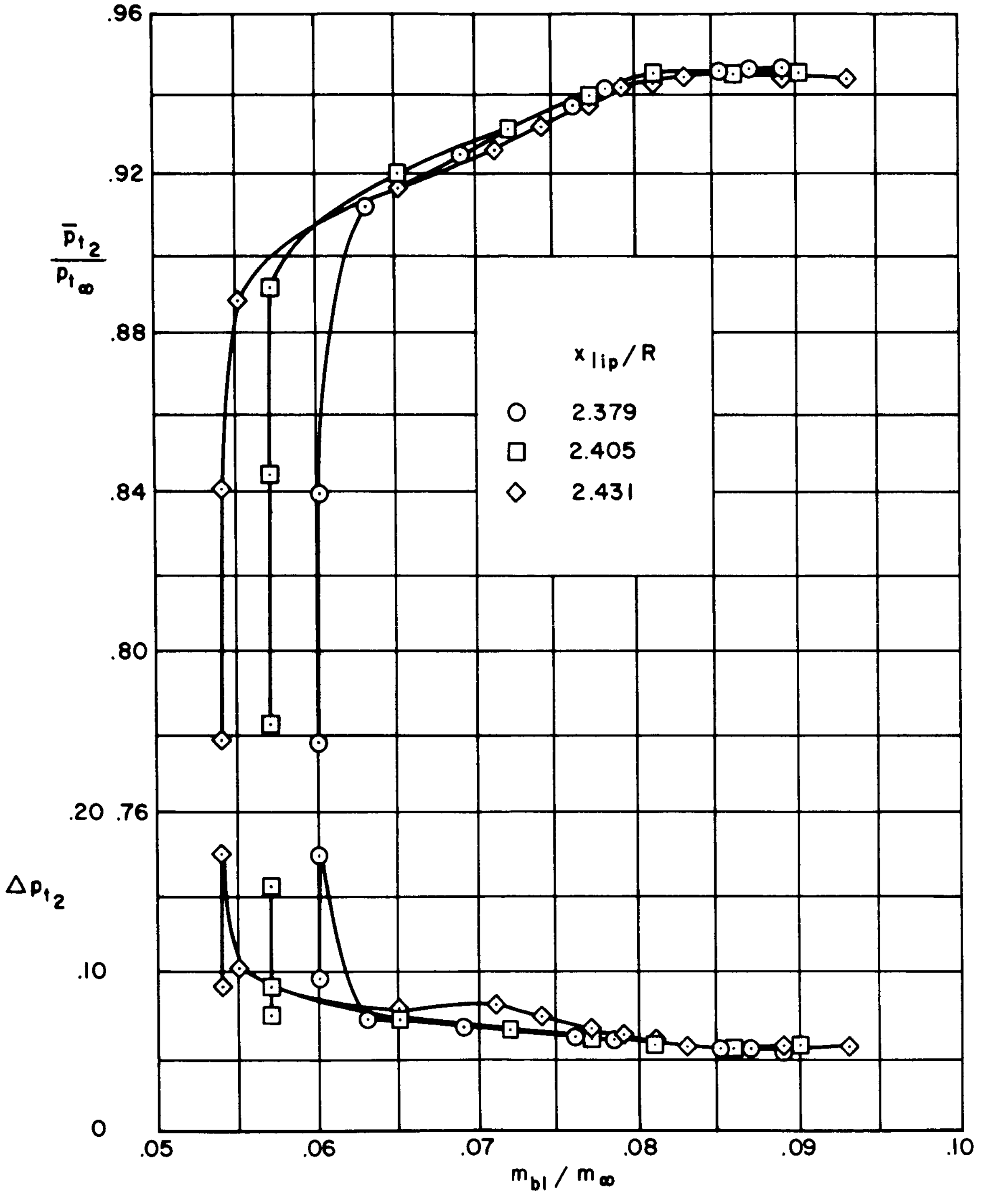

(a) Bleed configuration A.

Figure 14. – Supercritical performance for various positions of the cowl lip; $M_\infty = 2.60$, $\alpha = 0°$, $m_{bp}/m_\infty = 0$, $\theta_2 = 0°$, vortex generator configuration AA.

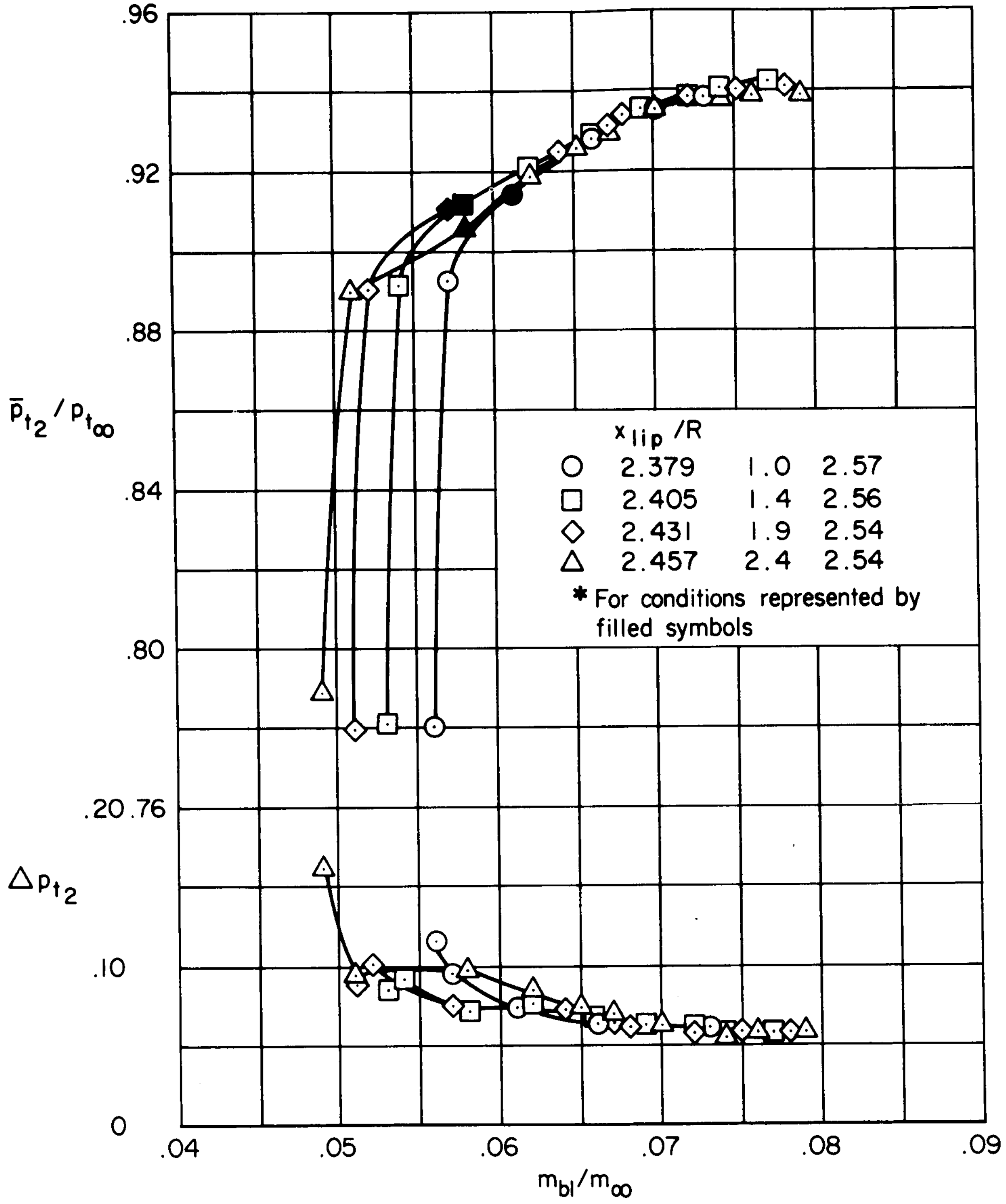

(b) Bleed configuration B-1.

Figure 14. – Continued.

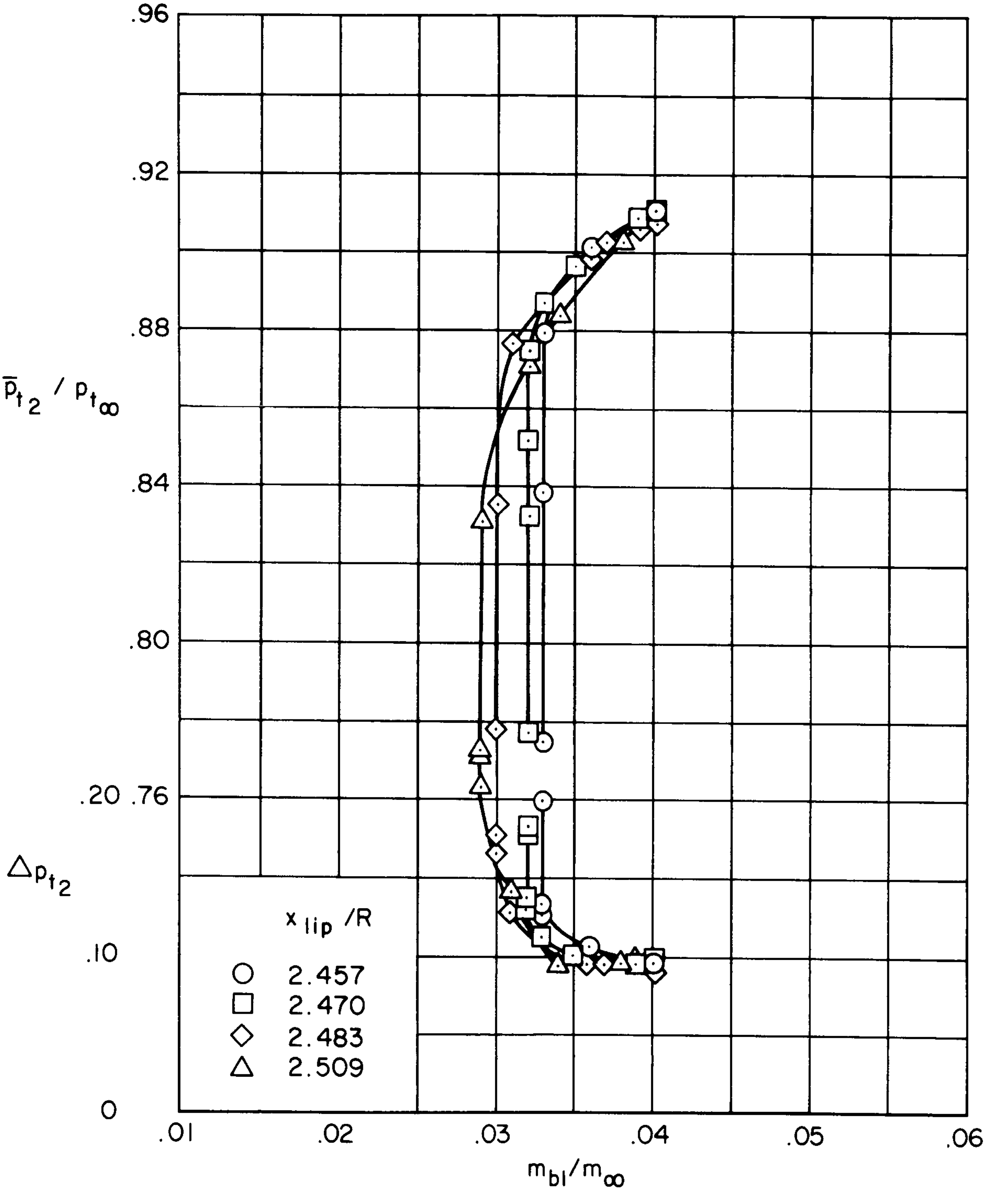

(c) Bleed configuration C.

Figure 14. – Concluded.

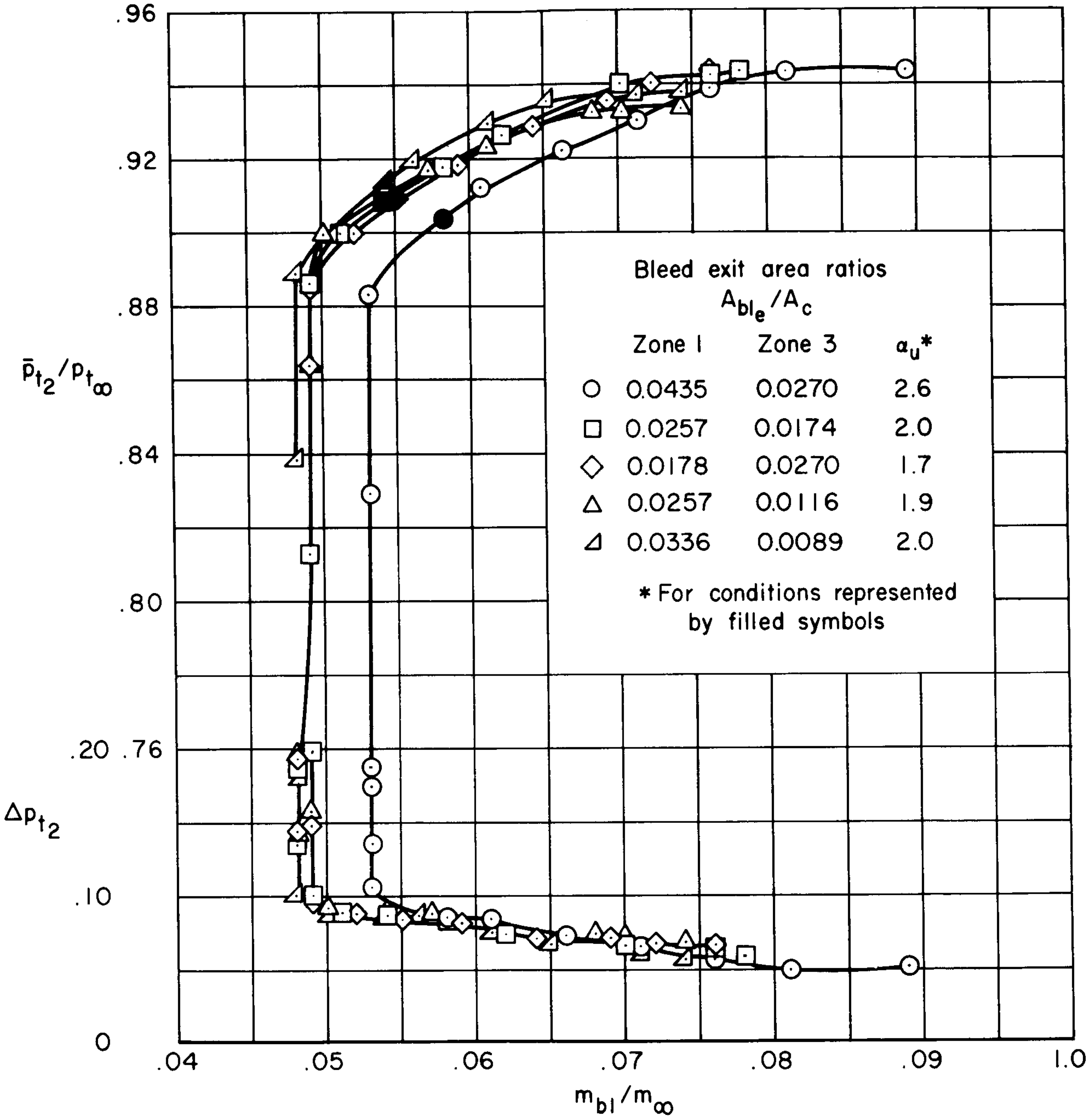

Figure 15. – Effect of cowl bleed on the supercritical performance; $M_\infty = 2.65$, $\alpha = 0°$, $m_{bp}/m_\infty = 0$, $\theta_2 = 0°$, vortex generator configuration AA, bleed configuration A, $x_{lip}/R = 2.352$.

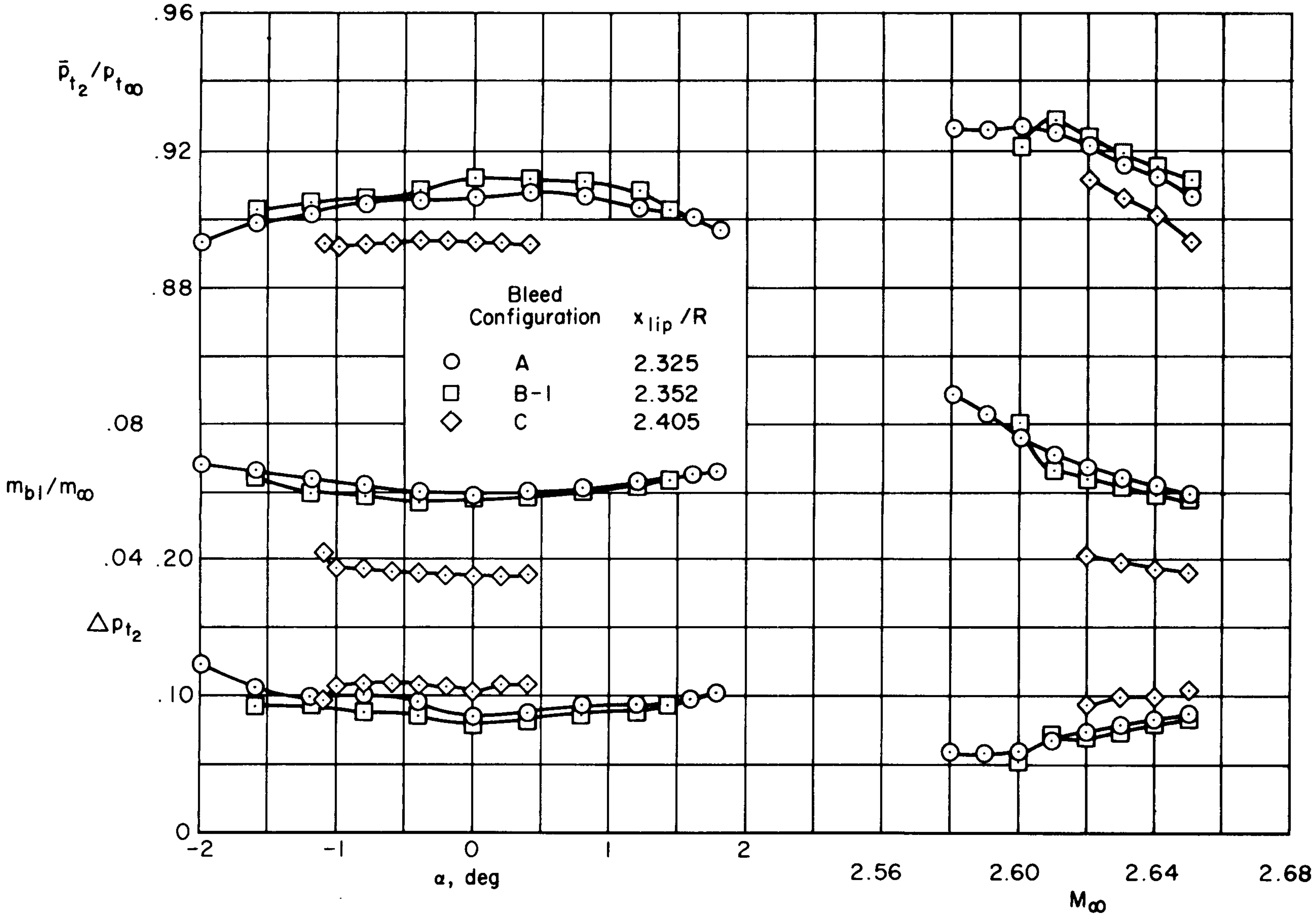

(a) Initial conditions, $M_\infty = 2.65, \alpha = 0°$.

Figure 16. – Performance with change in angle of attack or Mach number; $m_{bp}/m_\infty = 0$, $\theta_2 = 0°$, vortex generator configuration AA.

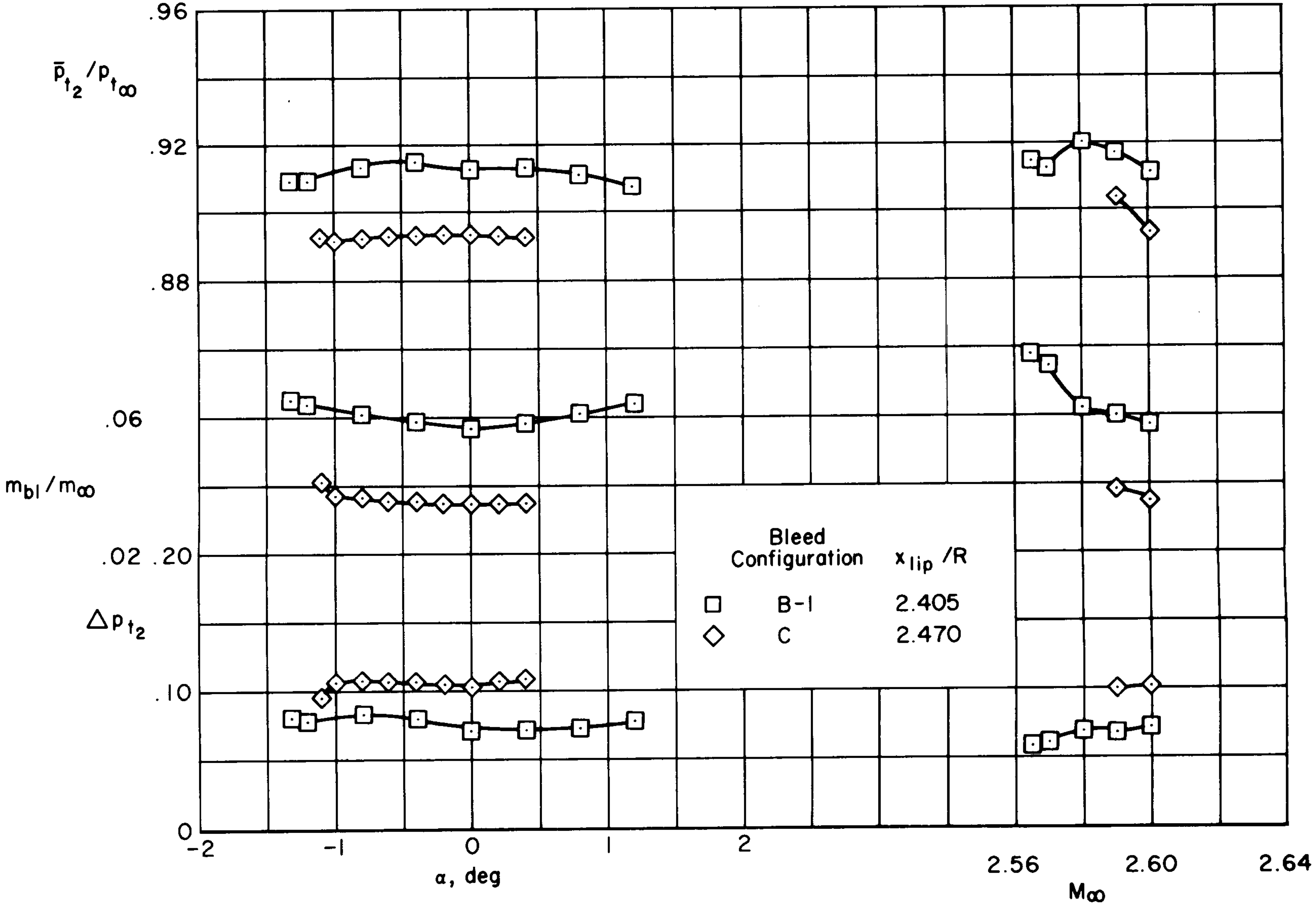

(b) Initial conditions; $M_\infty = 2.60, \alpha = 0°$.

Figure 16. – Concluded.

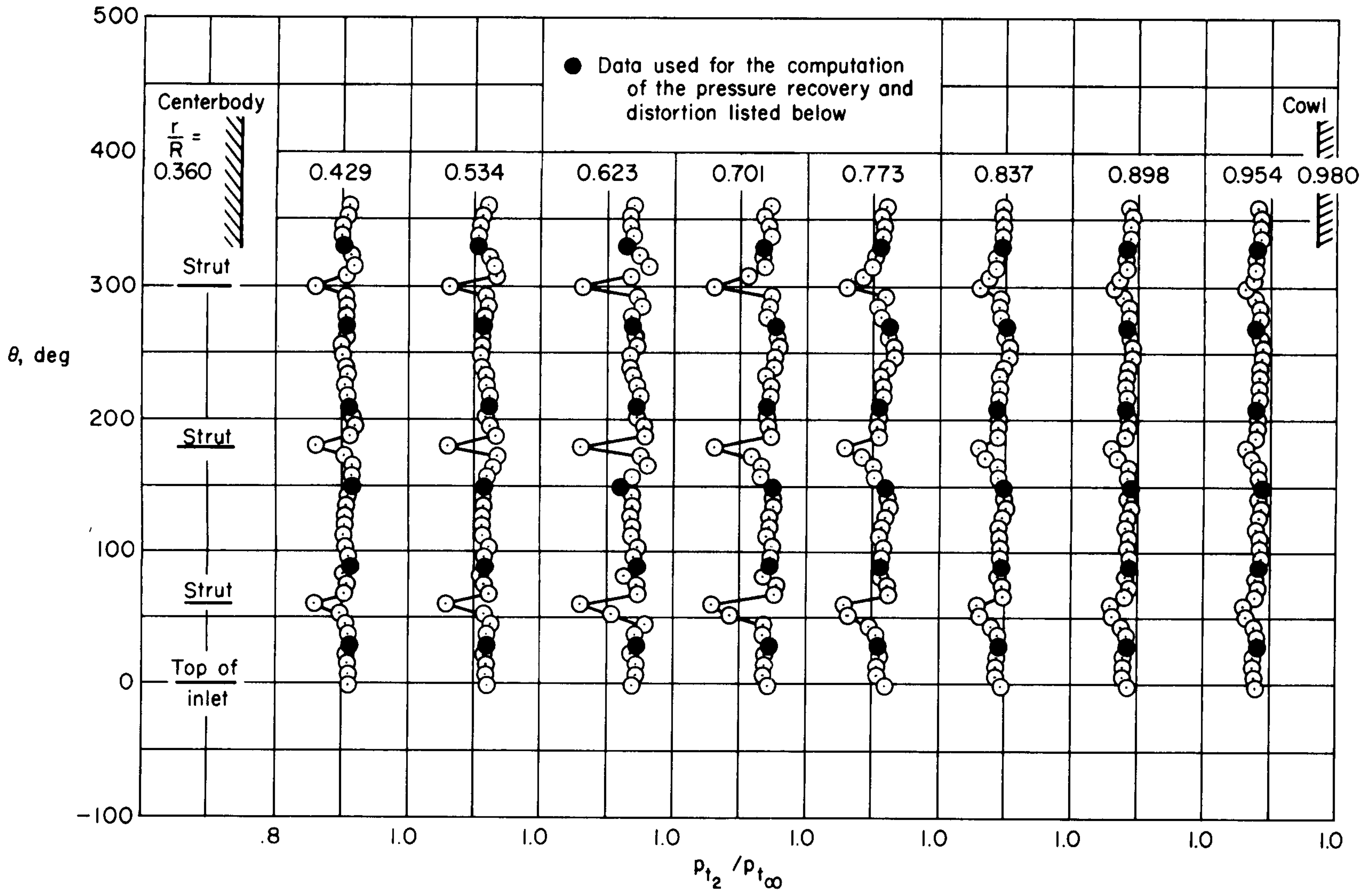

(a) $\alpha = 0°$, $\bar{p}_{t_2}/p_{t_\infty} = 0.911$, $m_{bl}/m_\infty = 0.061$, $\Delta p_{t_2} = 0.083$

Figure 17. – Circumferential total-pressure profiles at angle of attack; $M_\infty = 2.65$, $m_{bp}/m_\infty = 0$, vortex generator configuration AA, bleed configuration A, $x_{lip}/R = 2.325$.

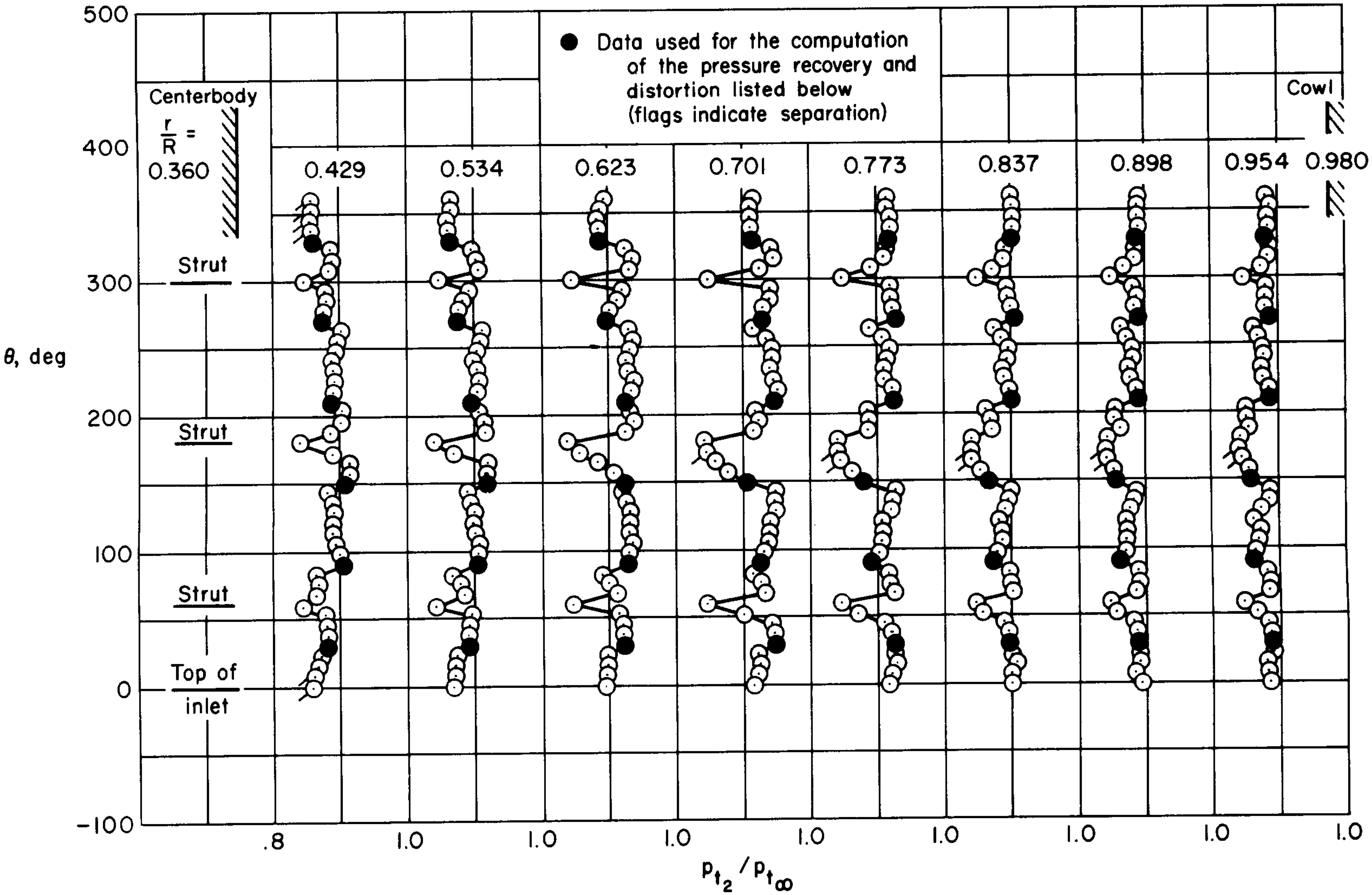

(b) $\alpha = 1.9°$, $\bar{p}_{t_2}/p_{t_\infty} = 0.897$, $m_{bl}/m_\infty = 0.067$, $\Delta p_{t_2} = 0.102$

Figure 17. – Continued.

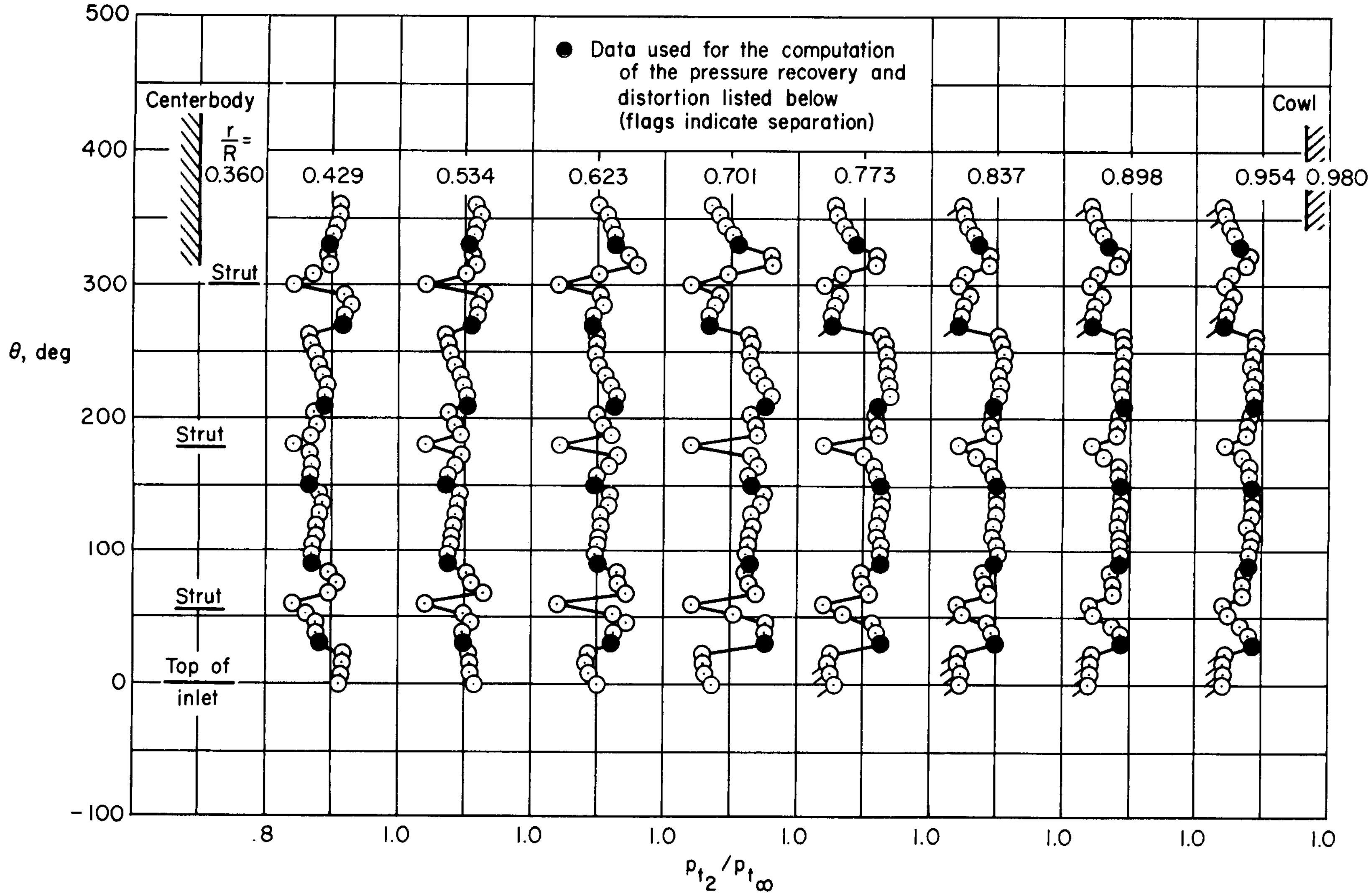

(c) $\alpha = -1.9°, \bar{p}_{t_2}/p_{t_\infty} = 0.894, m_{bl}/m_\infty = 0.068, \Delta p_{t_2} = 0.122$

Figure 17. – Concluded.

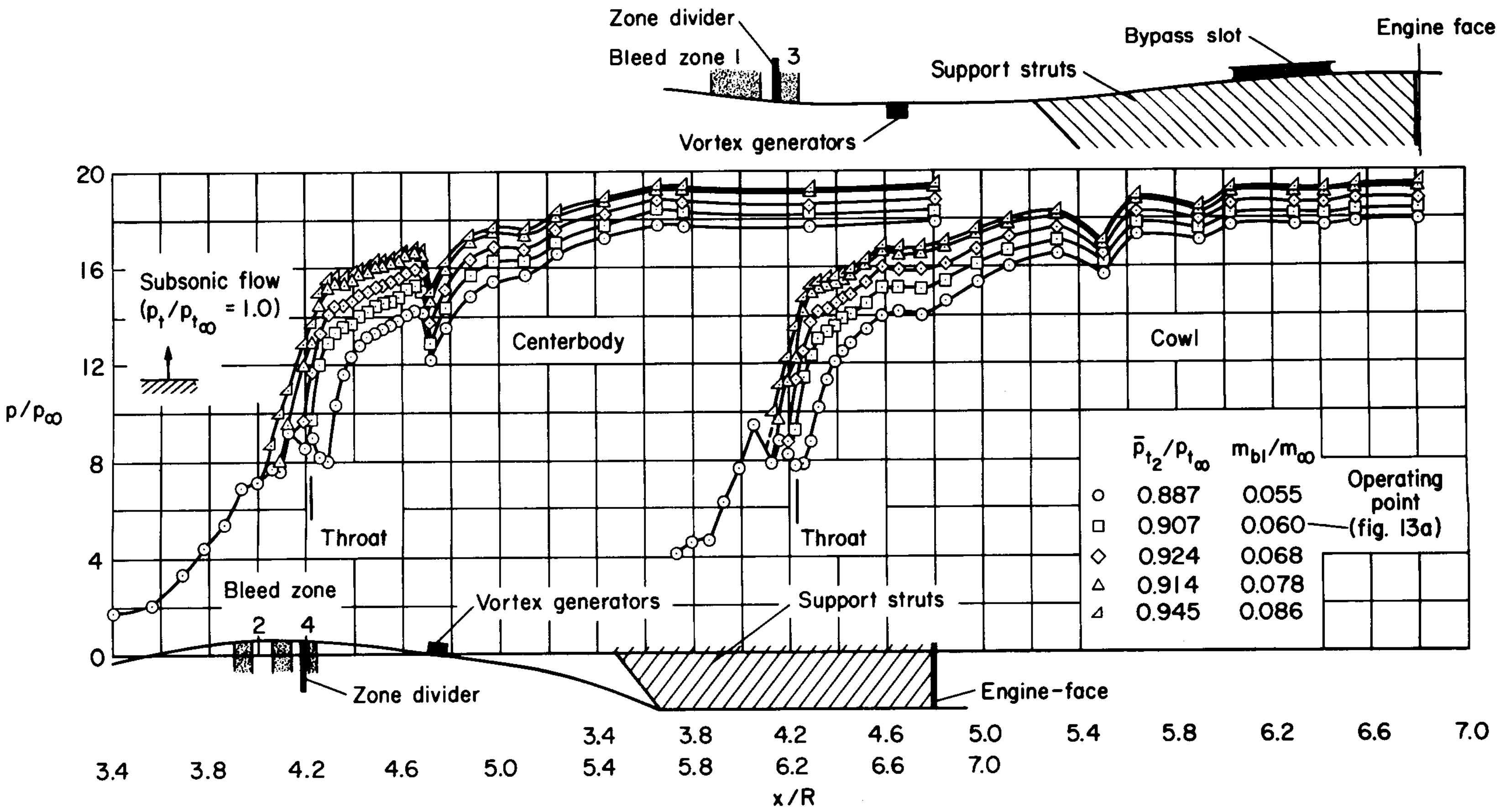

(a) $M_\infty = 2.65$, $x_{lip}/R = 2.325$

Figure 18. – Static-pressure distributions; $\alpha = 0°$, $m_{bp}/m_\infty = 0$, $\theta_2 = 0°$, vortex generator configuration AA, bleed configuration A.

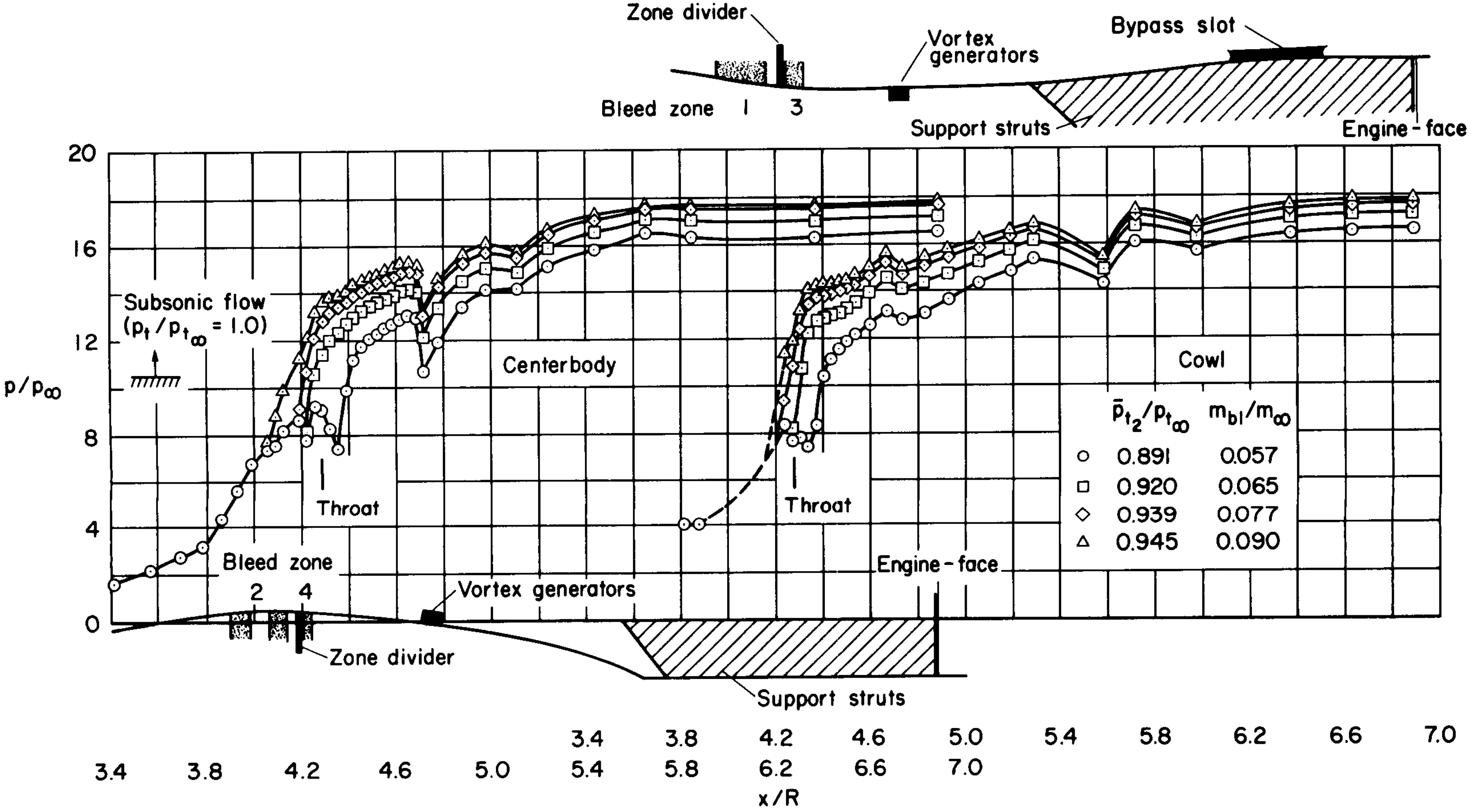

(b) $M_\infty = 2.60, x_{lip}/R = 2.405$

Figure 18. – Concluded.

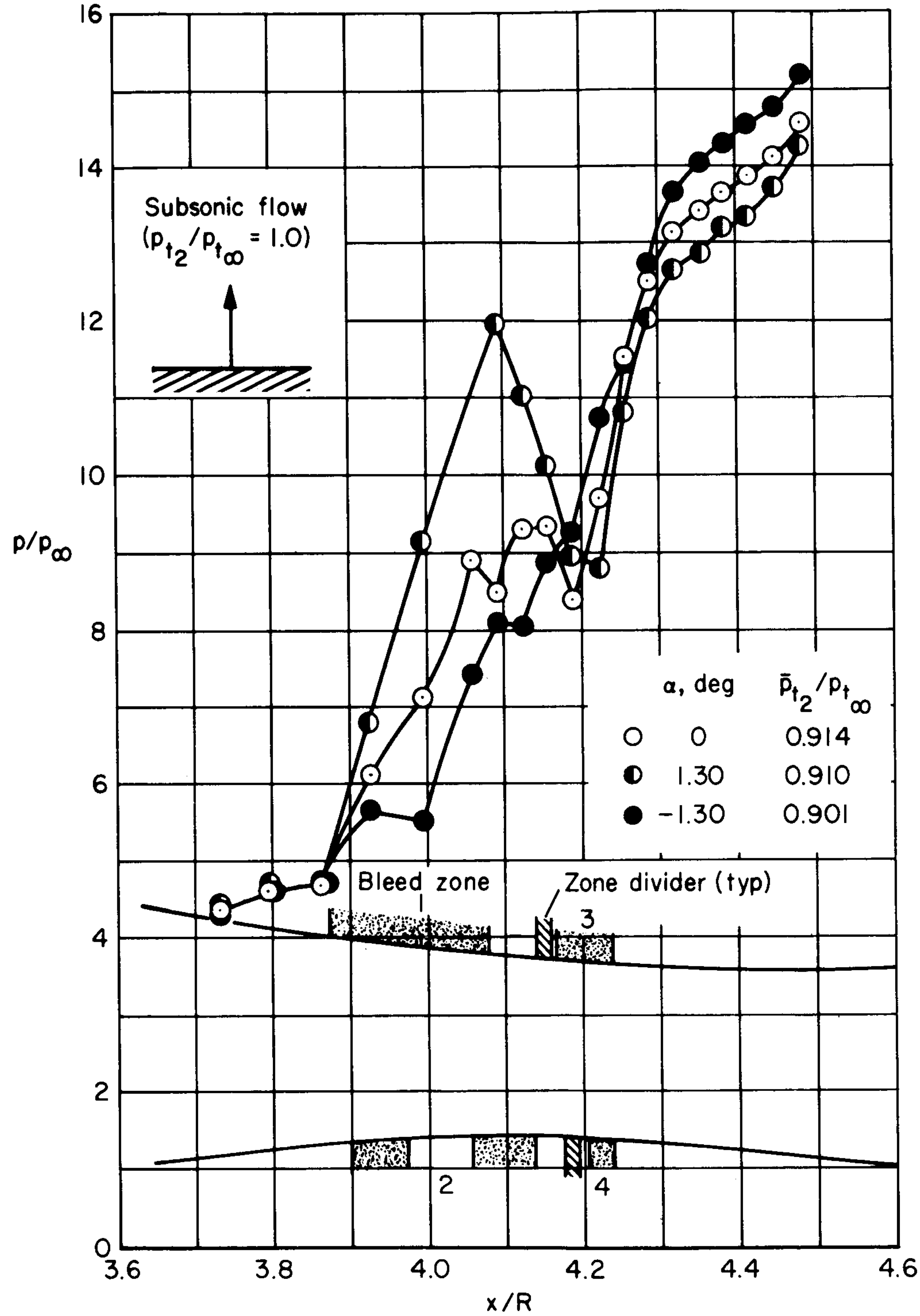

Figure 19. – Cowl static-pressure distributions at angle of attack; M_∞ = 2.65, bleed configuration A, x_{lip}/R = 2.325.

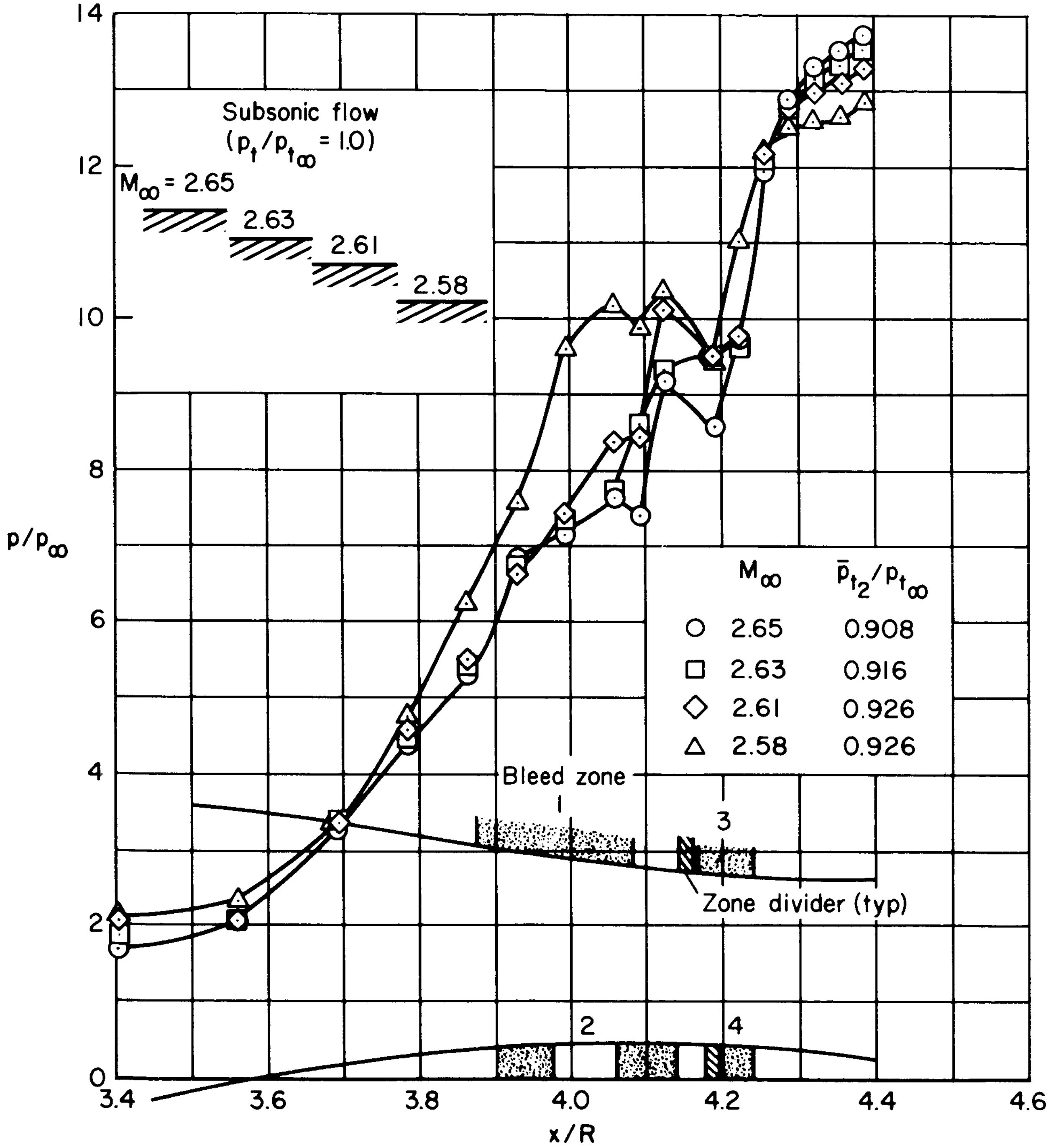

Figure 20. – Effect of Mach number on the centerbody static-pressure distributions; $\alpha = 0°$, bleed configuration A, $x_{lip}/R = 2.325$.

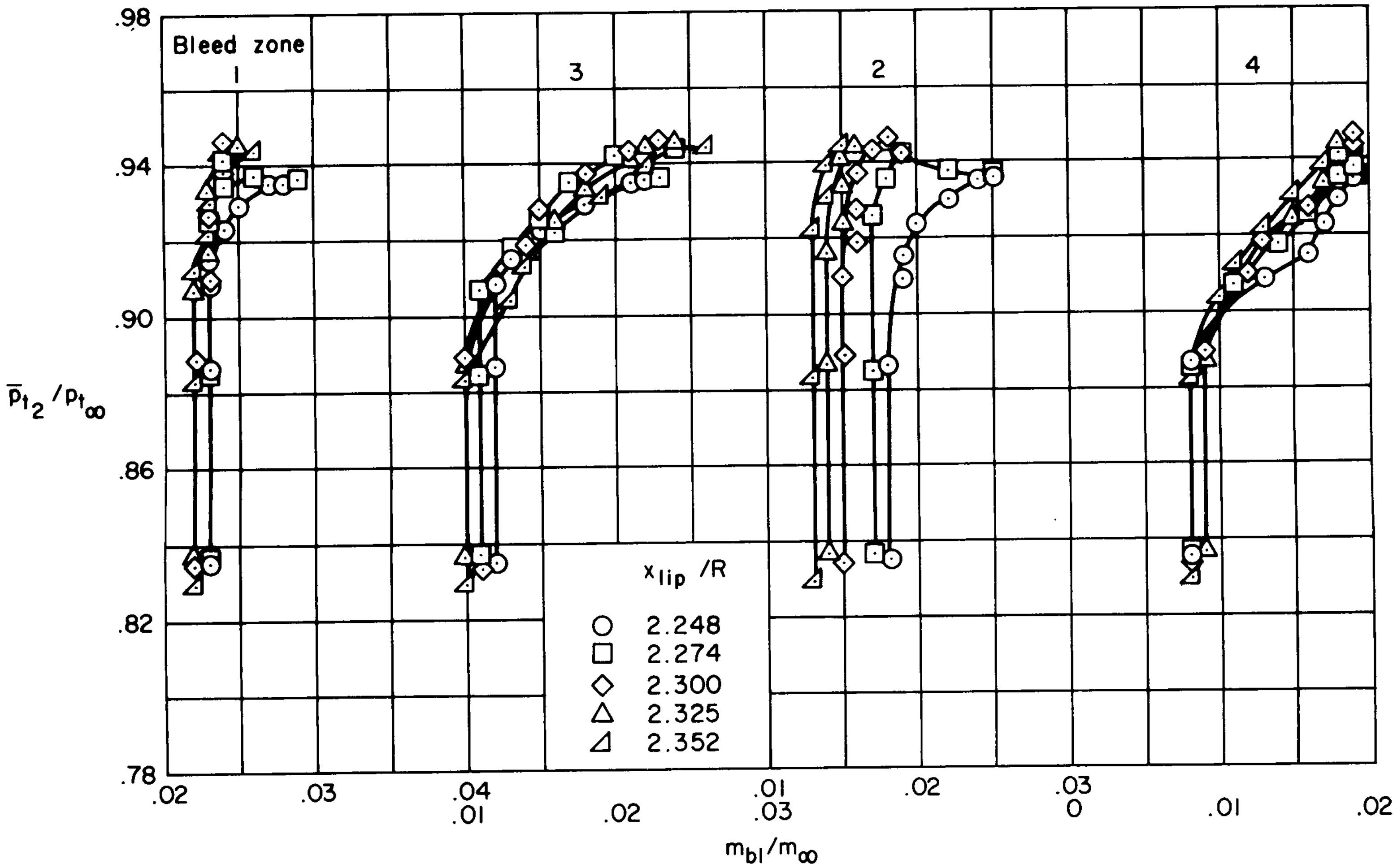

(a) Bleed configuration A.

Figure 21. – Supercritical bleed flow in the individual zones; $M_\infty = 2.65$, $\alpha = 0°$, $m_{bp}/m_\infty = 0$, $\theta_2 = 0°$, vortex generator configuration AA.

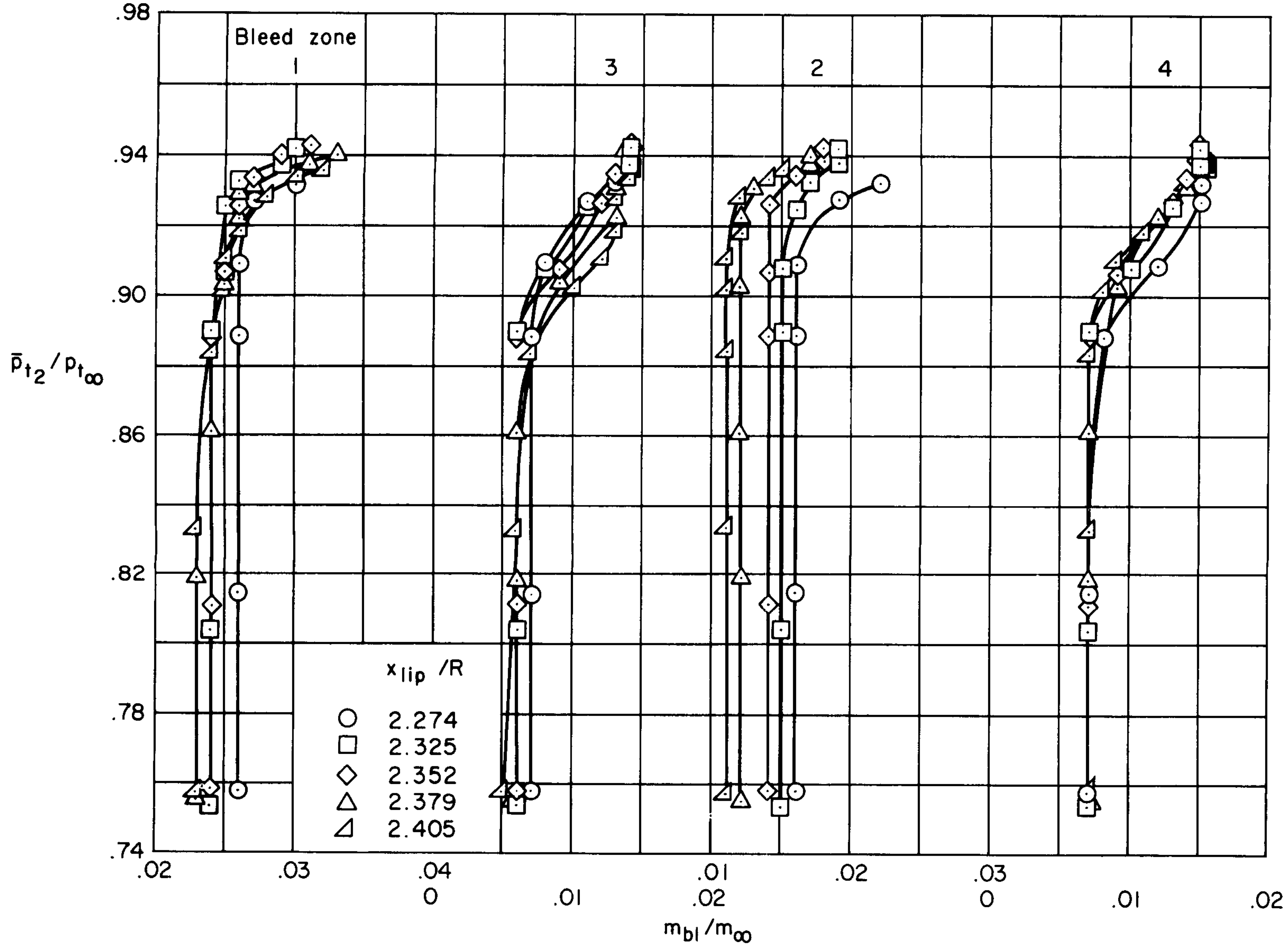

(b) Bleed configuration B-1.

Figure 21. – Continued.

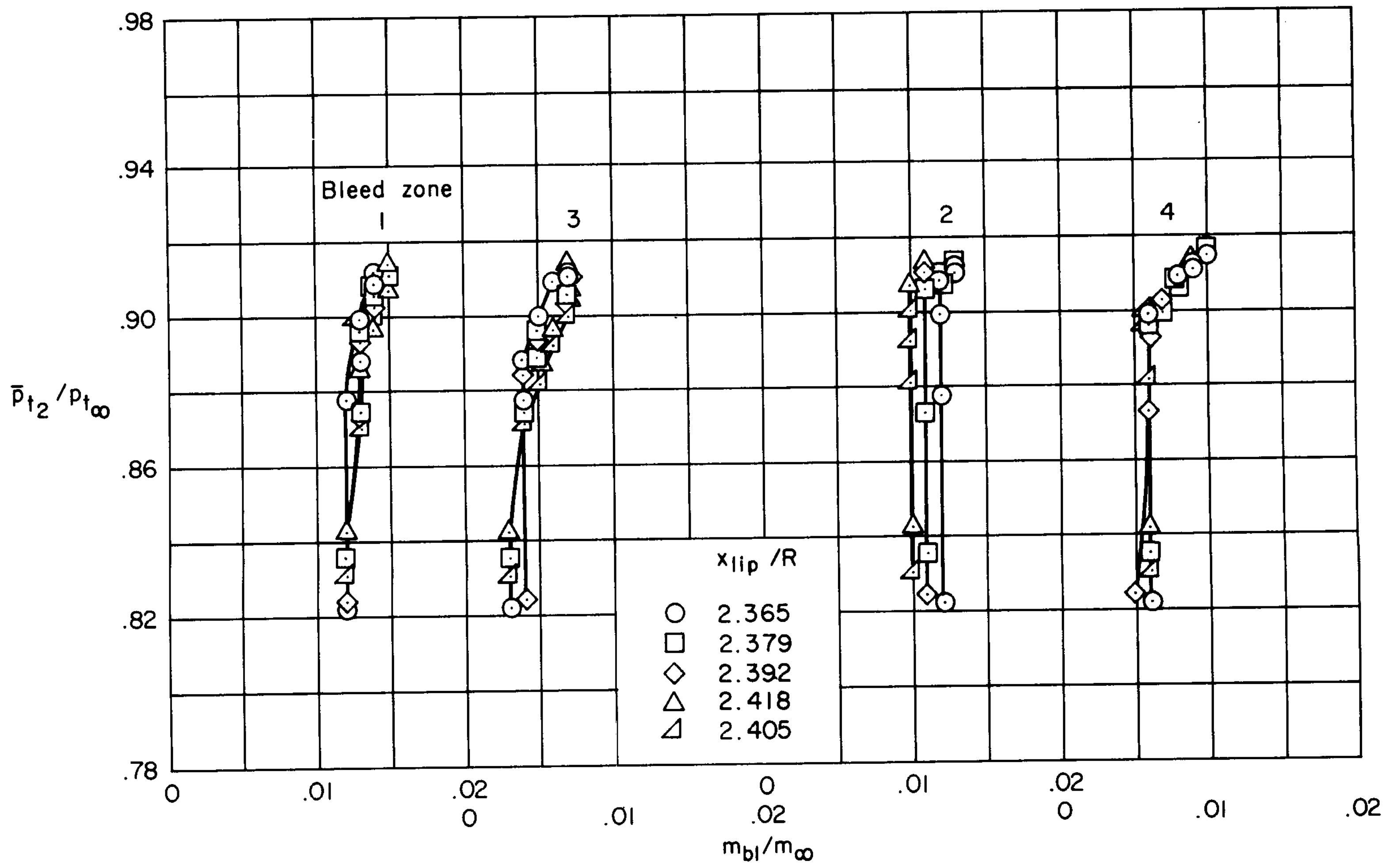

(c) Bleed configuration C.

Figure 21. – Concluded.

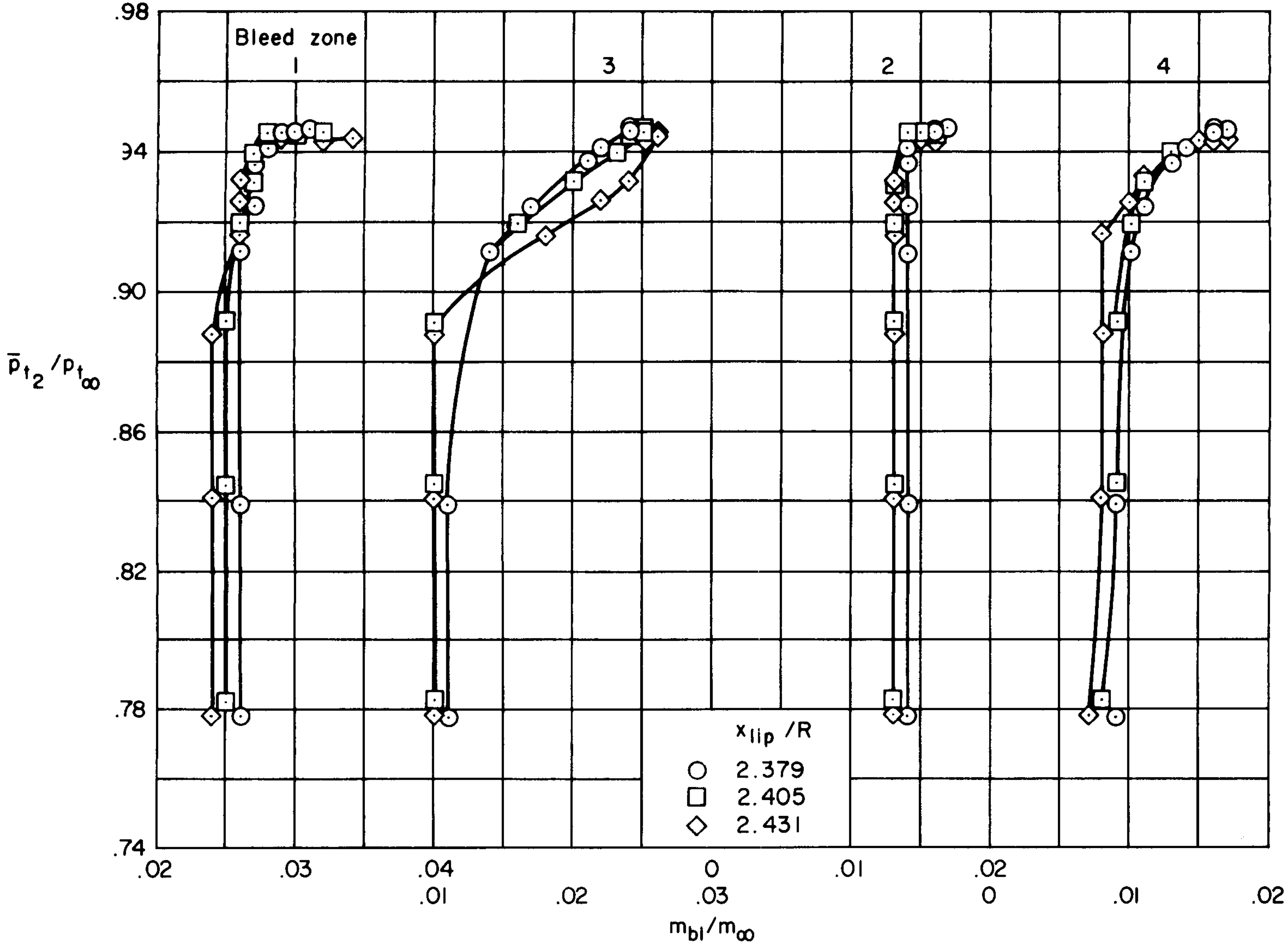

(a) Bleed configuration A.

Figure 22. – Supercritical bleed flow in the individual zones; $M_\infty = 2.60$, $\alpha = 0°$, $m_{bp}/m_\infty = 0$, $\theta_2 = 0°$, vortex generator configuration AA.

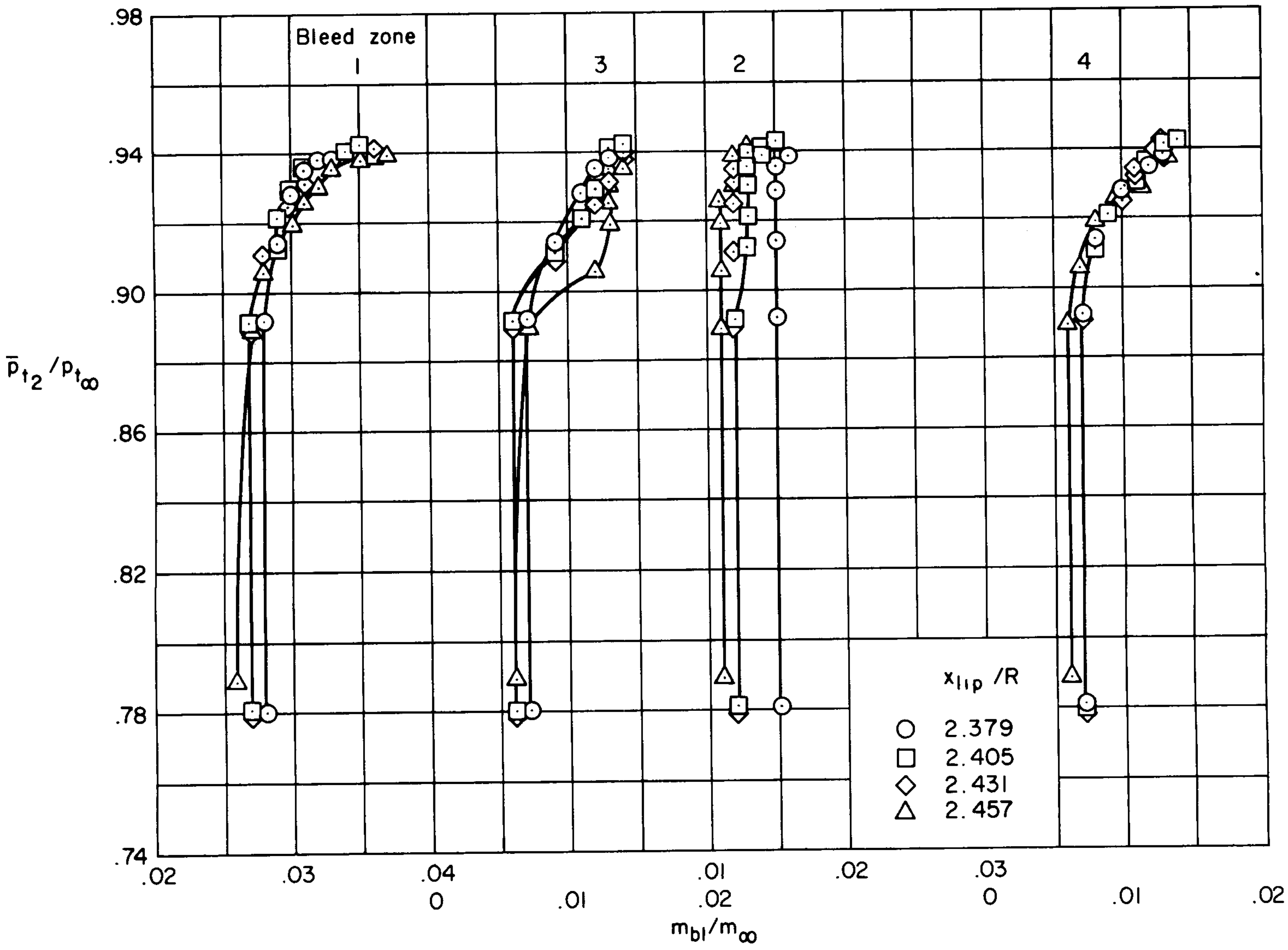

(b) Bleed configuration B-1.

Figure 22. – Continued.

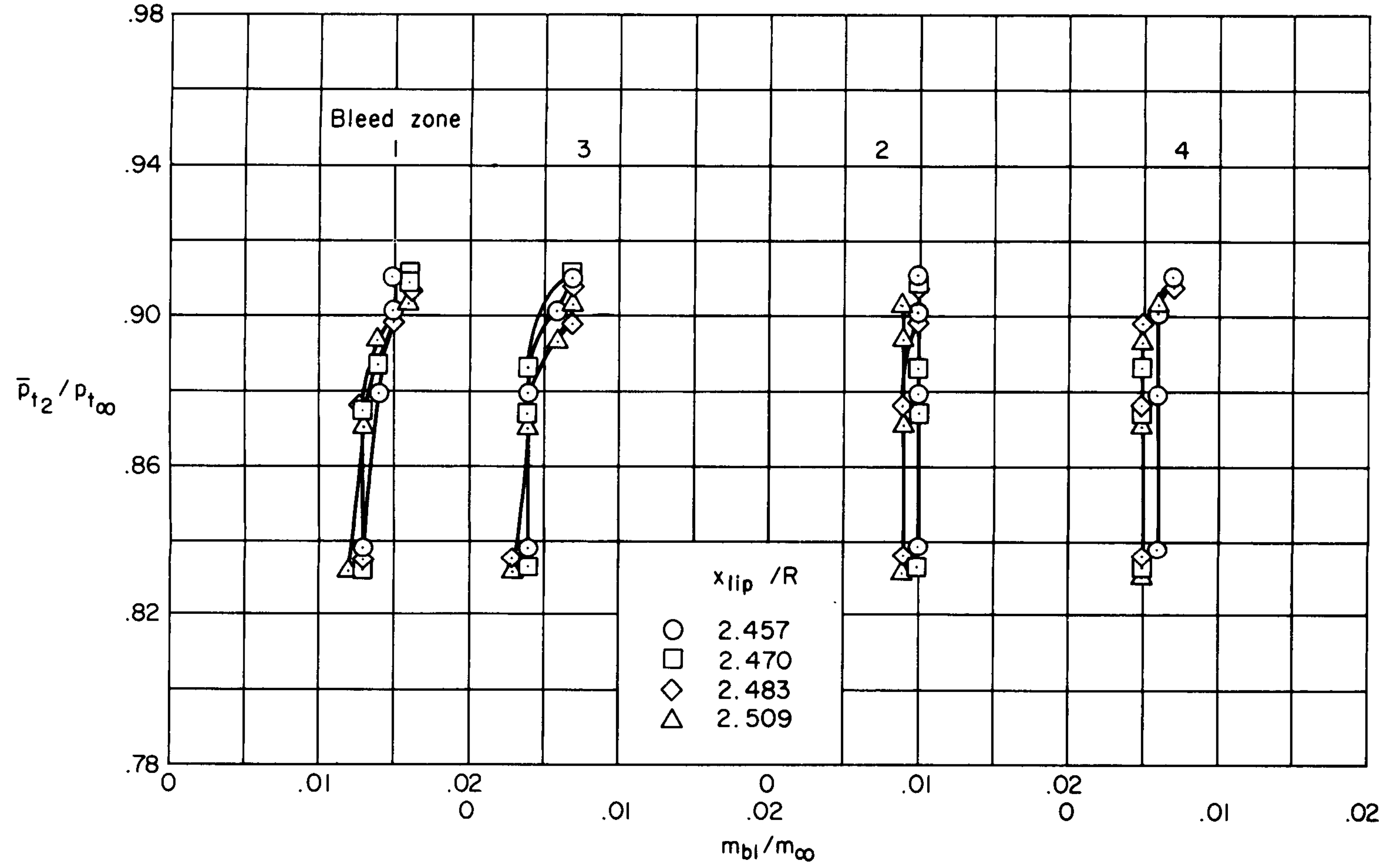

(c) Bleed configuration C.

Figure 22. – Concluded.

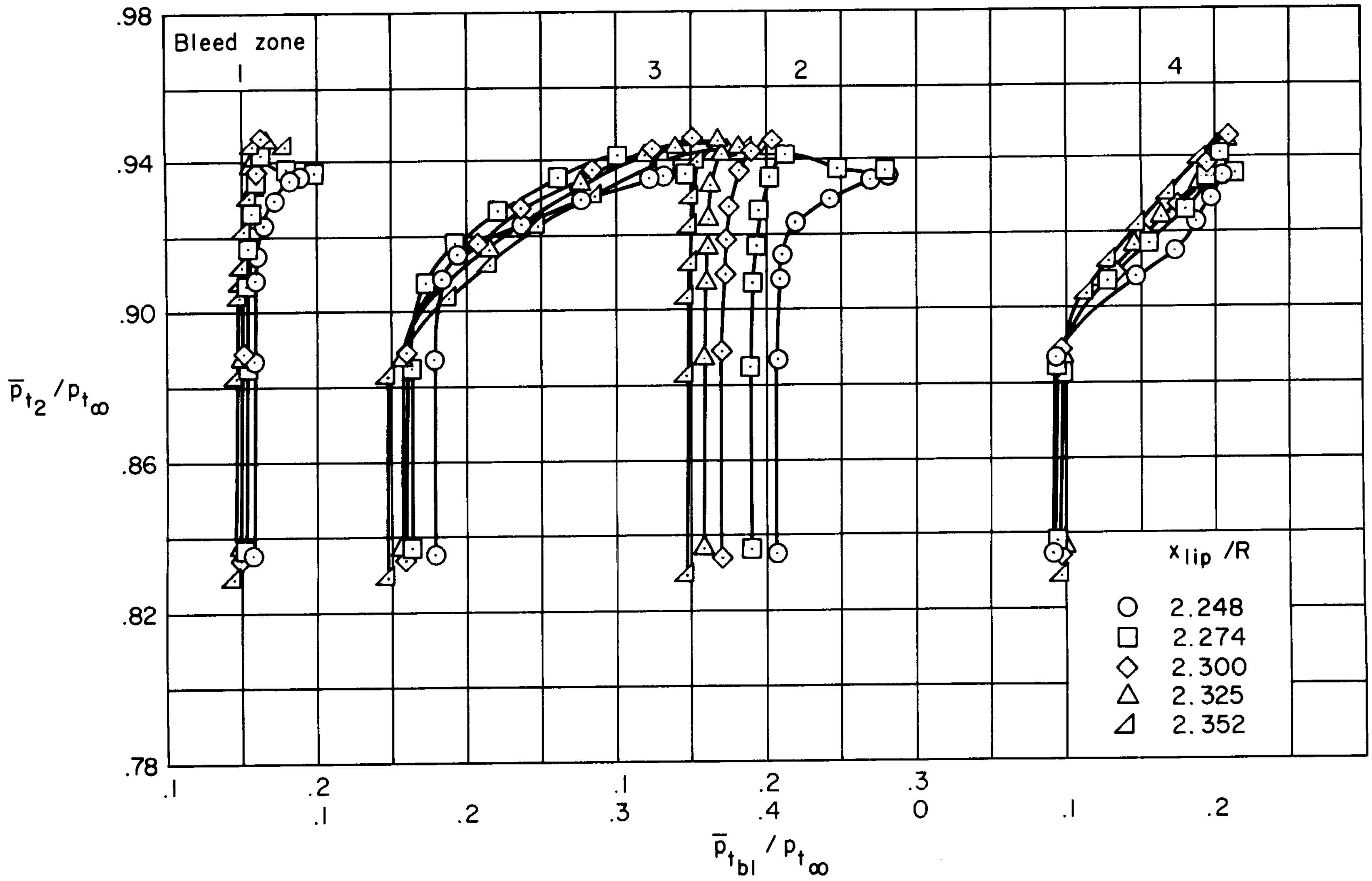

(a) Bleed configuration A.

Figure 23. – Bleed plenum-chamber pressure recoveries; $M_\infty = 2.65, \alpha = 0°, m_{bp}/m_\infty = 0, \theta_2 = 0°$; vortex generator configuration AA.

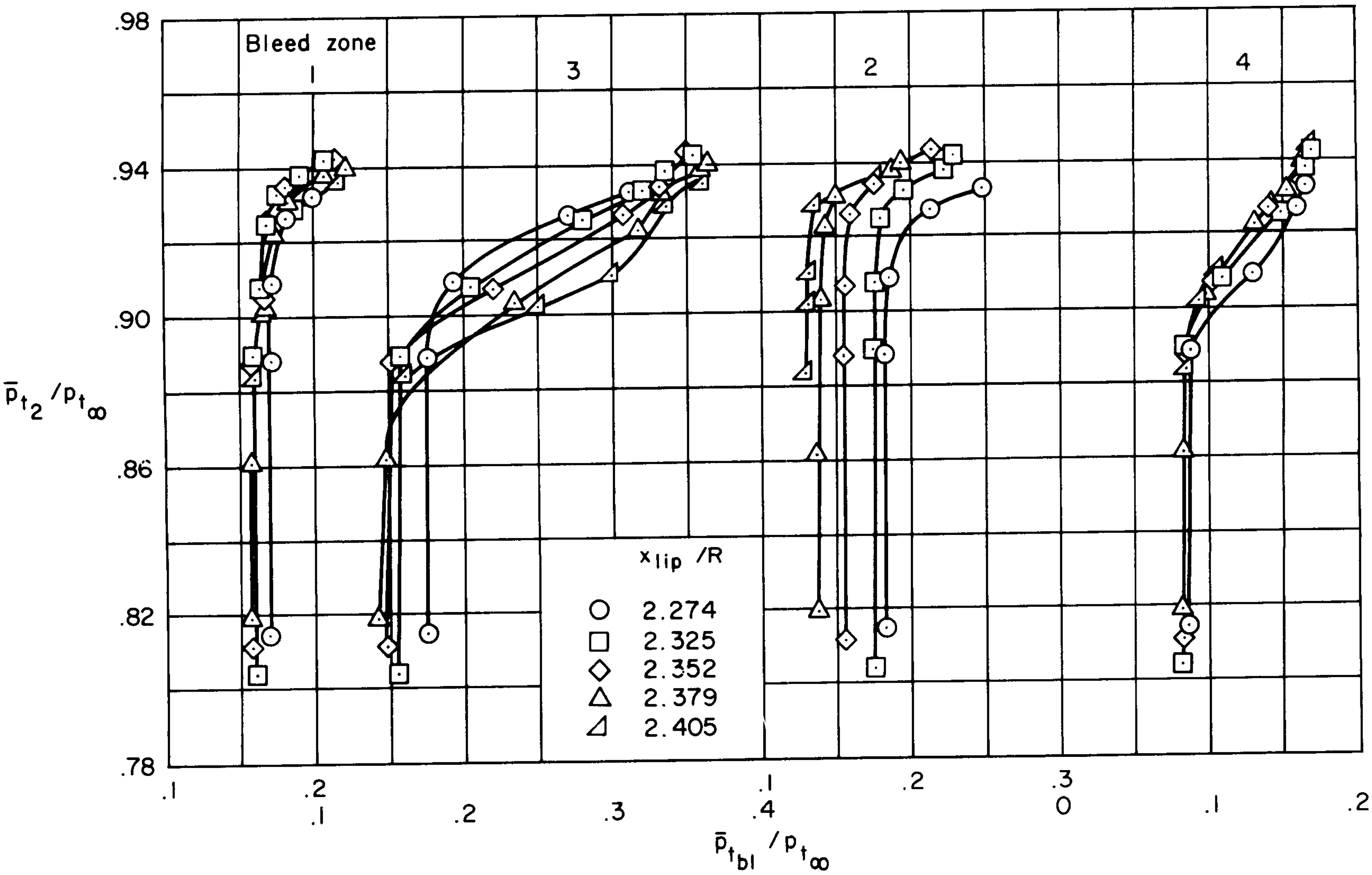

(b) Bleed configuration B-1.

Figure 23. – Continued.

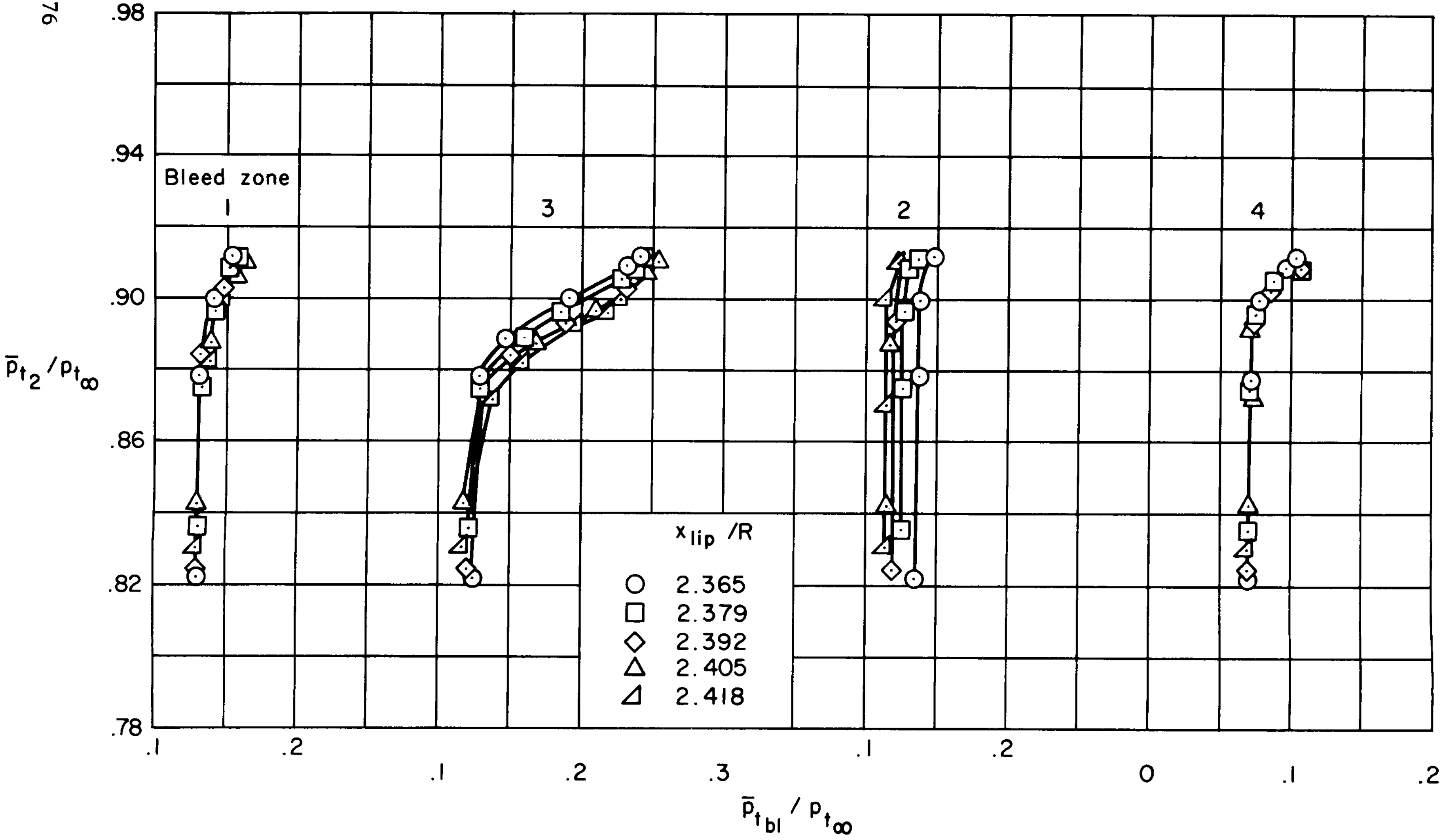

(c) Bleed configuration C.

Figure 23. – Concluded.

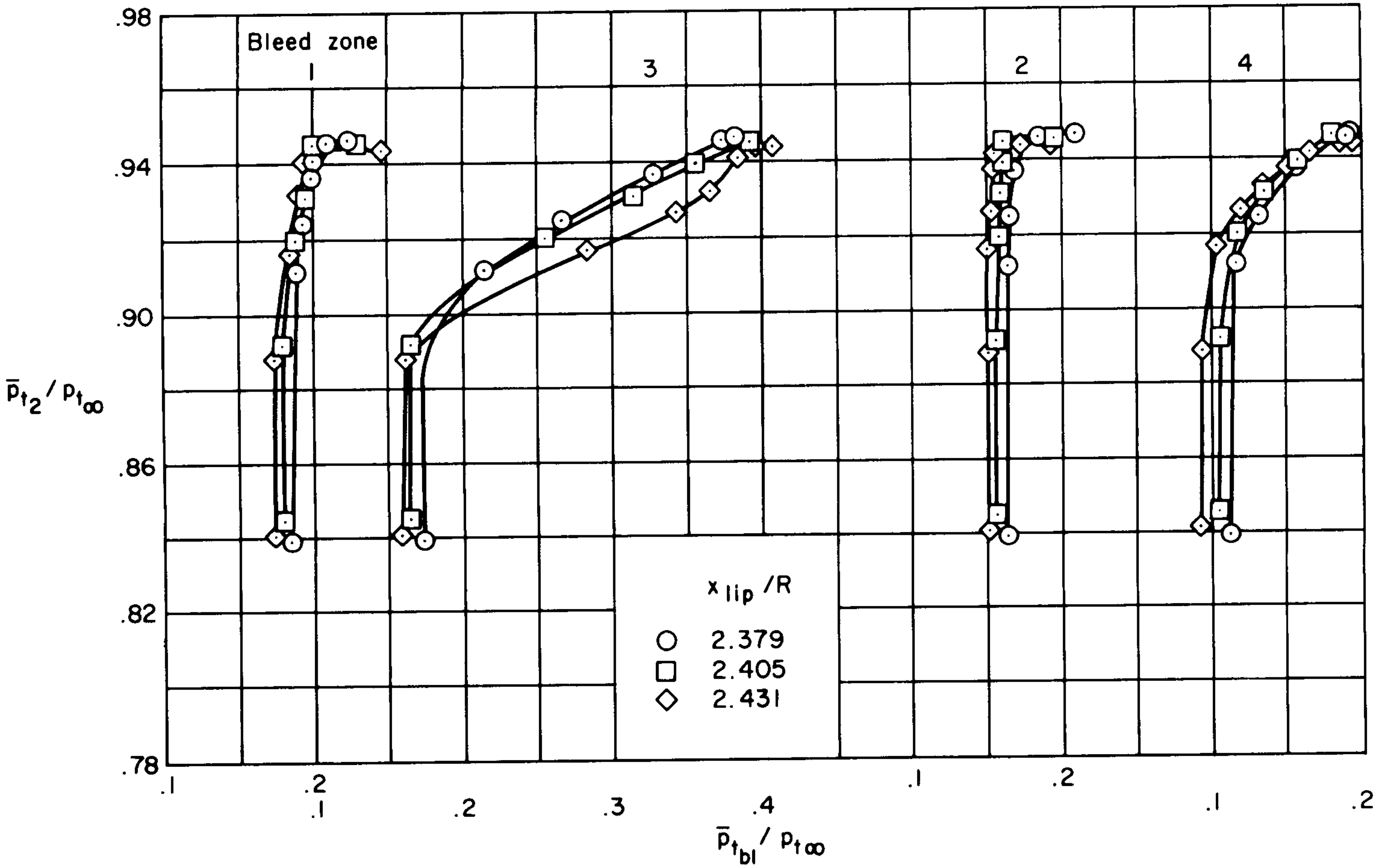

(a) Bleed configuration A.

Figure 24. – Bleed plenum-chamber pressure recoveries; $M_\infty = 2.60, \alpha = 0^\circ, m_{bp}/m_\infty = 0, \theta_2 = 0^\circ$; vortex generator configuration AA.

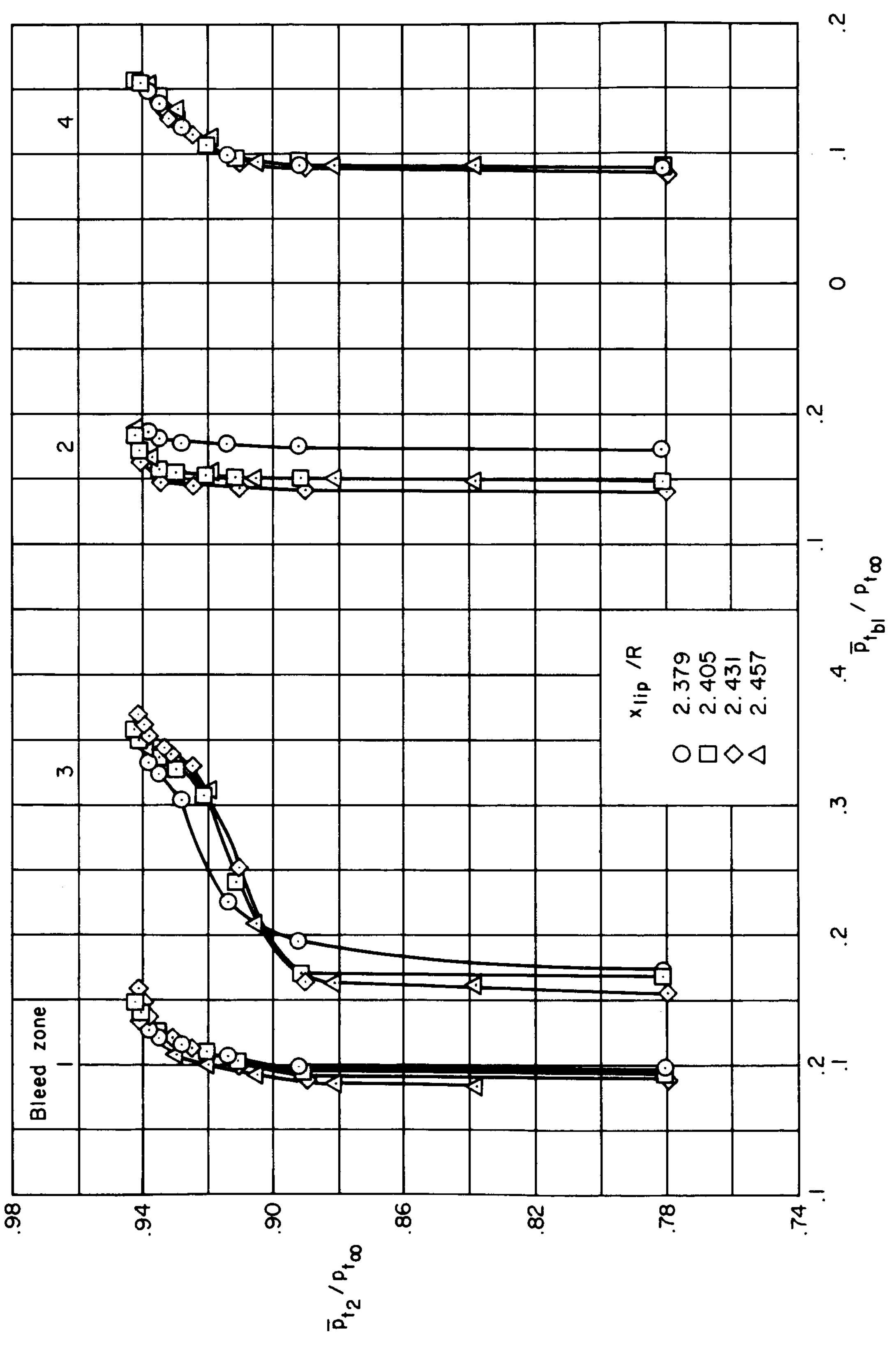

(b) Bleed configuration B-1.

Figure 24. – Continued.

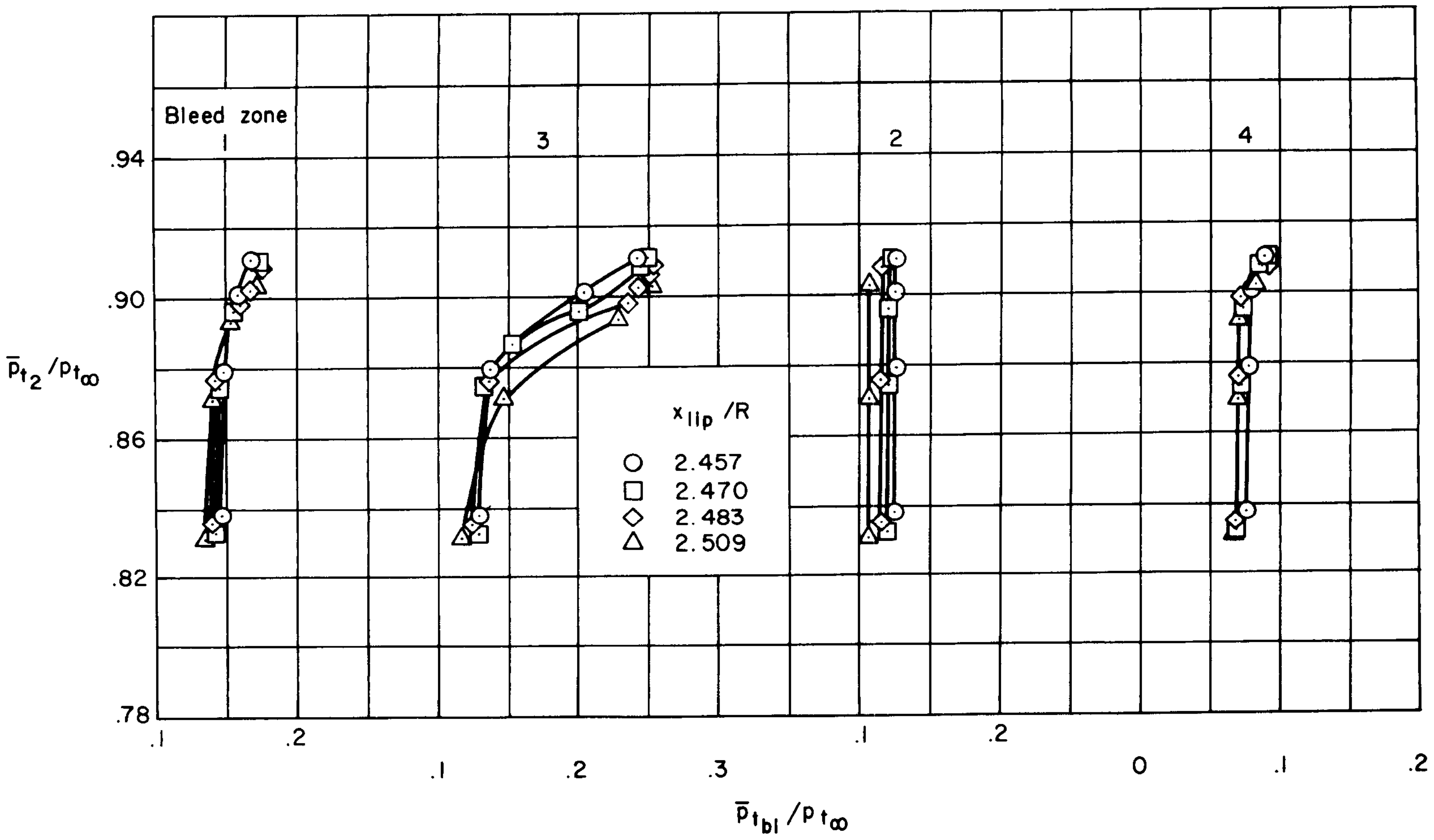

(c) Bleed configuration C.

Figure 24. – Concluded.

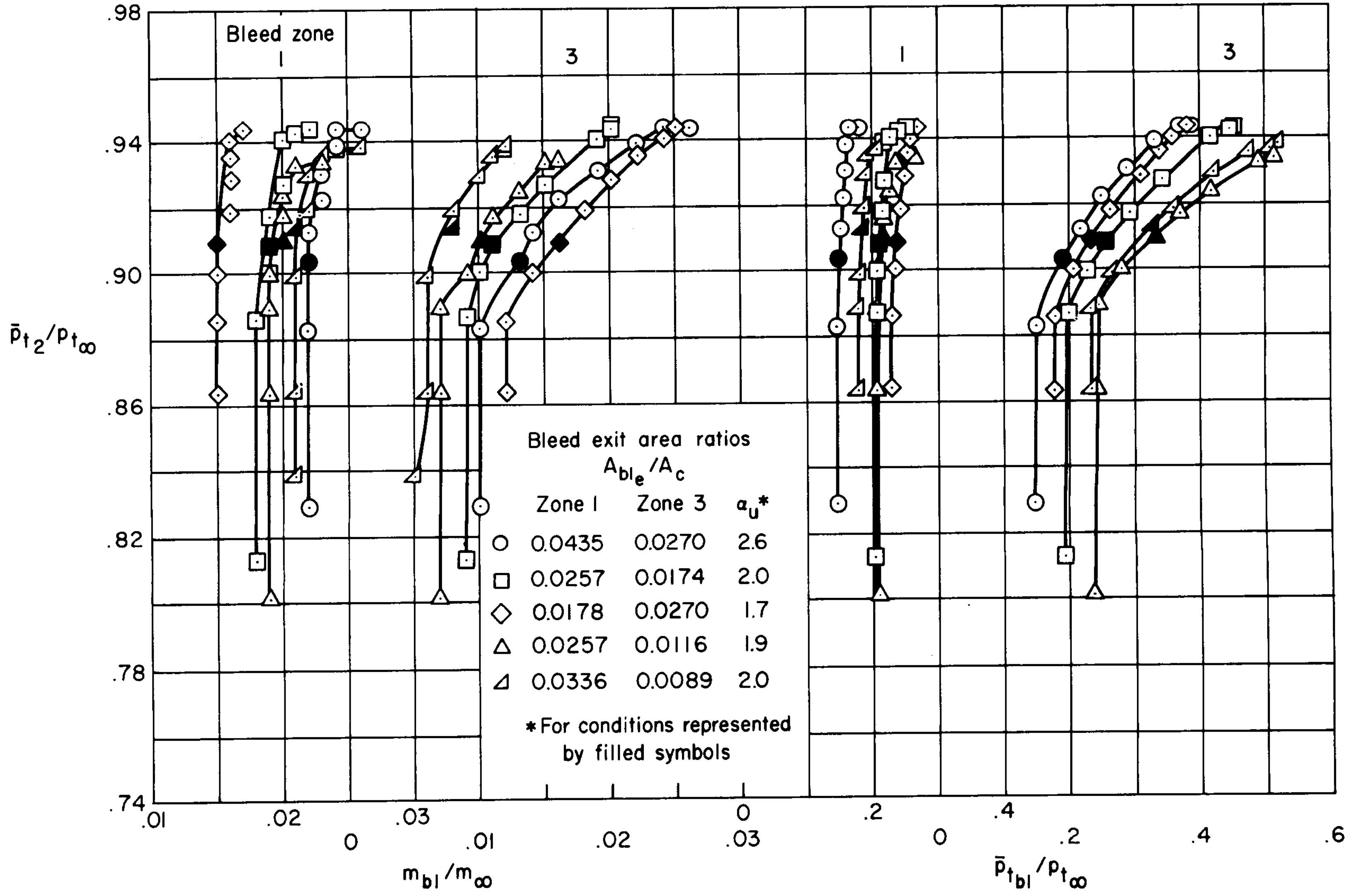

Figure 25. – Effect of exit area ratio on the cowl bleed and plenum chamber pressure recoveries, $M_\infty = 2.65$, $\alpha = 0°$, $m_{bp}/m_\infty = 0$, $\theta_2 = 0°$, vortex generator configuration AA, bleed configuration A, $x_{lip}/R = 2.352$.

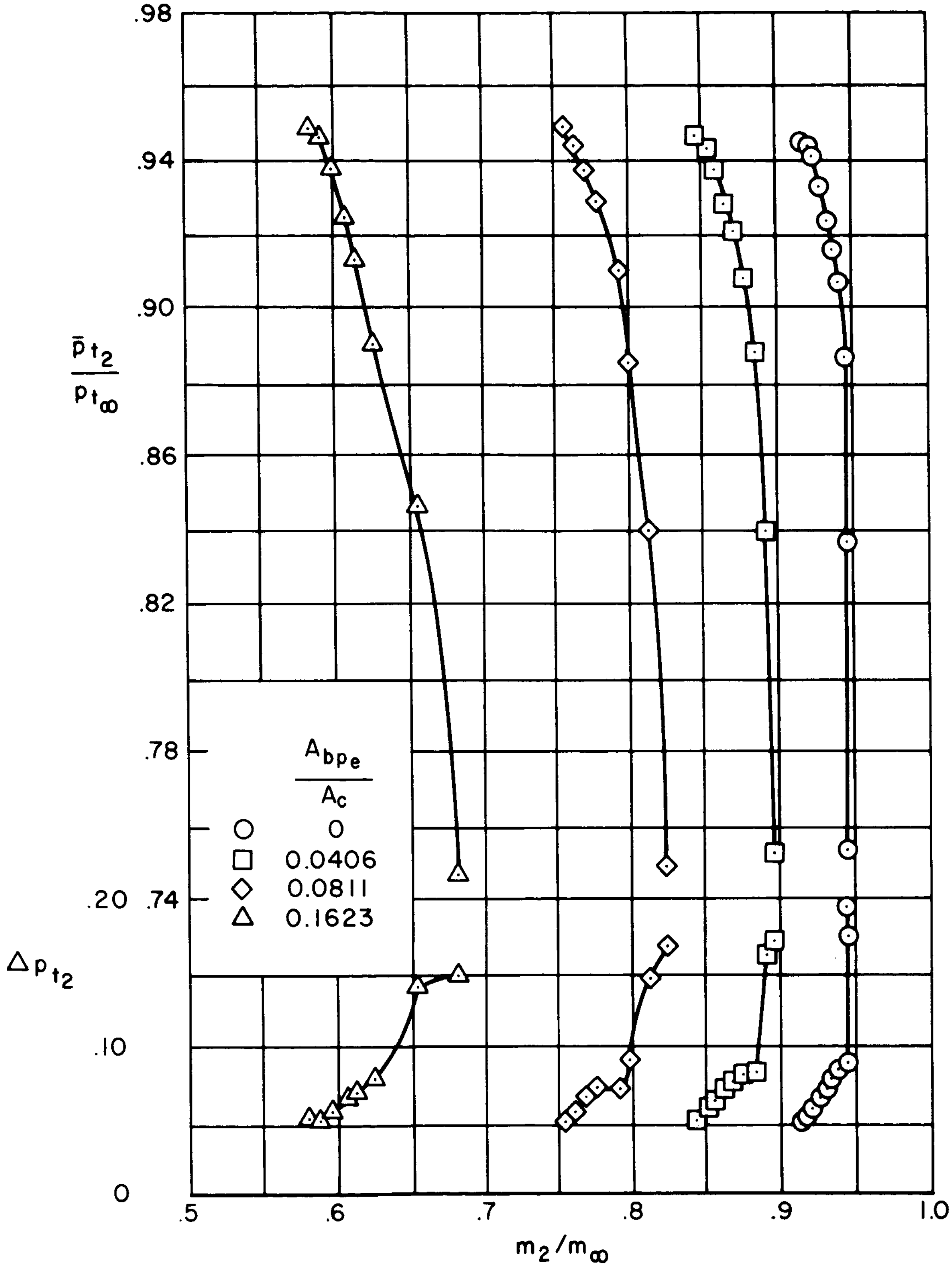

(a) Bleed configuration A, $x_{lip}/R = 2.325$.

Figure 26. – Supercritical performance with bypass; $M_\infty = 2.65$, $\alpha = 0°$, $\theta_2 = 0°$, vortex generator configuration AA.

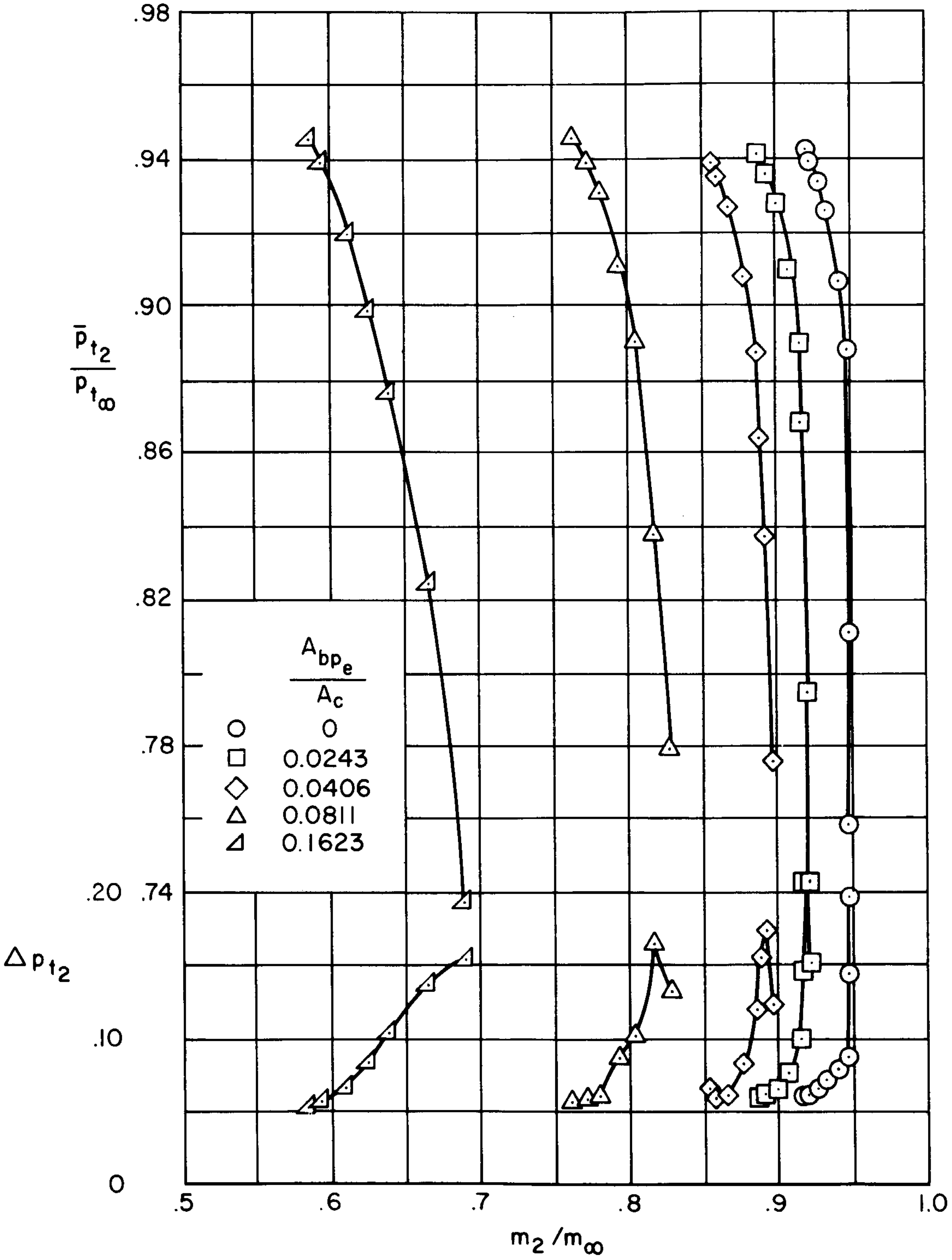

(b) Bleed configuration B-1, $x_{lip}/R = 2.352$.

Figure 26. – Continued.

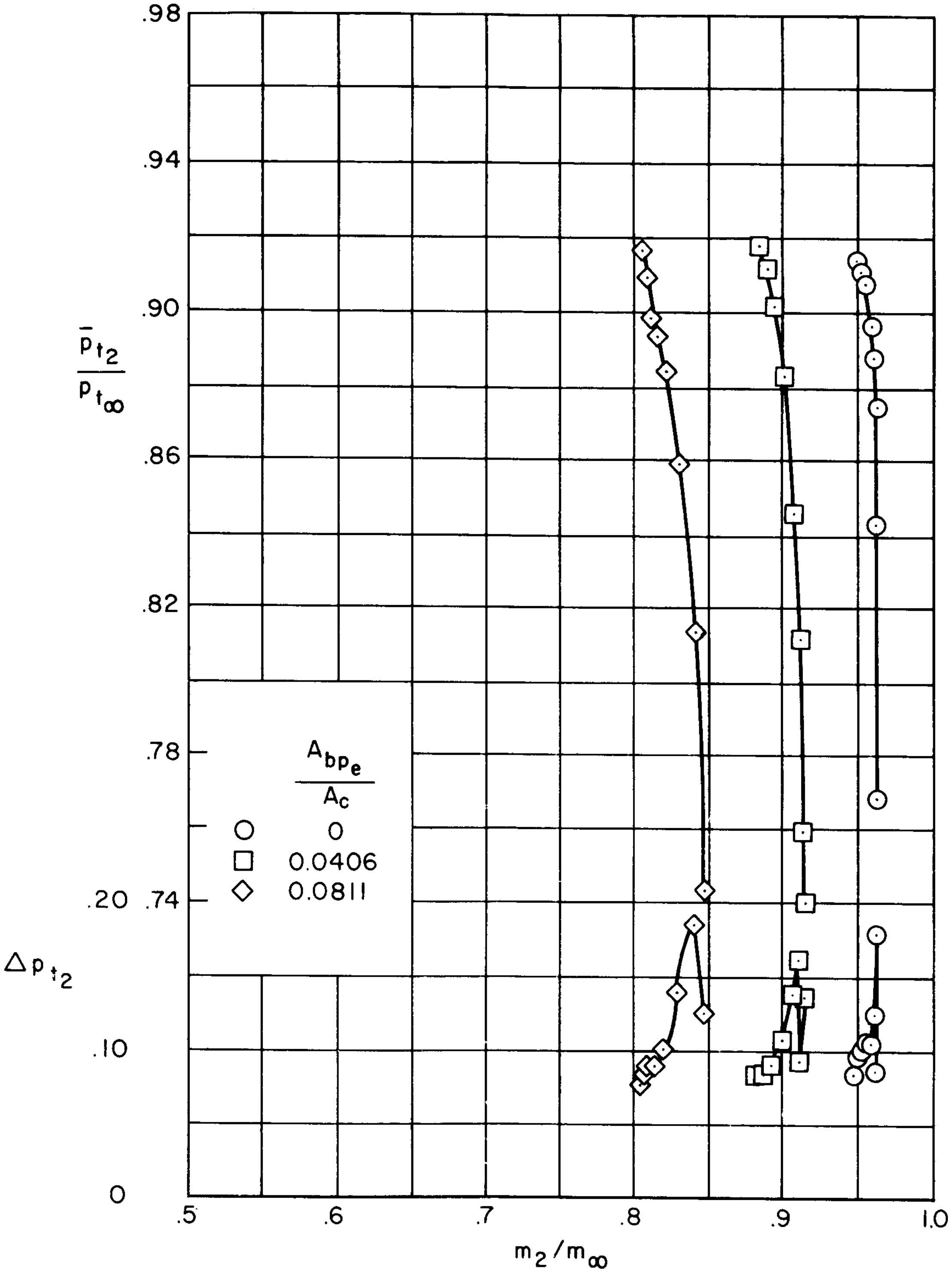

(c) Bleed configuration C, x_{lip}/R = 2.405.

Figure 26. – Concluded.

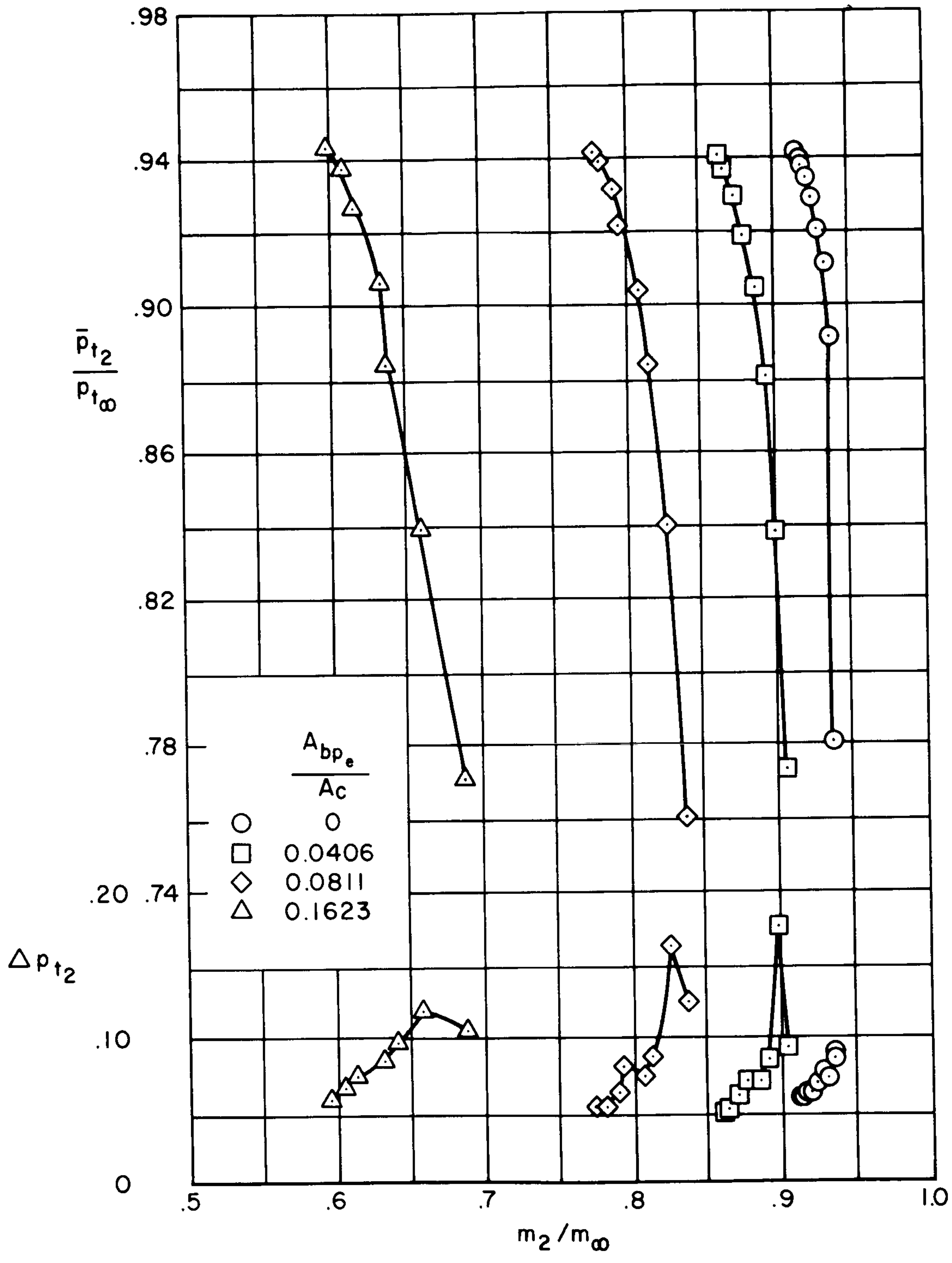

Figure 27. – Supercritical performance with bypass; $M_\infty = 2.60$, $\alpha = 0°$, $\theta_2 = 0°$, vortex generator configuration AA, bleed configuration B-1, $x_{lip}/R = 2.405$.

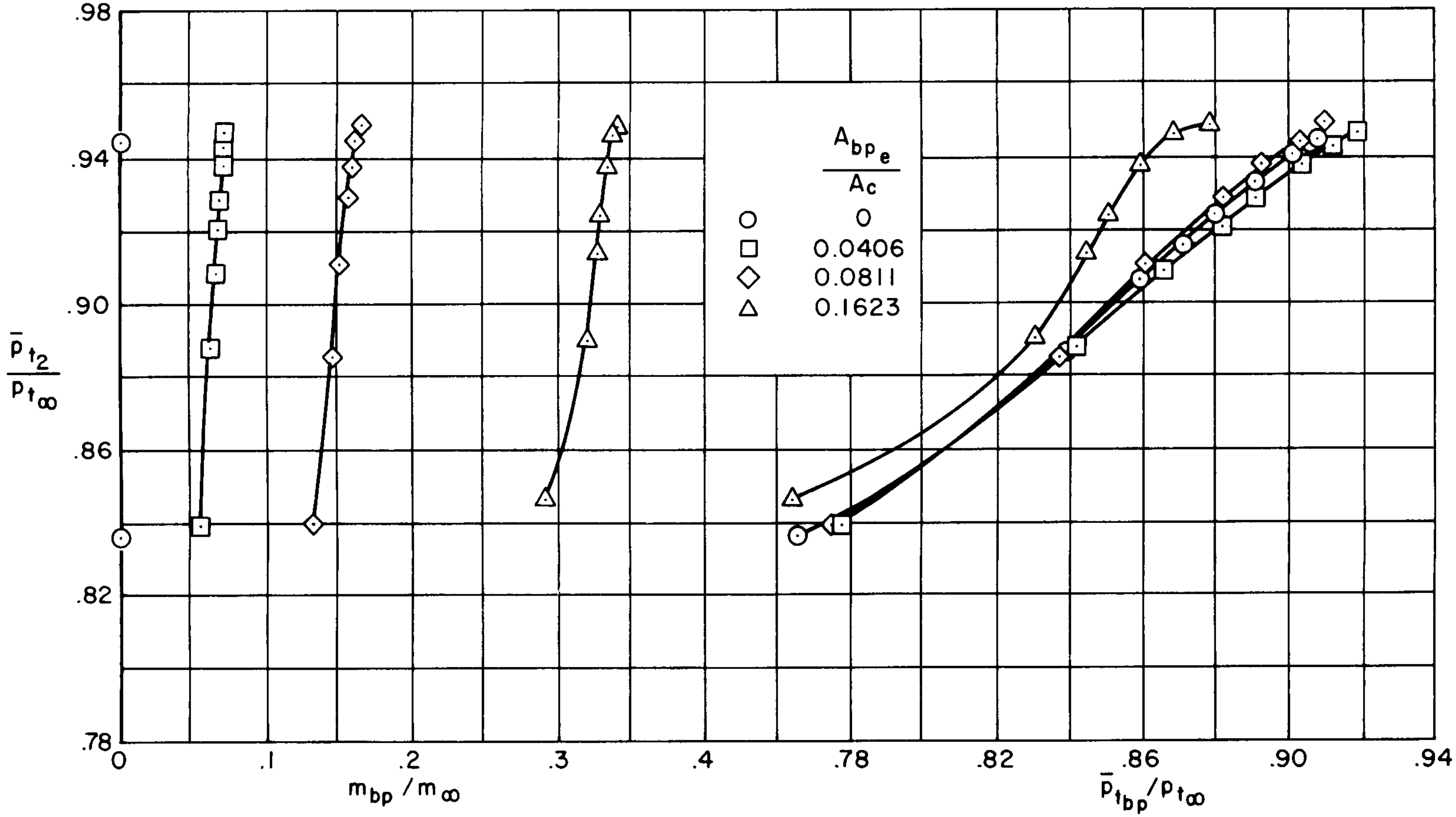

(a) Bleed configuration A, x_{lip}/R = 2.325.

Figure 28. – Bypass mass flow and plenum chamber pressure recovery; $M_\infty = 2.65, \alpha = 0°, \theta_2 = 0°$, vortex generator configuration AA.

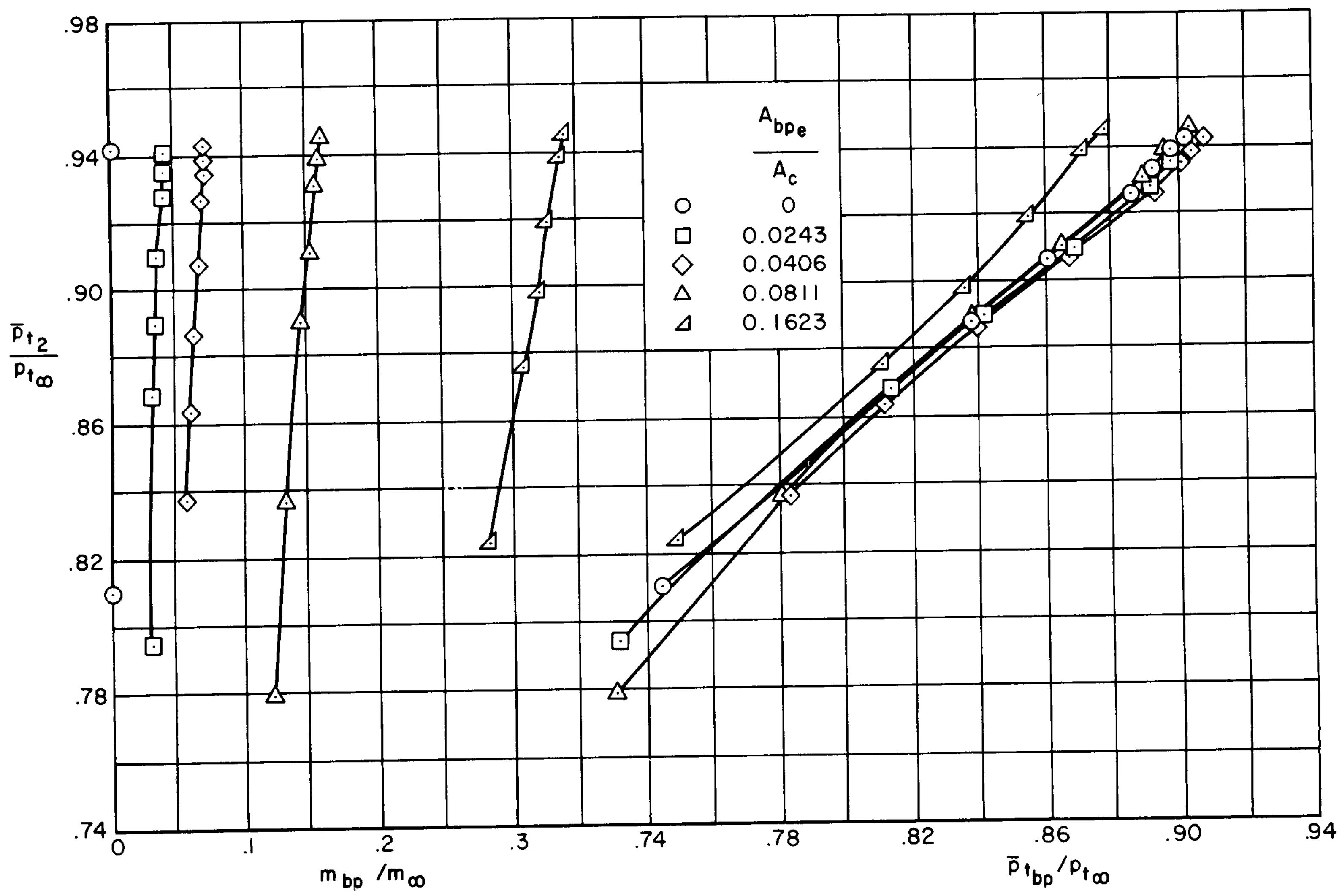

(b) Bleed configuration B-1, $x_{lip}/R = 2.352$.

Figure 28. – Continued.

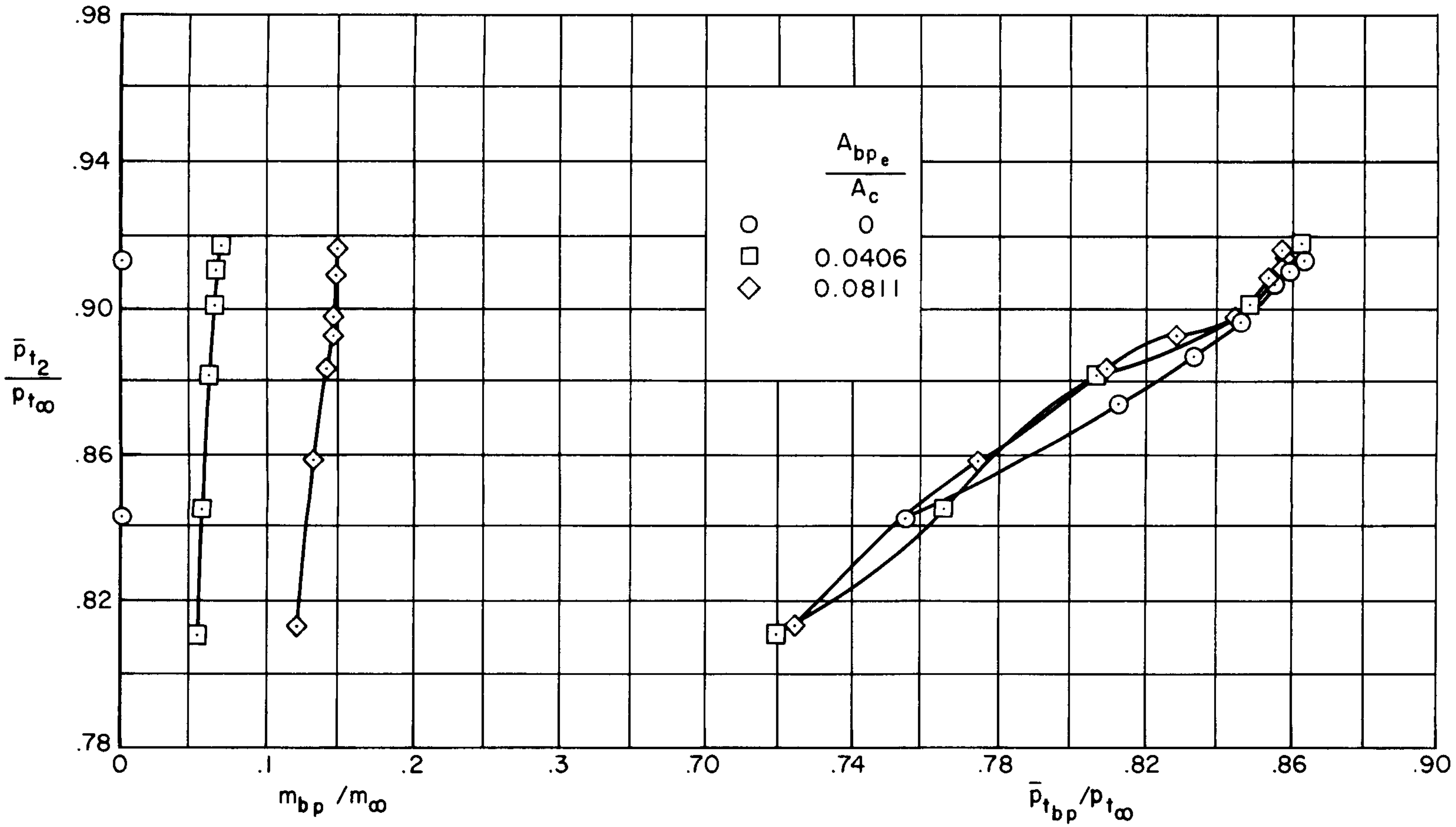

(c) Bleed configuration C, $x_{lip}/R = 2.405$.

Figure 28. – Concluded.

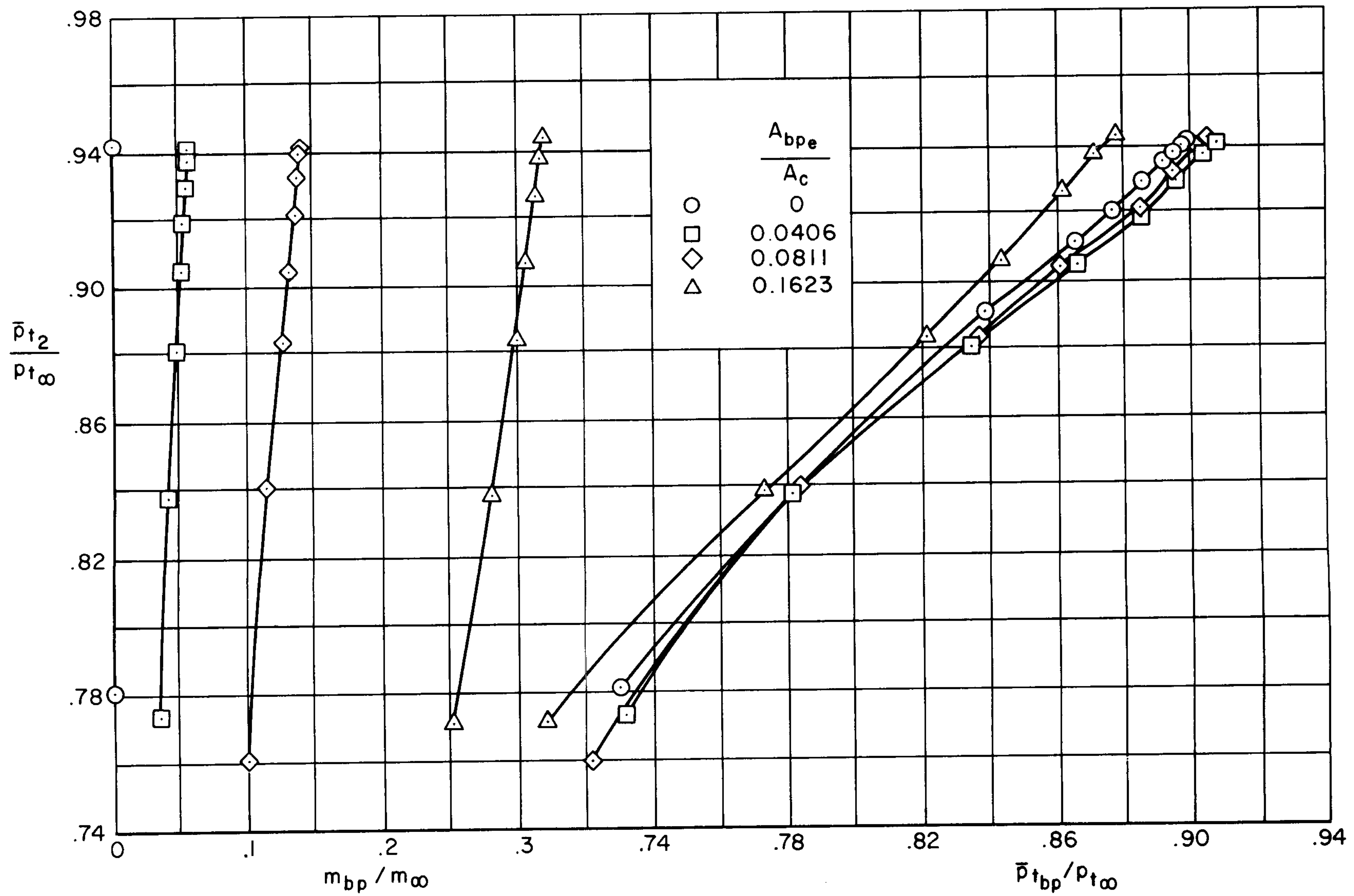

Figure 29. – Bypass mass flow and plenum chamber pressure recovery; $M_\infty = 2.60$, $\alpha = 0°$, $\theta_2 = 0°$, vortex generator configuration AA, bleed configuration B-1, $x_{lip}/R = 2.405$.

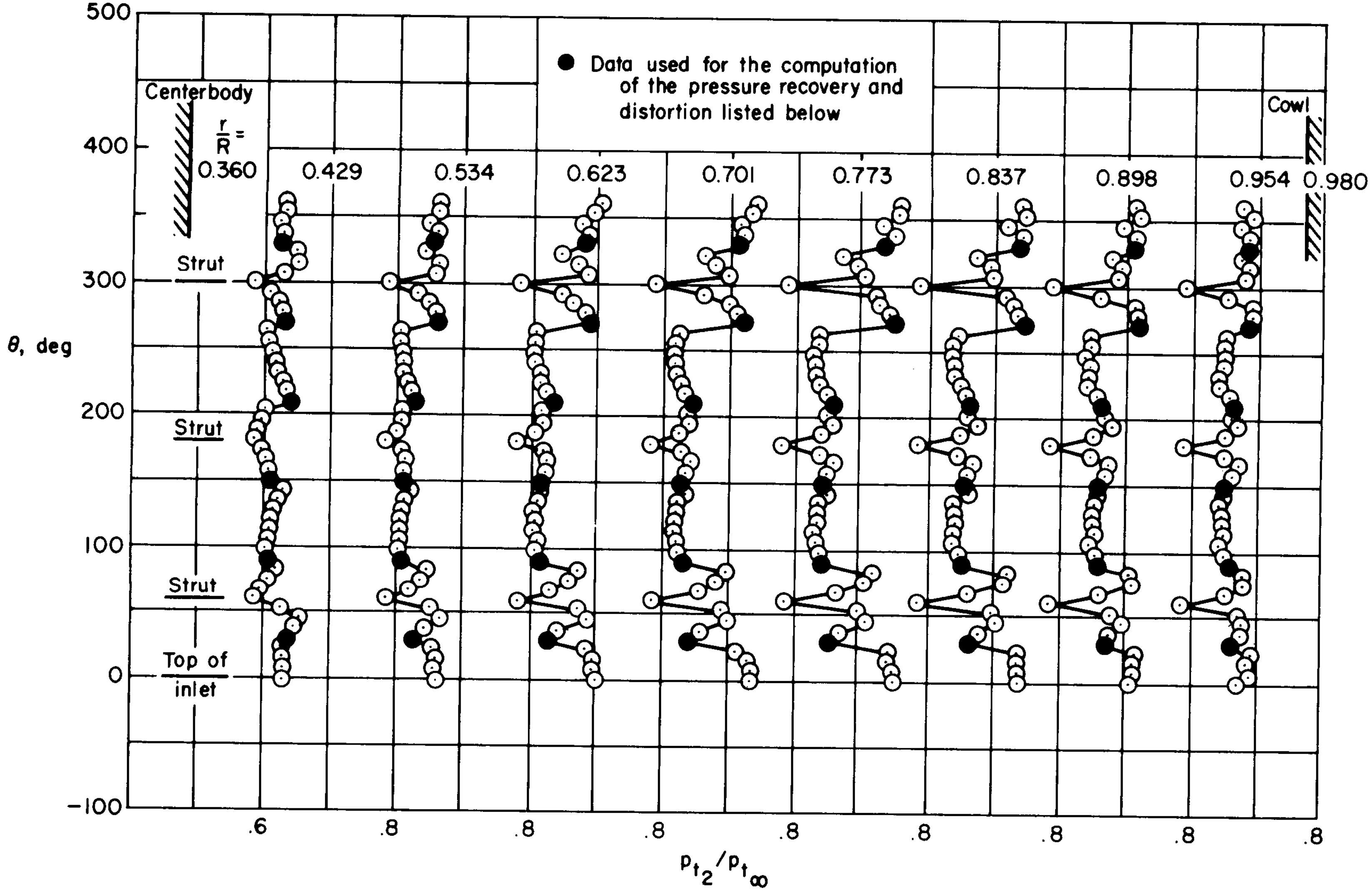

(a) $\alpha = 4.1°$, $\bar{p}_{t_2}/p_{t_\infty} = 0.660$, $m_{bl}/m_\infty = 0.042$, $\Delta p_{t_2} = 0.219$

Figure 30. – Circumferential total-pressure profiles at angle of attack, $M_\infty = 2.65$, $m_{bp}/m_\infty = 0$, vortex generator configuration AA, bleed configuration A, $x_{lip}/R = 2.981$.

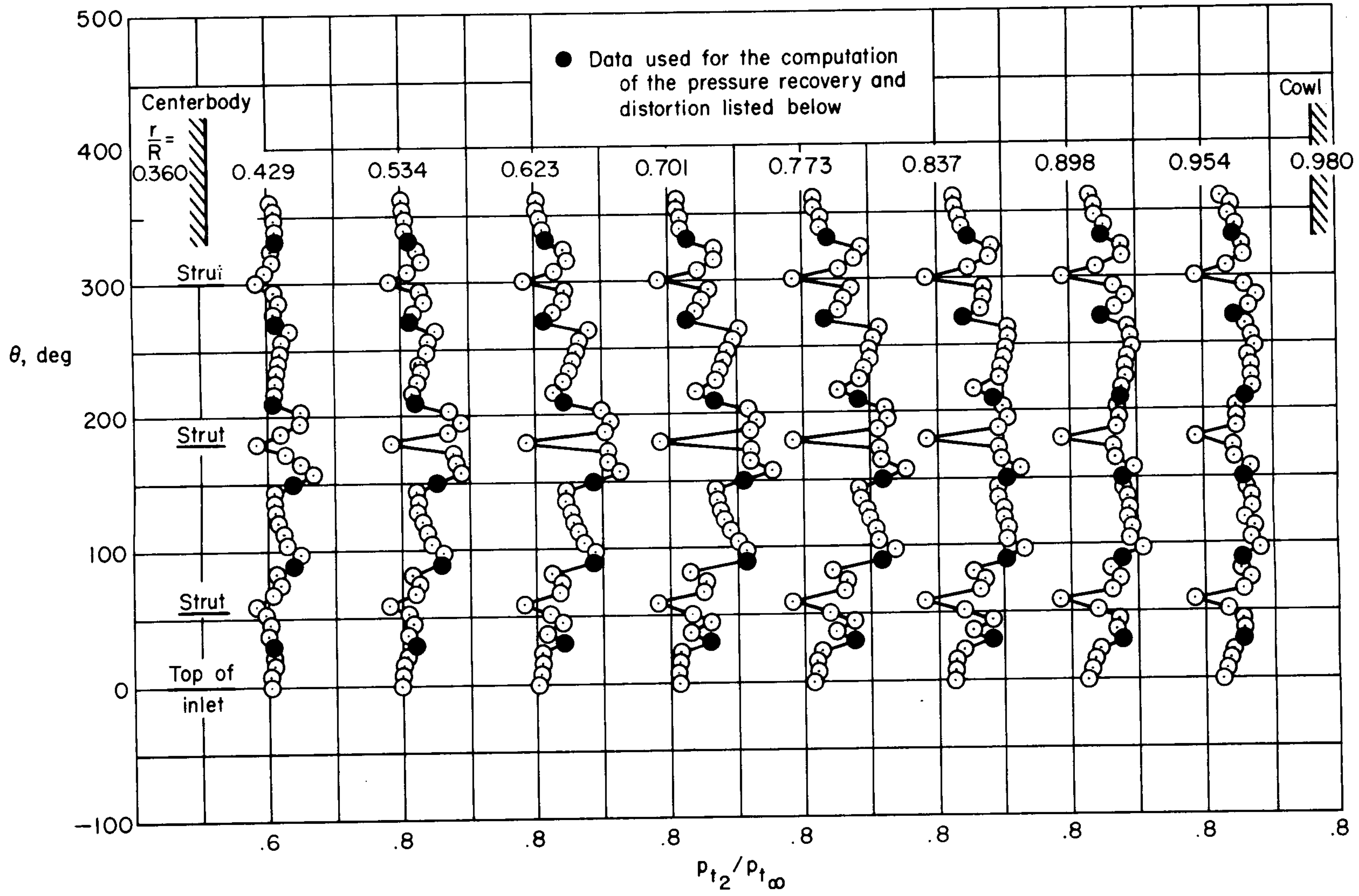

(b) $\alpha = -3.9°$, $\bar{p}_{t_2}/p_{t_\infty} = 0.654$, $m_{bl}/m_\infty = 0.045$, $\Delta p_{t_2} = 0.171$

Figure 30. – Concluded.

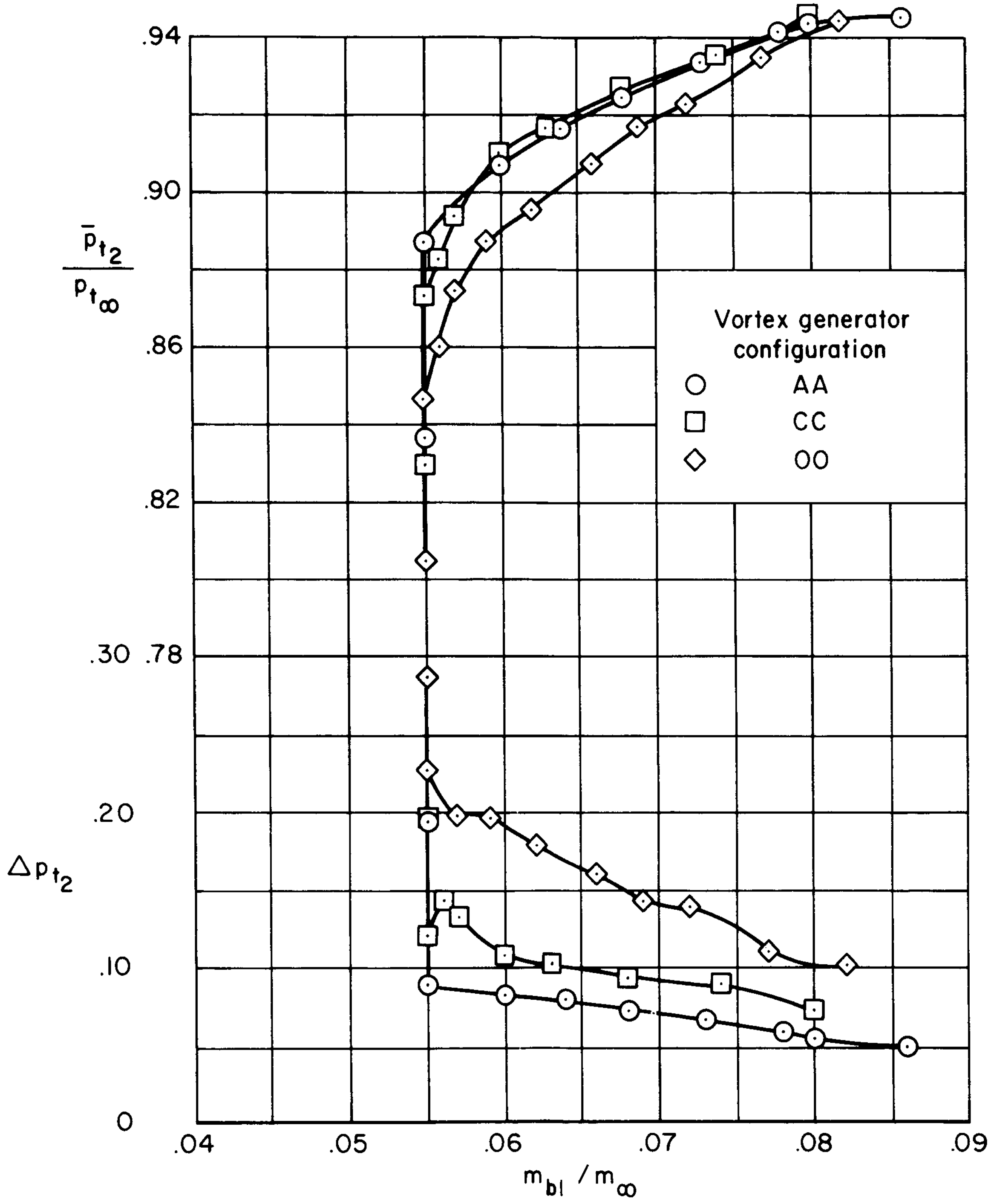

(a) Bleed configuration A, $x_{lip}/R = 2.325$.

Figure 31. – Effect of vortex generator configuration on the supercritical performance; $M_\infty = 2.65$, $\alpha = 0^\circ$, $m_{bp}/m_\infty = 0$, $\theta_2 = 0^\circ$.

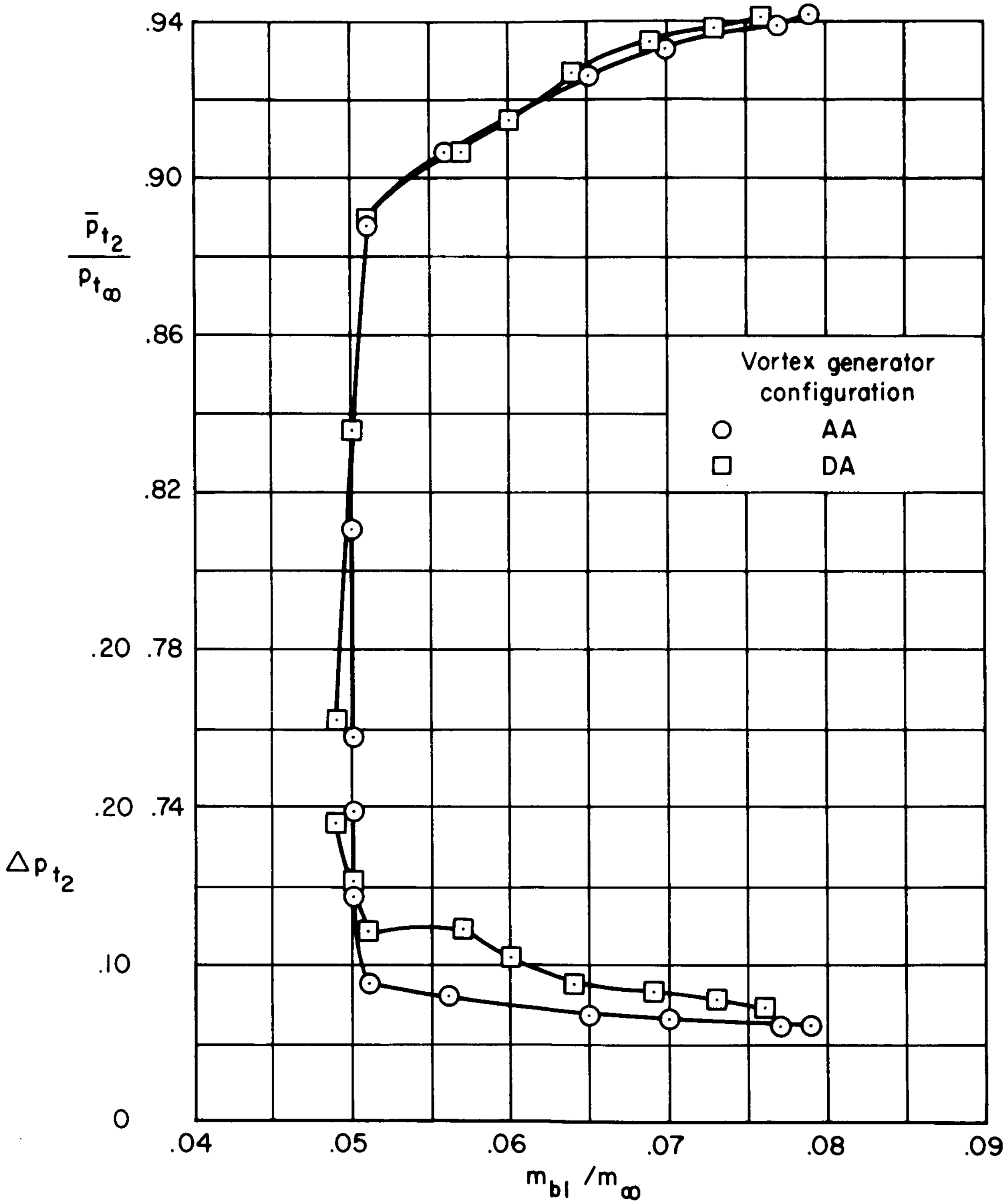

(b) Bleed configuration B-1, $x_{lip}/R = 2.352$.

Figure 31. – Concluded.

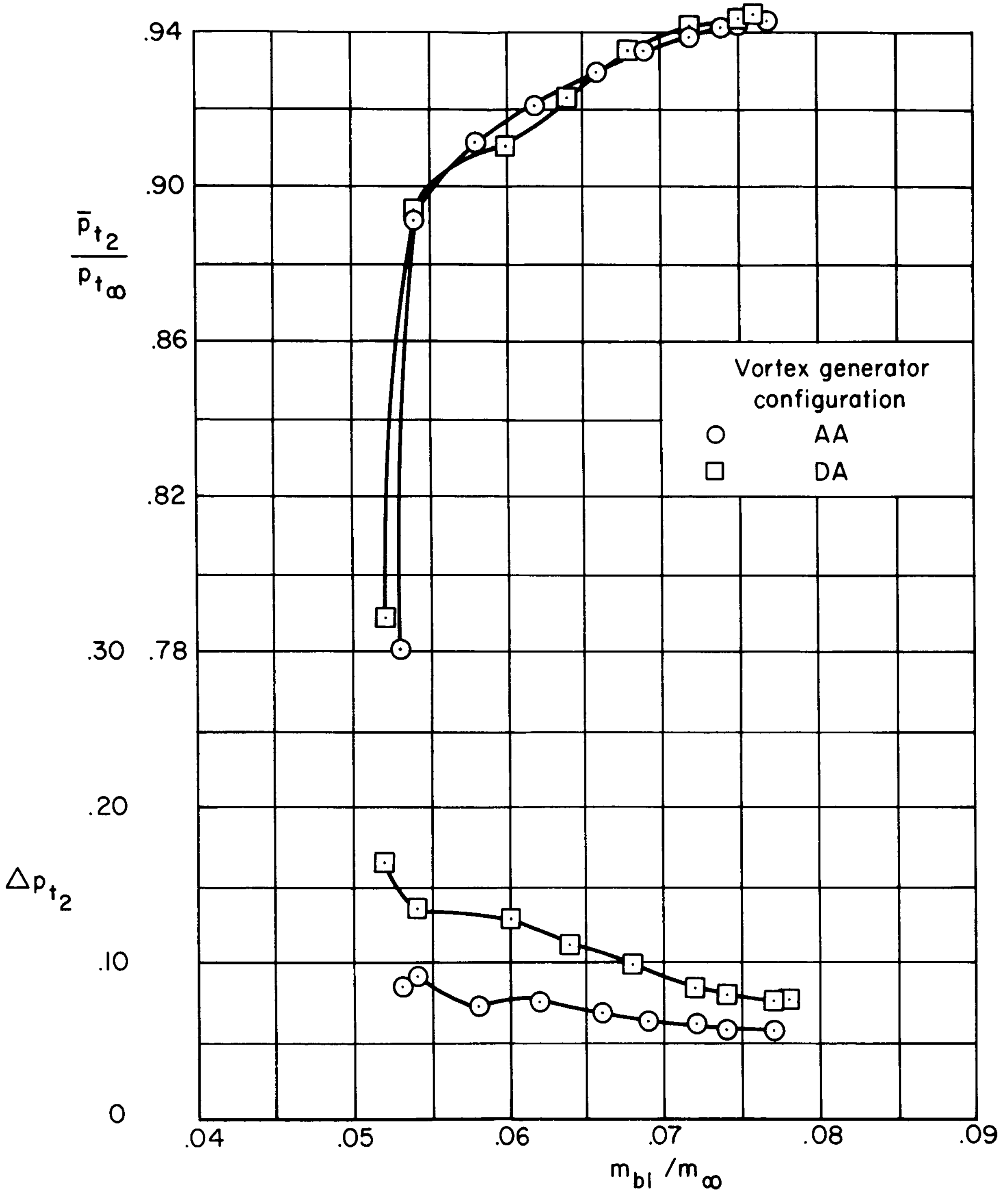

Figure 32. – Effect of vortex generator configuration on the supercritical performance; $M_\infty = 2.60$, $\alpha = 0°$, $m_{bp}/m_\infty = 0$, $\theta_2 = 0°$, bleed configuration B-1, $x_{lip}/R = 2.405$.

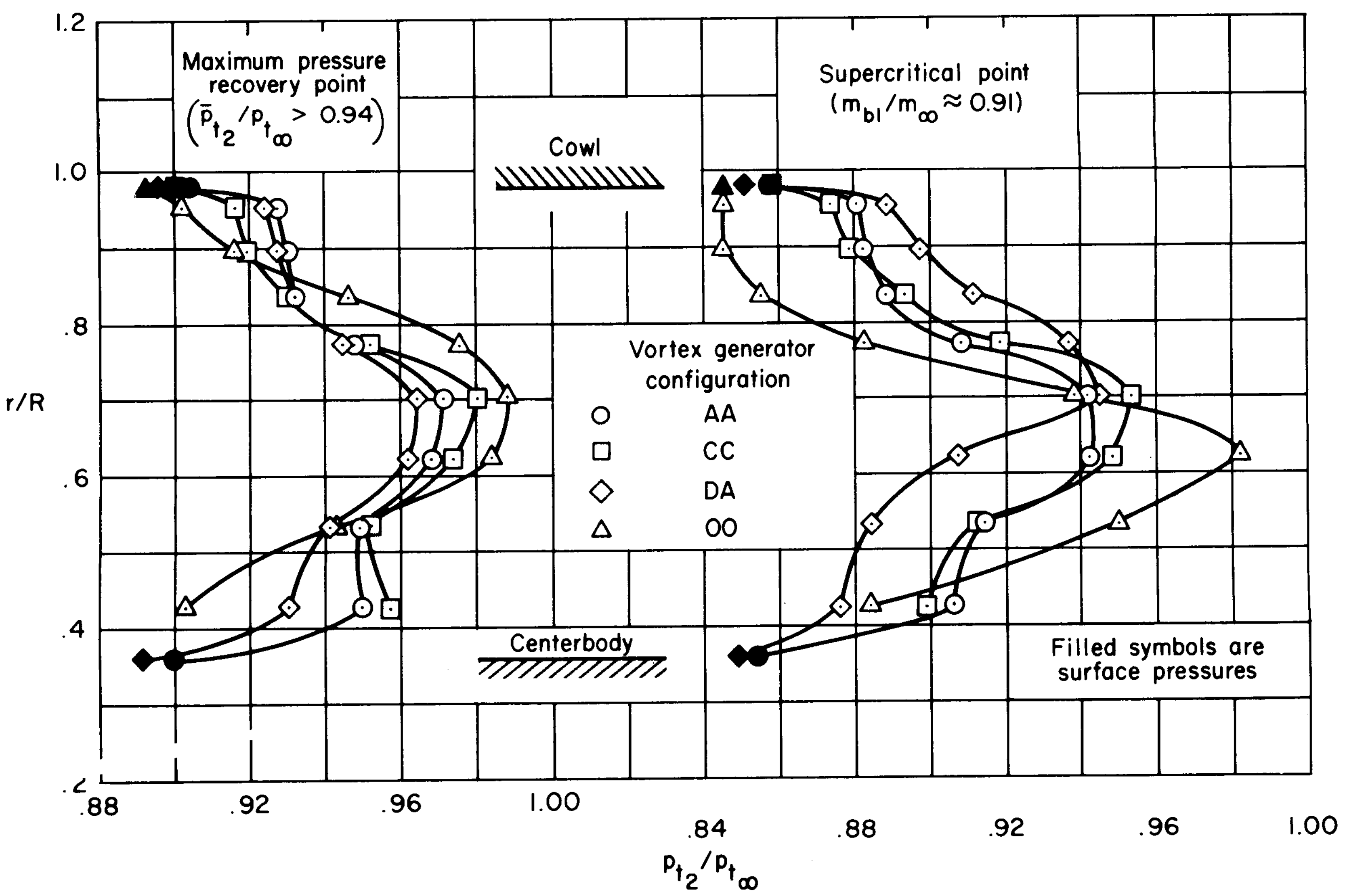

Figure 33. – Effect of vortex generator configuration on the radial total pressure profiles; $M_\infty = 2.65$, $\alpha = 0°$, $m_{bp}/m_\infty = 0$.

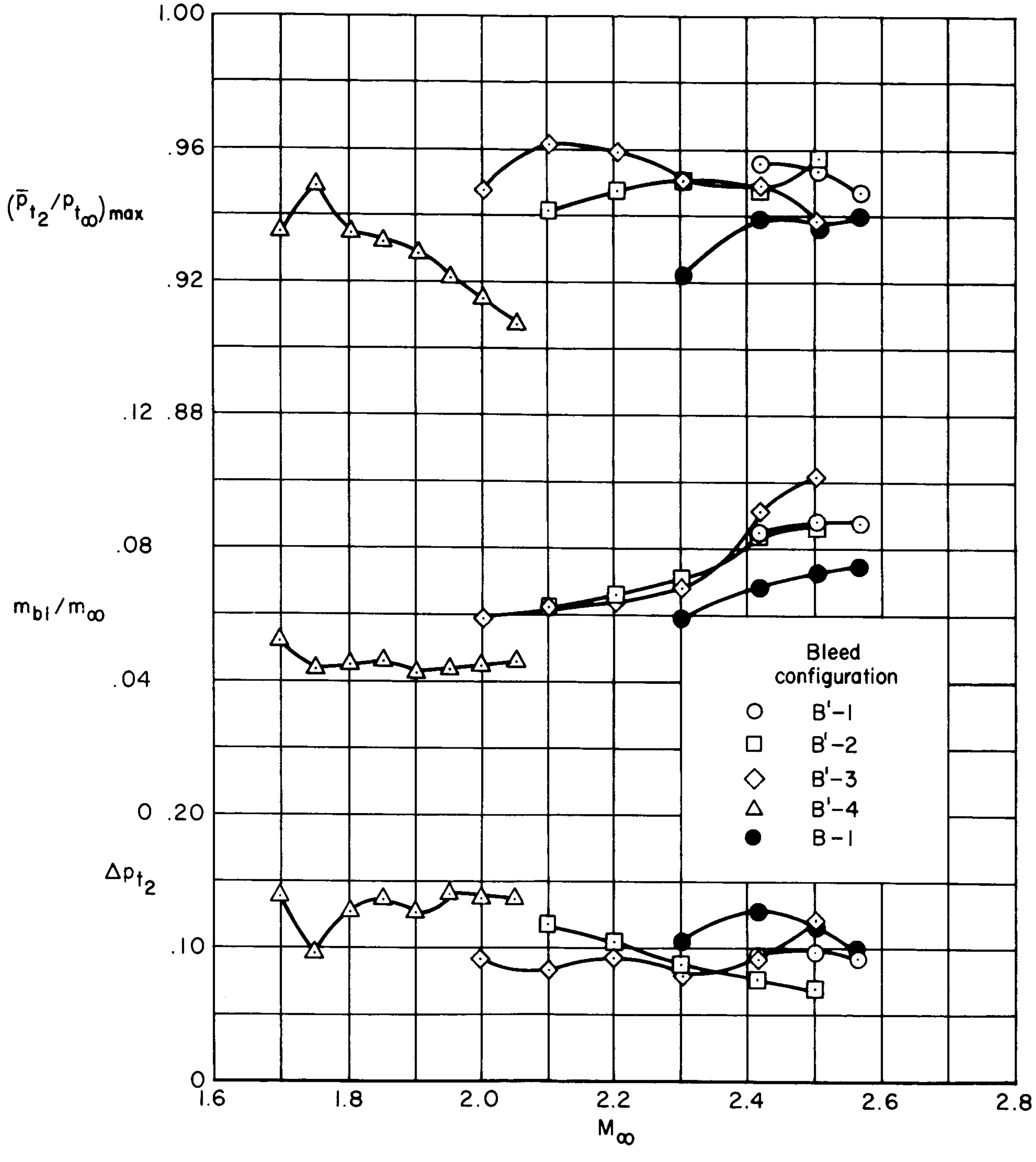

Figure 34. – Maximum performance with various bleed configurations; $\alpha = 0°$, $\theta_2 = 0°$, vortex generator configuration 00.

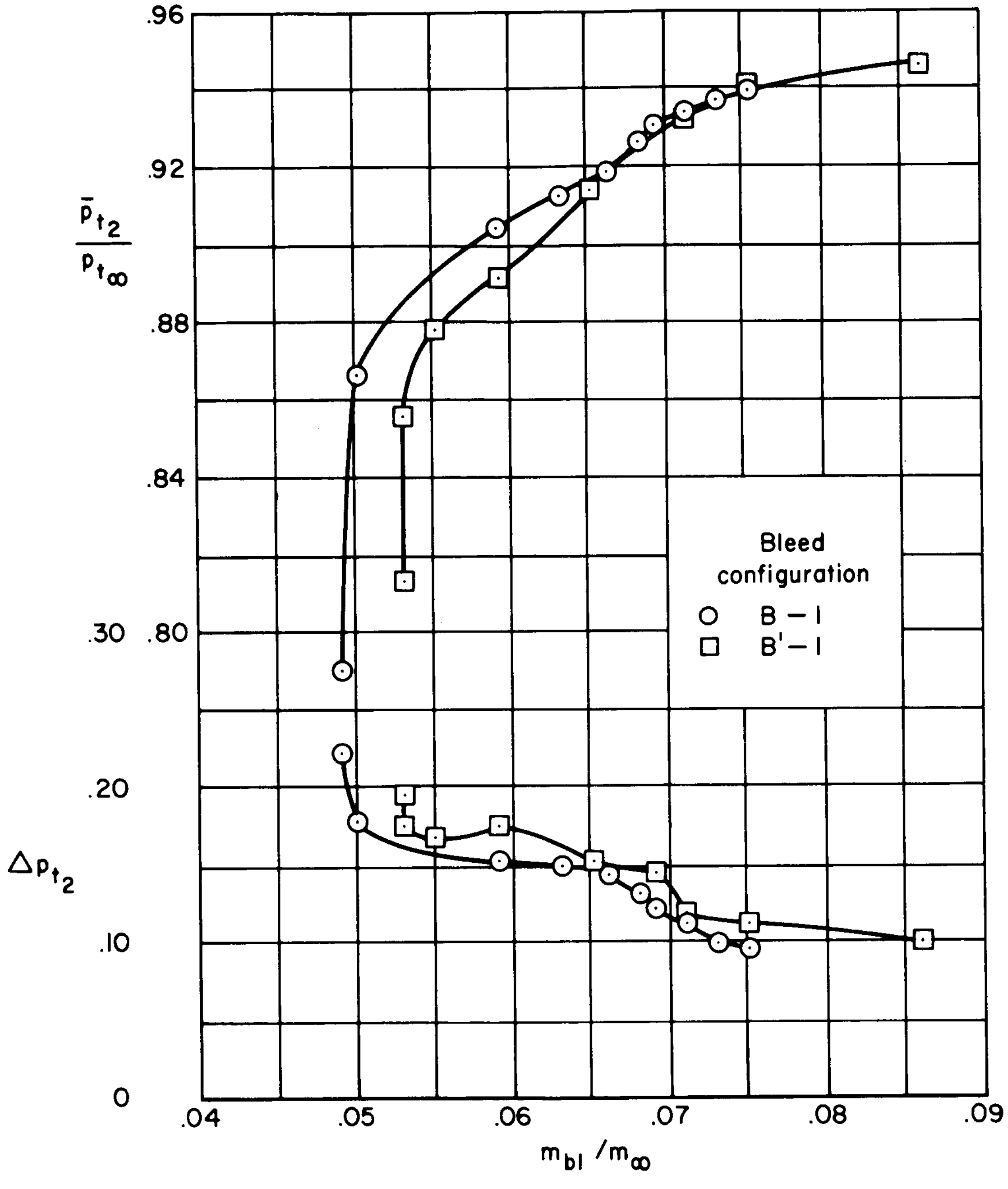

(a) $M_\infty = 2.56, x_{lip}/R = 2.483$

Figure 35. – Supercritical performance with various bleed configurations; $\alpha = 0°, m_{bp}/m_\infty = 0$, $\theta_2 = 0°$, vortex generator configuration 00.

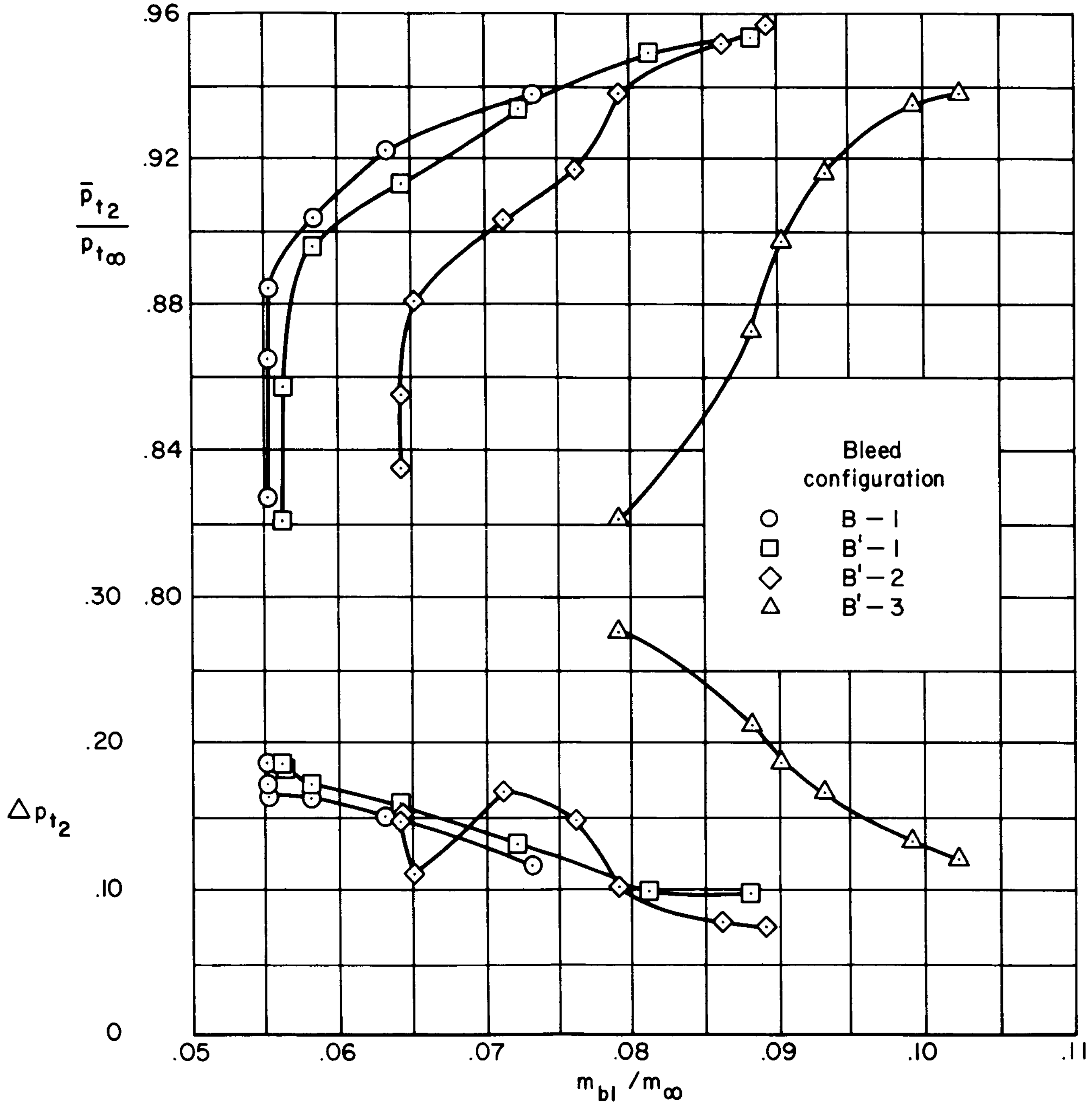

(b) $M_\infty = 2.50$, $x_{lip}/R = 2.562$

Figure 35. – Continued.

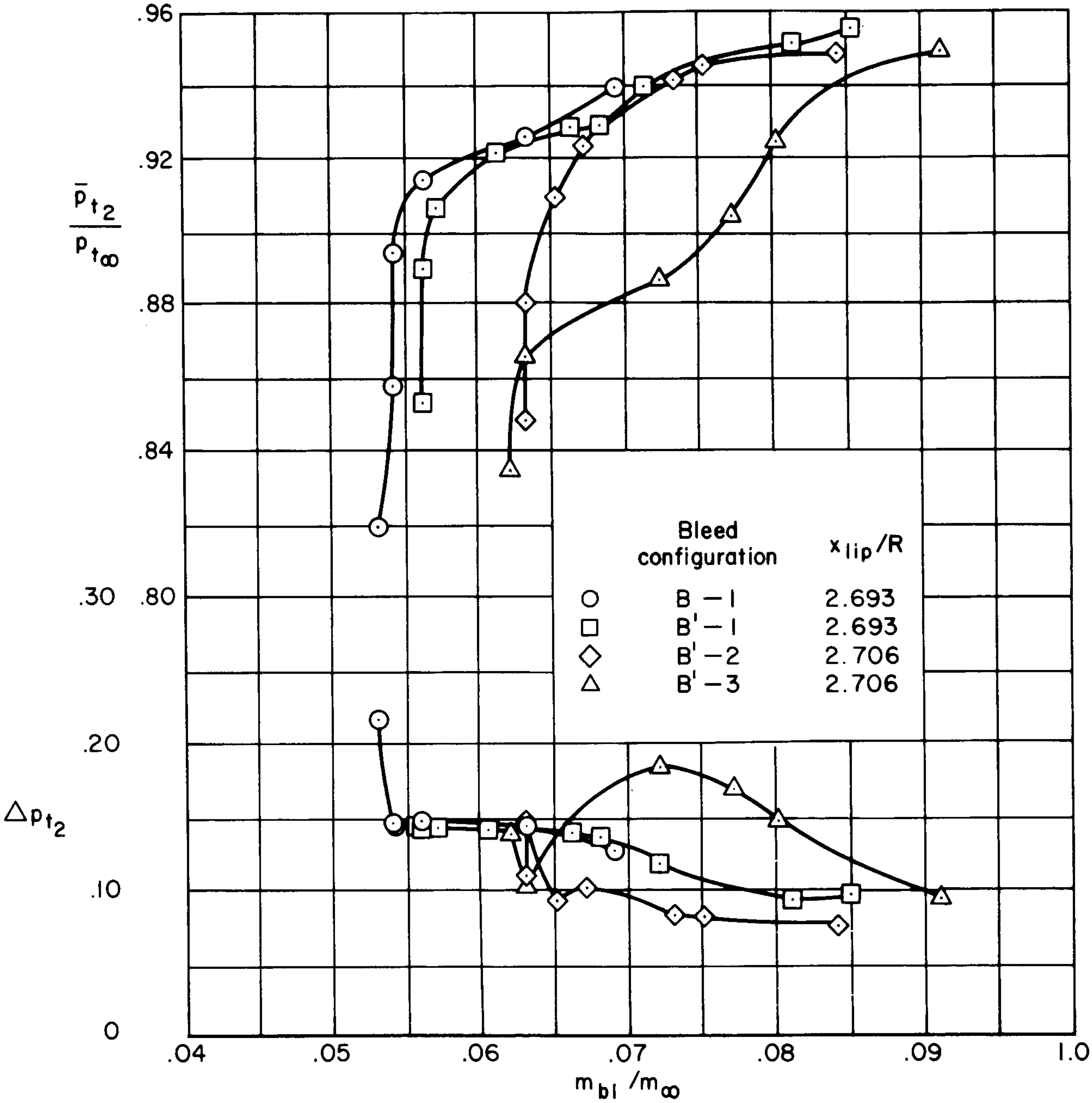

(c) $M_\infty = 2.41$

Figure 35. – Continued.

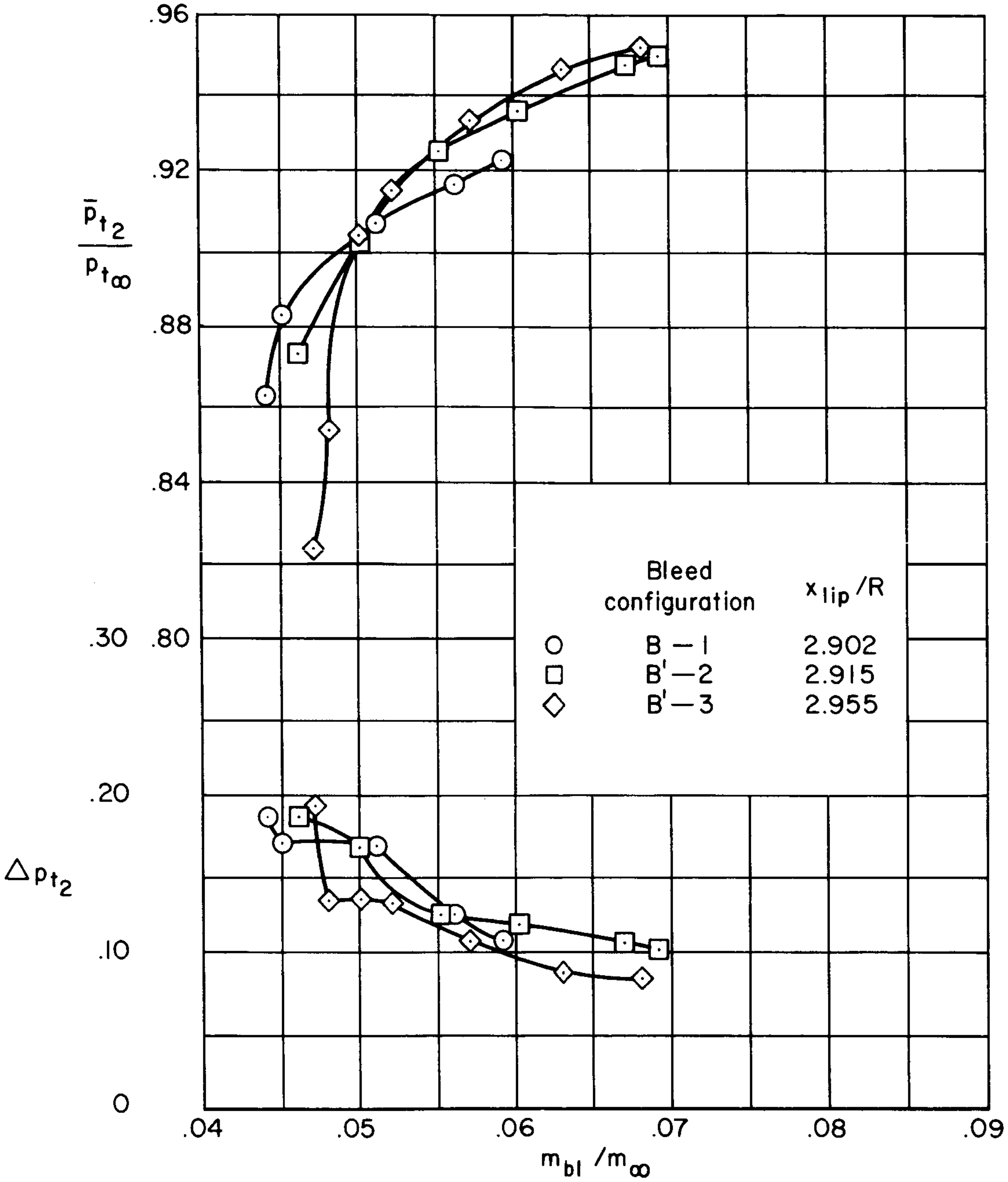

(d) $M_\infty = 2.30$

Figure 35. – Continued.

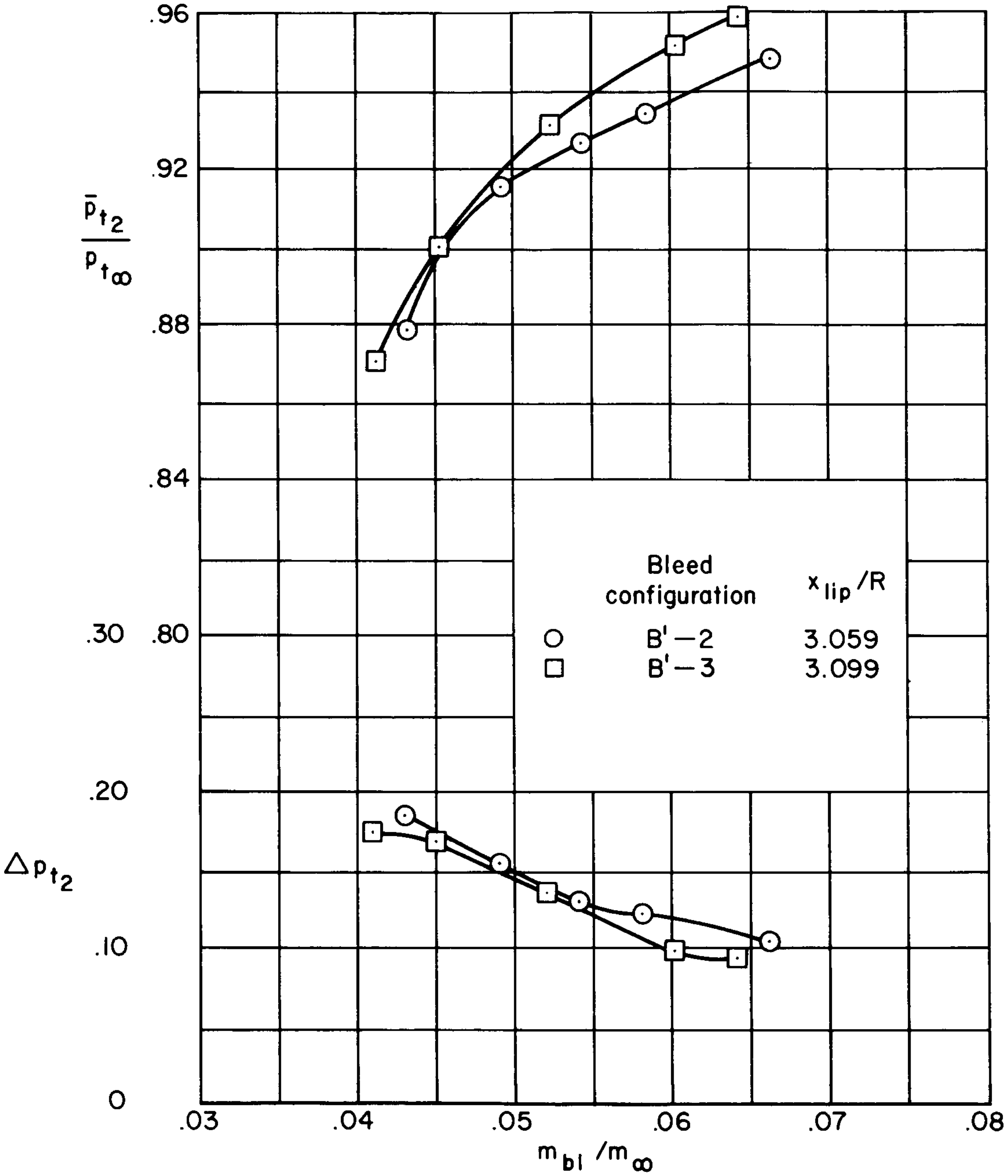

(e) $M_\infty = 2.20$

Figure 35. – Continued.

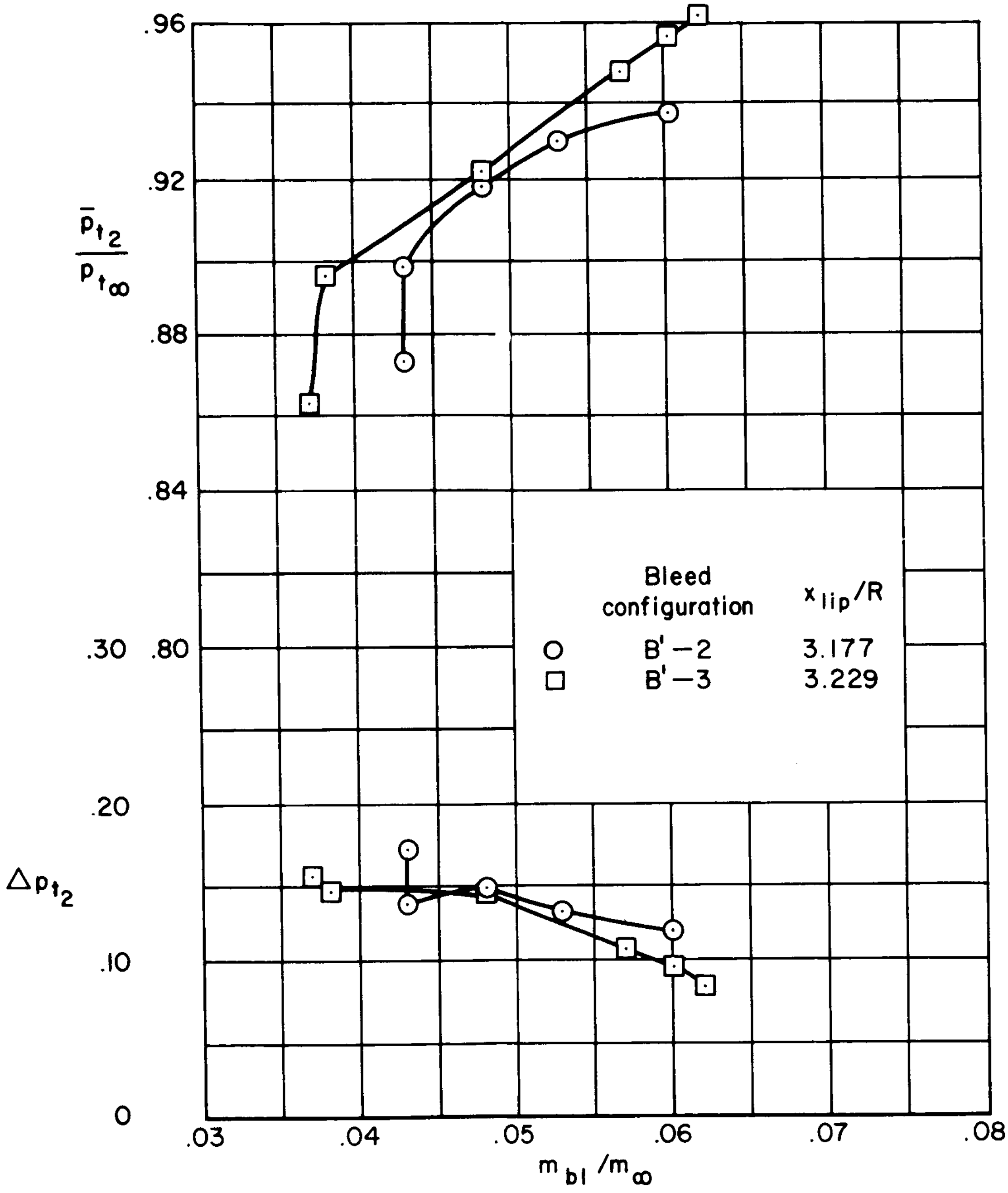

(f) $M_\infty = 2.10$

Figure 35. – Continued.

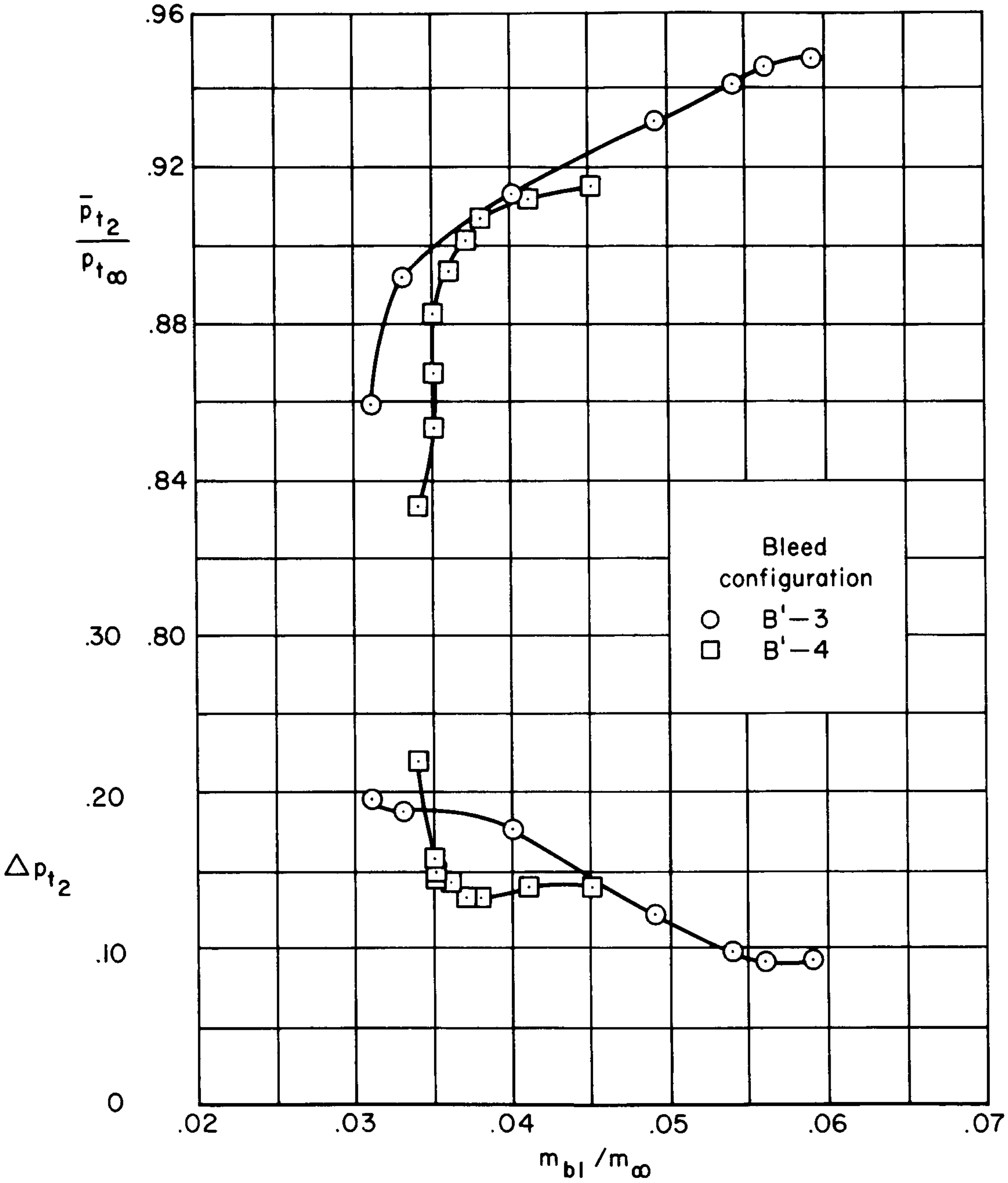

(g) $M_\infty = 2.00$, $x_{lip}/R = 3.373$

Figure 35. – Concluded.

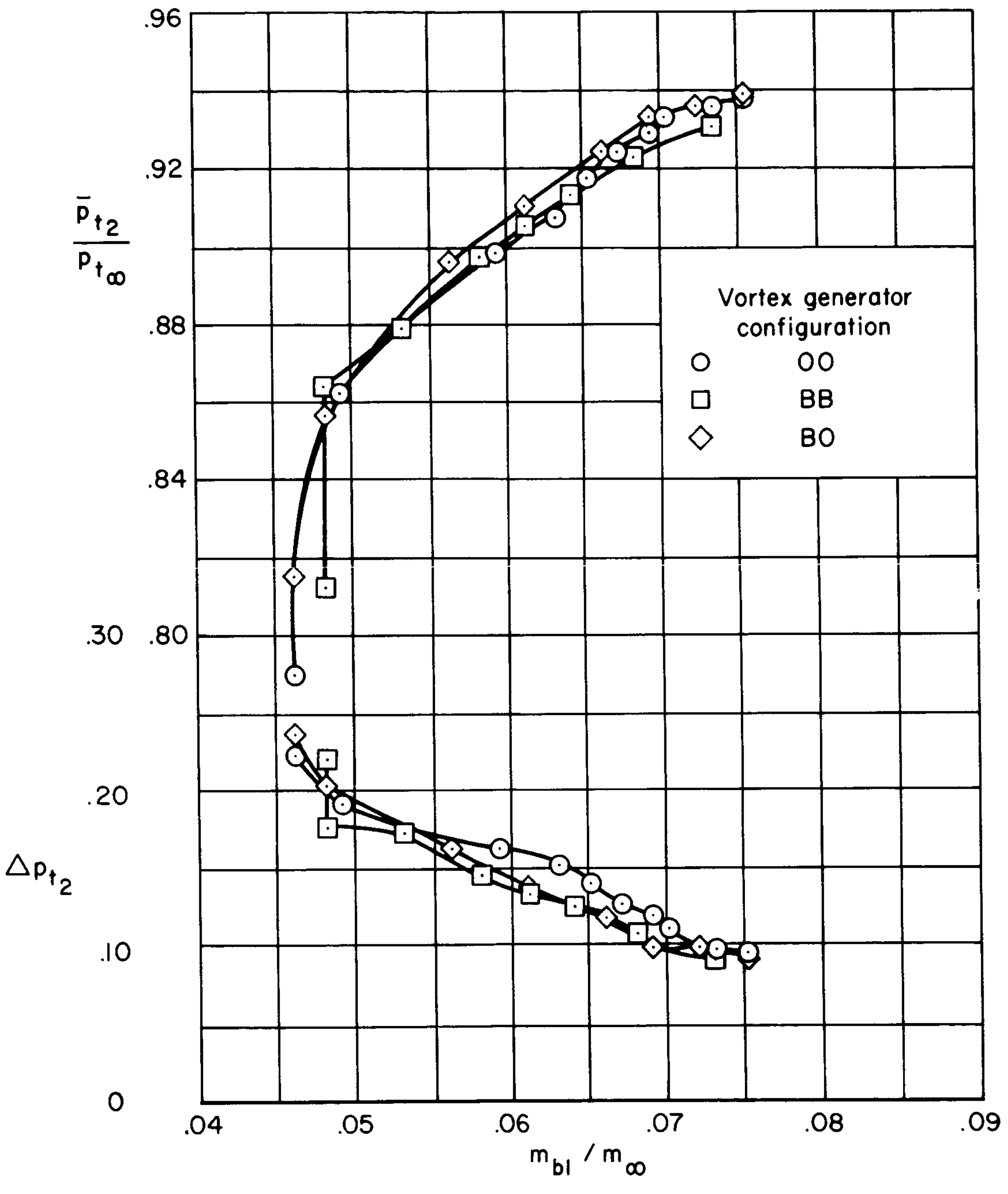

(a) Bleed configuration B-1.

Figure 36. – Supercritical performance with various vortex generator configurations; $M_\infty = 2.56$, $\alpha = 0°$, $m_{bp}/m_\infty = 0$, $\theta_2 = 0°$, $x_{lip}/R = 2.509$.

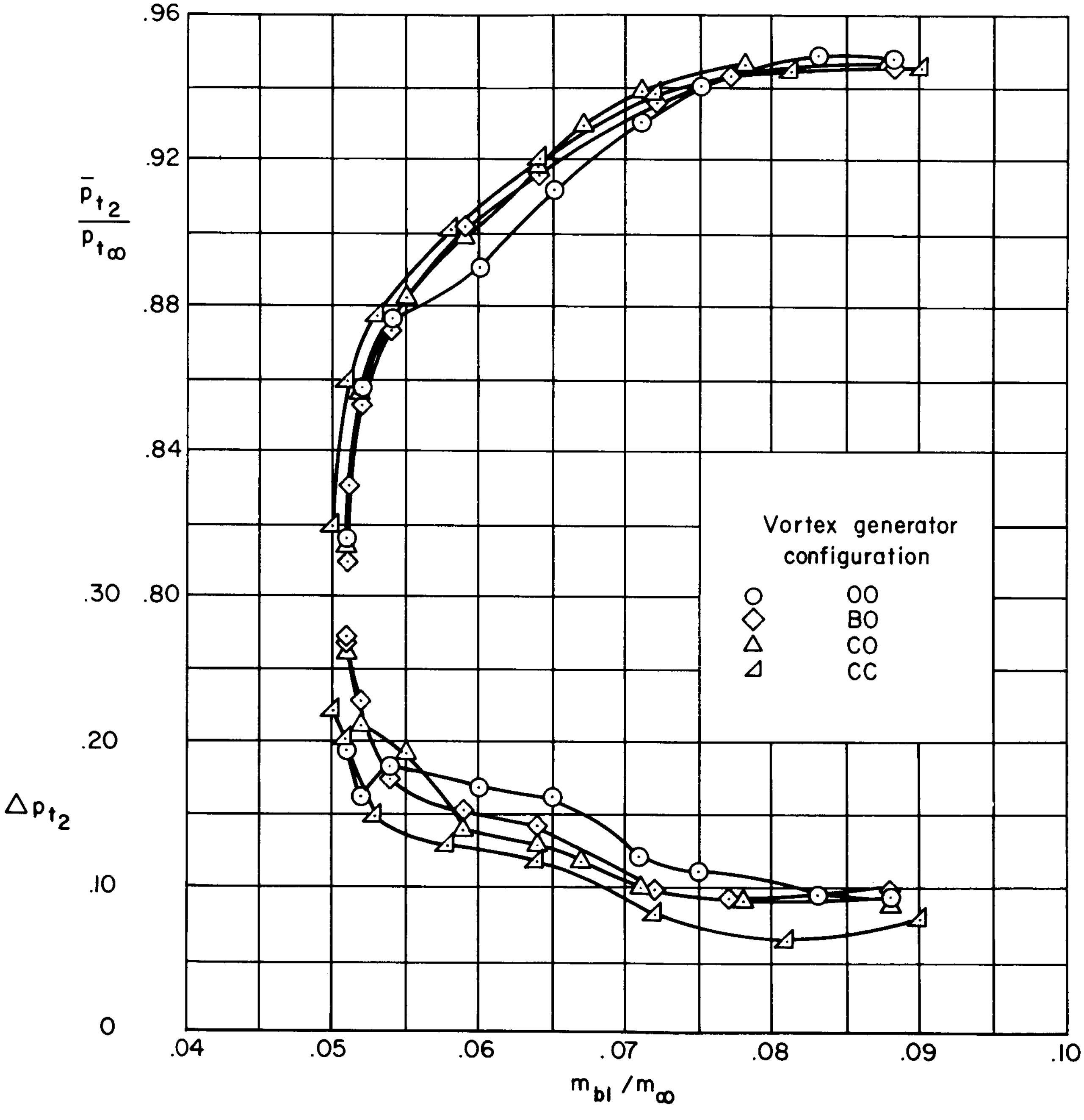

(b) Bleed configuration B′-1.

Figure 36. – Concluded.

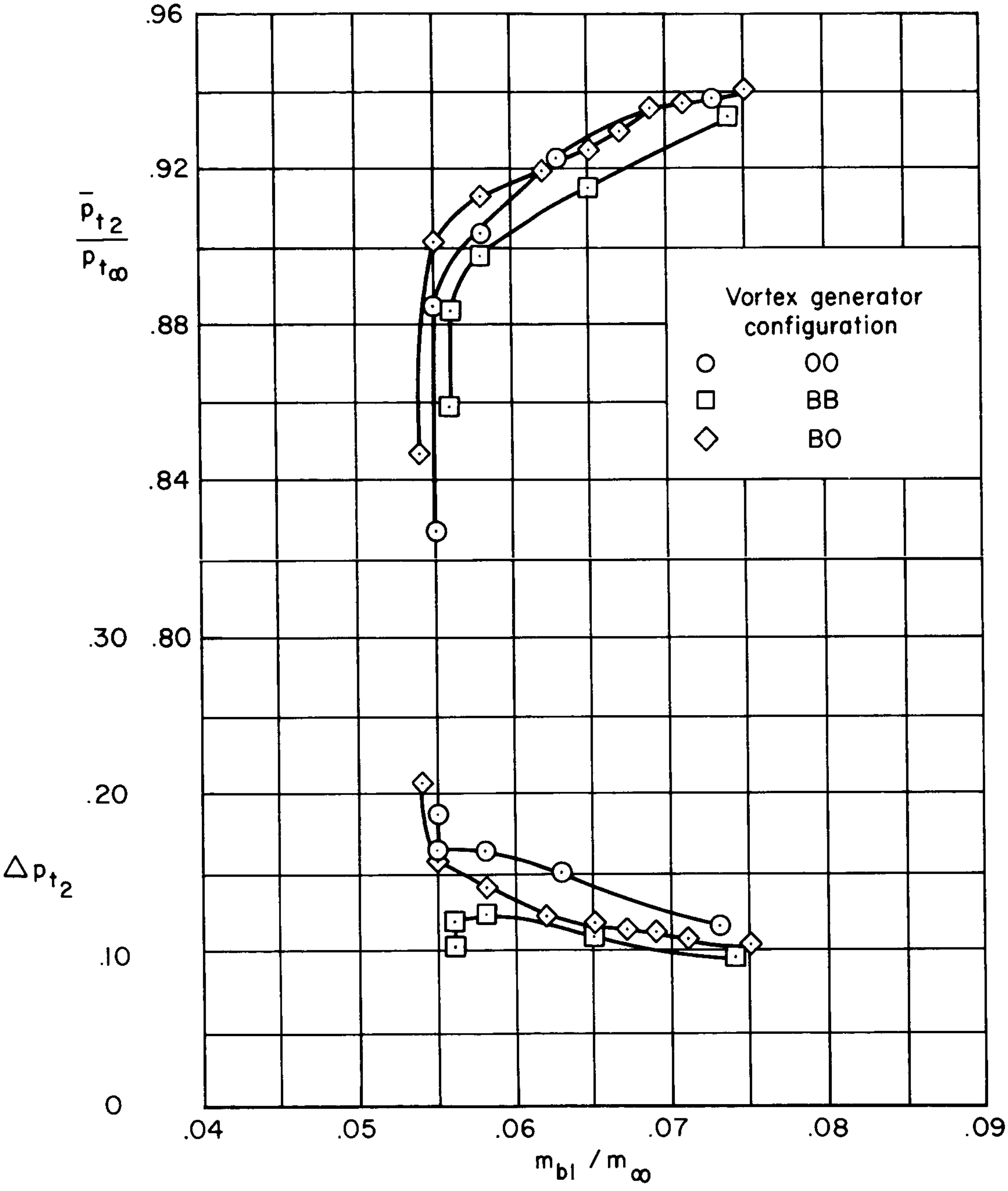

(a) Bleed configuration B-1, $x_{lip}/R = 2.562$.

Figure 37. – Supercritical performance with various vortex generator configurations; $M_\infty = 2.50$, $\alpha = 0°$, $m_{bp}/m_\infty = 0$, $\theta_2 = 0°$.

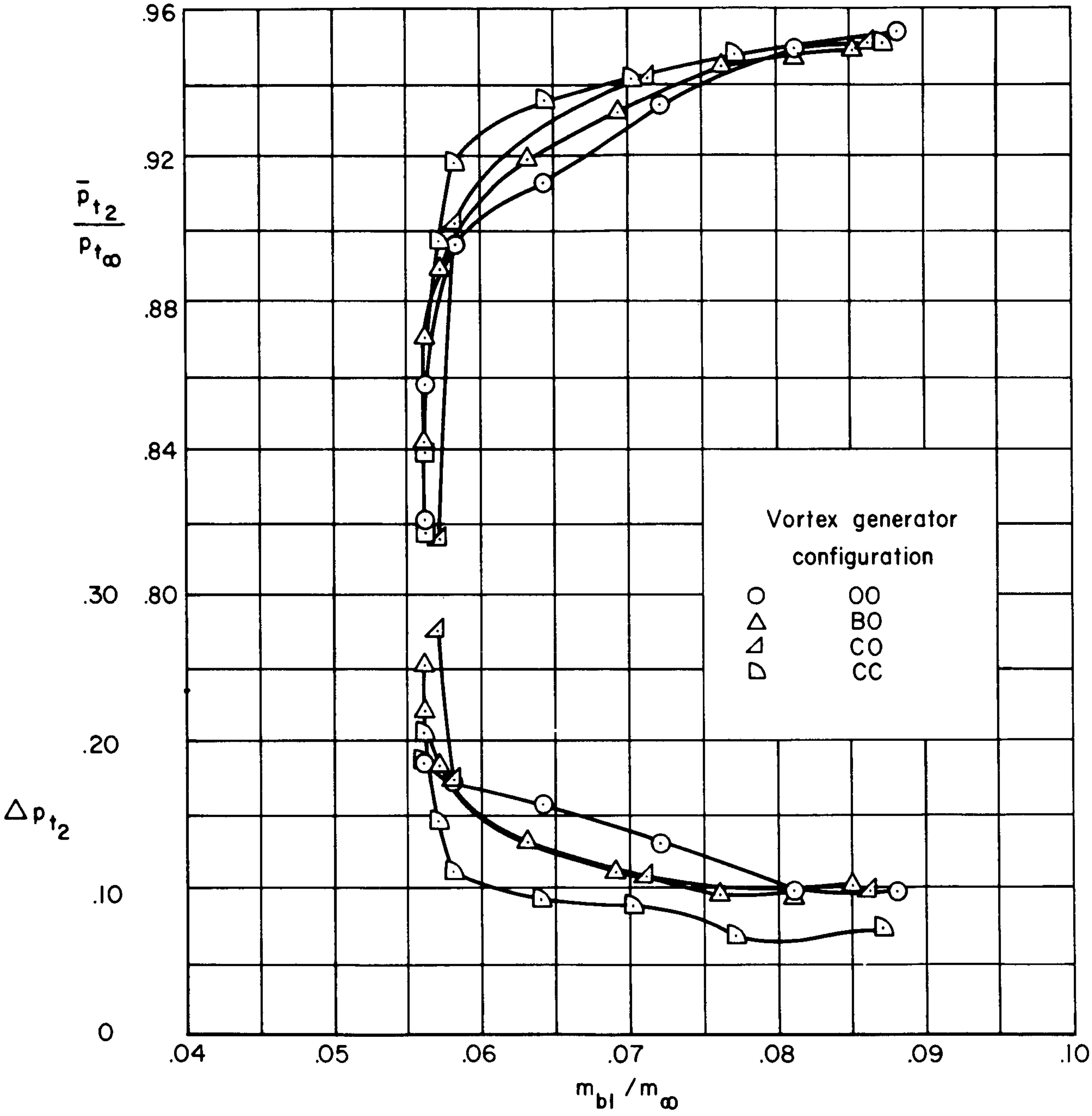

(b) Bleed configuration B′-1, $x_{lip}/R = 2.562$.

Figure 37. – Continued.

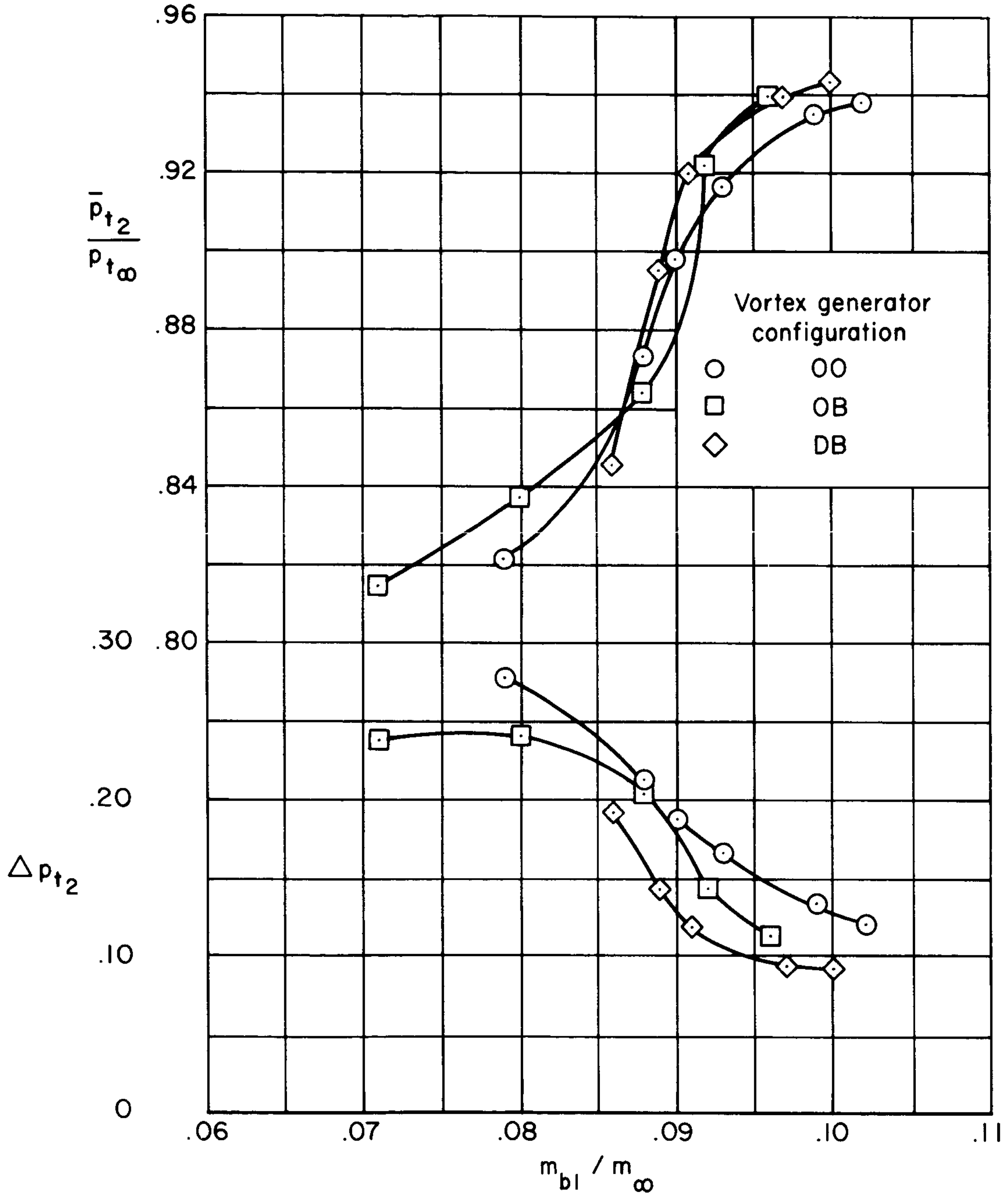

(c) Bleed configuration B'-3, $x_{lip}/R = 2.549$.

Figure 37. – Concluded.

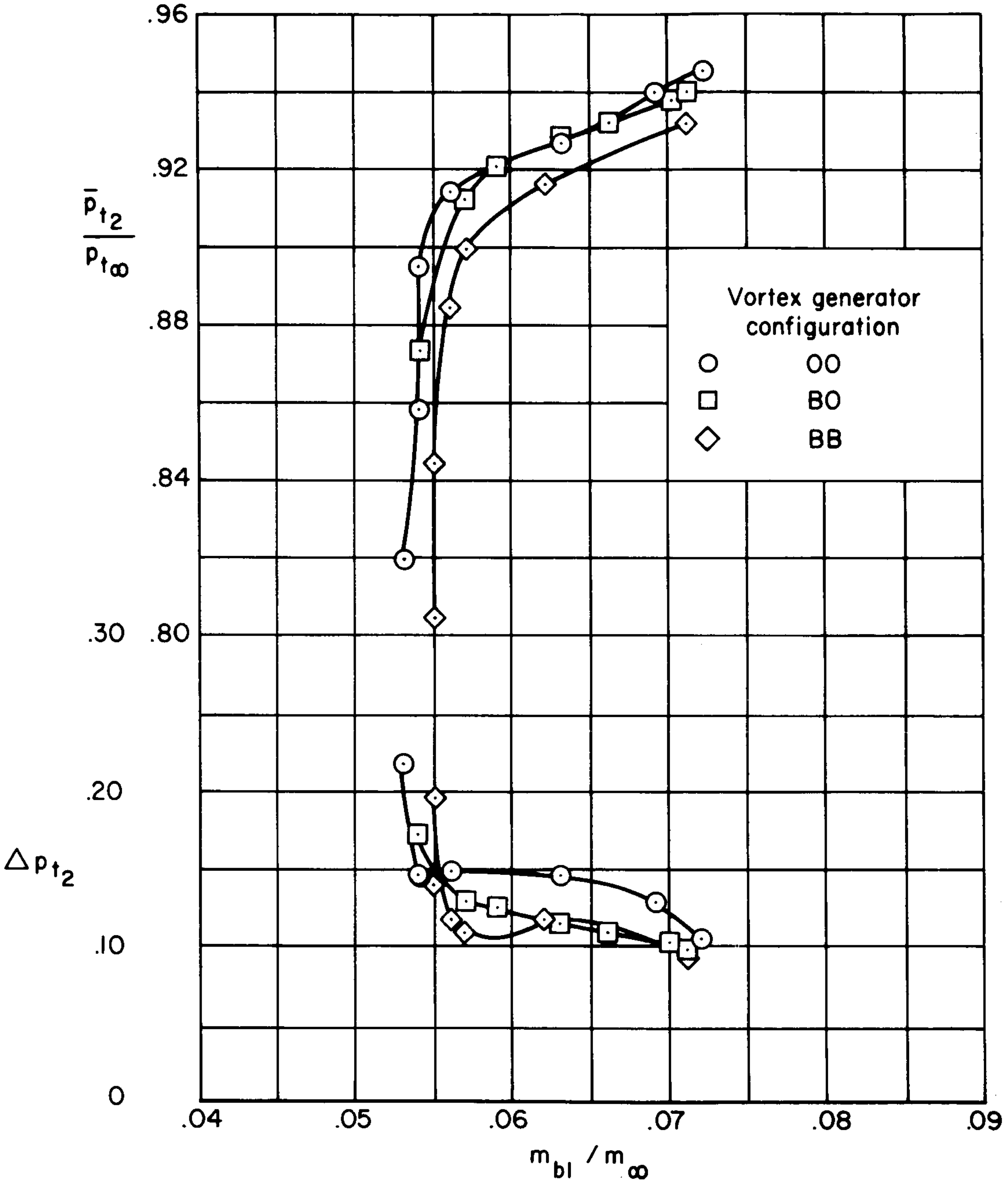

(a) Bleed configuration B-1, $x_{lip}/R = 2.693$.

Figure 38. – Supercritical performance with various vortex generator configurations; $M_\infty = 2.41$, $\alpha = 0°$, $m_{bp}/m_\infty = 0$, $\theta_2 = 0°$.

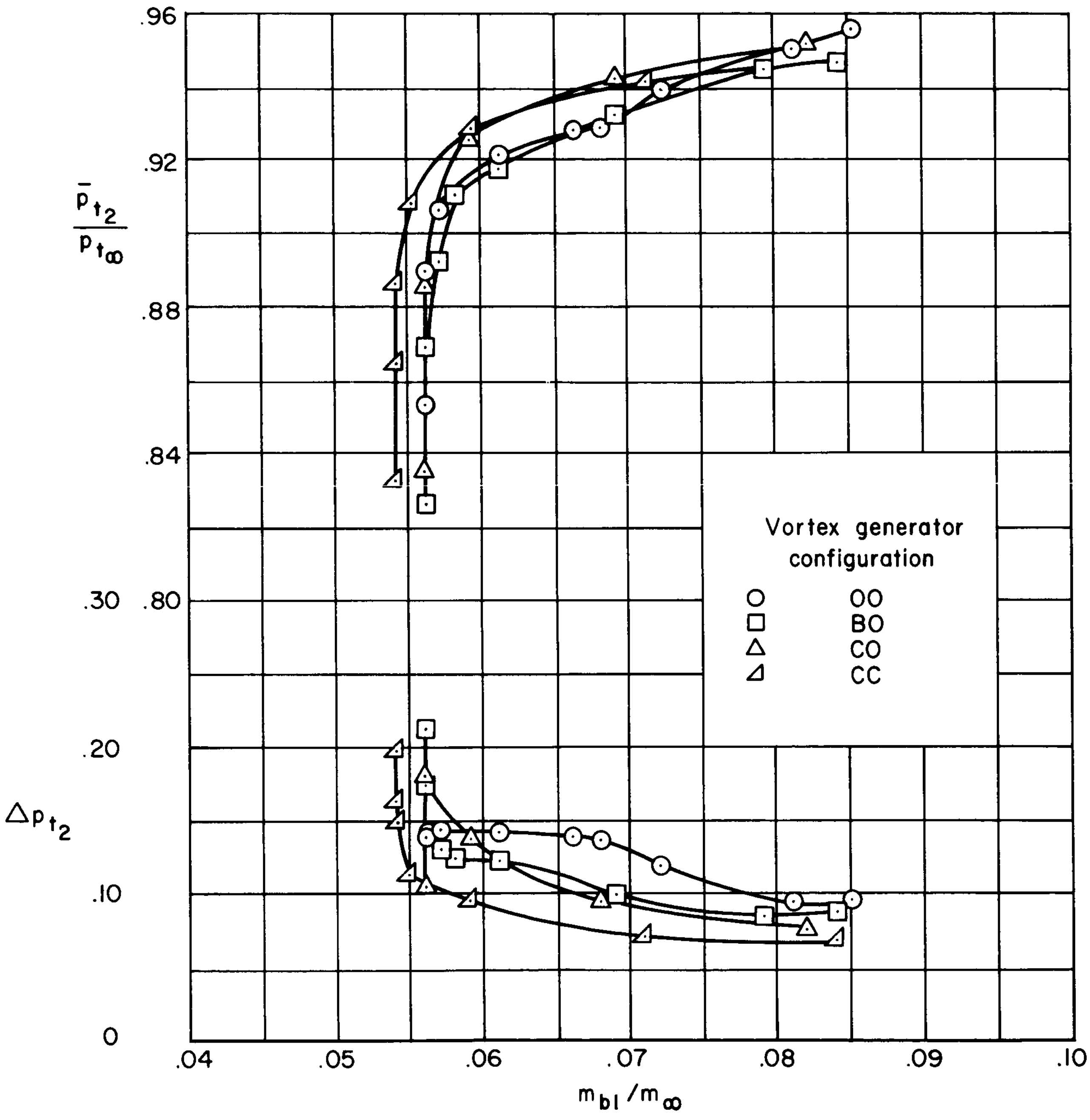

(b) Bleed configuration B′-1, $x_{lip}/R = 2.693$.

Figure 38. – Continued.

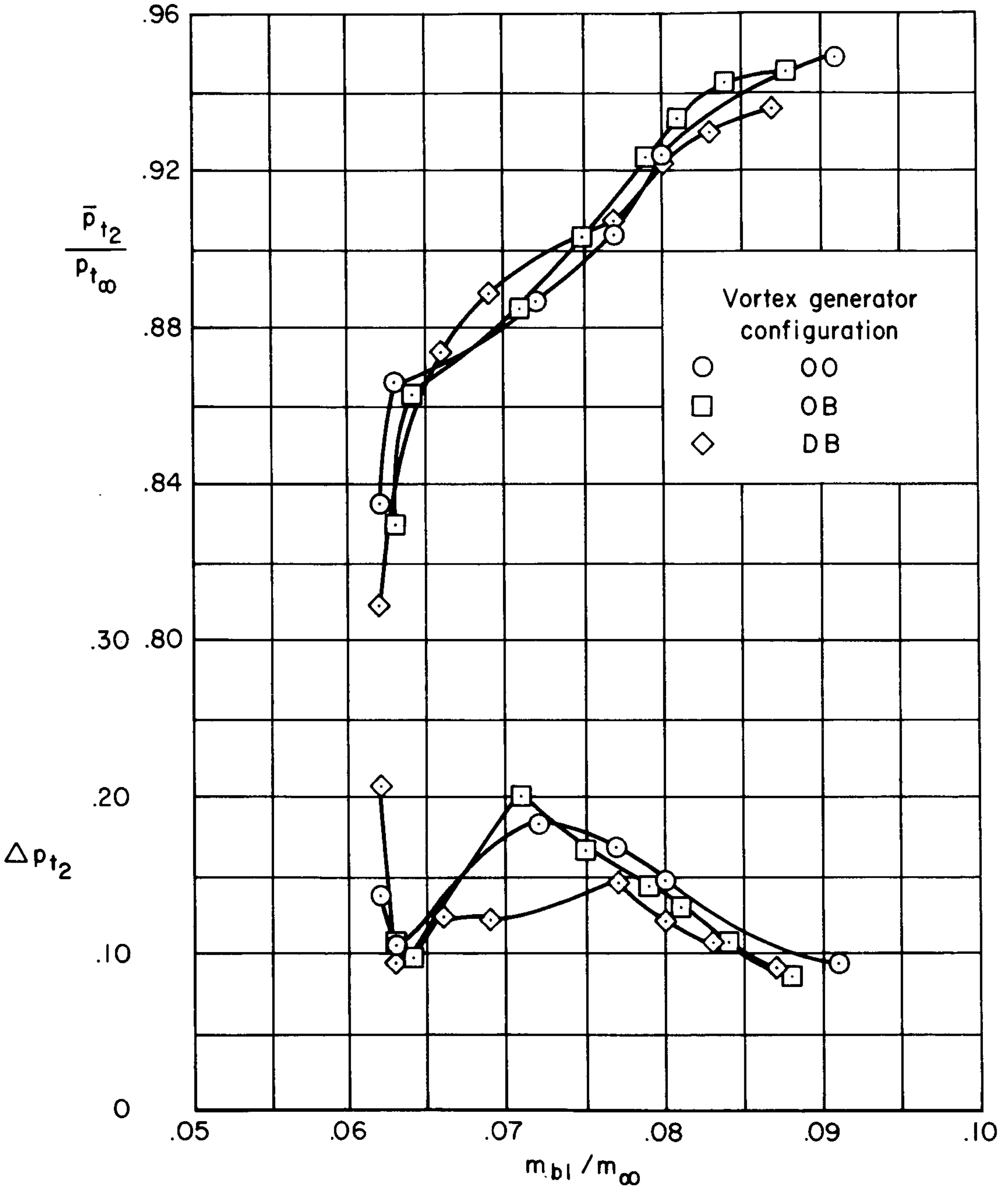

(c) Bleed configuration B-3, $x_{lip}/R = 2.706$.

Figure 38. – Concluded.

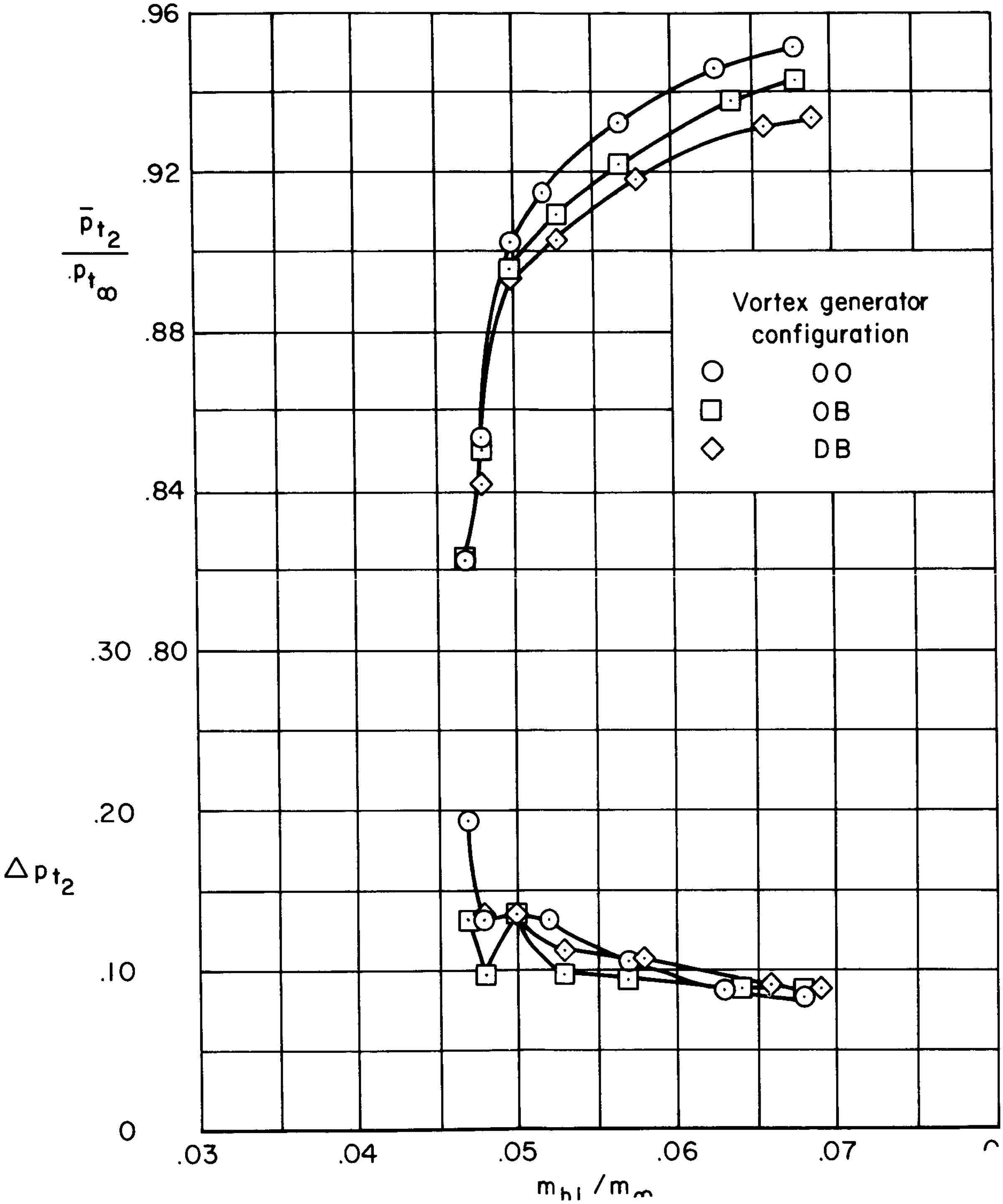

Figure 39. – Supercritical performance with various vortex generator configurations; $M_\infty = 2.30$, $\alpha = 0°$, $m_{bp}/m_\infty = 0$, $\theta_2 = 0°$, $x_{lip}/R = 2.955$, bleed configuration B′-3.

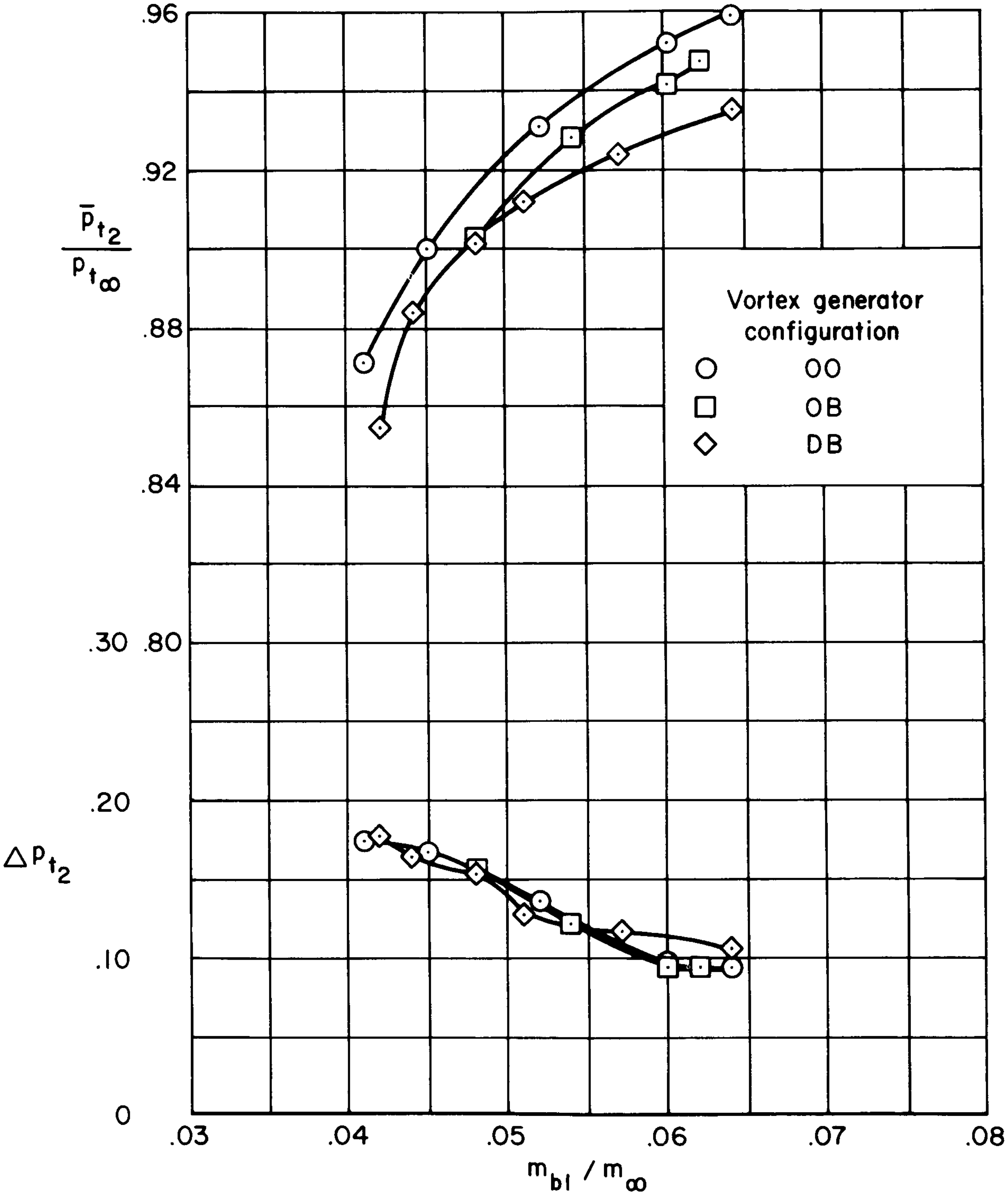

Figure 40. – Supercritical performance with various vortex generator configurations; $M_\infty = 2.20$, $\alpha = 0°$, $m_{bp}/m_\infty = 0$, $\theta_2 = 0°$, $x_{lip}/R = 3.099$, bleed configuration B'-3.

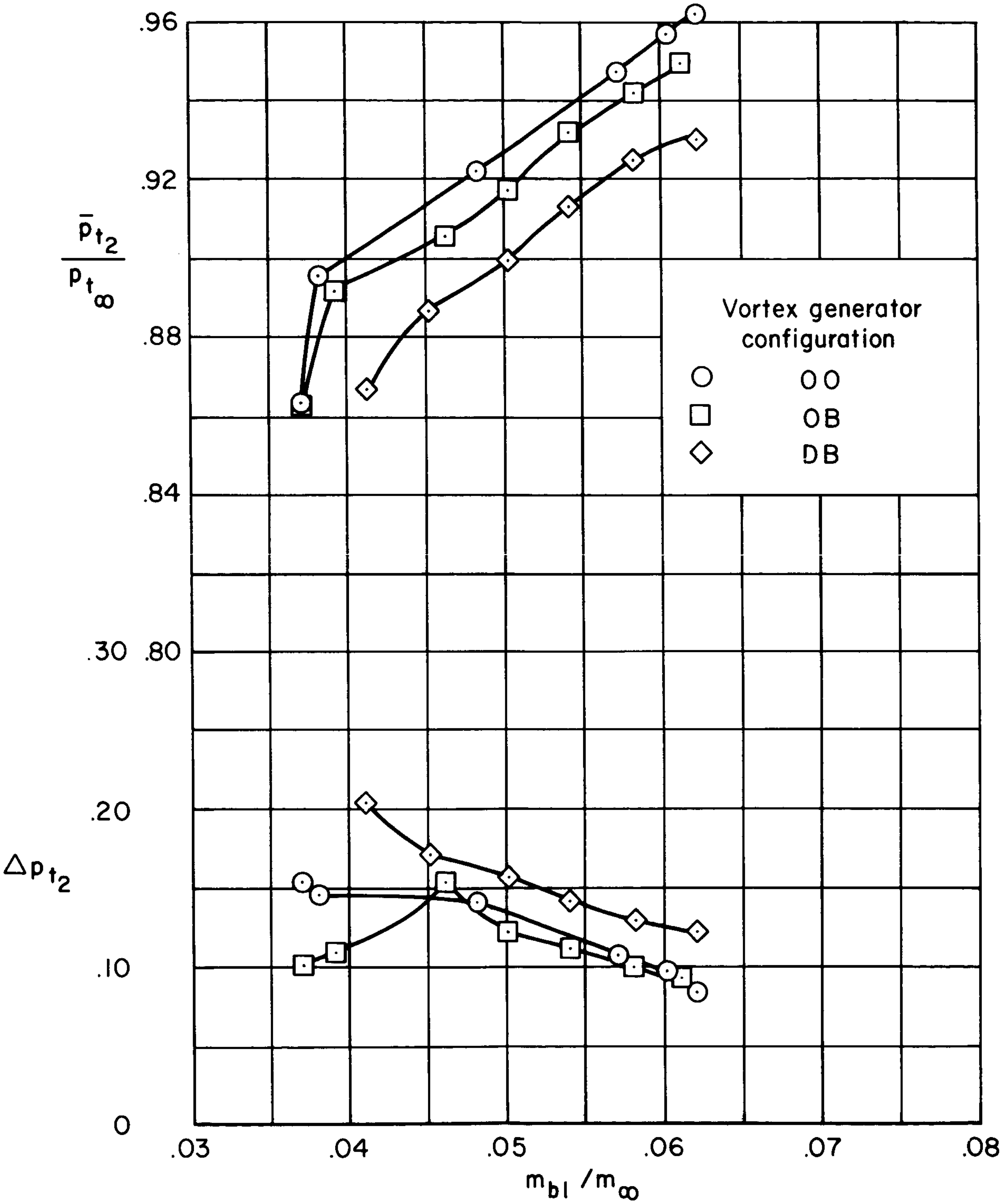

Figure 41. – Supercritical performance with various vortex generator configurations; $M_\infty = 2.10$, $\alpha = 0°$, $m_{bp}/m_\infty = 0$, $\theta_2 = 0°$, $x_{lip}/R = 3.229$, bleed configuration B-3.

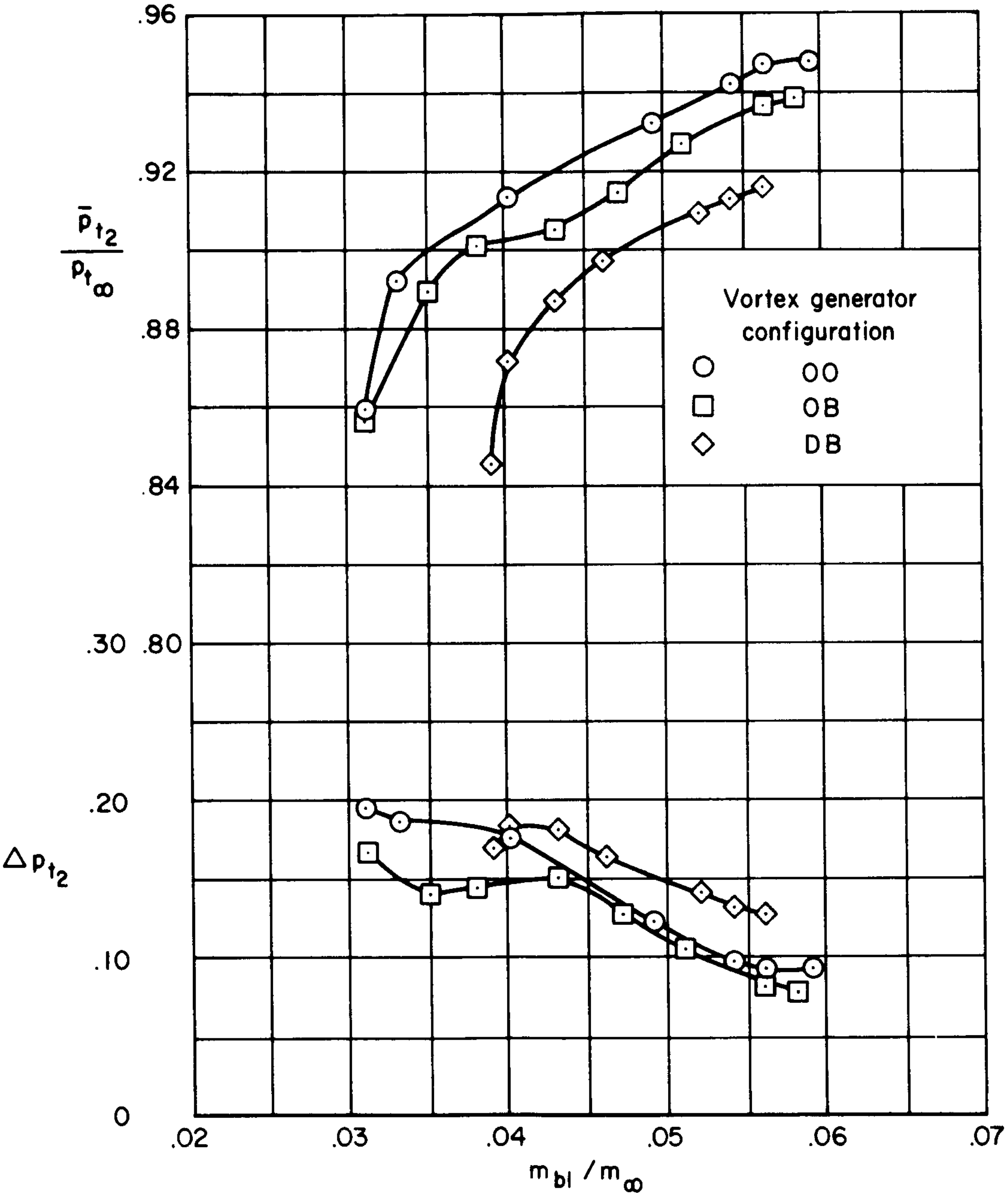

(a) Bleed configuration B'-3.

Figure 42. – Supercritical performance with various vortex generator configurations; $M_\infty = 2.00$, $\alpha = 0^\circ$, $m_{bp}/m_\infty = 0$, $\theta_2 = 0^\circ$, $x_{lip}/R = 3.373$.

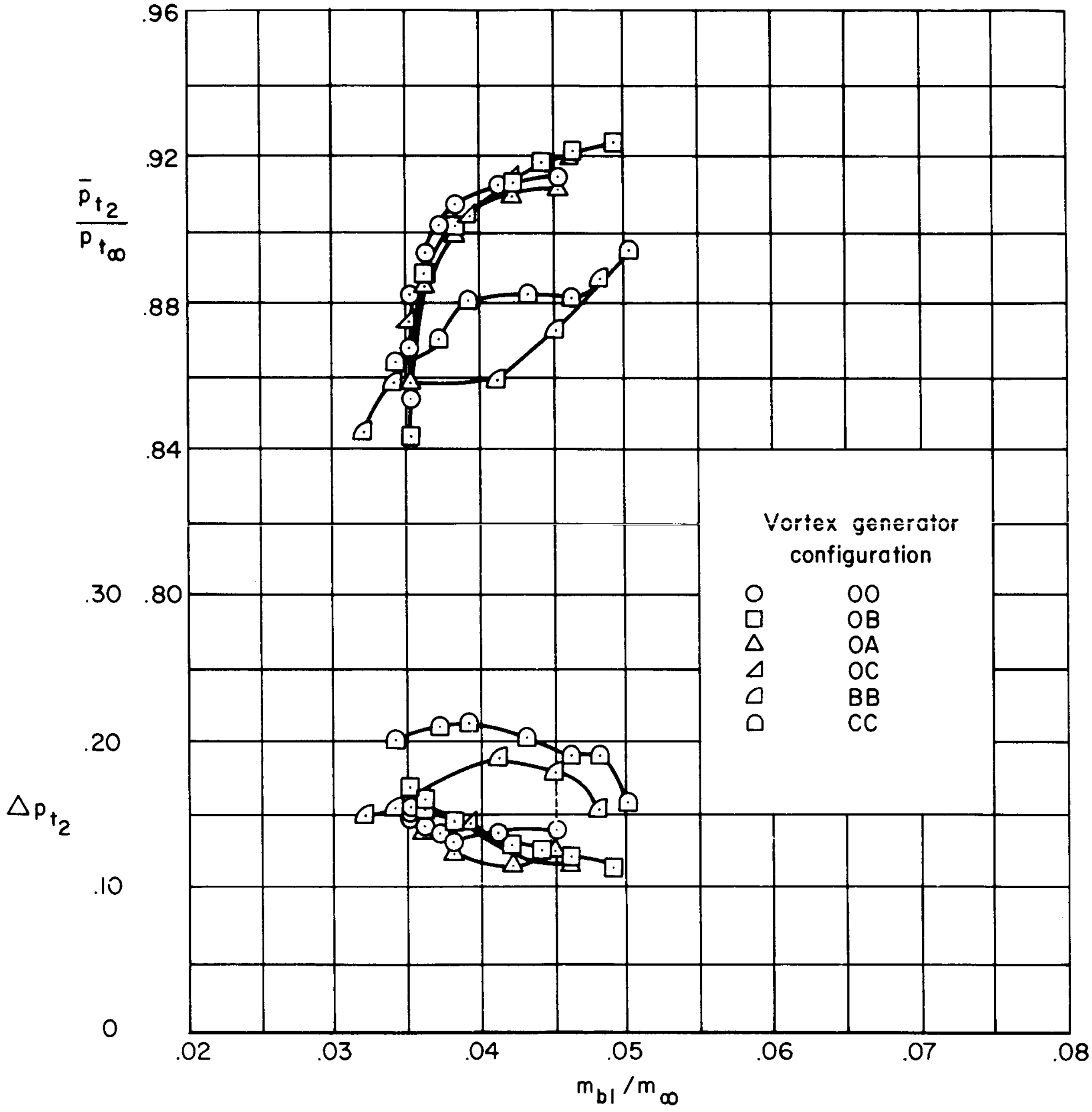

(b) Bleed configuration B′-4.

Figure 42. – Concluded.

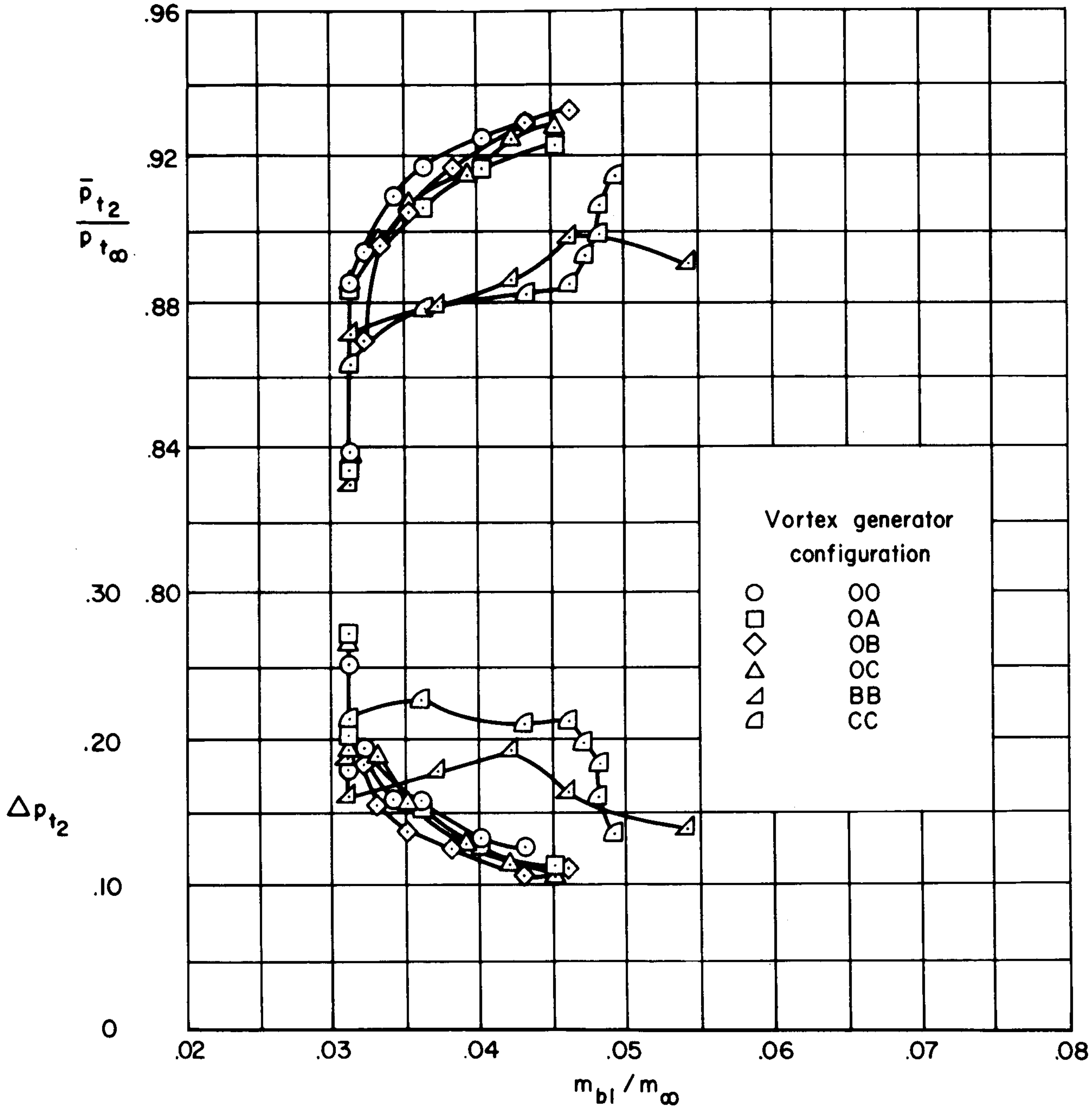

Figure 43. – Supercritical performance with various vortex generator configurations; $M_\infty = 1.90$, $\alpha = 0°$, $m_{bp}/m_\infty = 0$, $\theta_2 = 0°$, $x_{lip}/R = 3.478$, bleed configuration B-4.

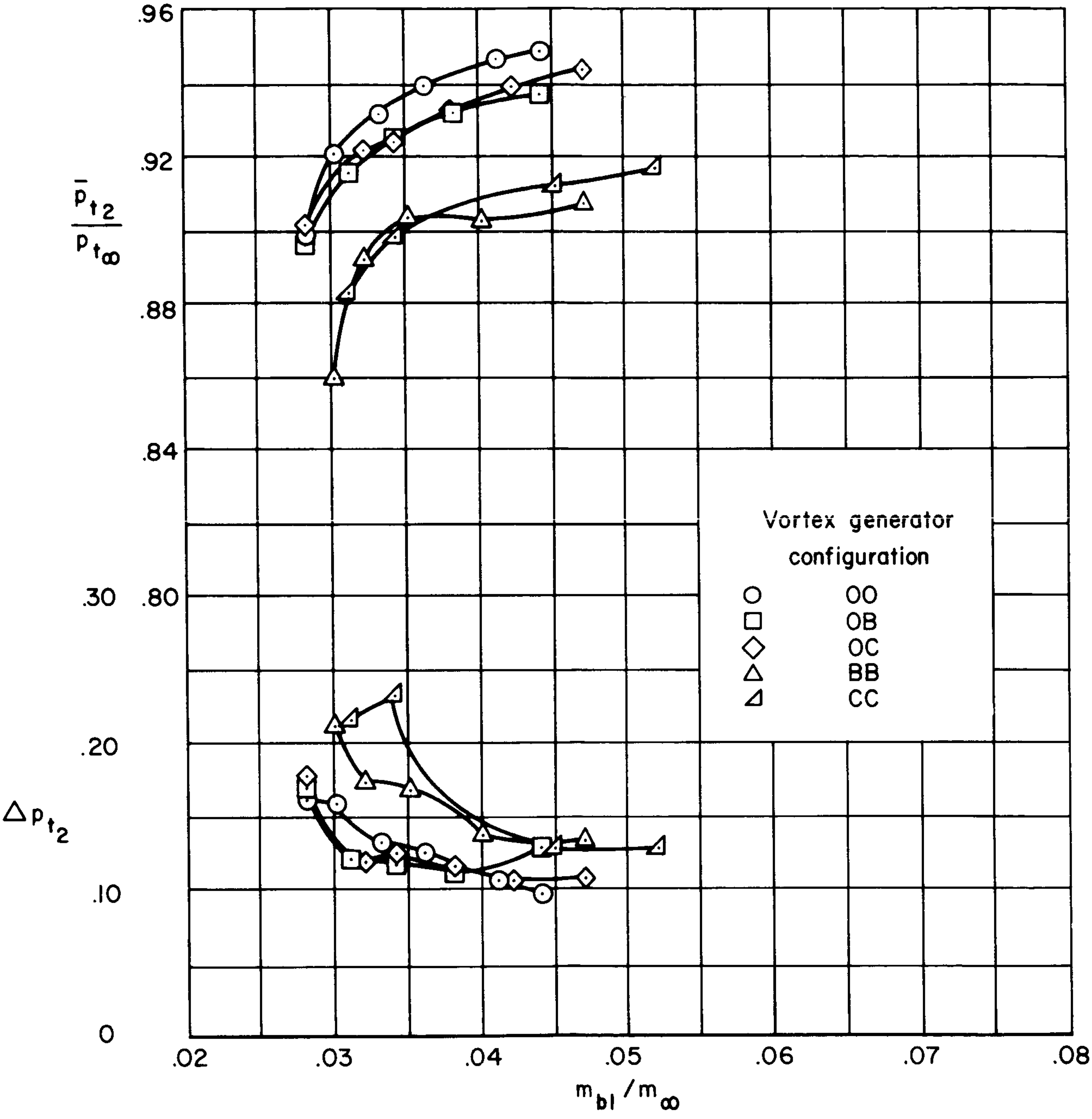

Figure 44. – Supercritical performance with various vortex generator configurations; $M_\infty = 1.75$, $\alpha = 0°$, $m_{bp}/m_\infty = 0$, $\theta_2 = 0°$, $x_{lip}/R = 3.583$, bleed configuration B-4.

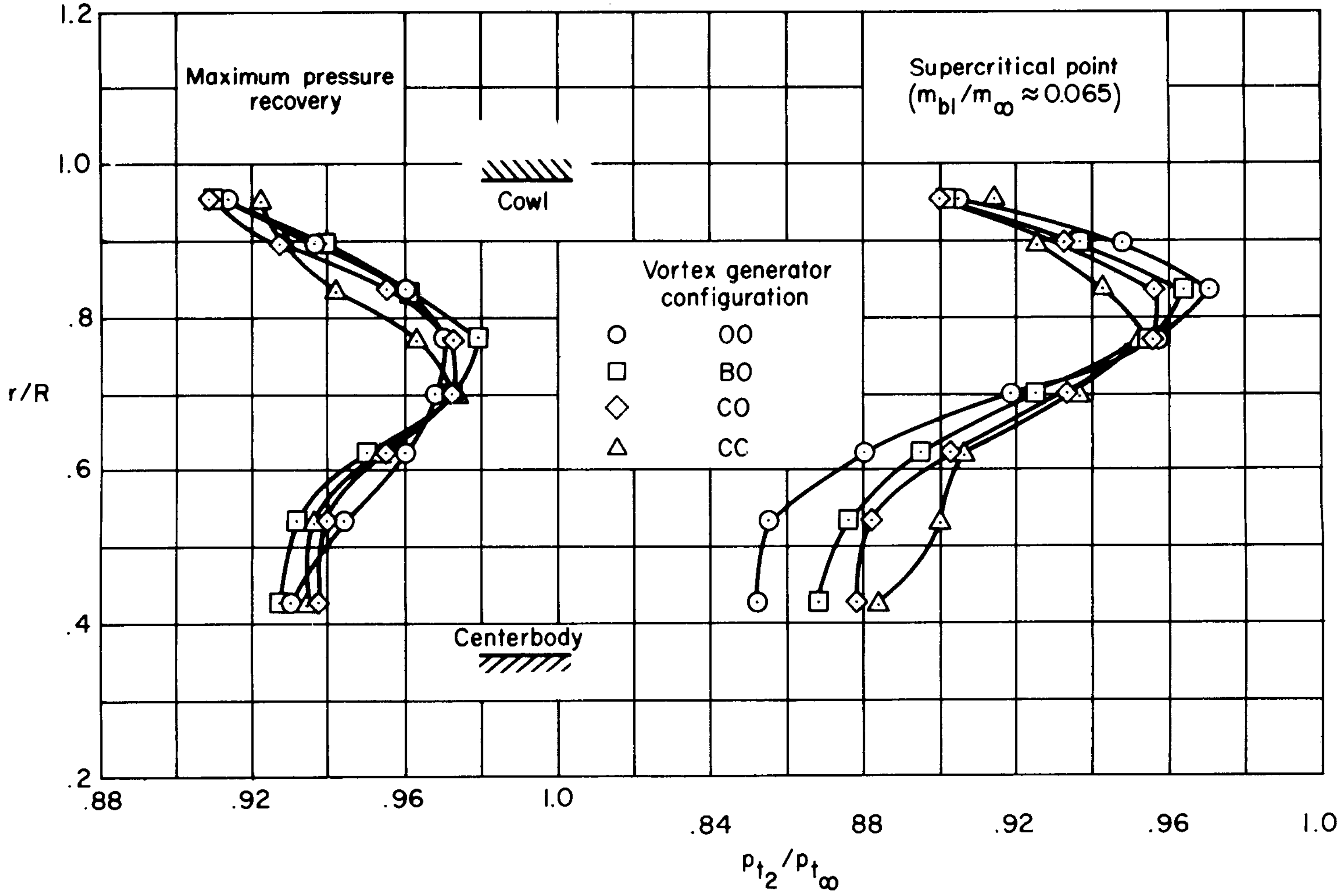

(a) $M_{\infty} = 2.56, x_{lip}/R = 2.509$, bleed configuration B'-1.

Figure 45. – Effect of vortex generator configuration on the radial total-pressure profiles; $\alpha = 0°, m_{bp}/m_{\infty} = 0, \theta_2 = 0°$.

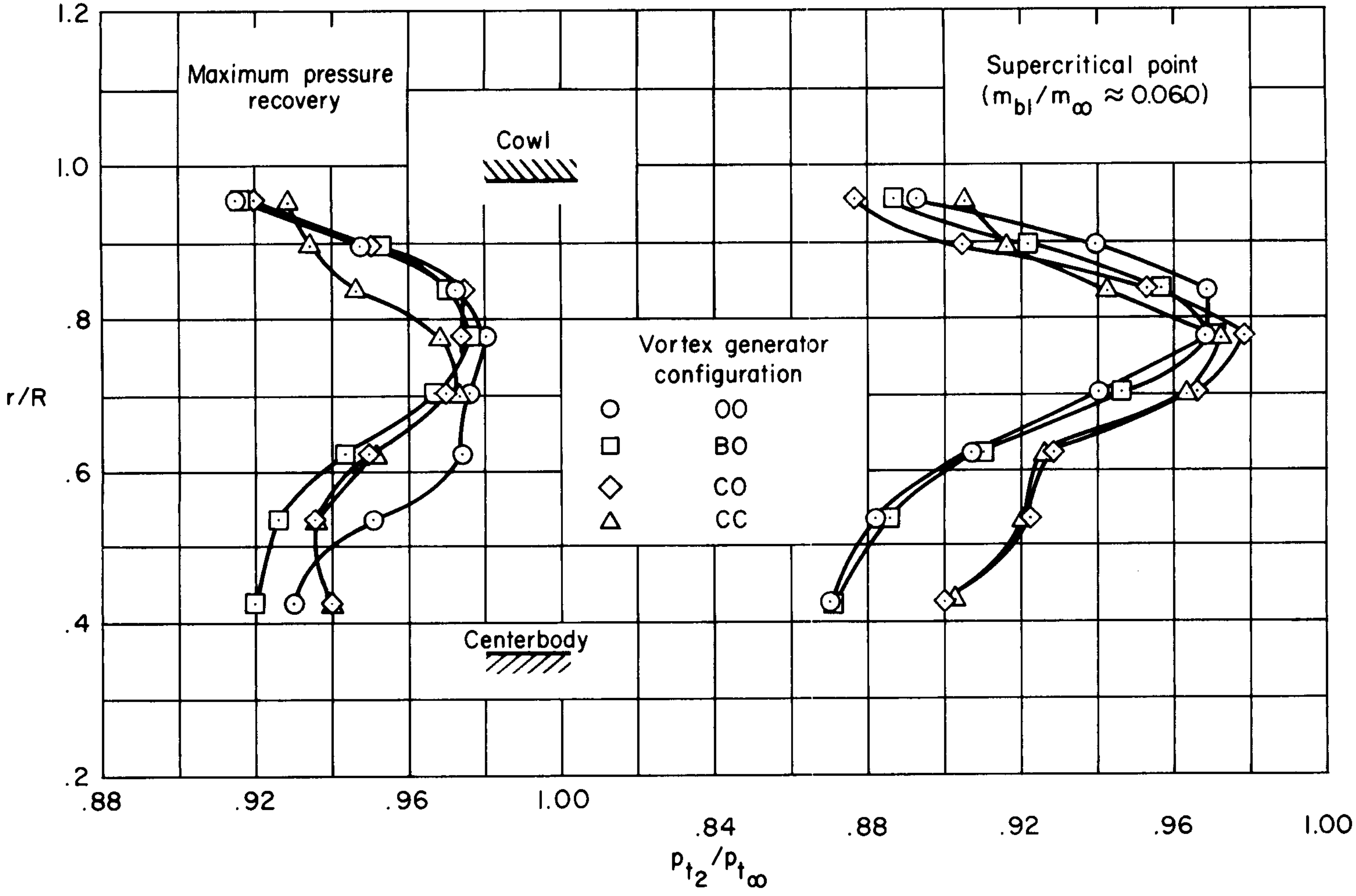

(b) $M_\infty = 2.41$, $x_{lip}/R = 2.693$, bleed configuration B′-1.

Figure 45. – Continued.

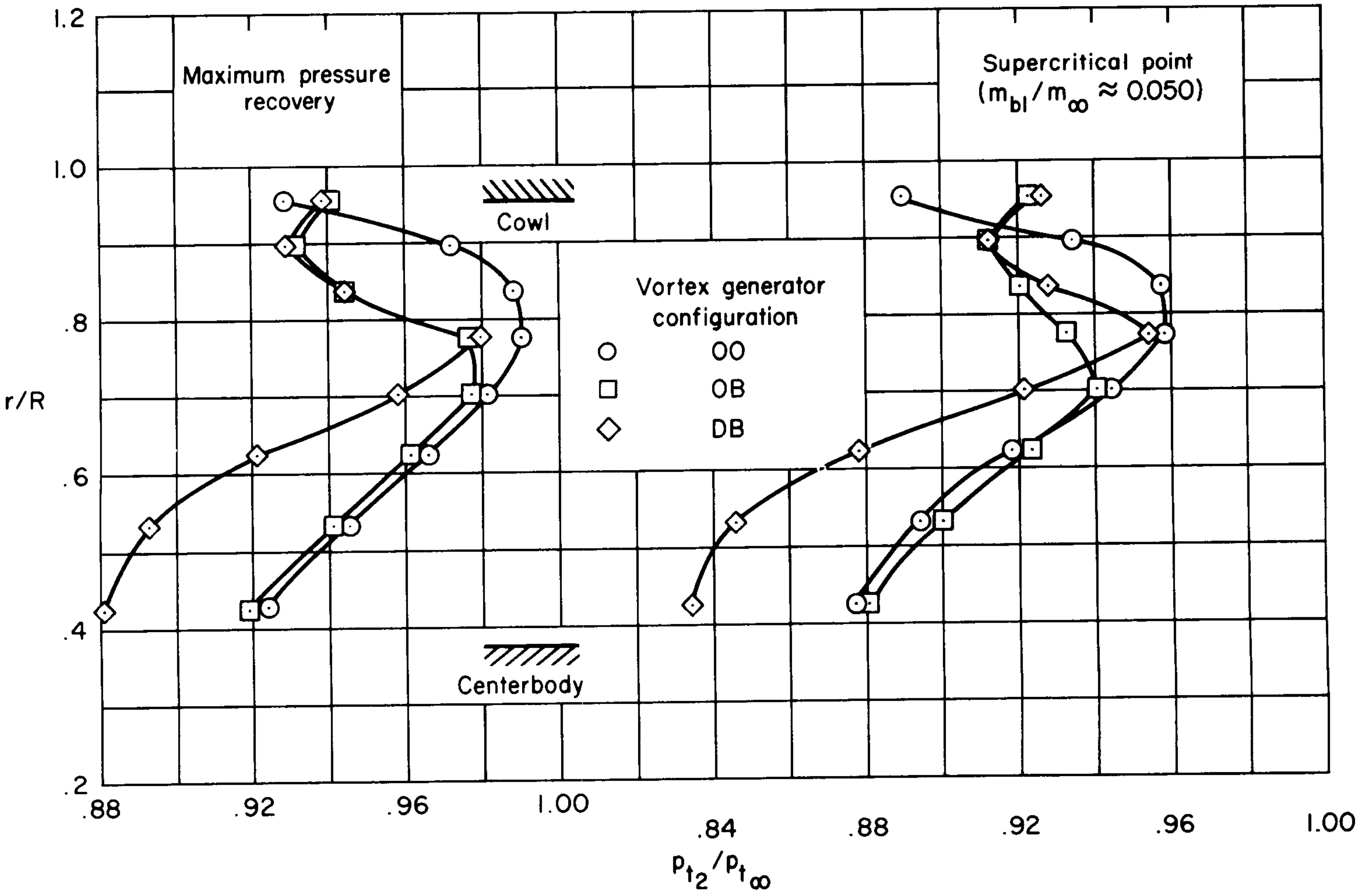

(c) $M_\infty = 2.10, x_{lip}/R = 3.229$, bleed configuration B'-3.

Figure 45. – Continued.

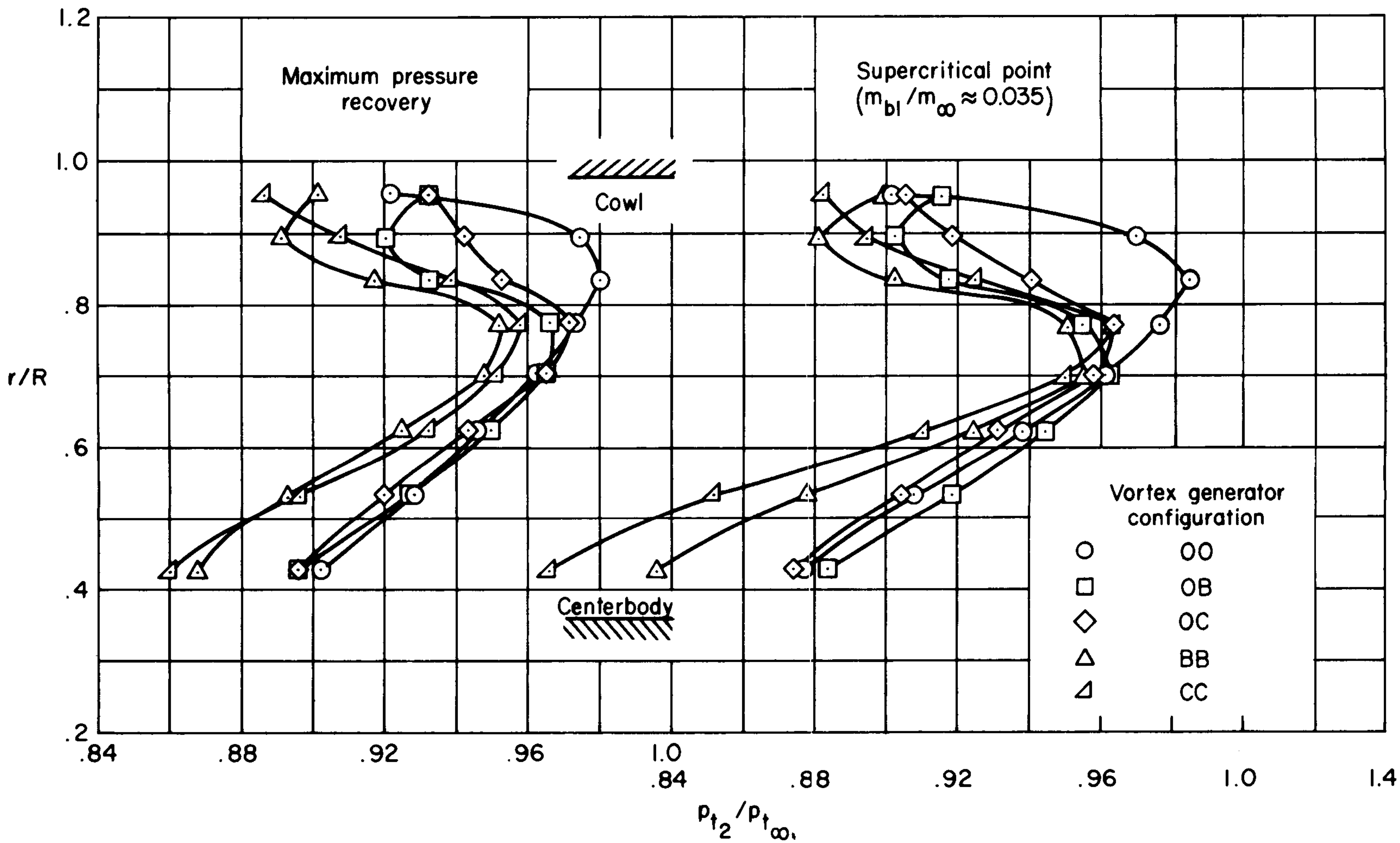

(d) $M_\infty = 1.75$, $x_{lip}/R = 3.583$, bleed configuration B-4.

Figure 45. – Concluded.

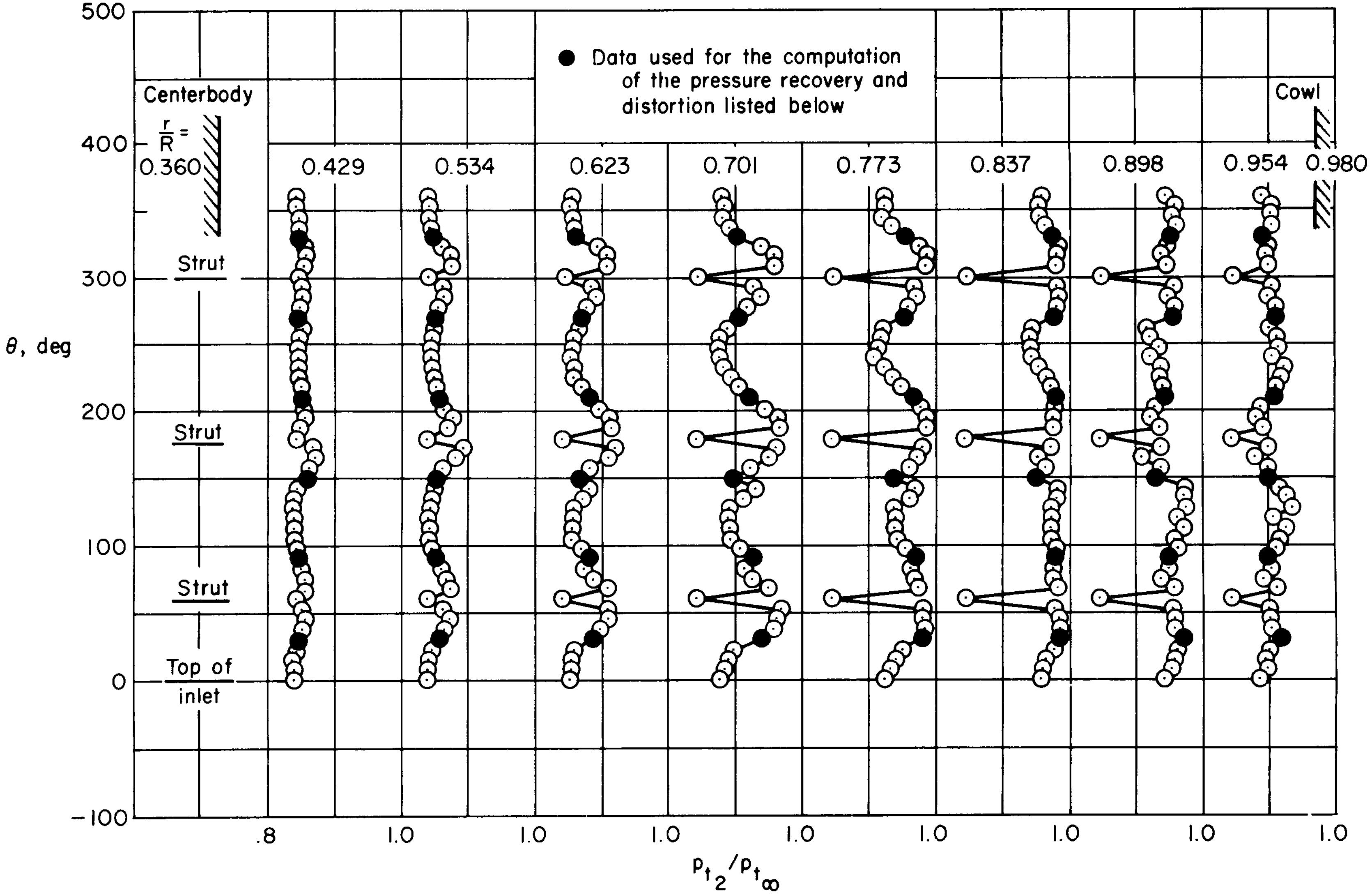

(a) $\bar{p}_{t_2}/p_{t_\infty} = 0.909$, $\Delta p_{t_2} = 0.152$, $m_{bl}/m_\infty = 0.063$, $M_\infty = 2.56$, $x_{lip}/R = 2.509$, bleed configuration B-1, vortex generator configuration 00.

Figure 46. – Circumferential total-pressure profiles; $\alpha = 0°$, $m_{bp}/m_\infty = 0$.

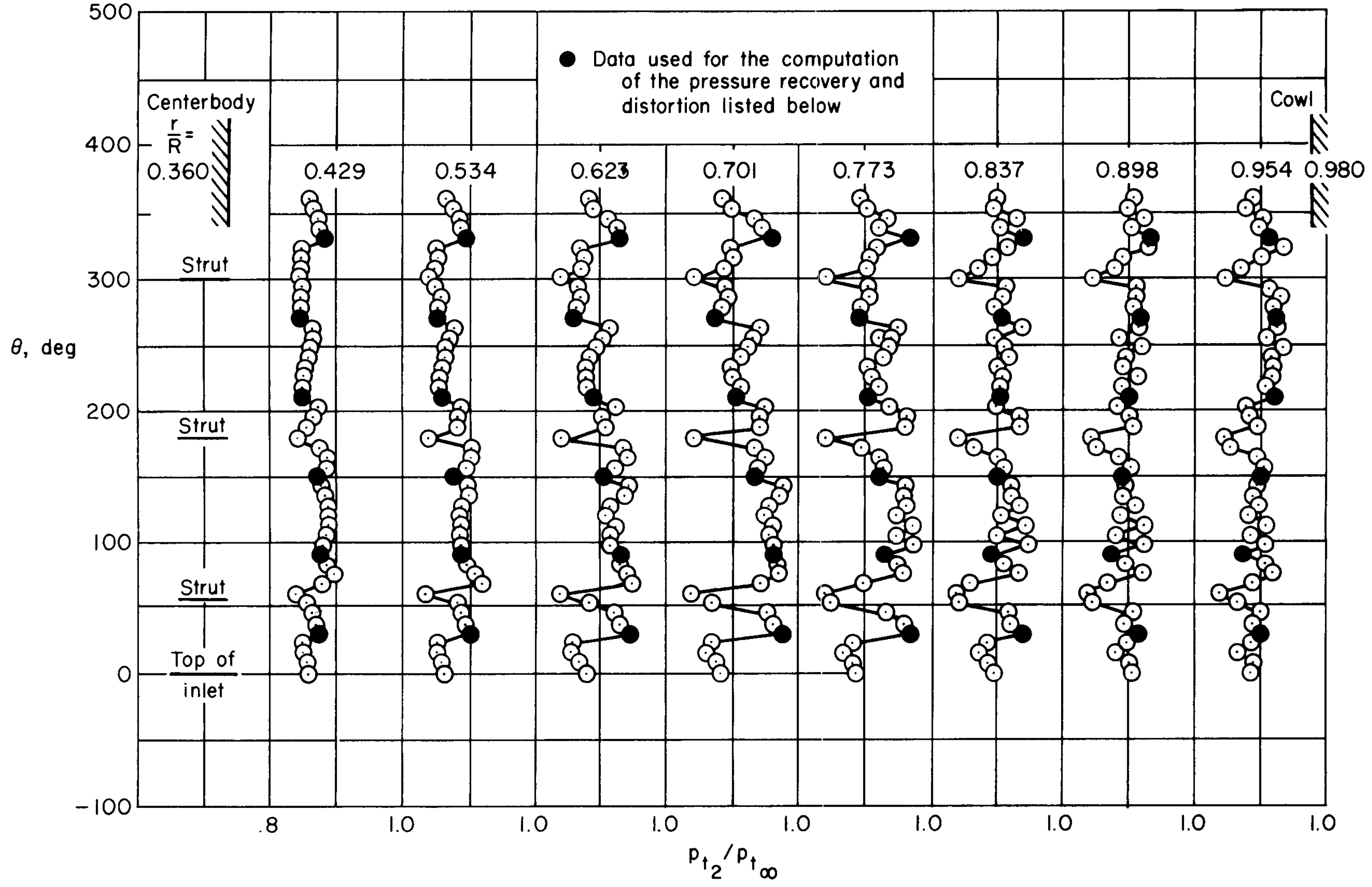

(b) $\bar{p}_{t_2}/p_{t_\infty} = 0.905$, $\Delta p_{t_2} = 0.144$, $m_{bl}/m_\infty = 0.059$, $M_\infty = 2.56$, $x_{lip}/R = 2.483$, bleed configuration B-1, vortex generator configuration BB.

Figure 46. – Continued.

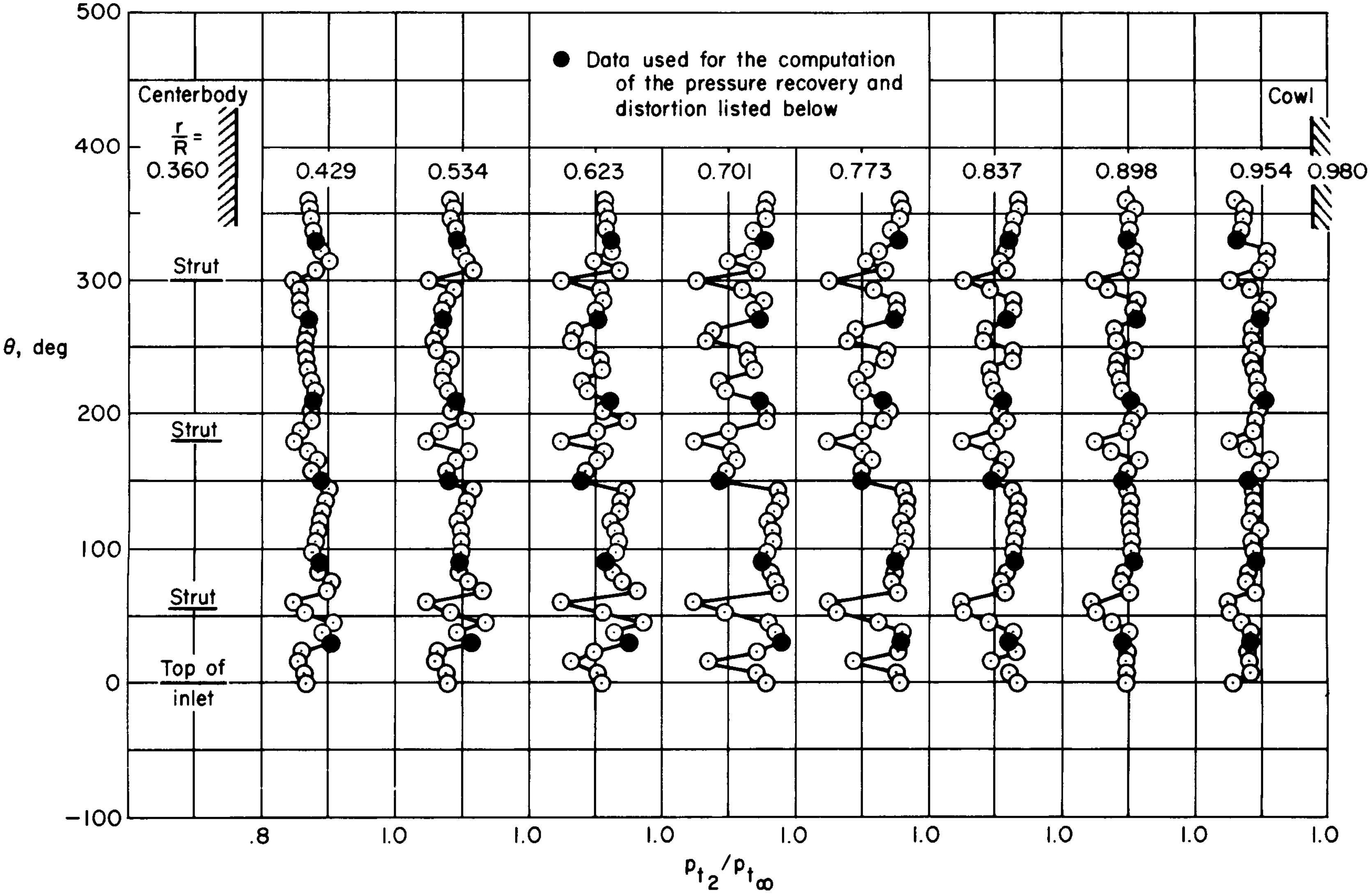

(c) $\bar{p}_{t_2}/p_{t_\infty}$ = 0.909, Δp_{t_2} = 0.128, m_{bl}/m_∞ = 0.058, M_∞ = 2.56, x_{lip}/R = 2.483, bleed configuration B'-1, vortex generator configuration CC.

Figure 46. – Concluded.

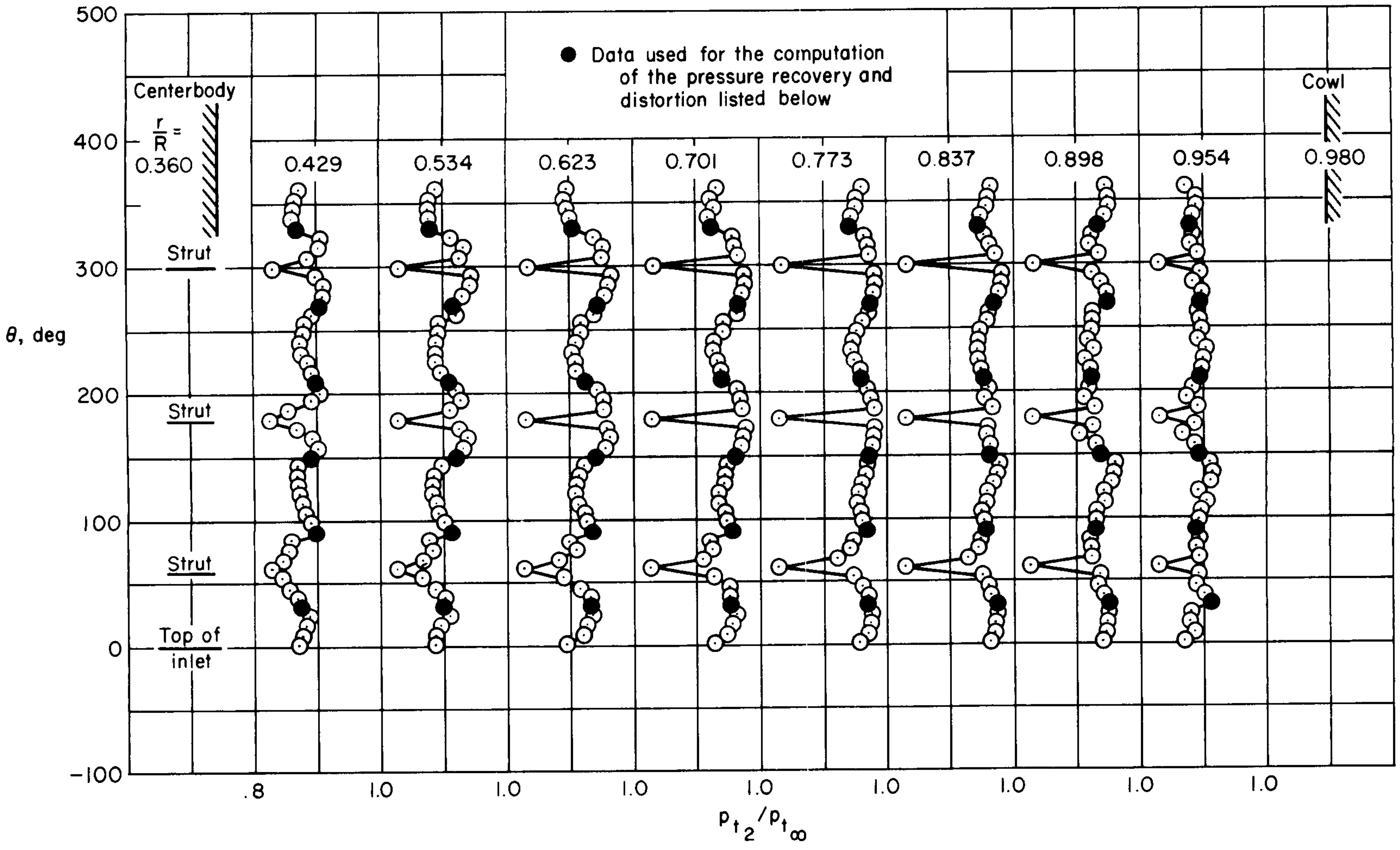

(a) $\bar{p}_{t_2}/p_{t_\infty} = 0.927$, $\Delta p_{t_2} = 0.114$, $m_{bl}/m_\infty = 0.050$, $M_\infty = 2.10$, $x_{lip}/R = 3.229$, bleed configuration B′-3, vortex generator configuration 00.

Figure 47. – Circumferential total-pressure profiles; $\alpha = 0°$, $m_{bp}/m_\infty = 0$.

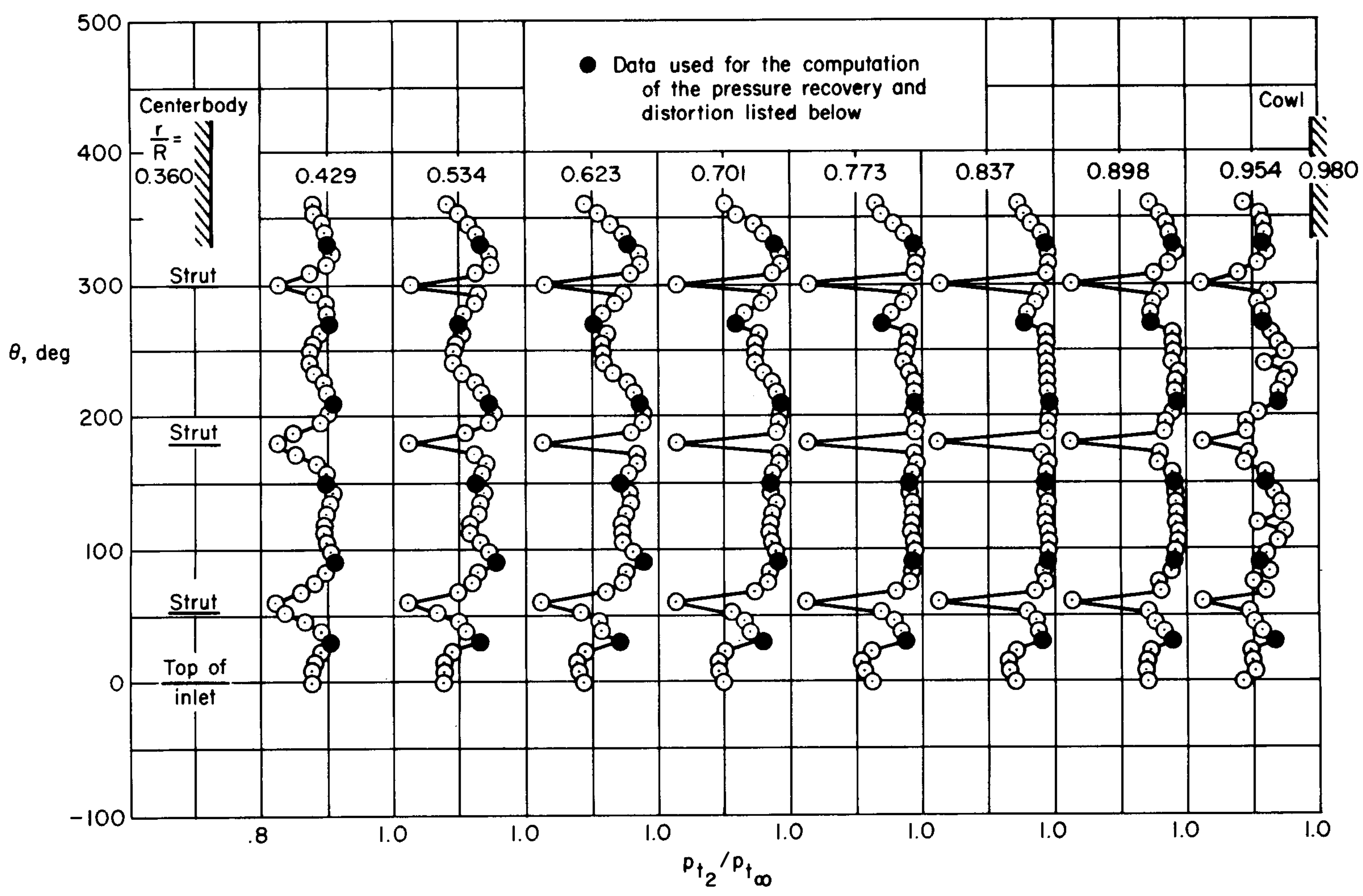

(b) $\bar{p}_{t_2}/p_{t_\infty} = 0.948$, $\Delta p_{t_2} = 0.099$, $m_{bl}/m_\infty = 0.044$, $M_\infty = 1.75$, $x_{lip}/R = 3.583$, bleed configuration B′-4, vortex generator configuration 00.

Figure 47. – Concluded.

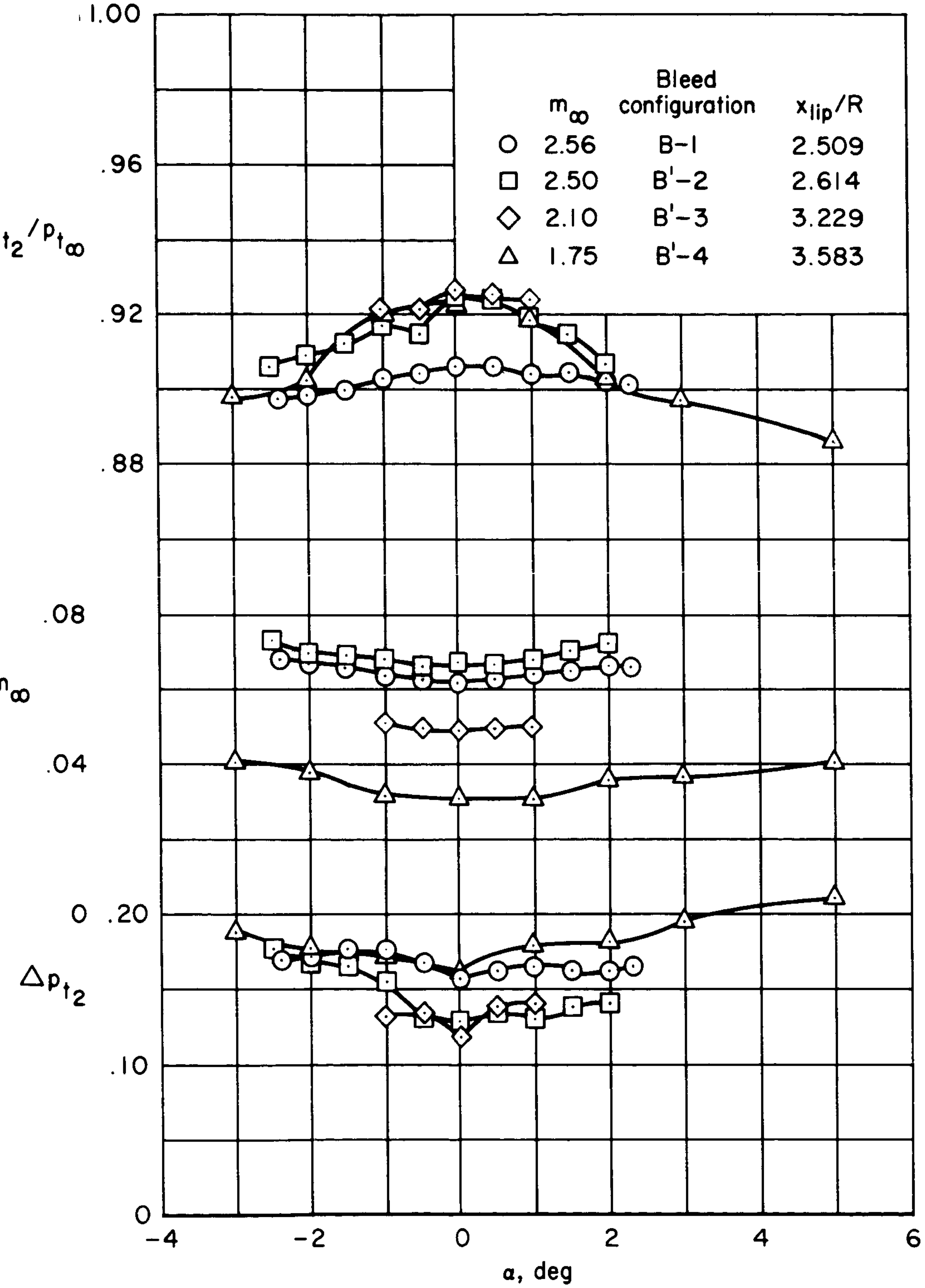

Figure 48. – Performance with changes in angle of attack; $m_{bp}/m_\infty = 0$, $\theta_2 = 0°$, vortex generator configuration 00.

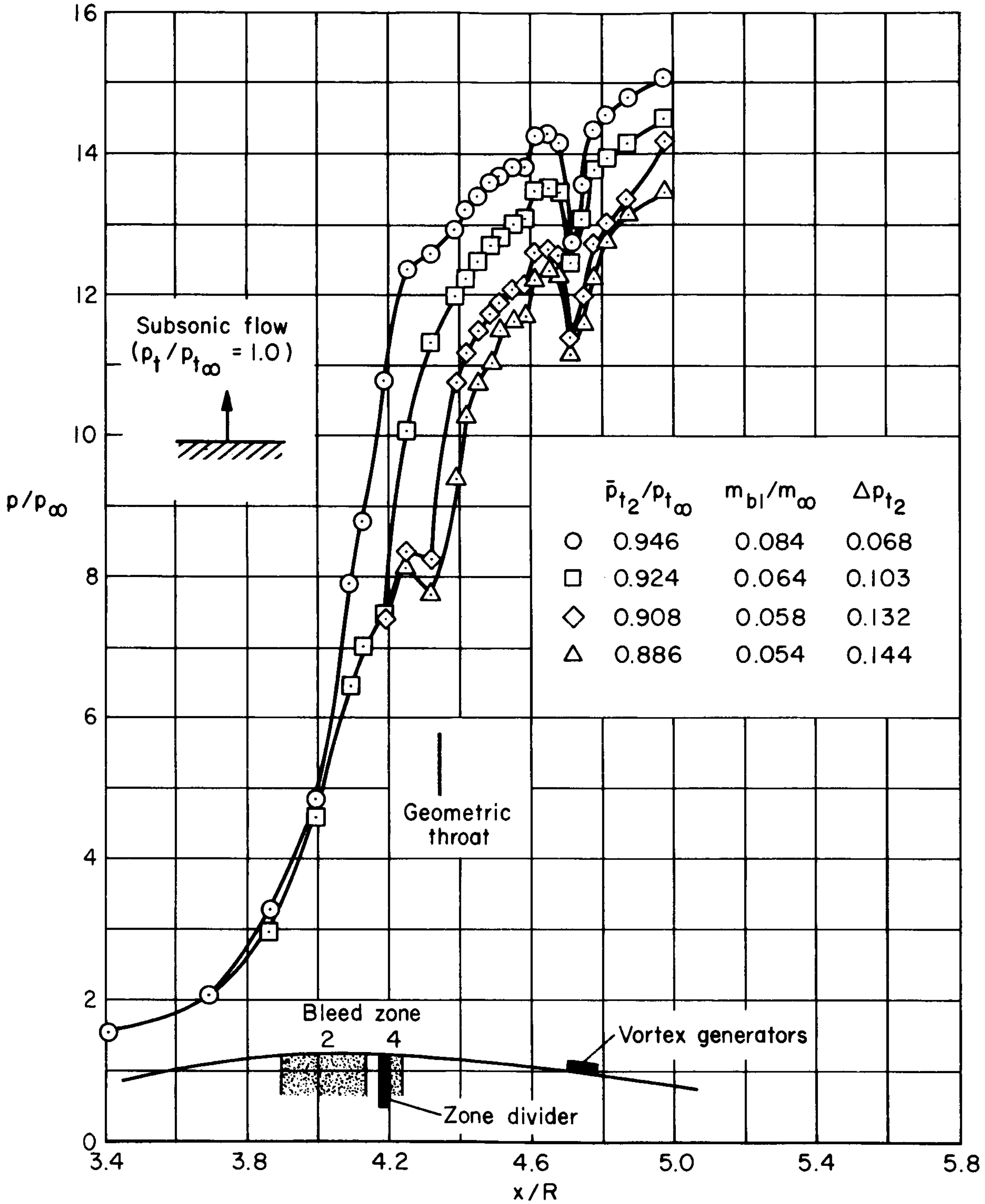

(a) M_∞ = 2.56, x_{lip}/R = 2.483, bleed configuration B'-1; vortex generator configuration CC.

Figure 49. – Centerbody static-pressure distributions; α = 0°, m_{bp}/m_∞ = 0.

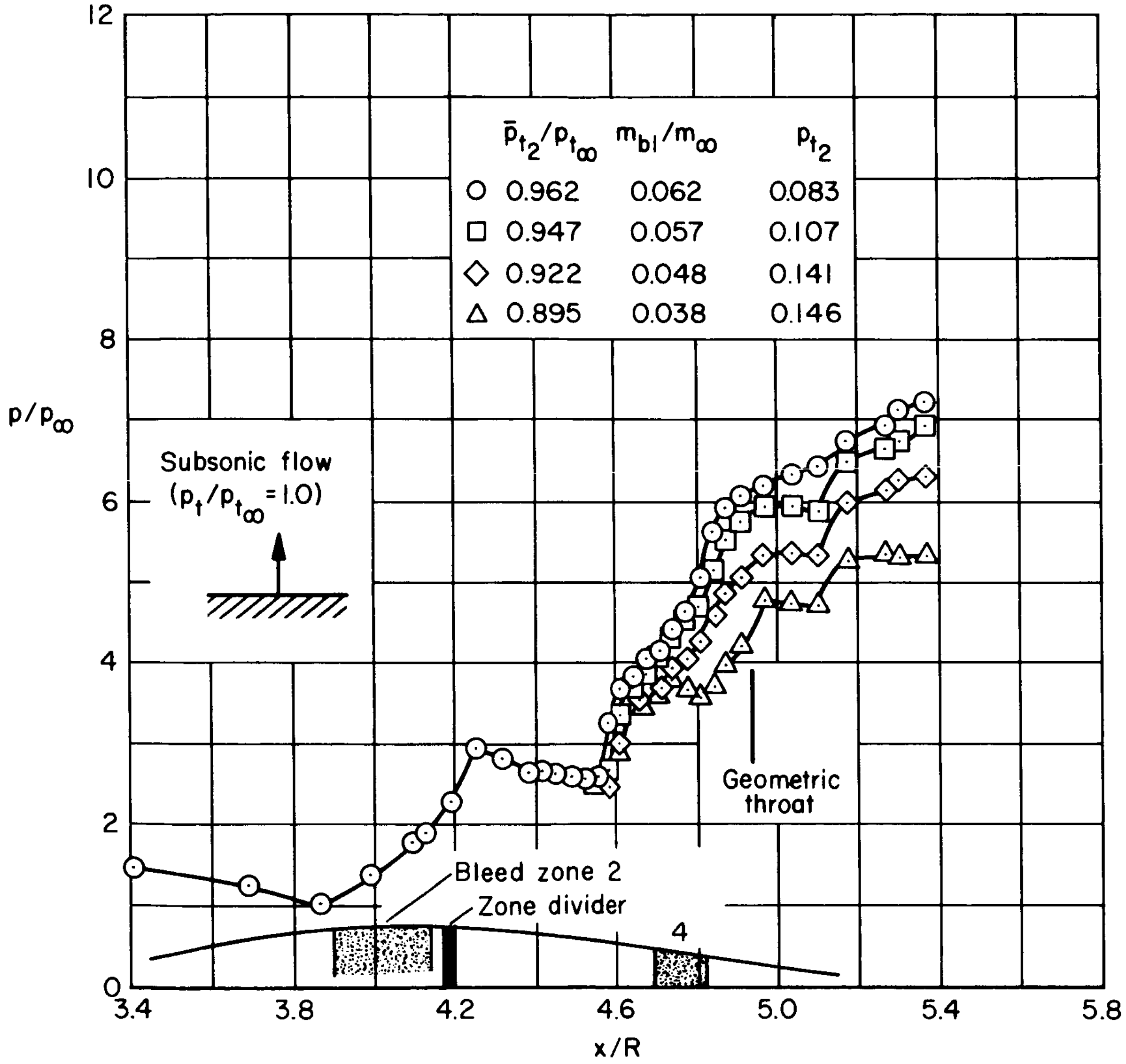

(b) M_∞ = 2.10, x_{lip}/R = 3.229, bleed configuration B′-3; vortex generator configuration 00.

Figure 49. – Continued.

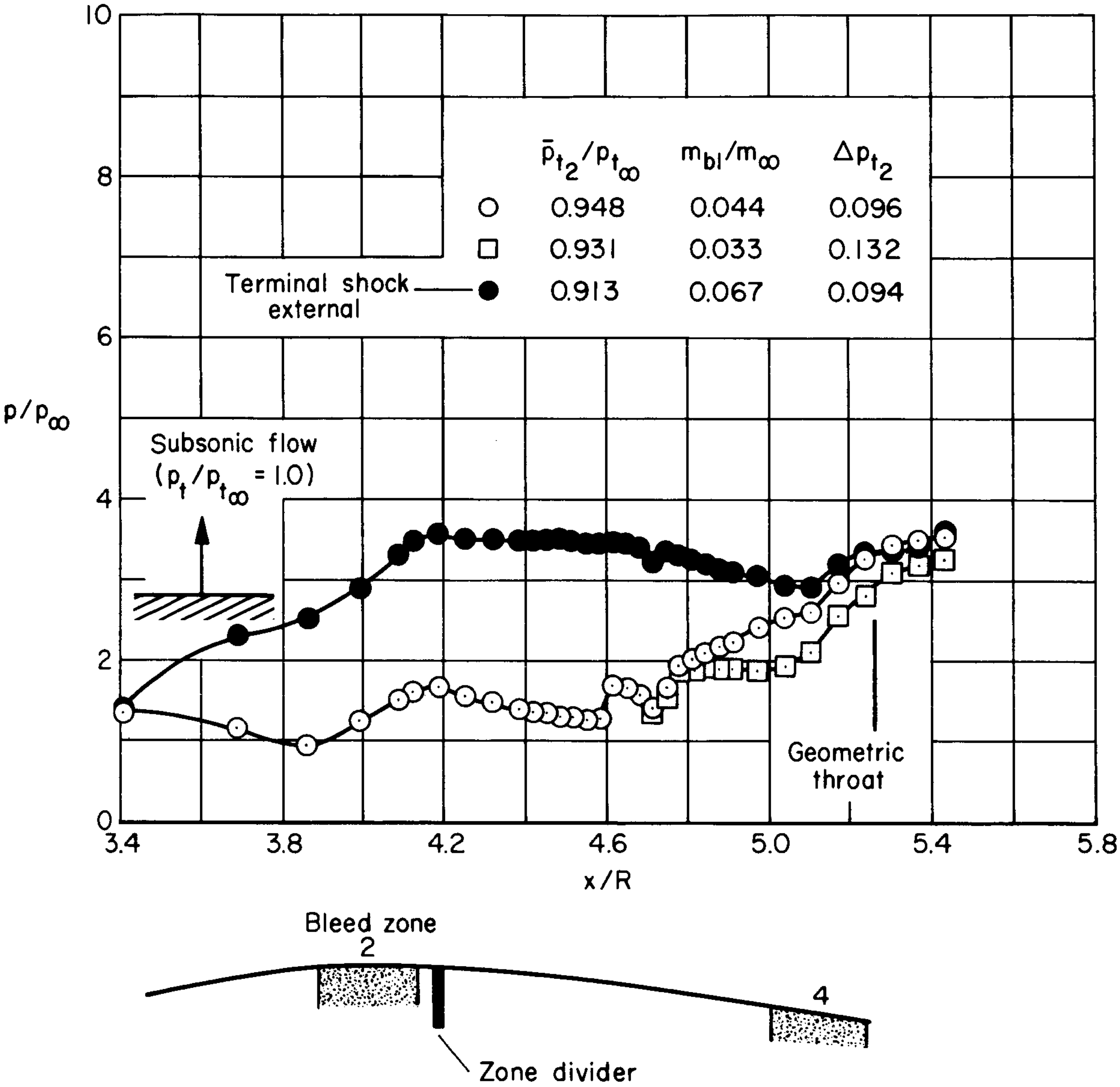

(c) $M_\infty = 1.75$, $x_{lip}/R = 3.583$, bleed configuration B-4; vortex generator configuration 00.

Figure 49. – Concluded.

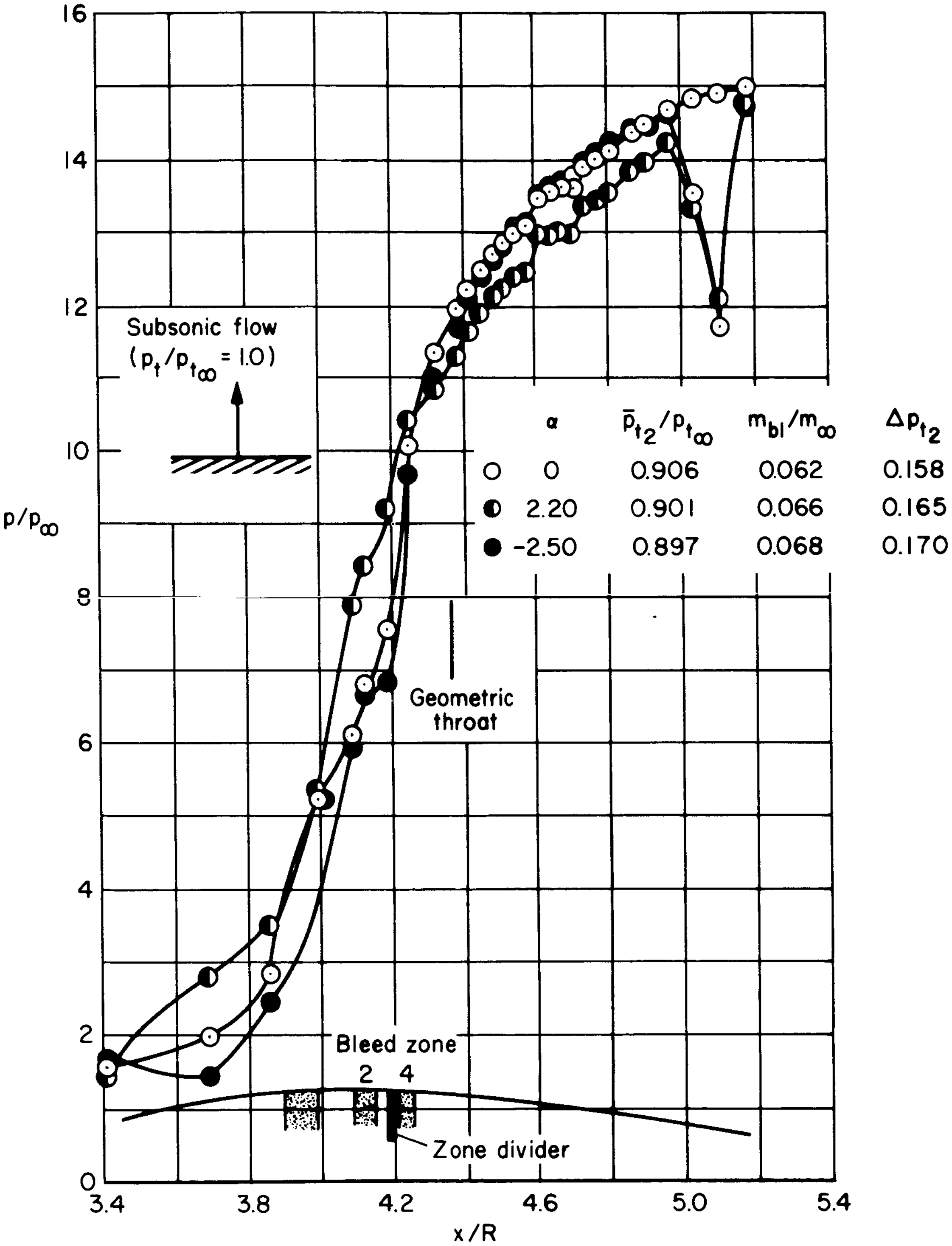

	α	$\bar{p}_{t_2}/p_{t_\infty}$	m_{bl}/m_∞	Δp_{t_2}
○	0	0.906	0.062	0.158
◐	2.20	0.901	0.066	0.165
●	-2.50	0.897	0.068	0.170

(a) $M_\infty = 2.56$, $x_{lip}/R = 2.509$, bleed configuration B-1.

Figure 50. — Centerbody static-pressure distributions at angle of attack, vortex generation configuration 00.

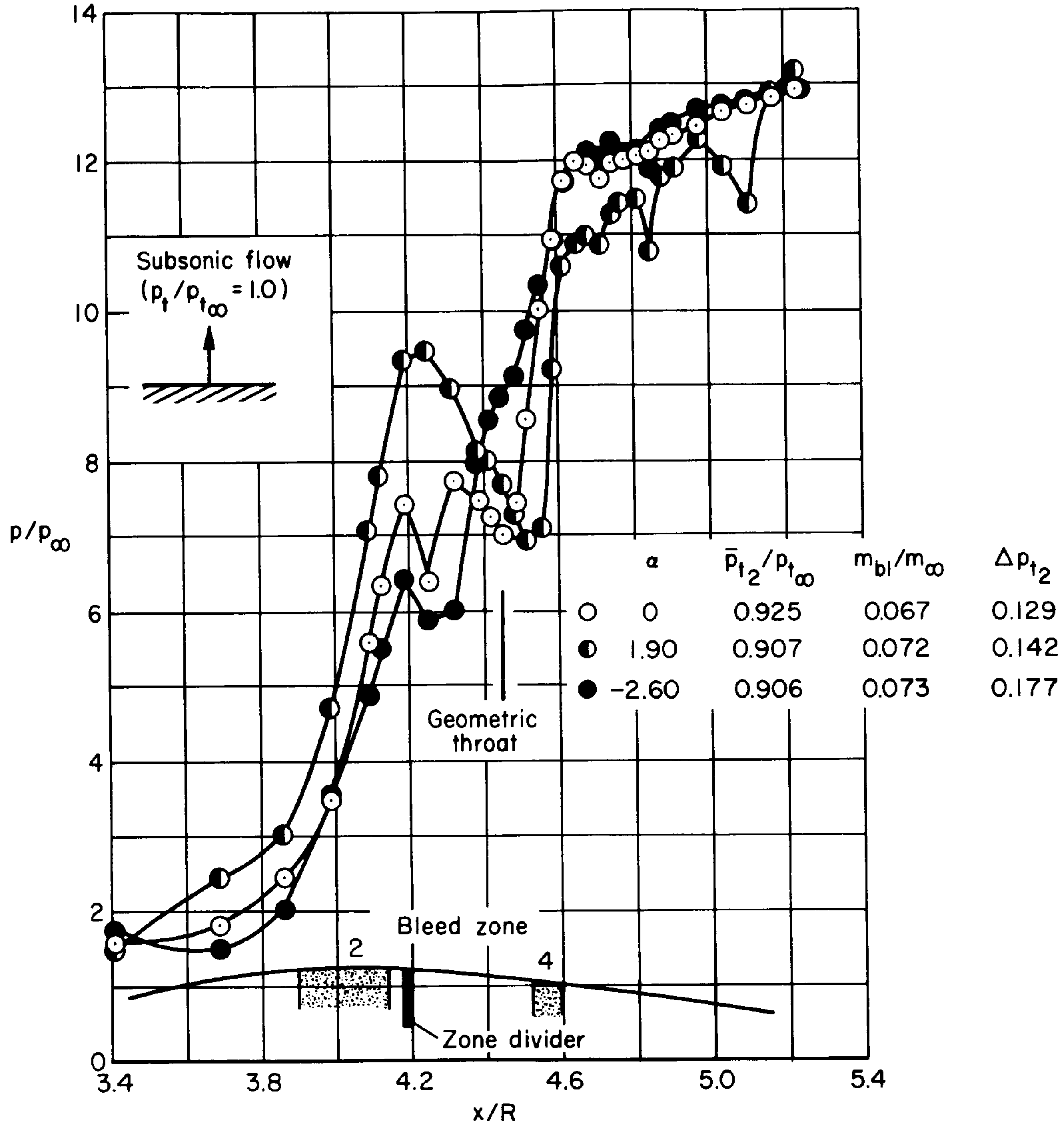

(b) $M_\infty = 2.50$, $x_{lip}/R = 2.614$, bleed configuration B′-2.

Figure 50. – Continued.

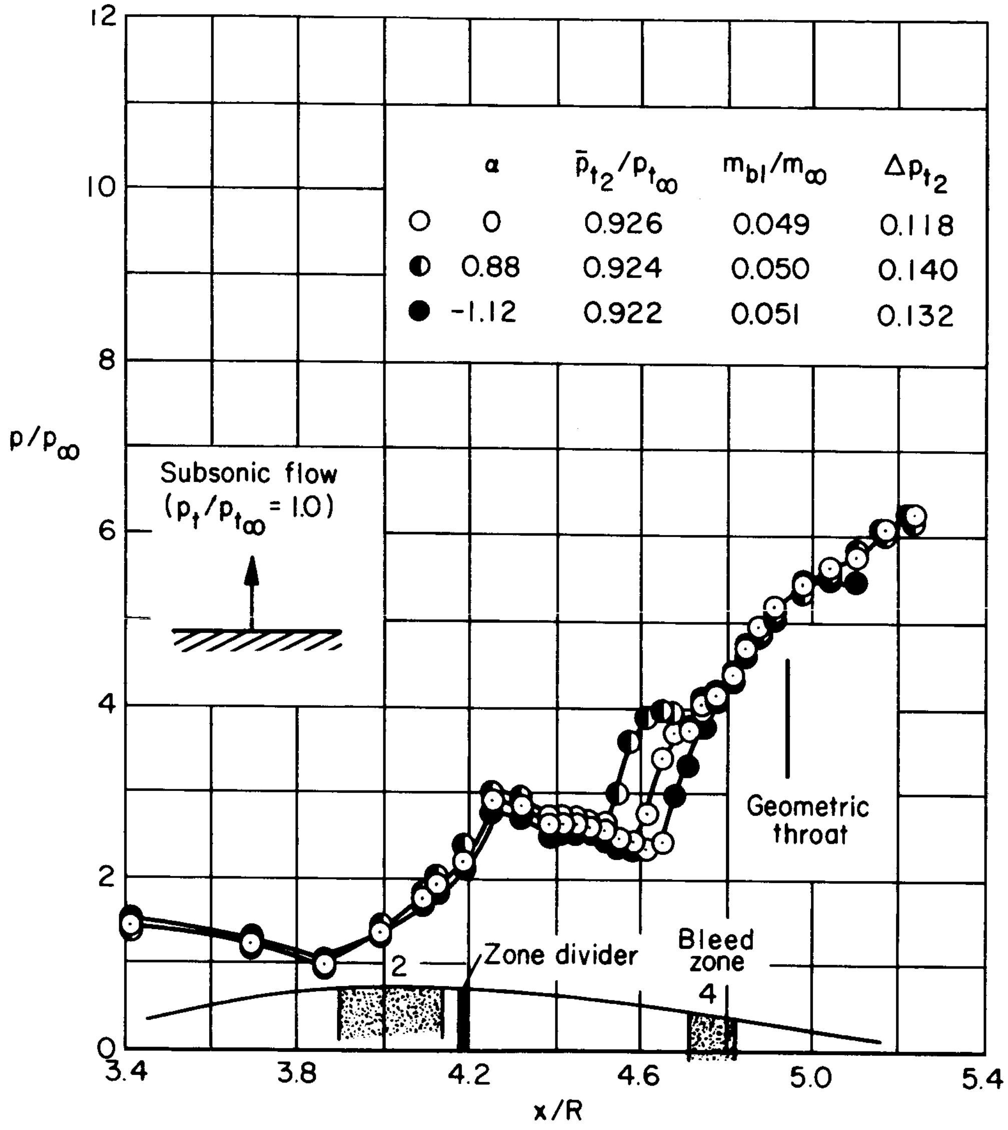

(c) $M_\infty = 2.10$, $x_{lip}/R = 3.229$, bleed configuration B'-3.

Figure 50. – Continued.

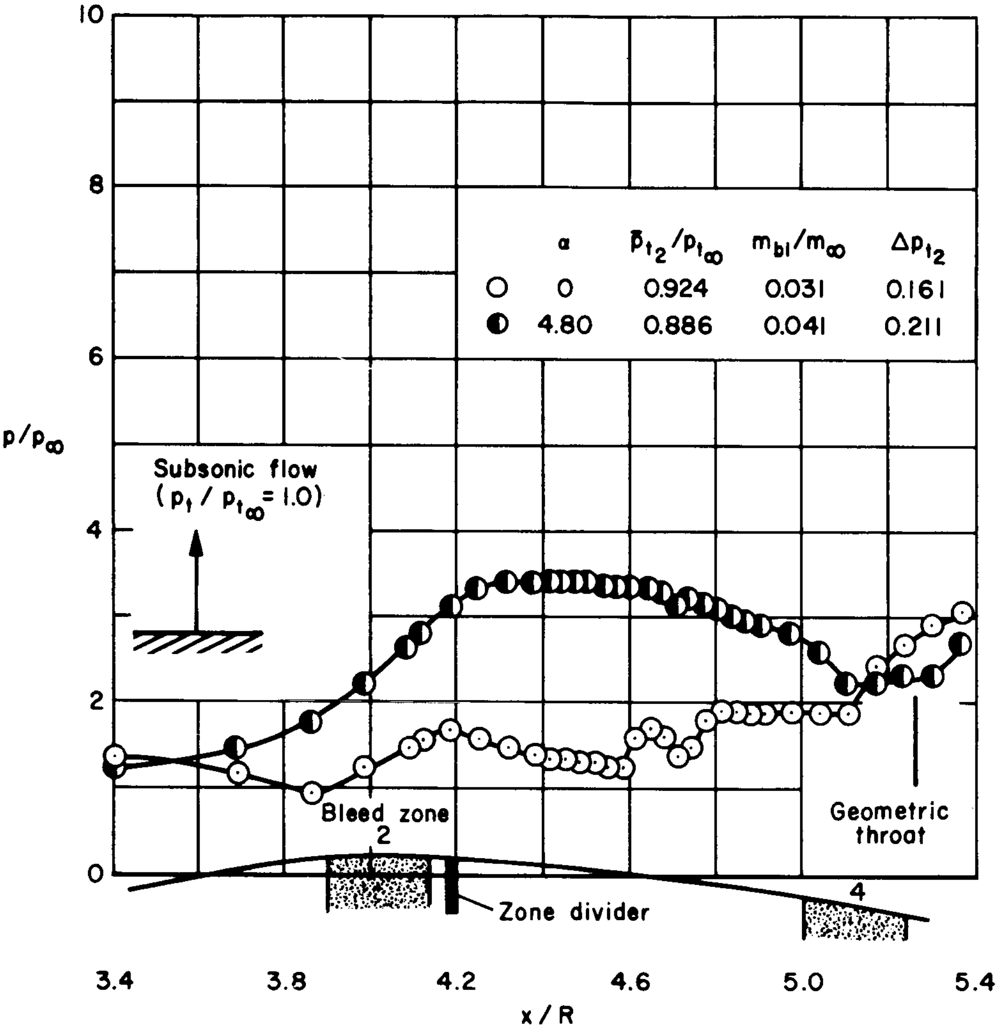

(d) $M_\infty = 1.75$, $x_{lip}/R = 3.583$, bleed configuration B'-4.

Figure 50. – Concluded.

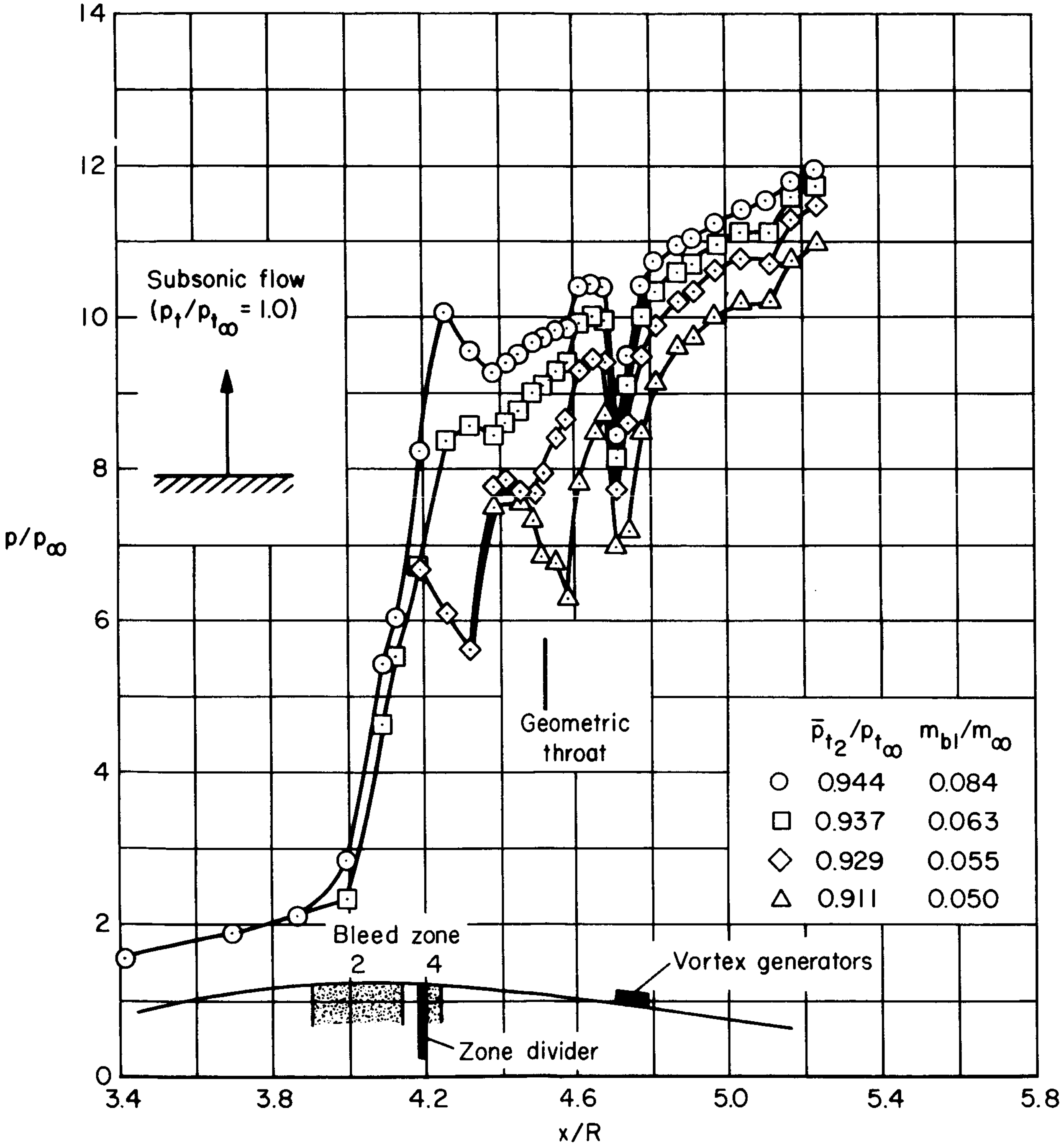

(a) $x_{lip}/R = 2.719$, bleed configuration B'-1, vortex generator configuration CC.

Figure 51. – Centerbody static-pressure distributions; $M_\infty = 2.41$, $\alpha = 0°$, $m_{bp}/m_\infty = 0$.

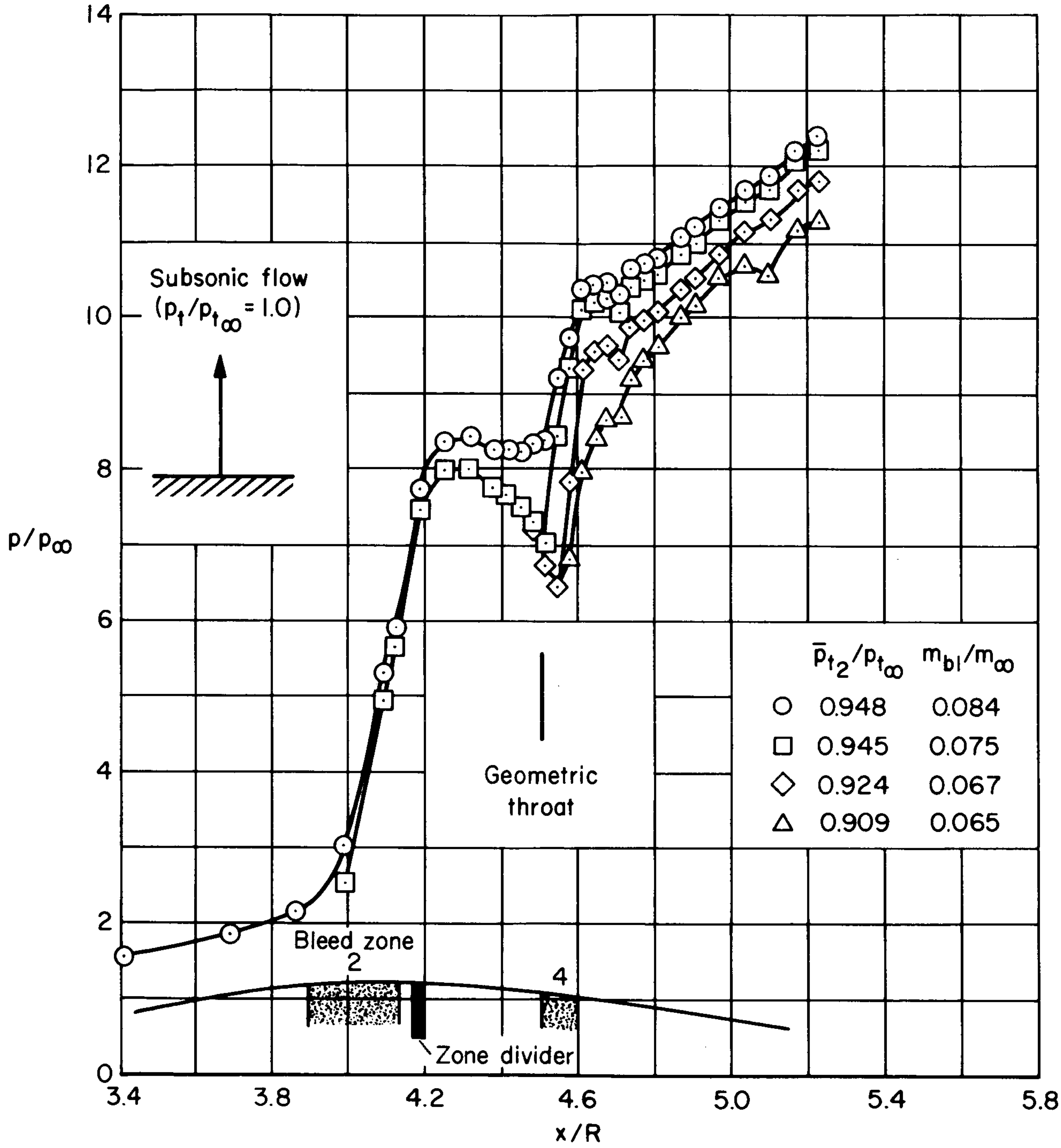

(b) $x_{lip}/R = 2.706$, bleed configuration B′-2, vortex generator configuration 00.

Figure 51. – Continued.

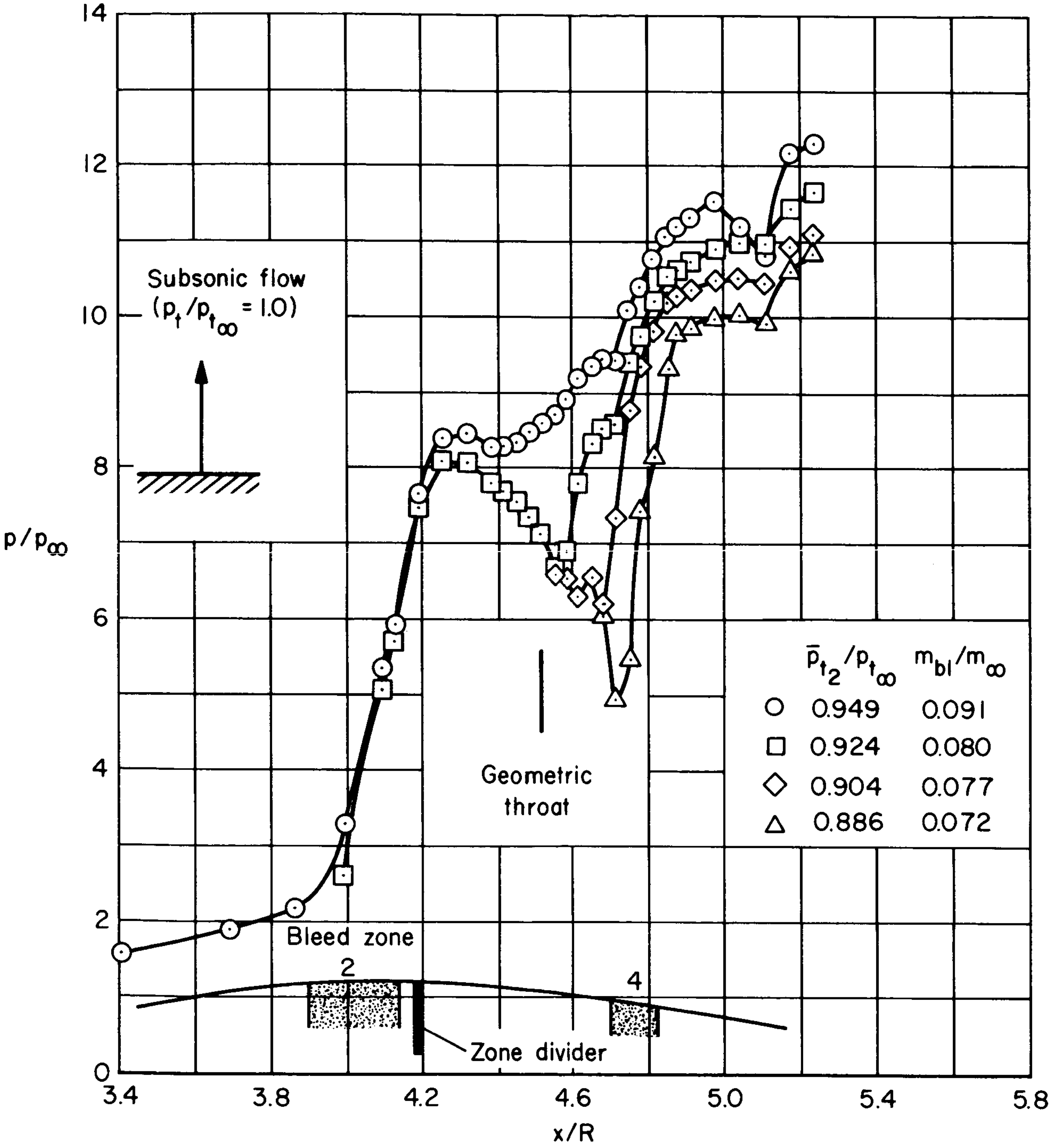

(c) x_{lip}/R = 2.706, bleed configuration B-3, vortex generator configuration 00.

Figure 51. – Concluded.

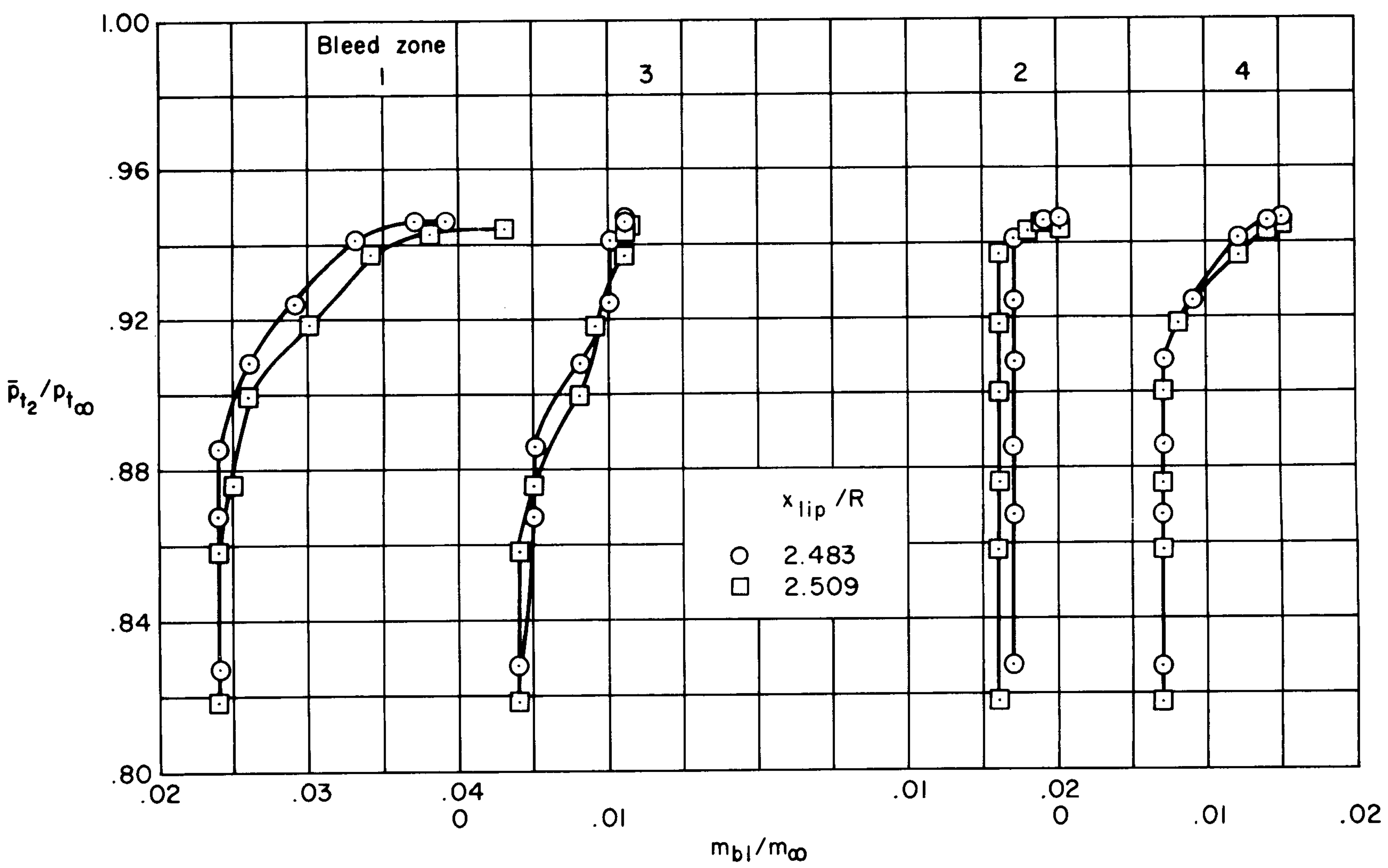

(a) M_∞ = 2.56, bleed configuration B'-1, vortex generator configuration CC.

Figure 52. – Supercritical bleed flow in the individual zones; $\alpha = 0°$, $\theta_2 = 0°$, $m_{bp}/m_\infty = 0$.

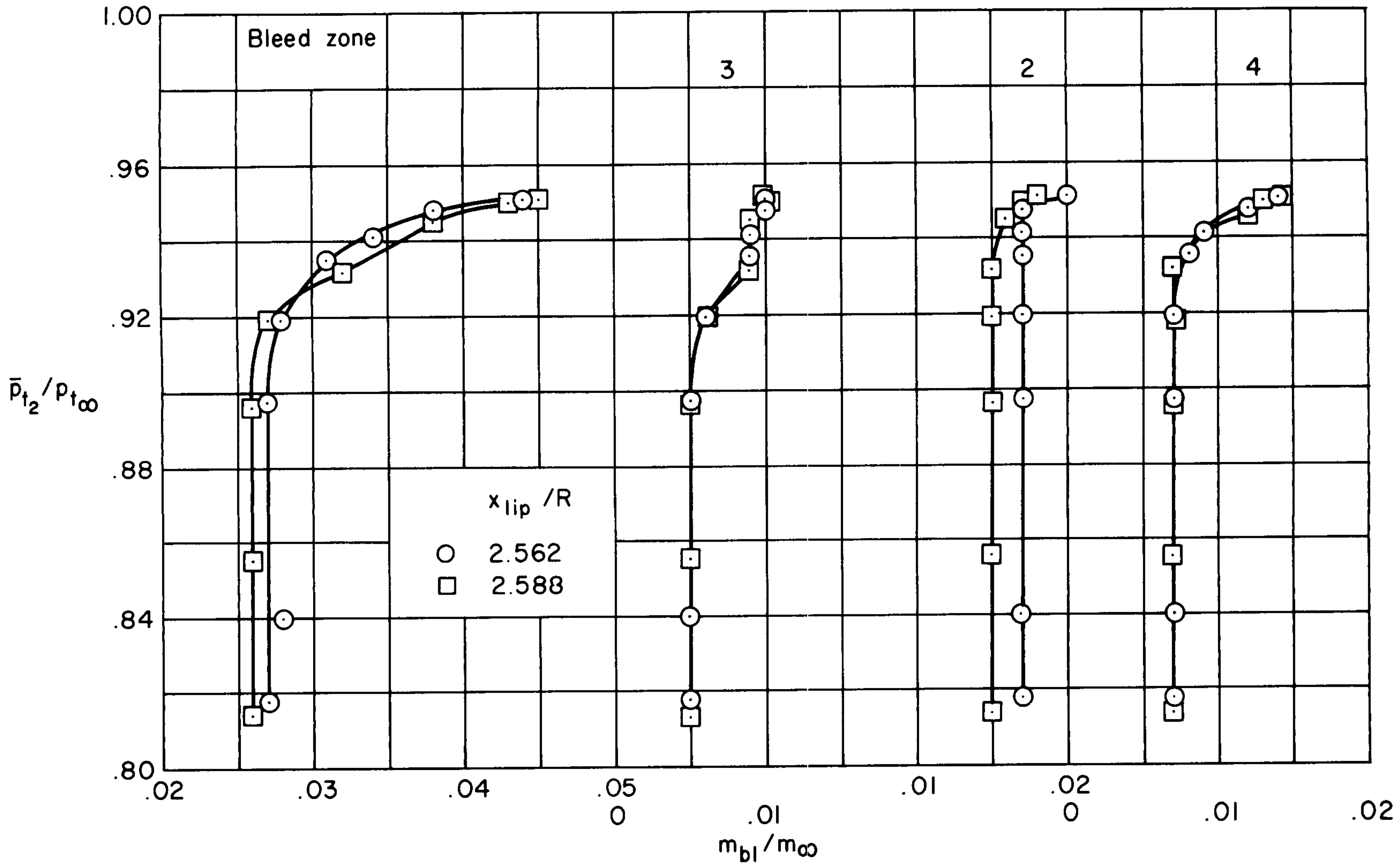

(b) M_∞ = 2.50, bleed configuration B′-1, vortex generator configuration CC.

Figure 52. – Continued.

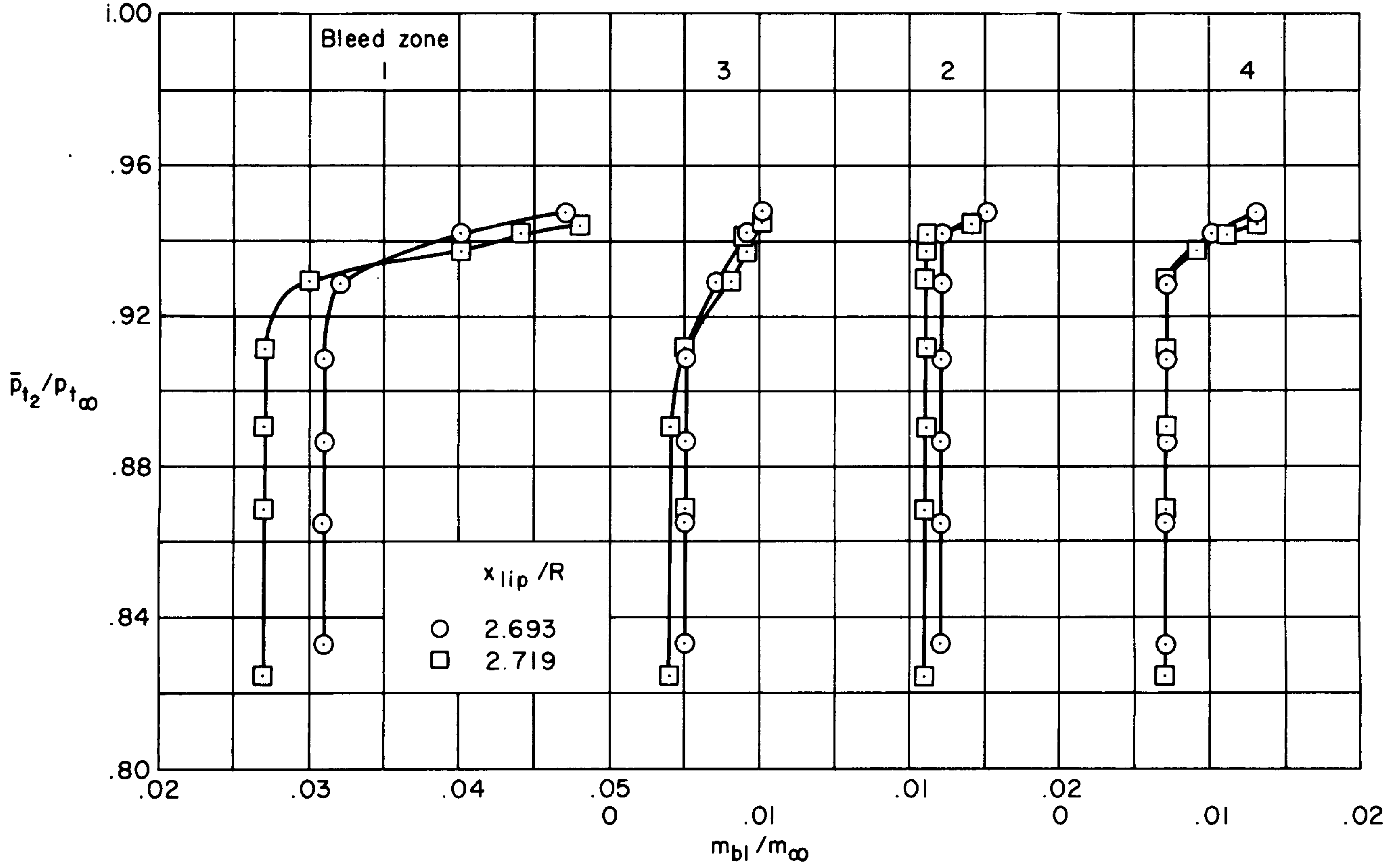

(c) $M_\infty = 2.41$, bleed configuration B′-1, vortex generator configuration CC.

Figure 52. – Continued.

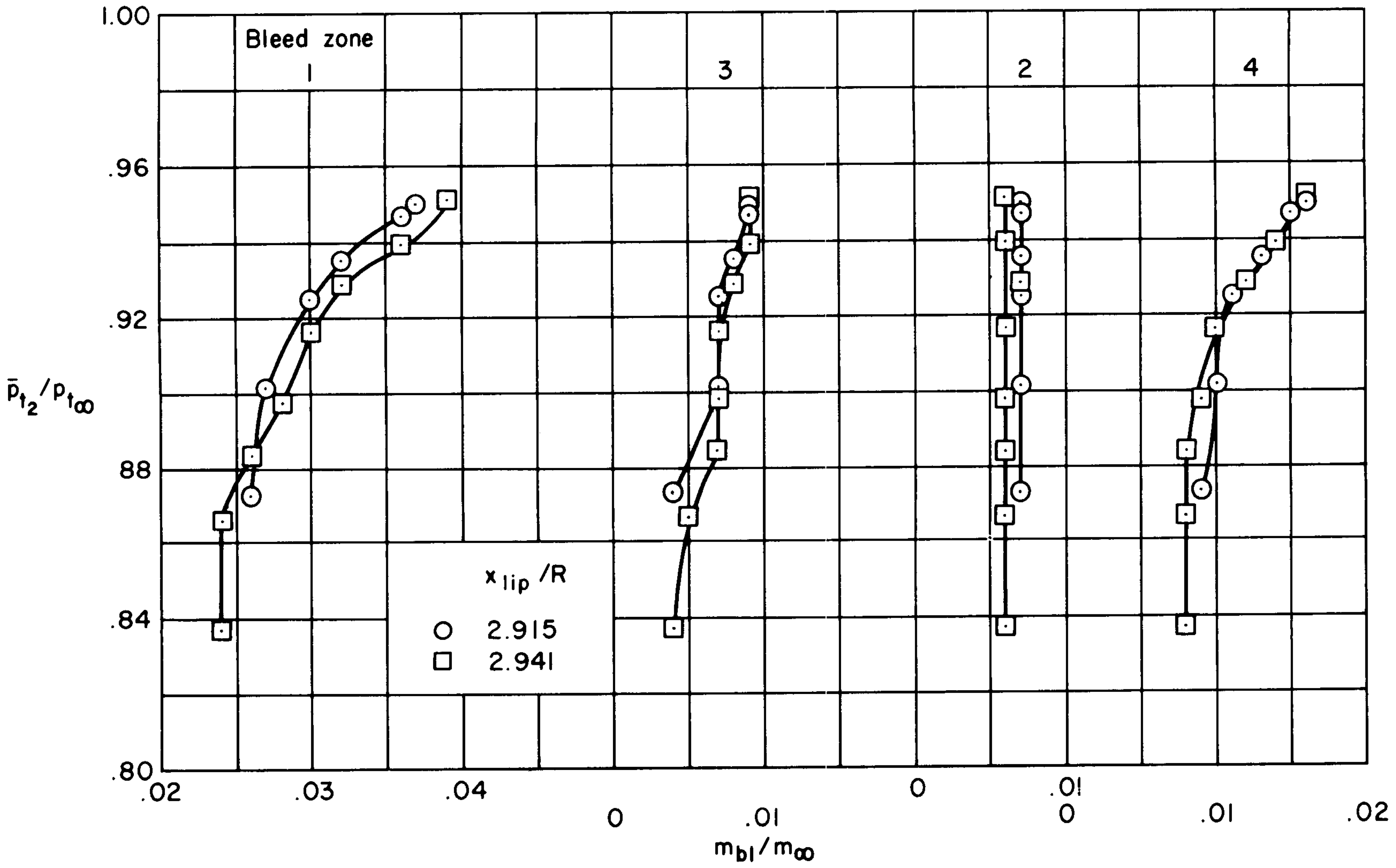

(d) $M_\infty = 2.30$, bleed configuration B′-2, vortex generator configuration 00.

Figure 52. – Continued.

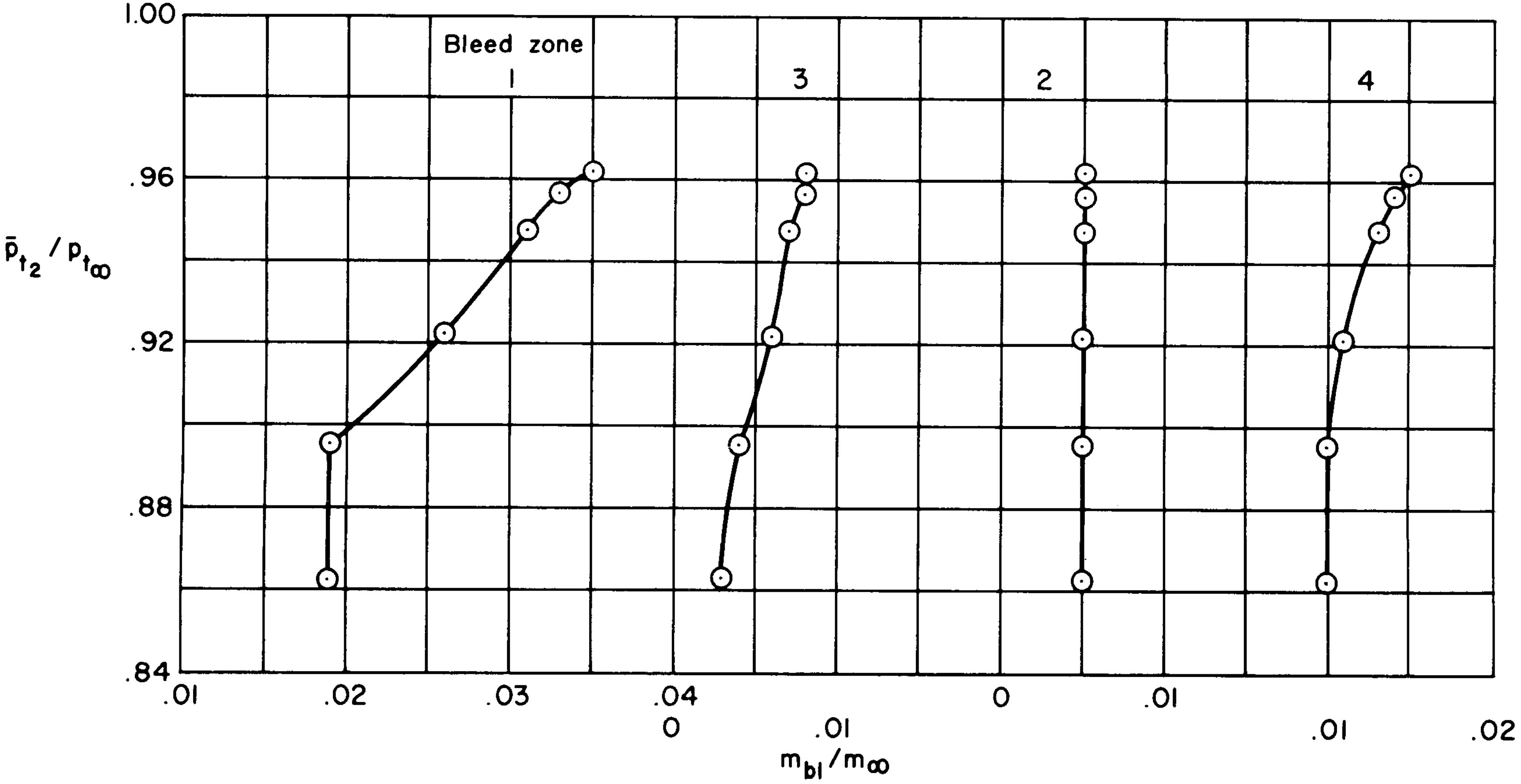

(e) $M_\infty = 2.10$, bleed configuration B′-3, vortex generator configuration 00, $x_{lip}/R = 3.229$.

Figure 52. – Continued.

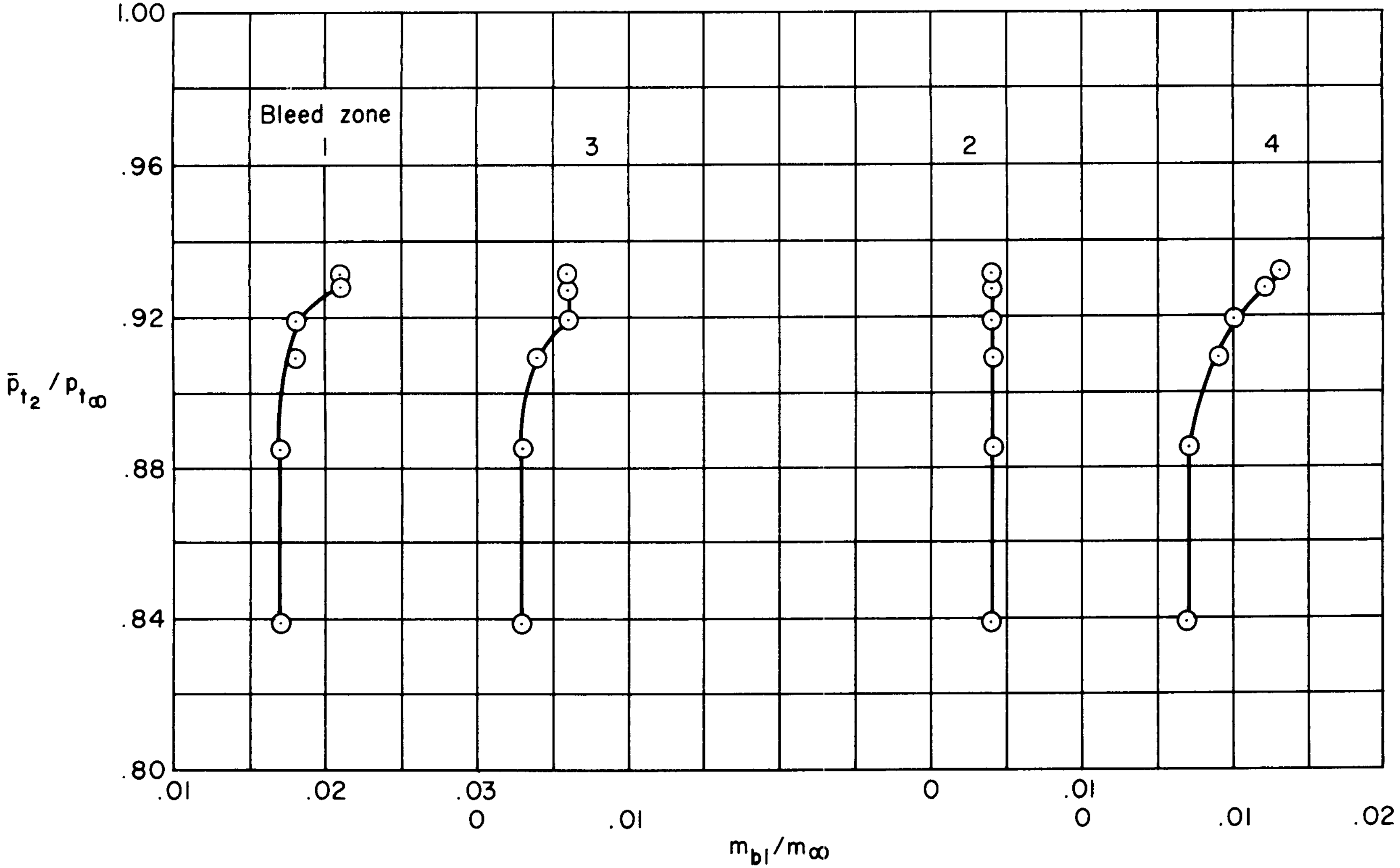

(f) $M_\infty = 1.90$, bleed configuration B′-4, vortex generator configuration 00, $x_{lip}/R = 3.478$.

Figure 52. – Continued

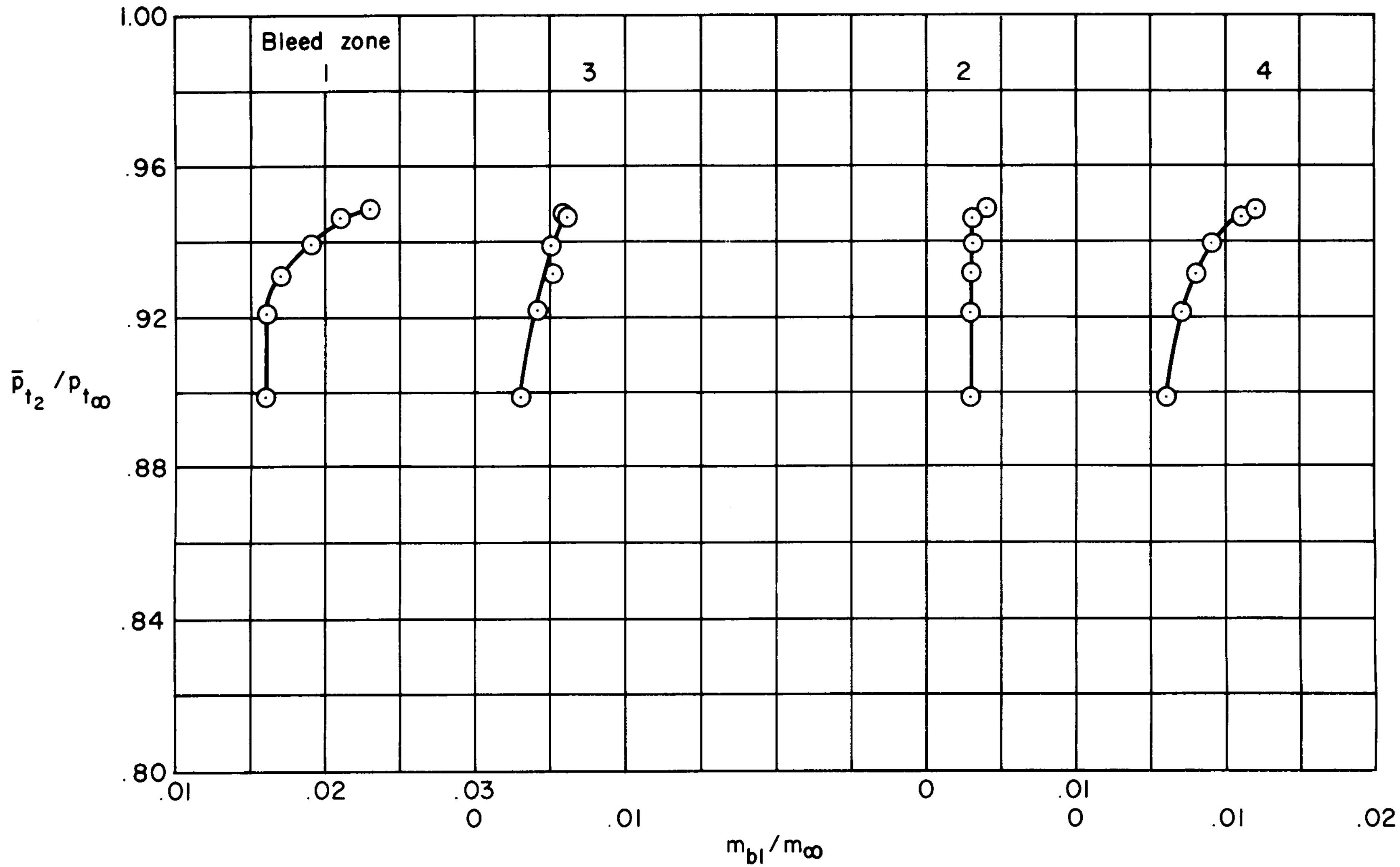

(g) $M_\infty = 1.75$, bleed configuration B′-4, vortex generator configuration 00, $x_{lip}/R = 3.583$.

Figure 52. – Concluded.

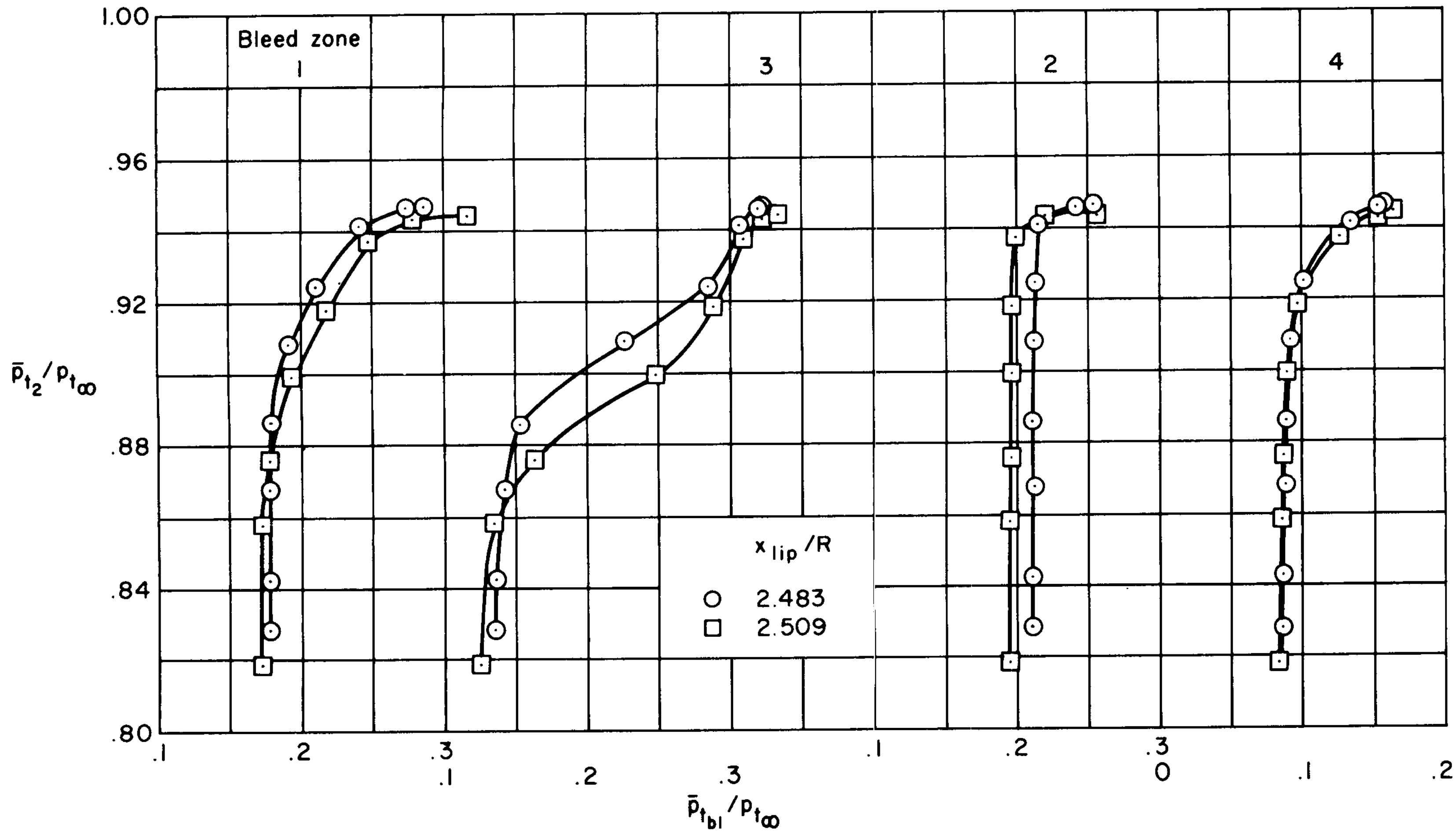

(a) $M_\infty = 2.56$, bleed configuration B′-1, vortex generator configuration CC.

Figure 53. – Plenum chamber pressure recoveries in the individual bleed zones, $\alpha = 0°$, $\theta_2 = 0°$, $m_{bp}/m_\infty = 0$.

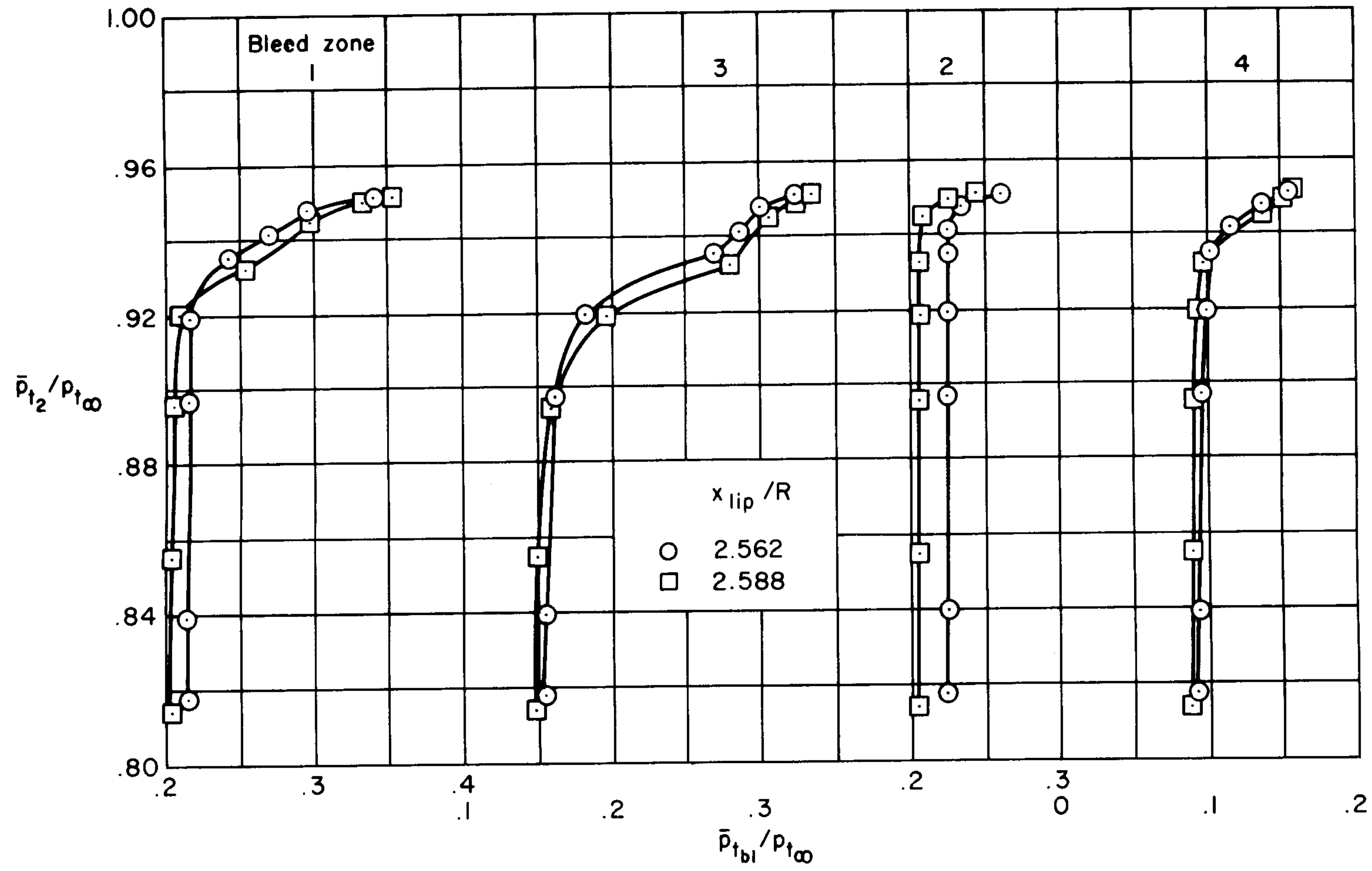

(b) $M_\infty = 2.50$, bleed configuration B′-1, vortex generator configuration CC.

Figure 53. – Continued.

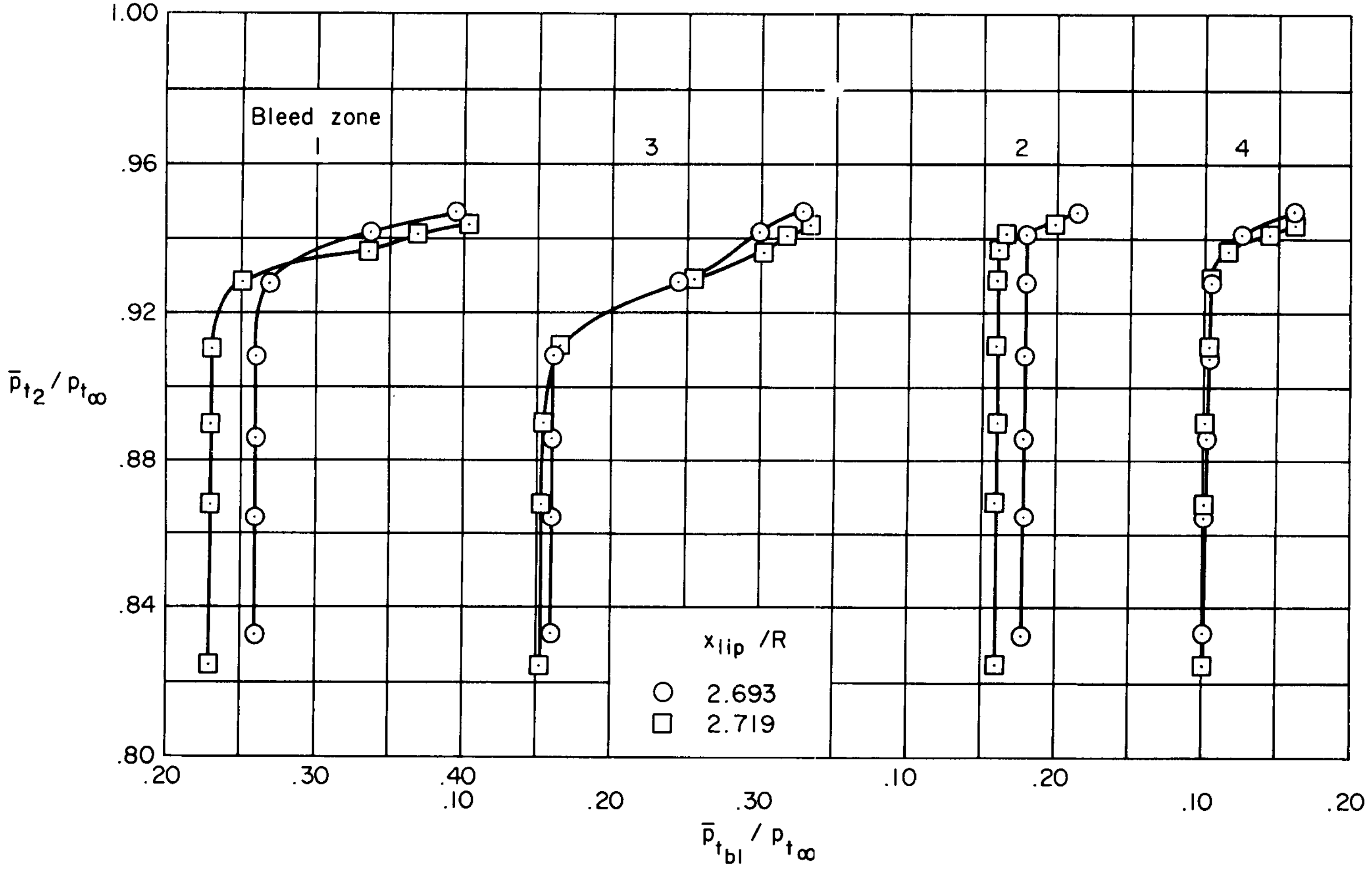

(c) $M_\infty = 2.41$, bleed configuration B'-1, vortex generator configuration CC.

Figure 53. – Continued.

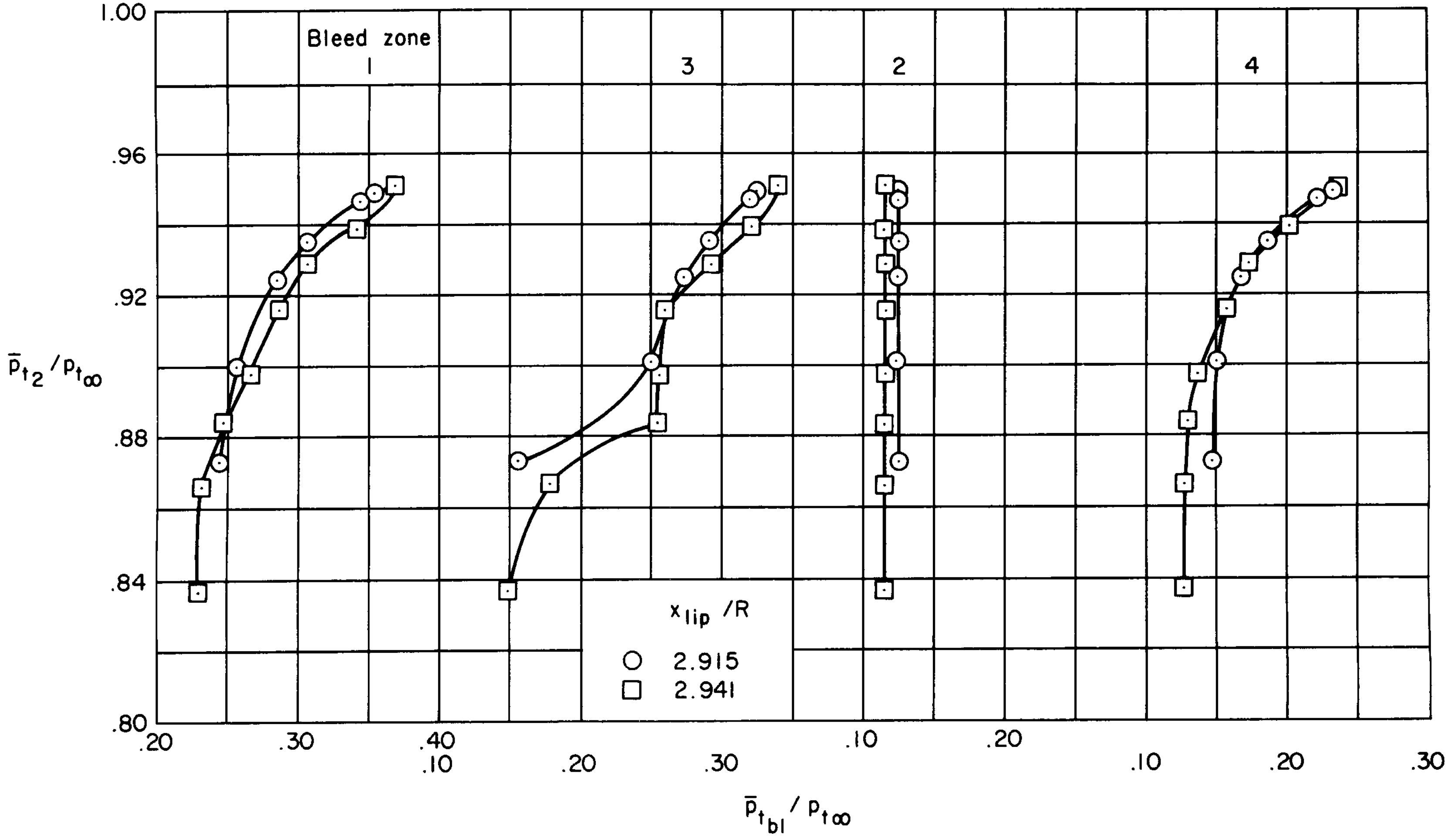

(d) $M_\infty = 2.30$, bleed configuration B′-2, vortex generator configuration 00.

Figure 53. – Continued.

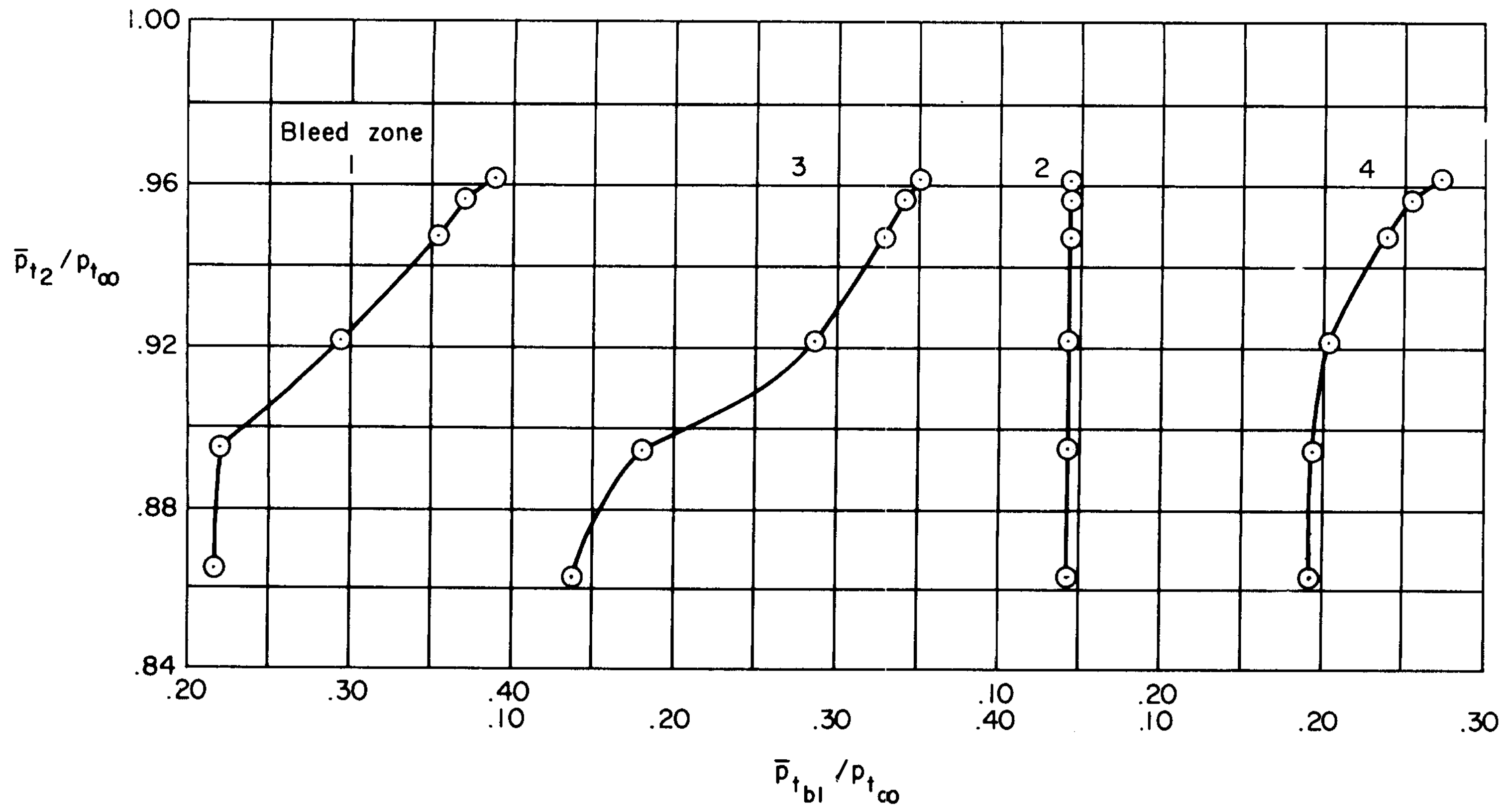

(e) $M_\infty = 2.10$, bleed configuration B′-3, vortex generator configuration 00, $x_{lip}/R = 3.229$.

Figure 53. – Continued.

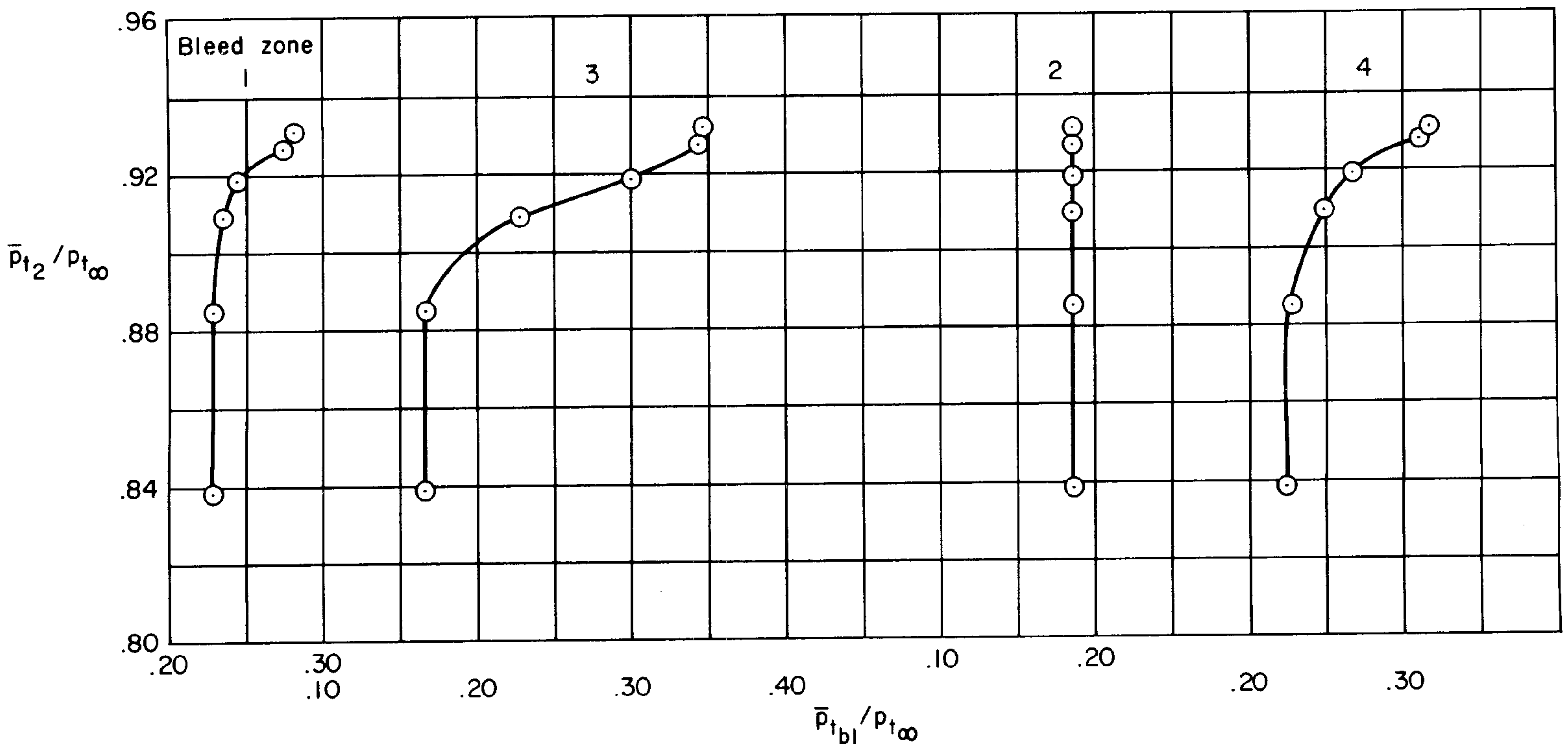

(f) $M_\infty = 1.90$, bleed configuration B′-4, vortex generator configuration 00, $x_{lip}/R = 3.478$.

Figure 53. – Continued.

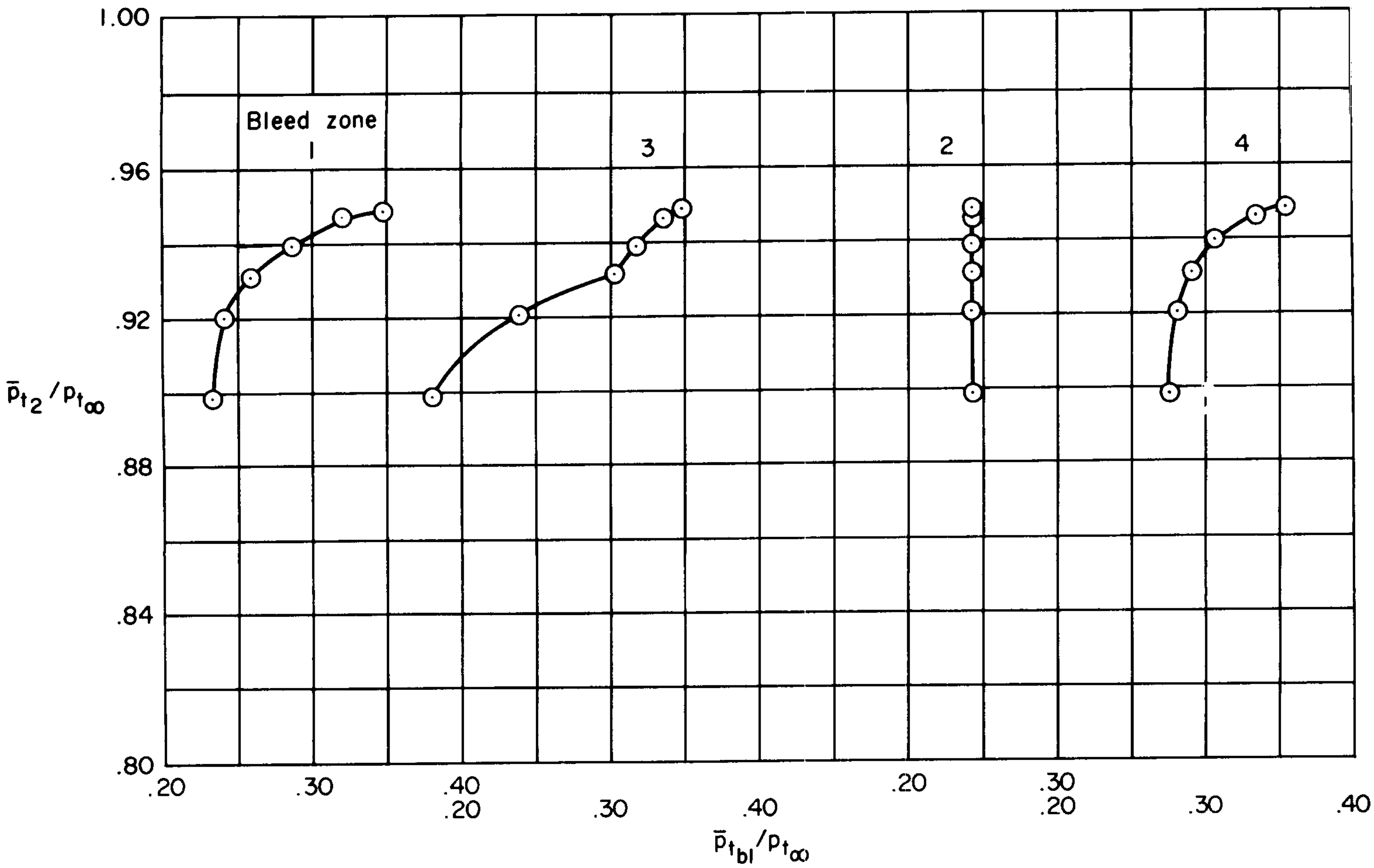

(g) $M_\infty = 1.75$, bleed configuration B′-4, vortex generator configuration OO, $x_{lip}/R = 3.583$.

Figure 53. – Concluded.

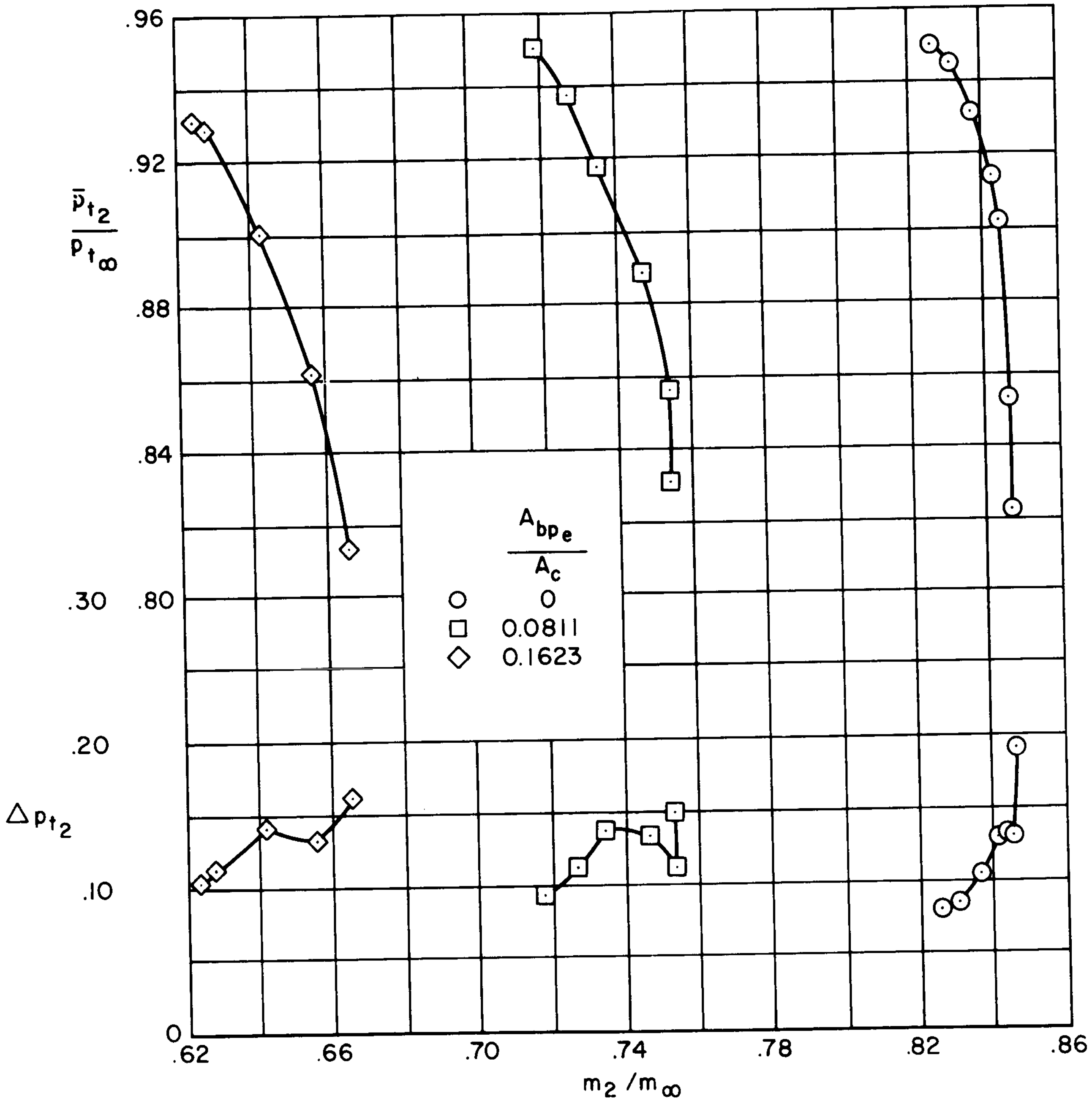

(a) $M_\infty = 2.30$, bleed configuration B'-3, $x_{lip}/R = 2.955$.

Figure 54. – Supercritical performance with bypass; $\alpha = 0°$, $\theta_2 = 0°$, vortex generator configuration 00.

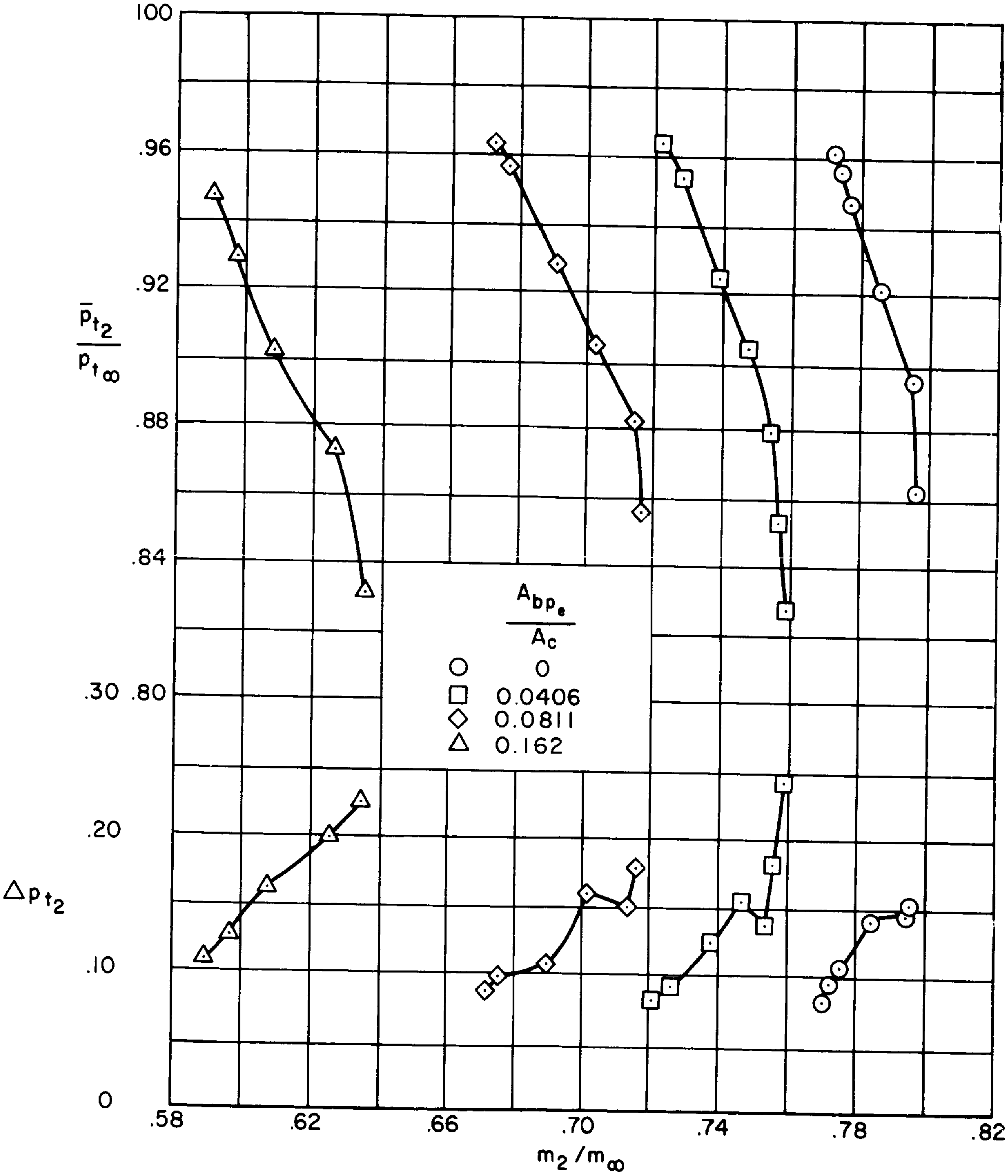

(b) $M_\infty = 2.10$, bleed configuration B′-3, $x_{lip}/R = 3.229$.

Figure 54. – Continued.

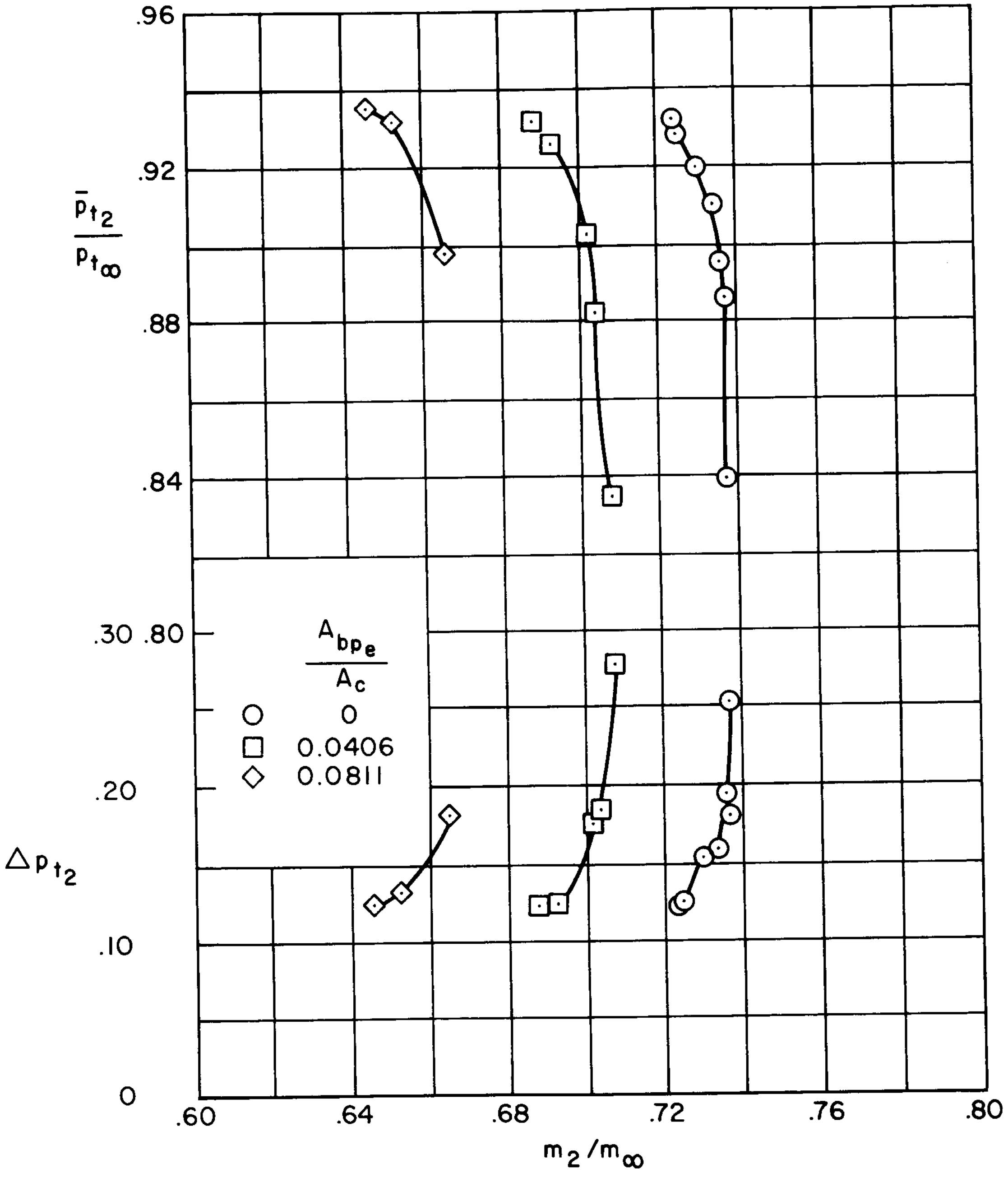

(c) $M_\infty = 1.90$, bleed configuration B'-4, $x_{lip}/R = 3.478$.

Figure 54. – Continued.

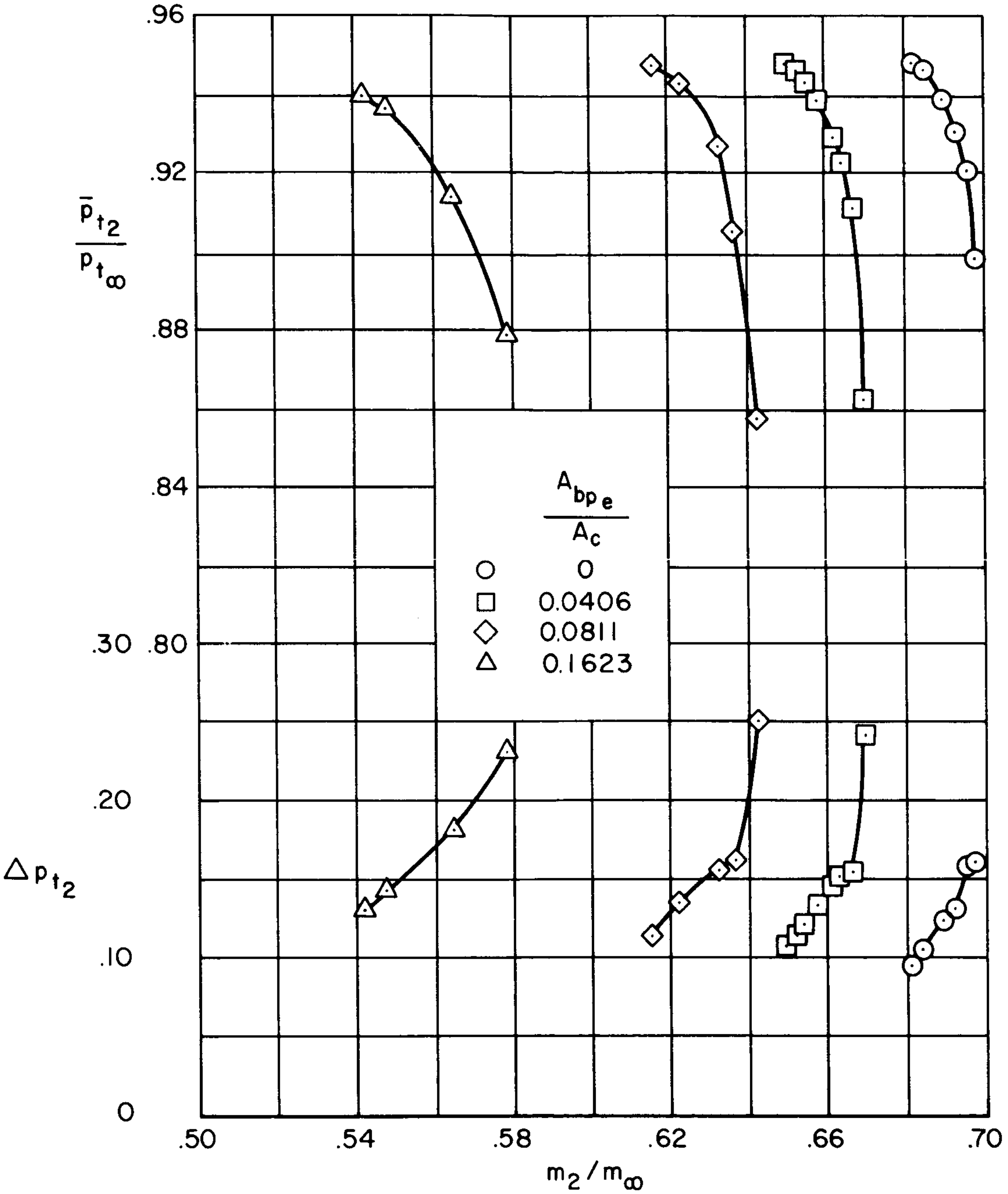

(d) $M_\infty = 1.75$, bleed configuration B'-4, $x_{lip}/R = 3.583$.

Figure 54. – Concluded.

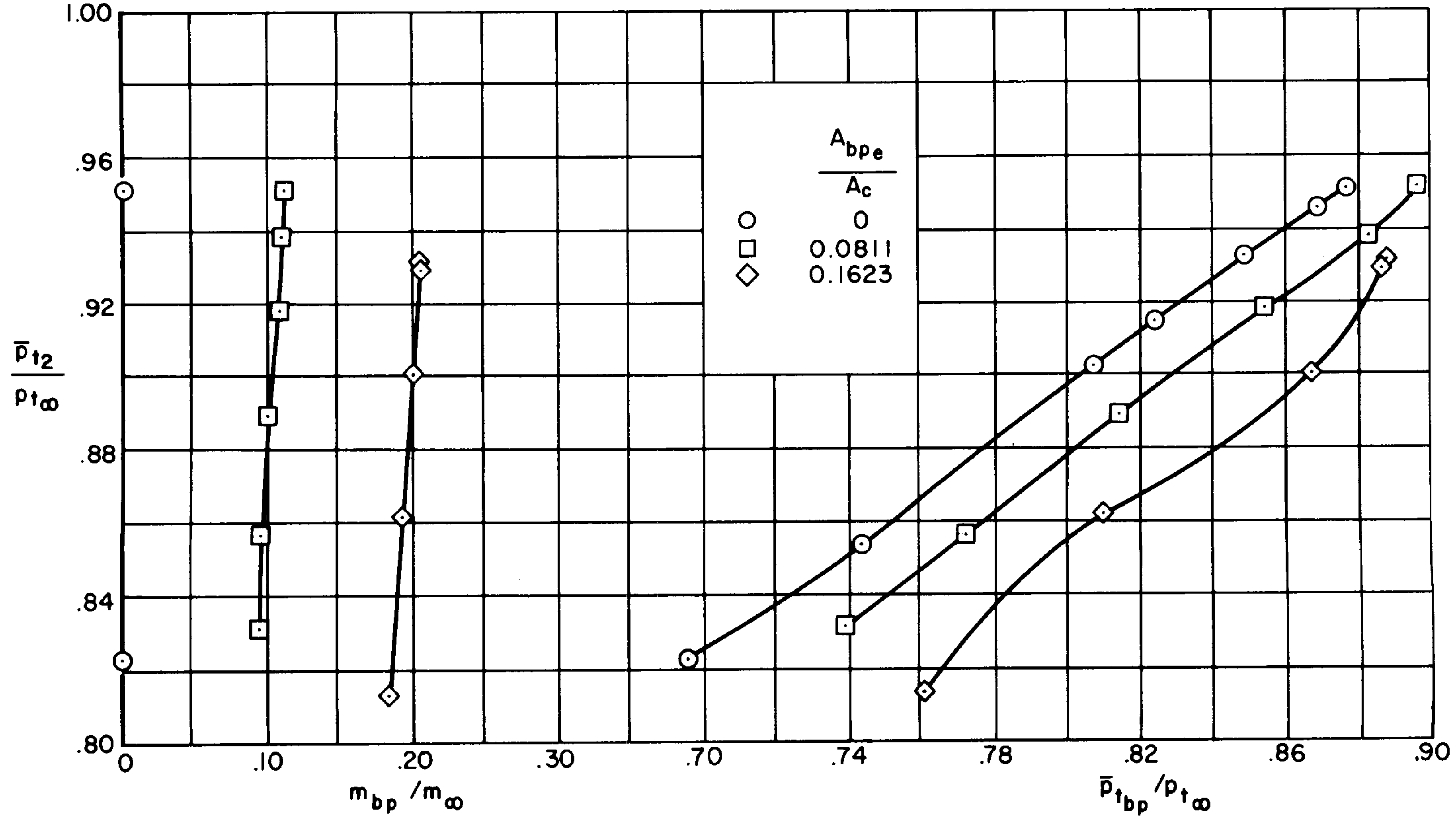

(a) $M_\infty = 2.30$, bleed configuration B′-3, $x_{lip}/R = 2.955$.

Figure 55. – Bypass mass flow and plenum chamber pressure recovery; $\alpha = 0°$, $\theta_2 = 0°$, vortex generator configuration 00.

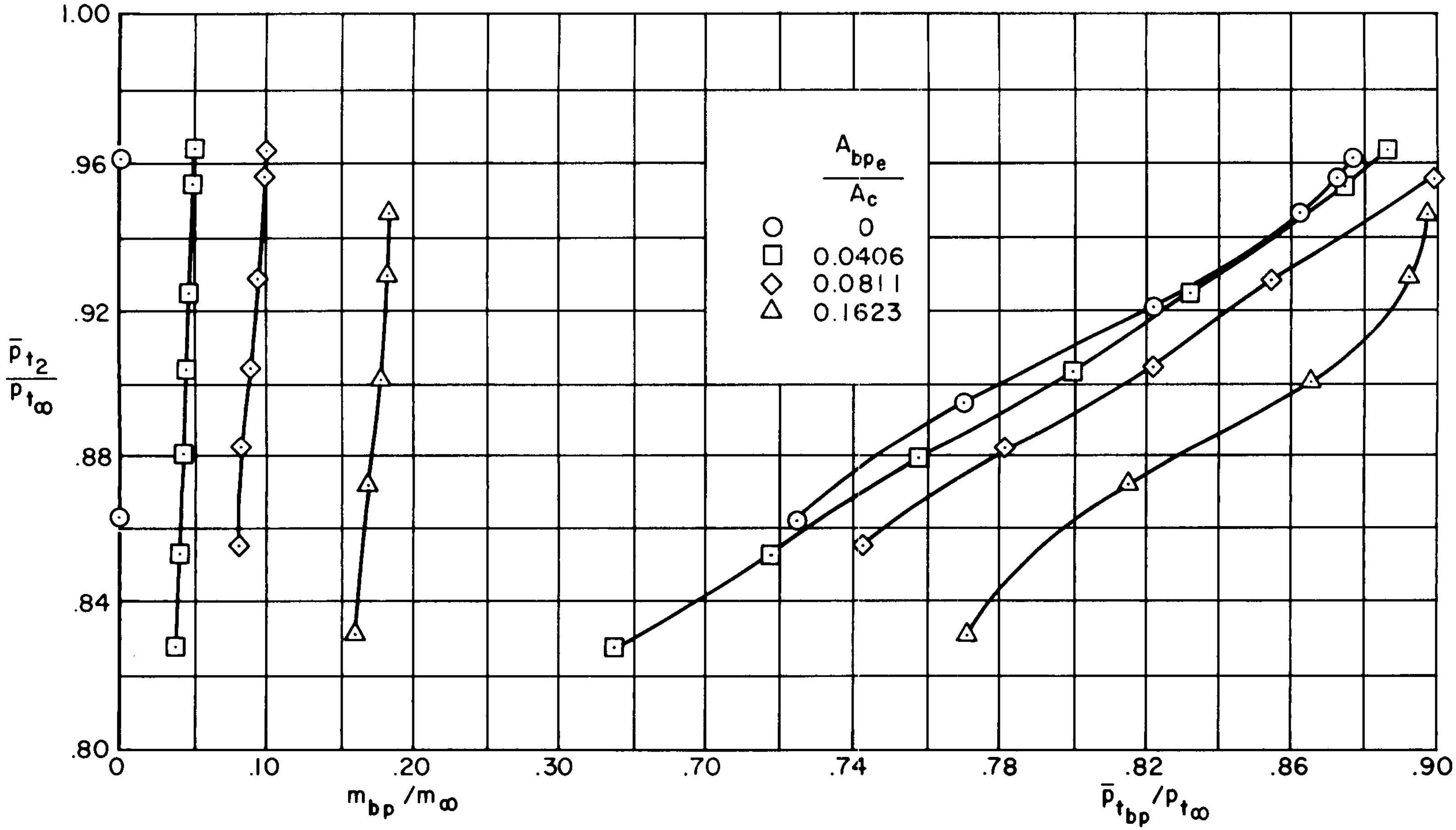

(b) $M_\infty = 2.10$, bleed configuration B′-3, $x_{lip}/R = 3.229$.

Figure 55. – Continued.

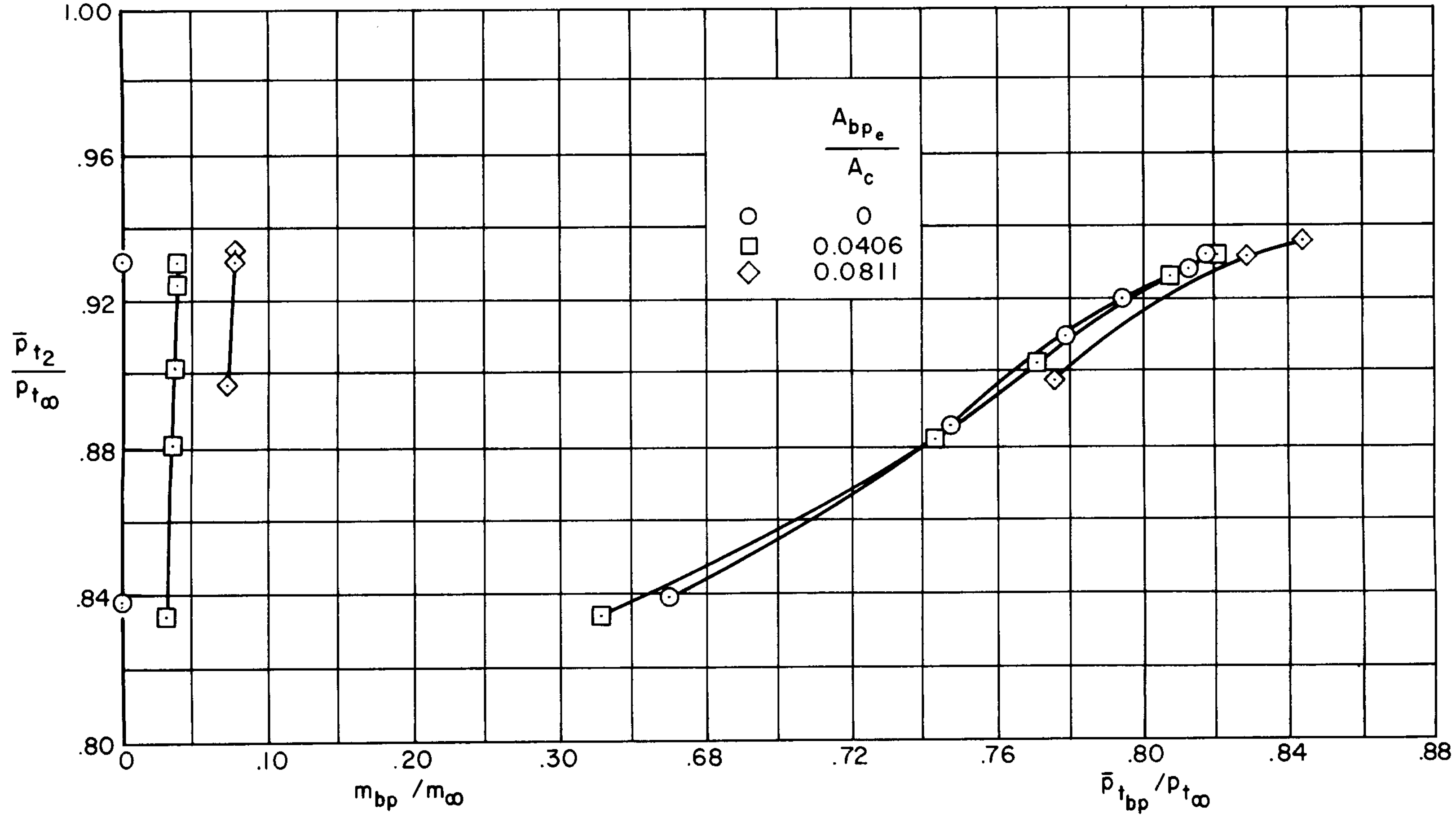

(c) $M_\infty = 1.90$, bleed configuration B′-4, $x_{lip}/R = 3.478$.

Figure 55. – Continued.

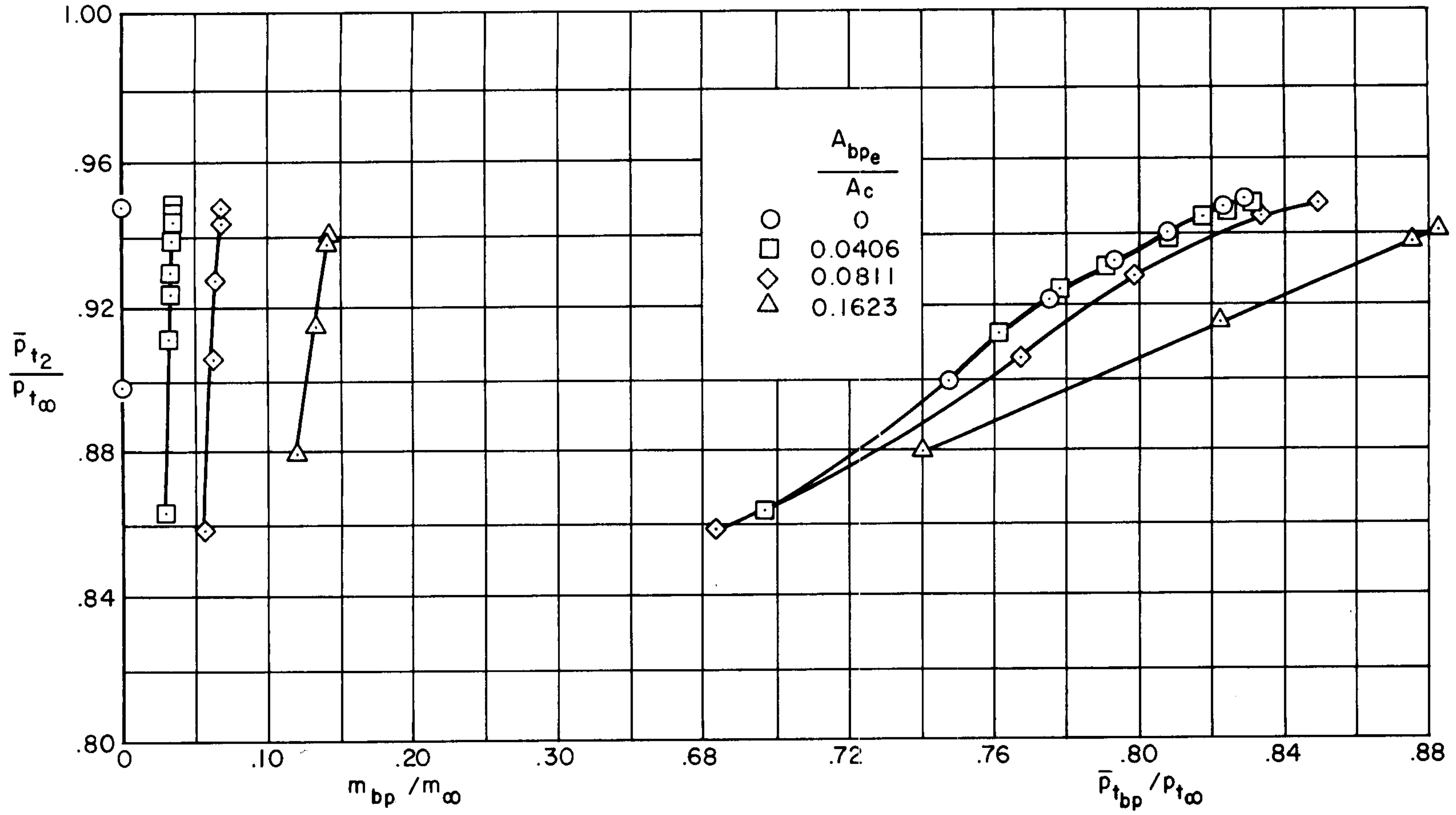

(d) $M_\infty = 1.75$, bleed configuration B′4, $x_{lip}/R = 3.583$.

Figure 55. – Concluded.

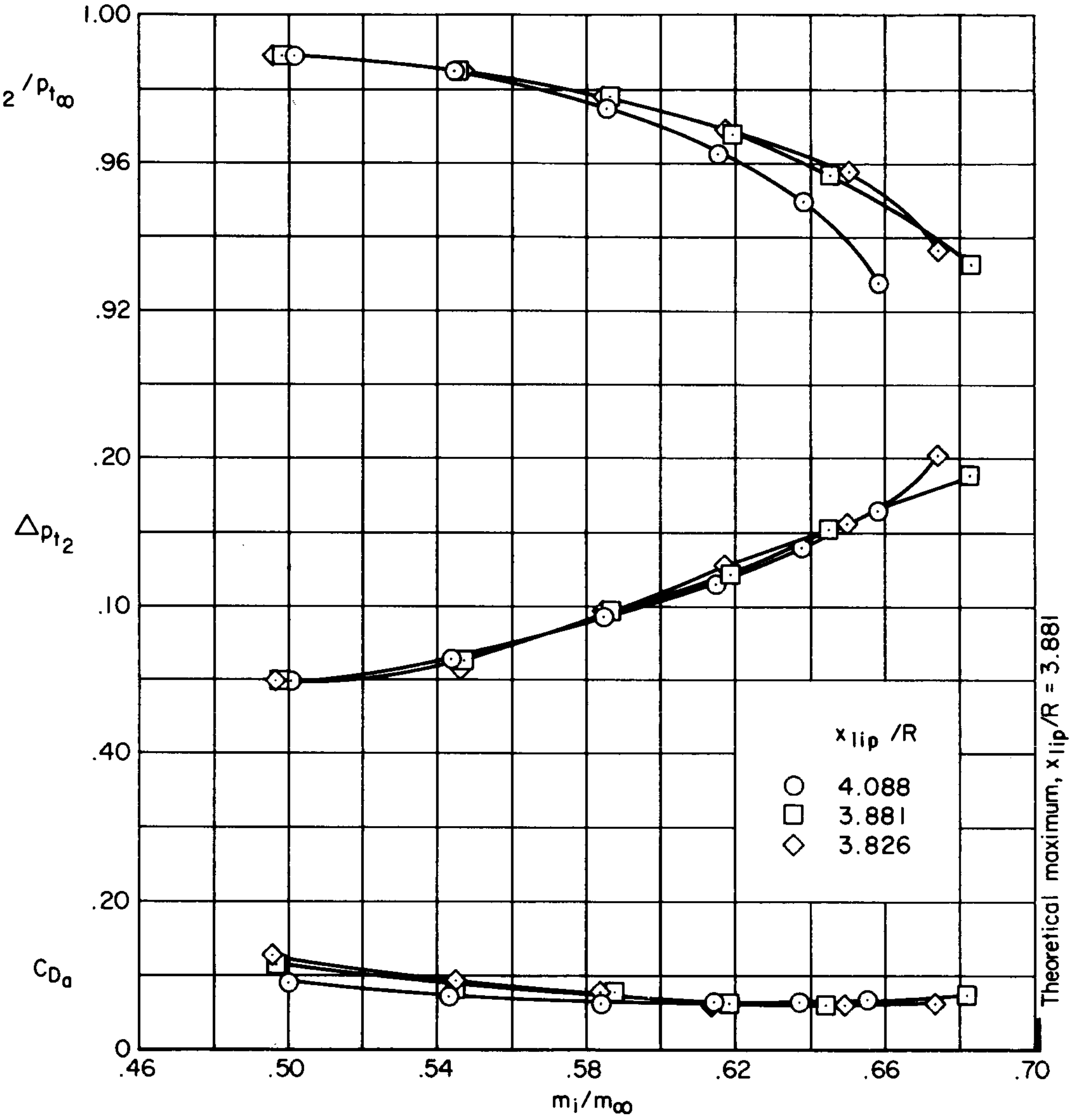

(a) $M_\infty = 0.6$

Figure 56. – Transonic performance; $\alpha = 0°$, $M_{bl}/M_\infty = 0$, $M_{bp}/M_\infty = 0$, $\theta_2 = 0°$, vortex generator configuration 00.

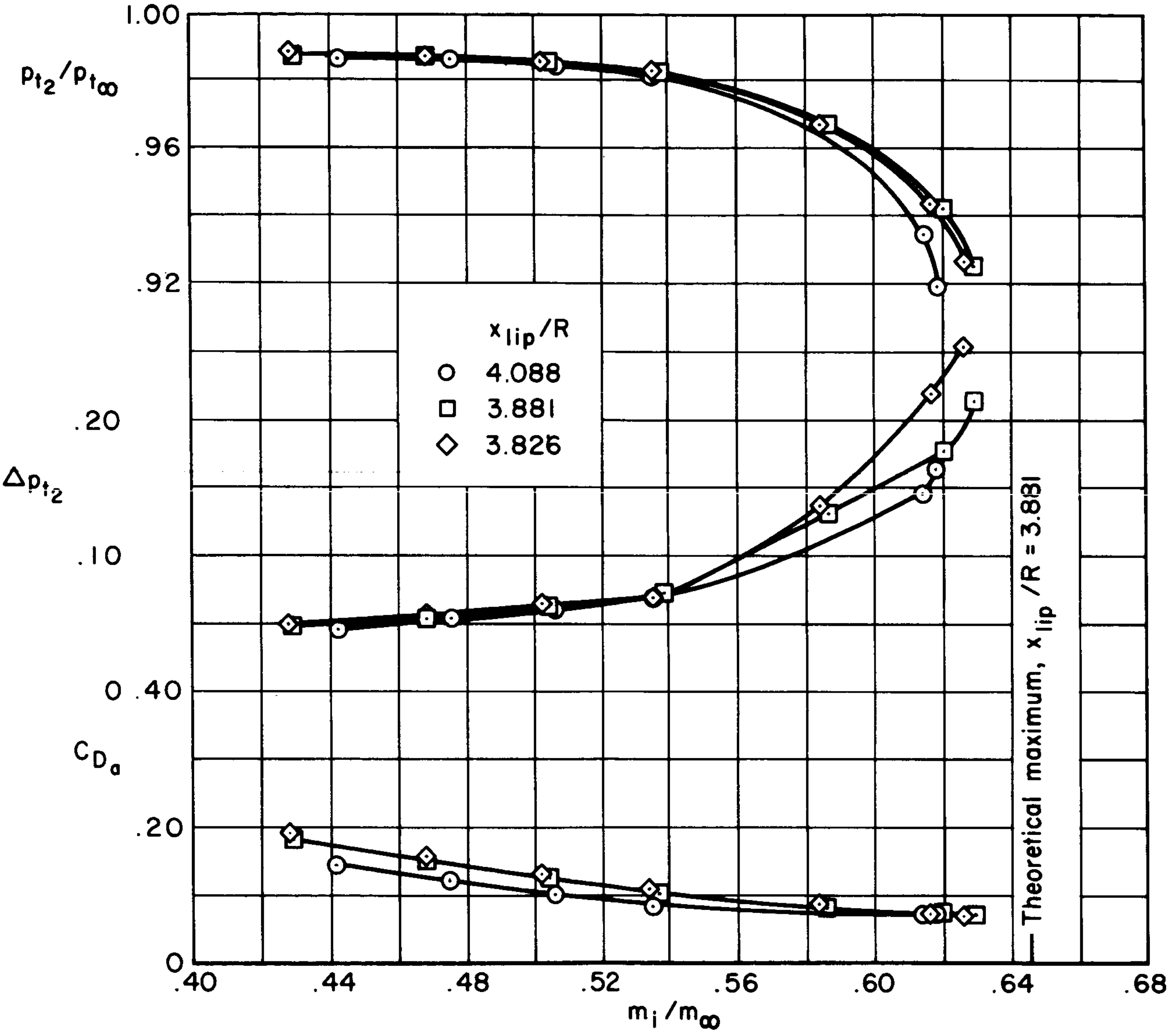

(b) $M_\infty = 0.7$

Figure 56. – Continued.

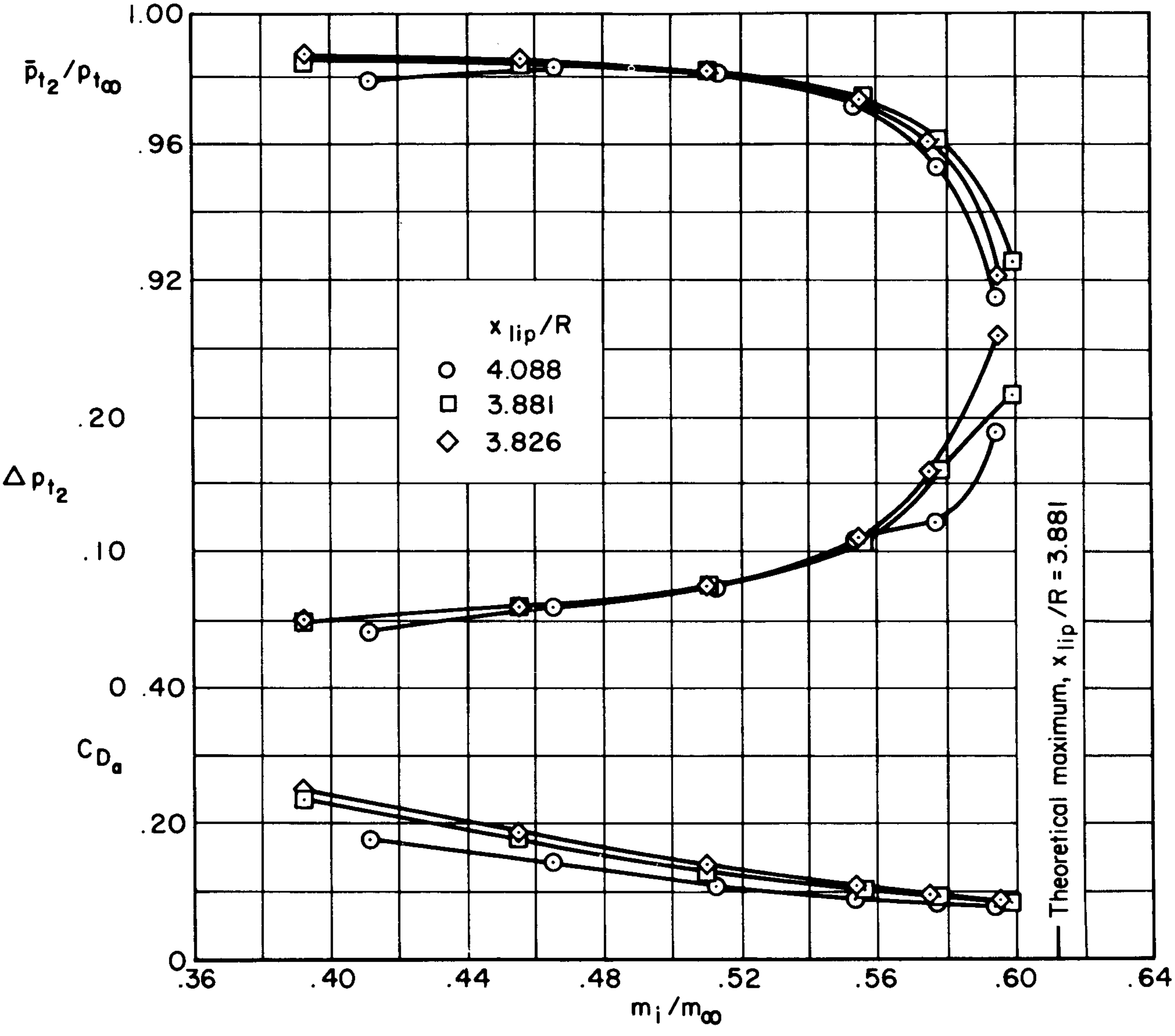

(c) $M_\infty = 0.8$

Figure 56. – Continued.

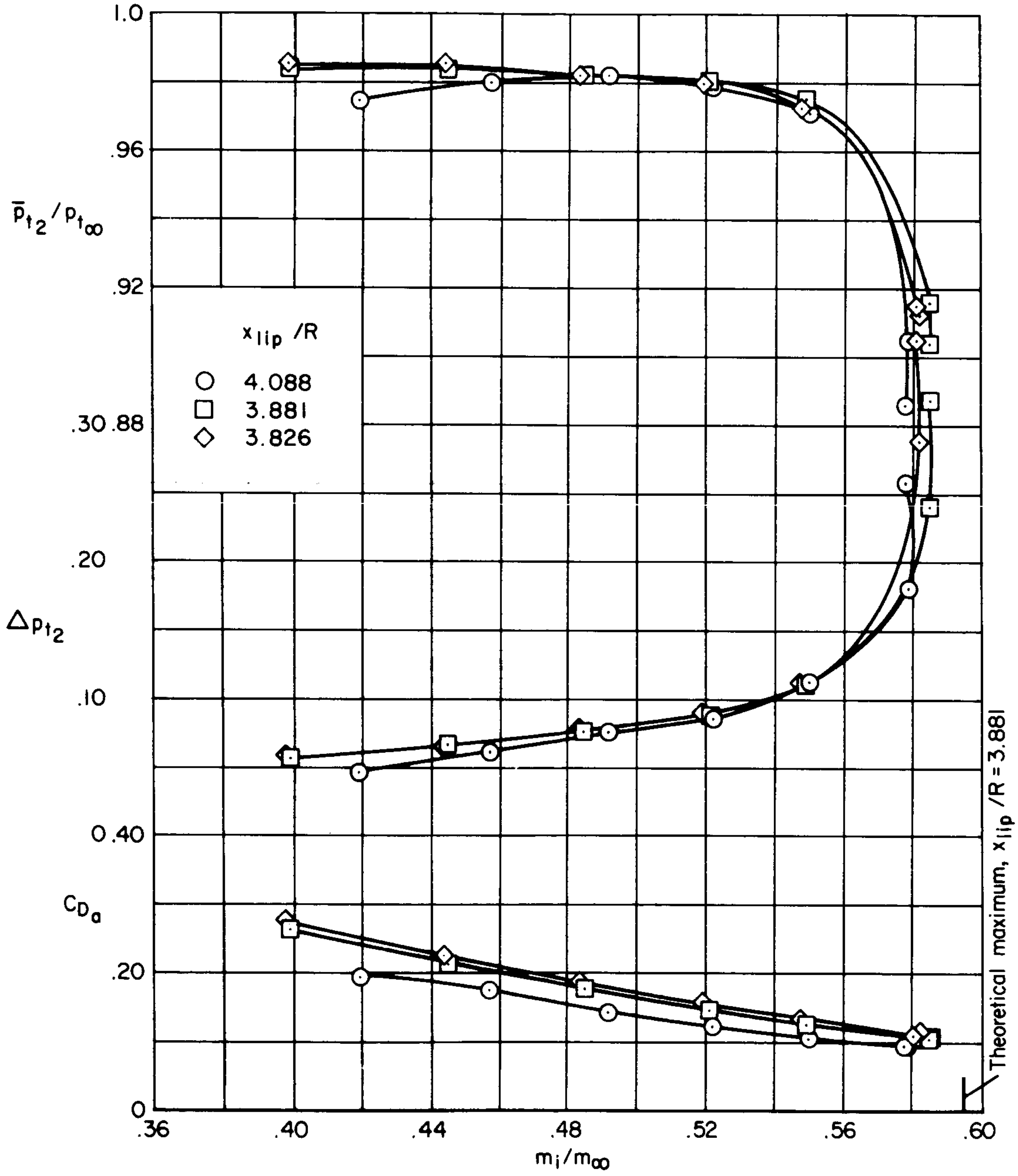

(d) $M_\infty = 0.9$

Figure 56. – Continued.

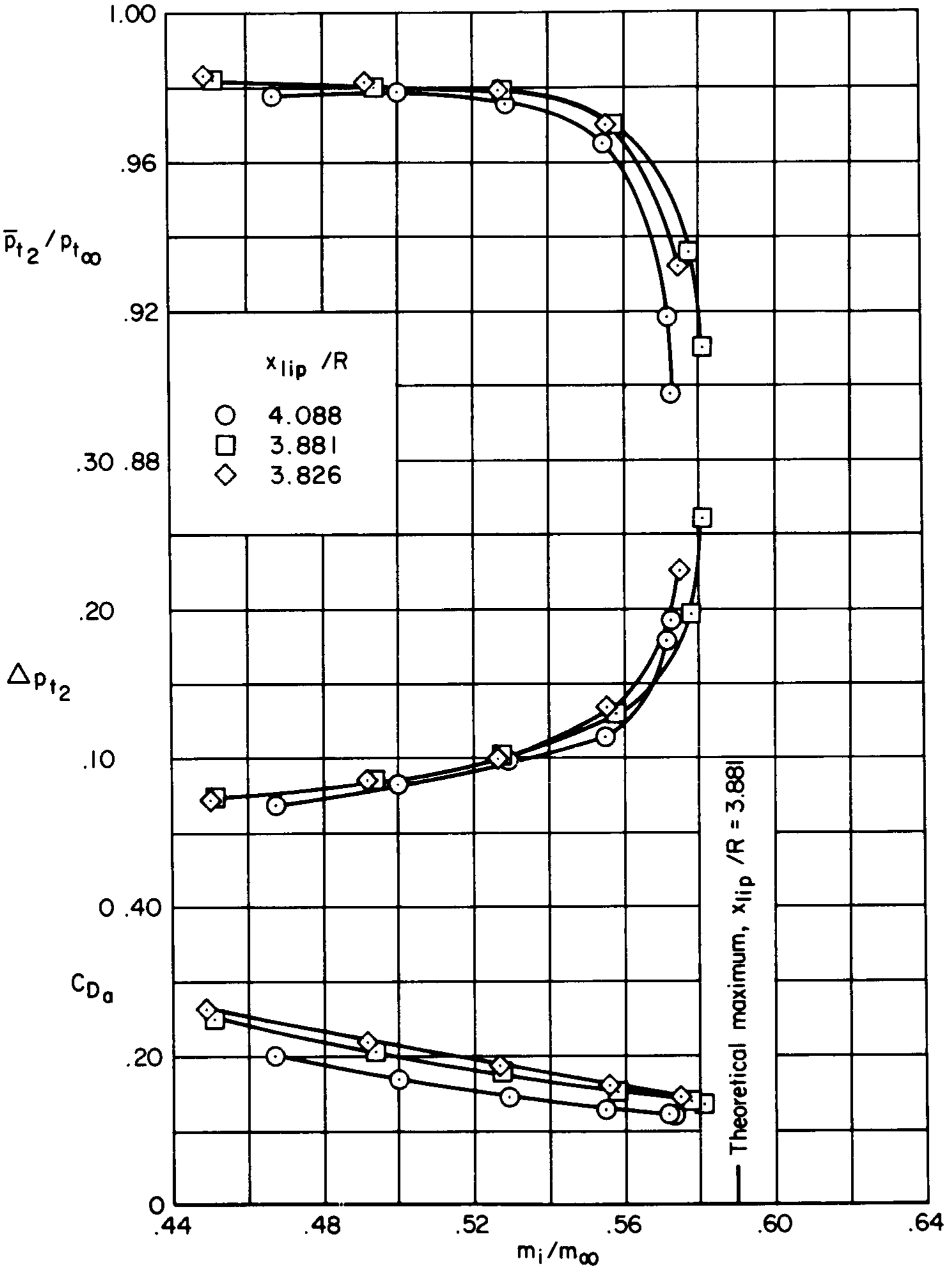

(e) $M_\infty = 1.0$

Figure 56. – Continued.

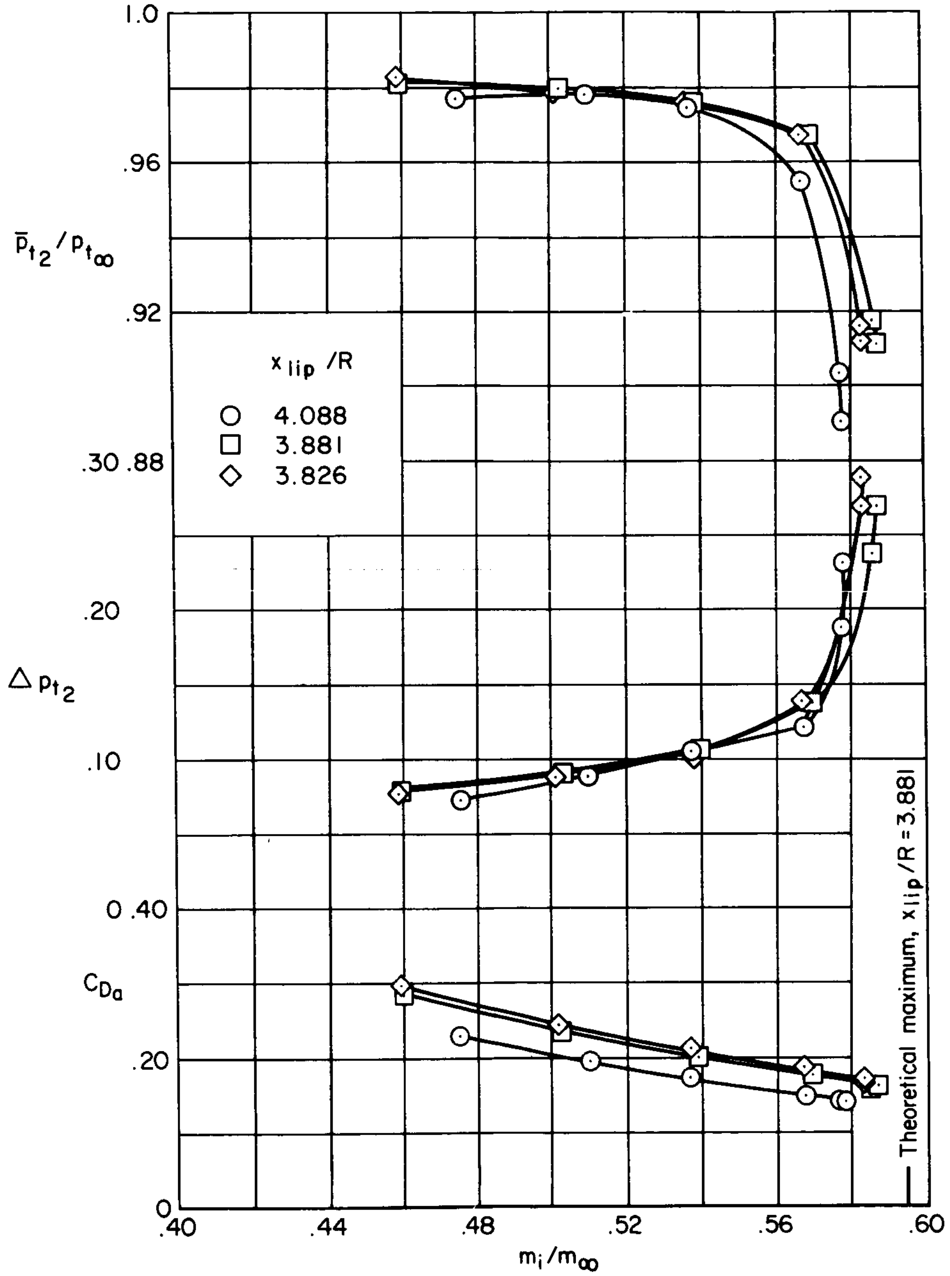

(f) $M_\infty = 1.1$

Figure 56. – Concluded.

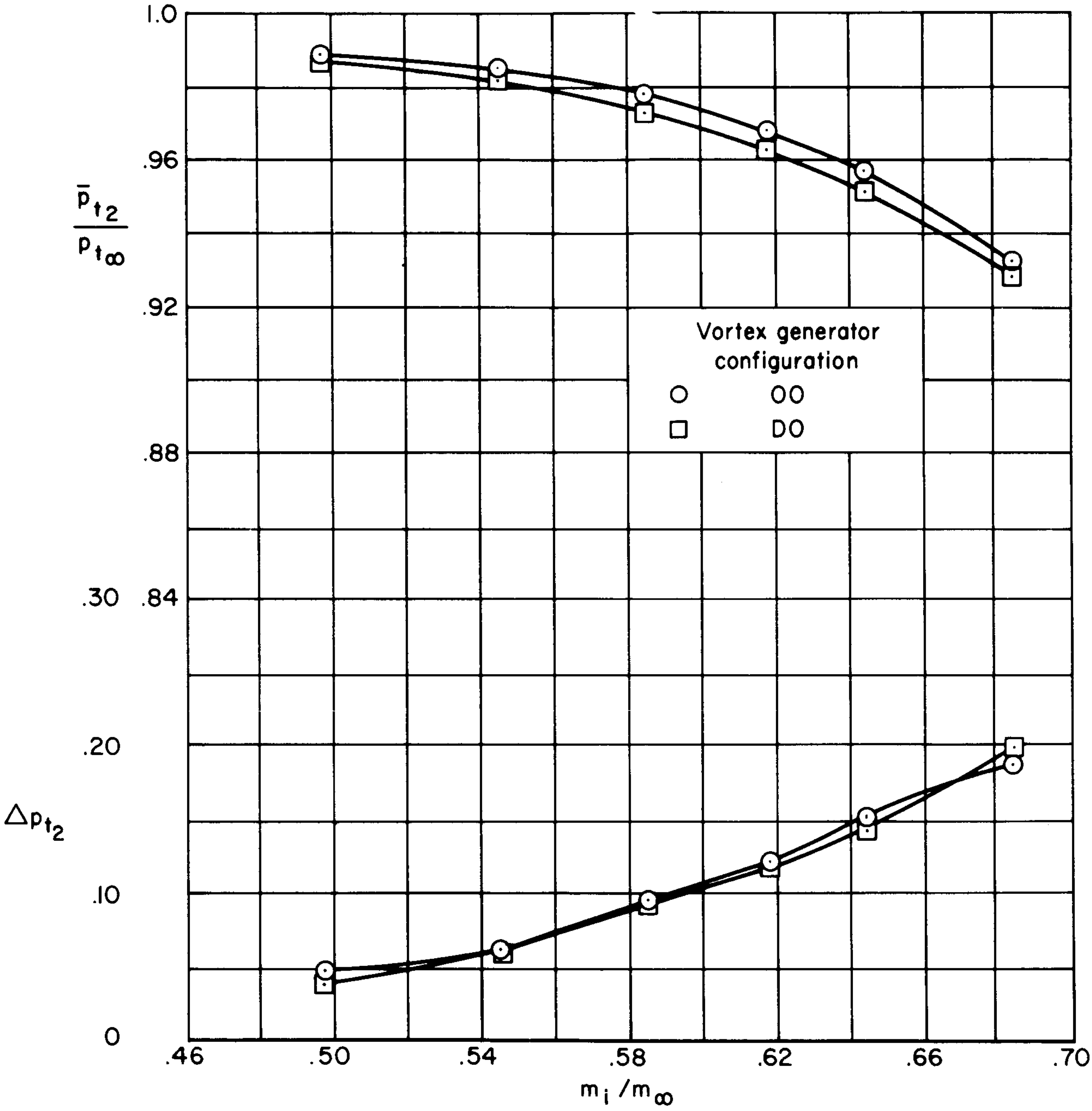

(a) $M_\infty = 0.6$

Figure 57. – Transonic performance with various vortex generator configurations; $\alpha = 0°$, $m_{bl}/m_\infty = 0$, $m_{bp}/m_\infty = 0$, $\theta_2 = 0°$, $x_{lip}/R = 3.881$.

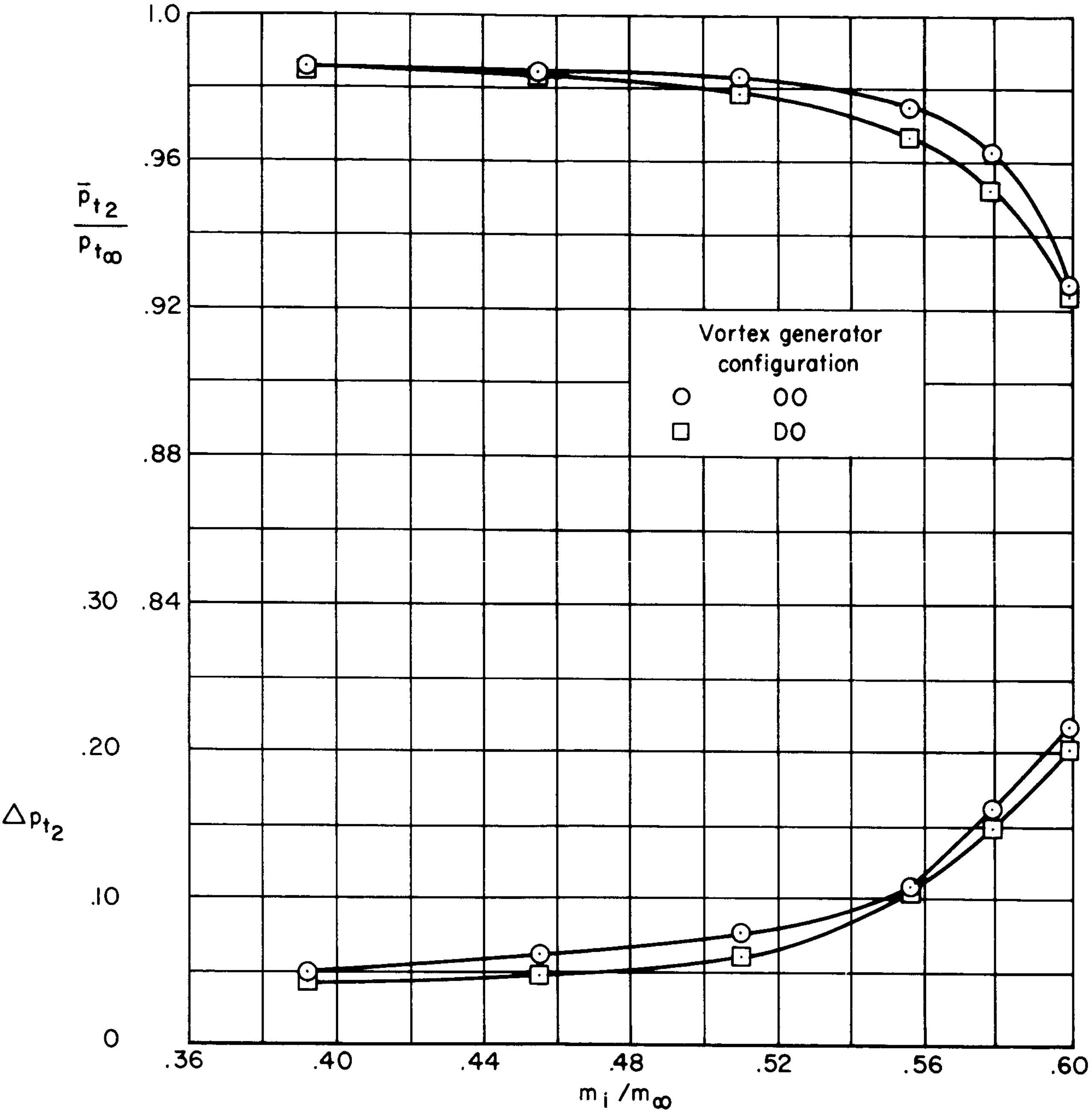

(b) $M_\infty = 0.8$

Figure 57. – Continued.

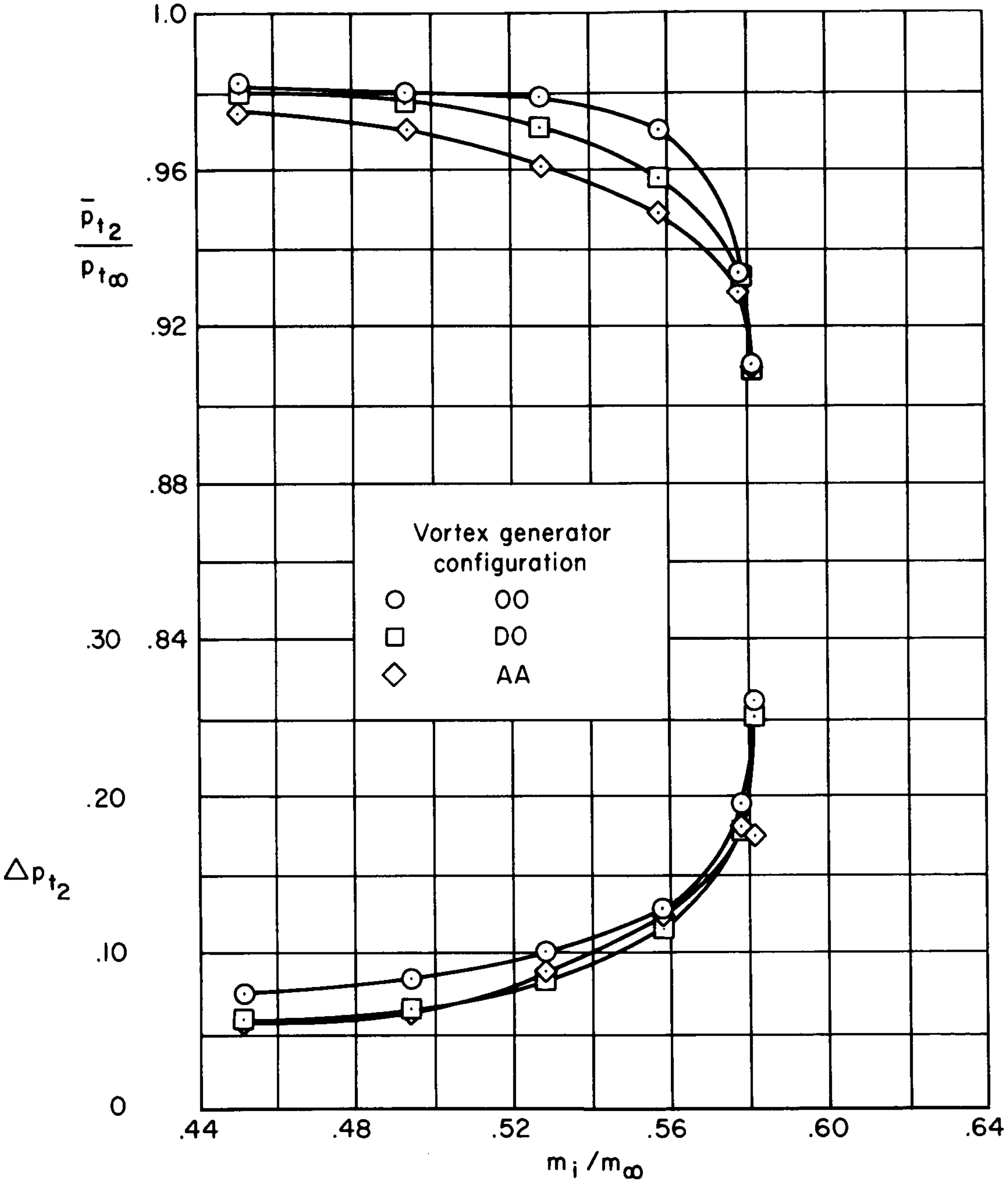

(c) $M_\infty = 1.0$

Figure 57. – Continued.

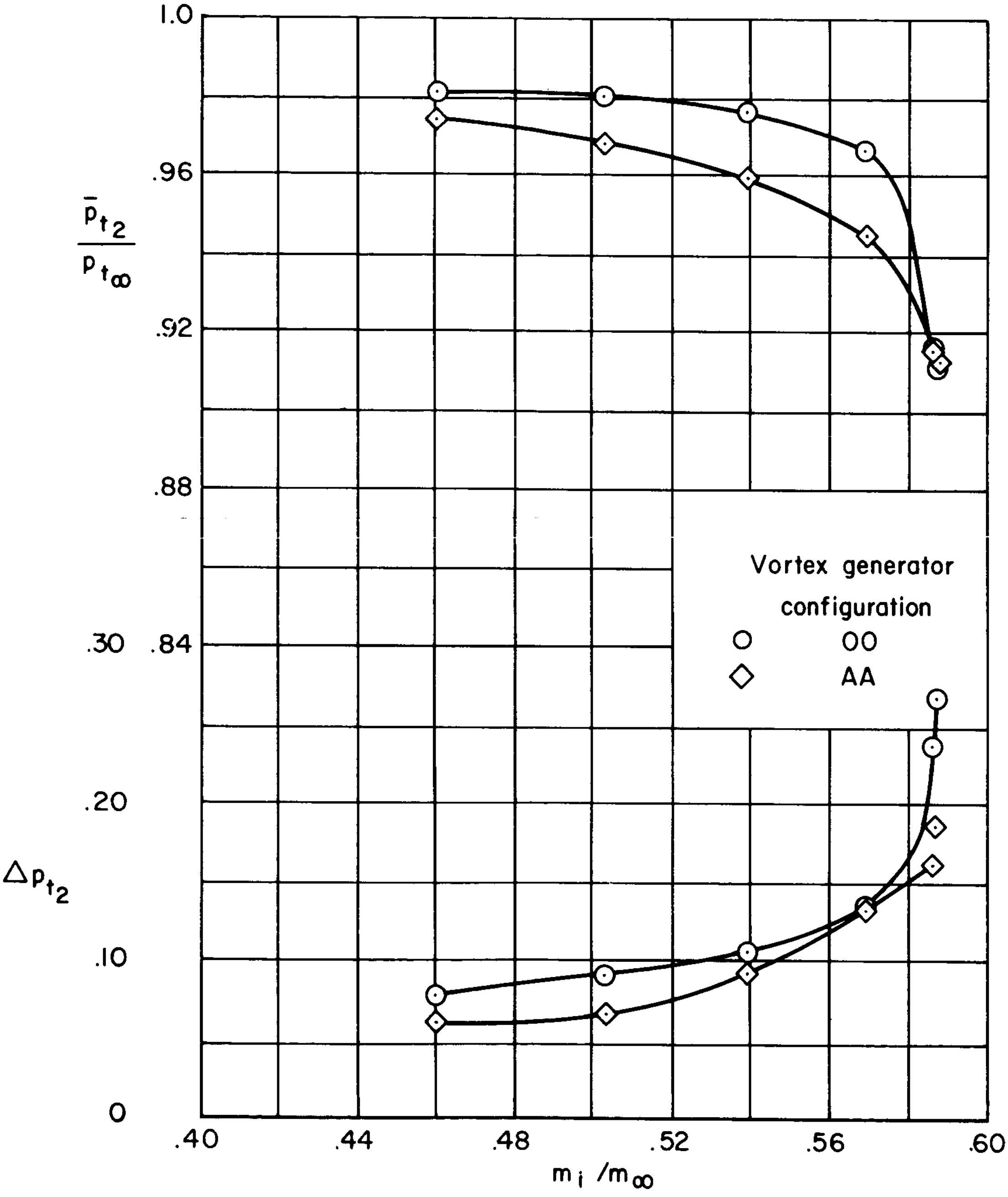

(d) $M_\infty = 1.1$

Figure 57. – Concluded.

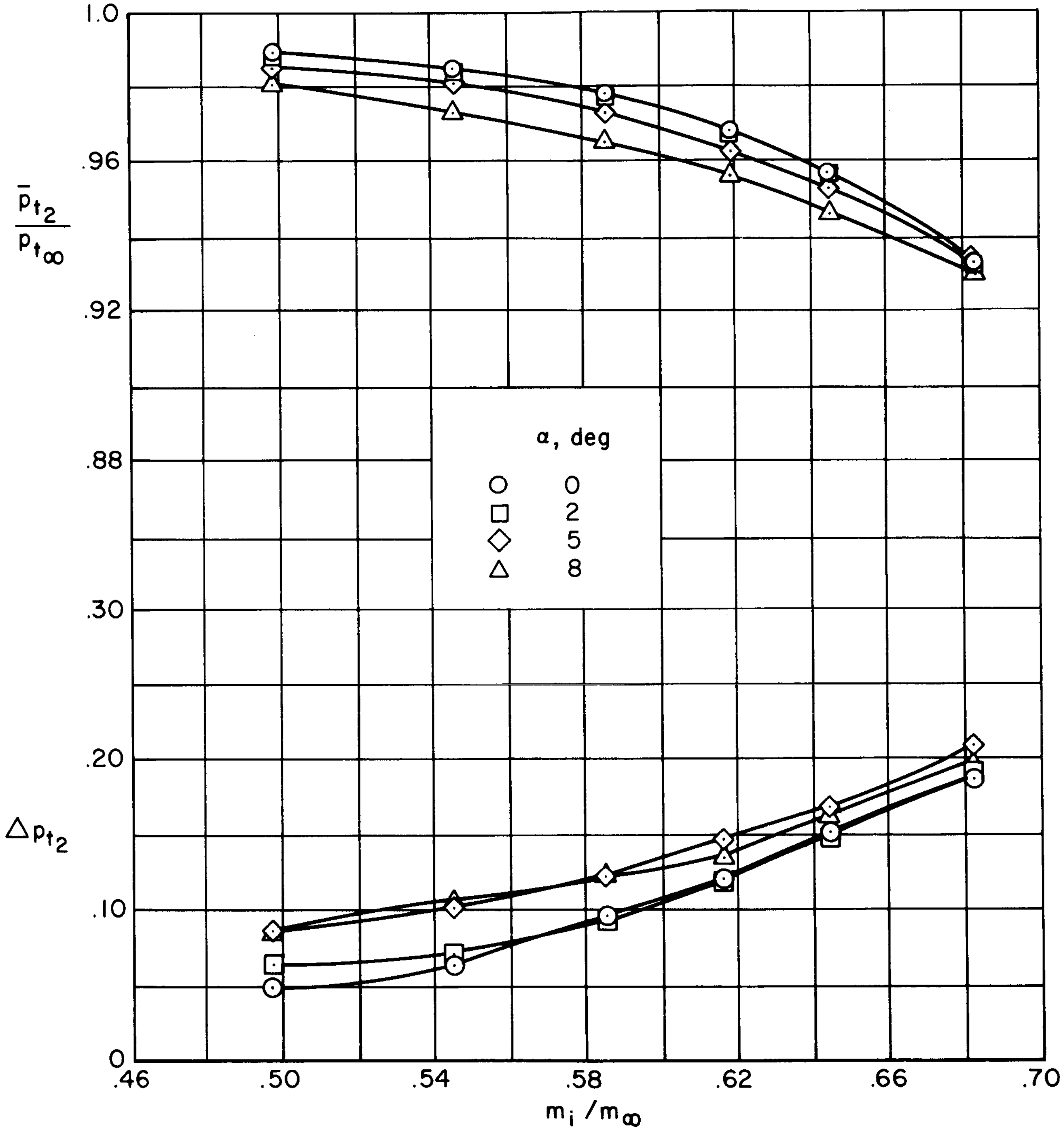

(a) $M_\infty = 0.6$

Figure 58. – Transonic performance at angle of attack, $m_{bl}/m_\infty = 0$, $m_{bp}/m_\infty = 0$, $\theta_2 = 0°$, $x_{lip}/R = 3.881$, vortex generator configuration 00.

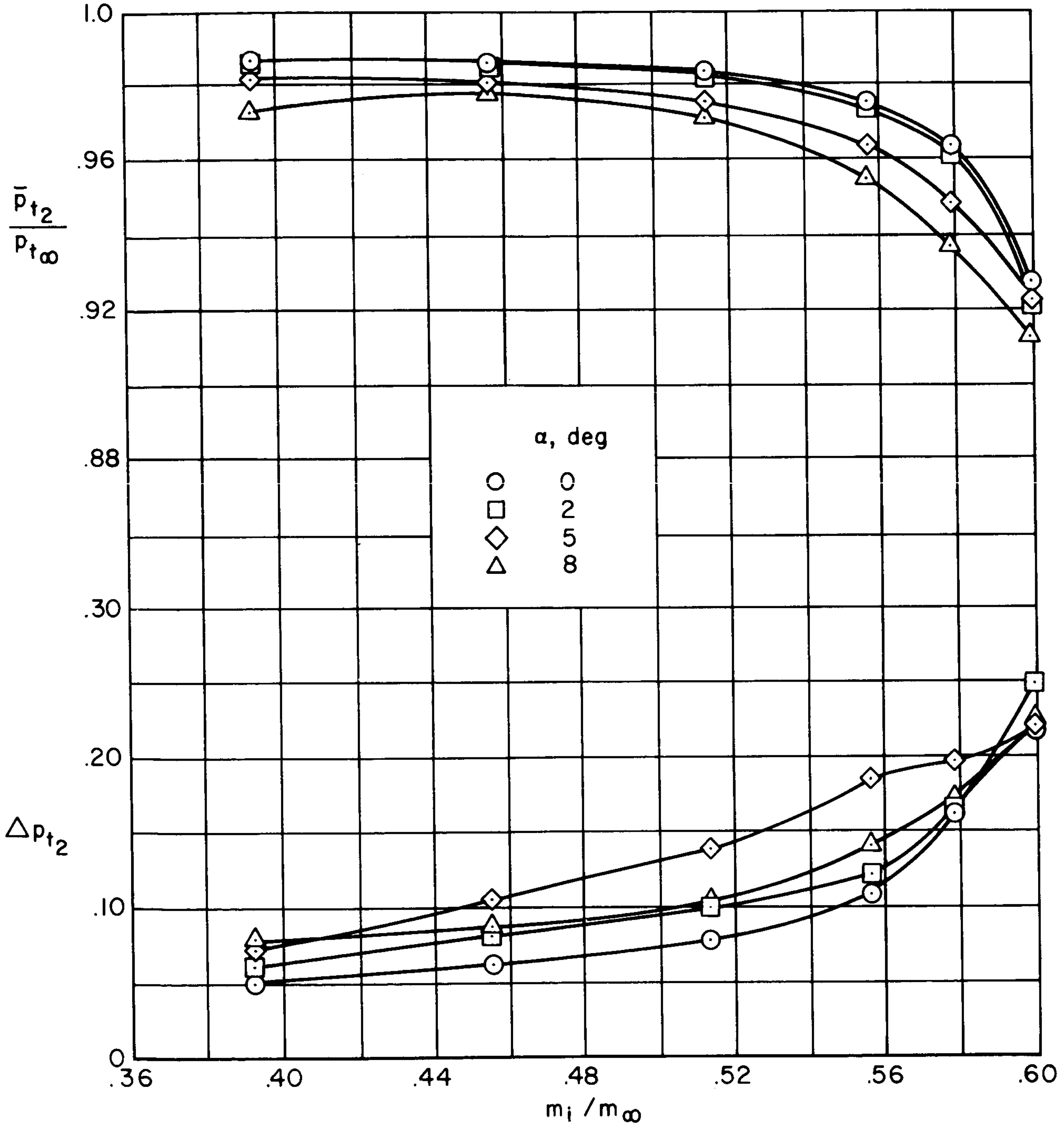

(b) $M_\infty = 0.8$

Figure 58. – Continued.

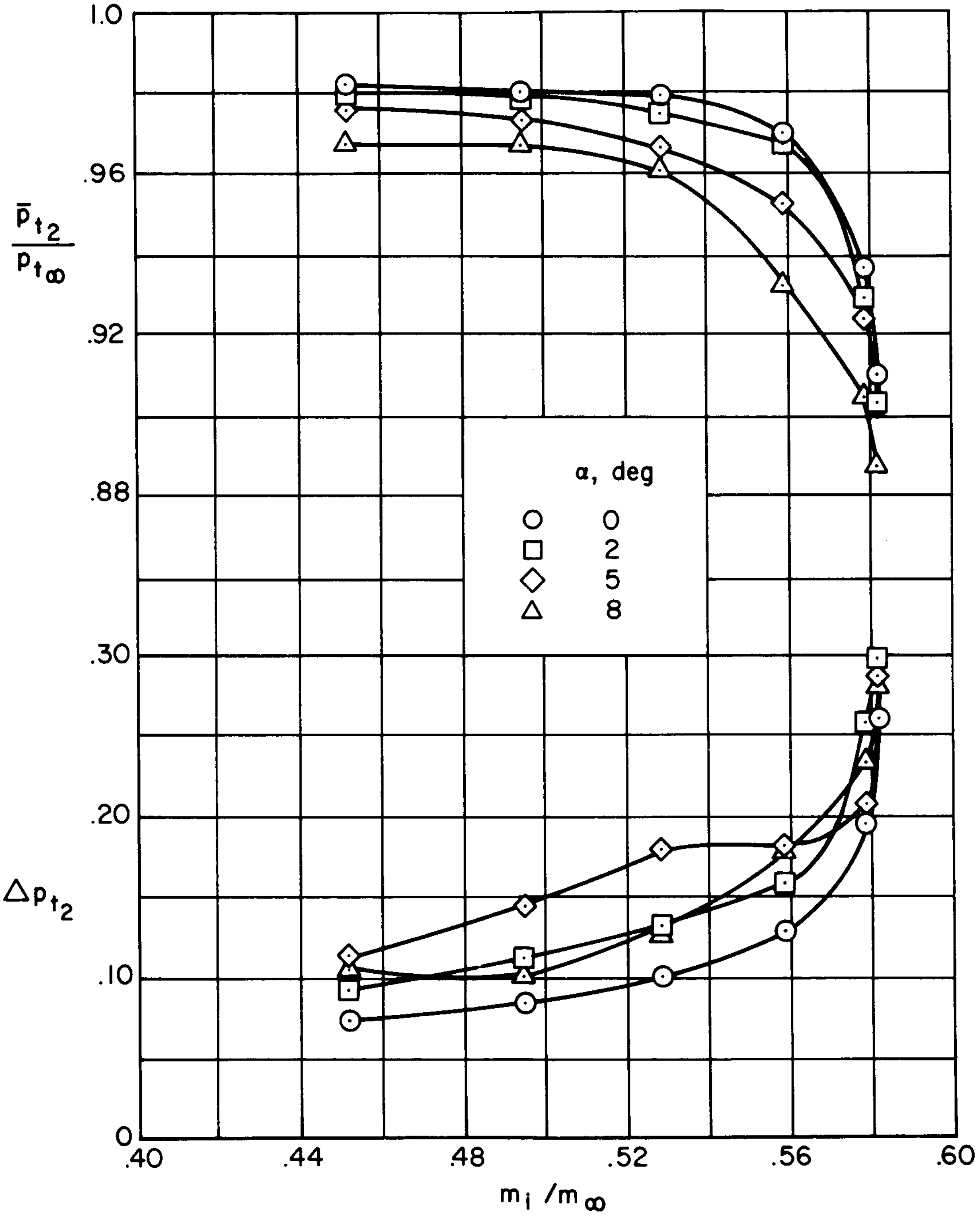

(c) $M_\infty = 1.0$

Figure 58. – Concluded.

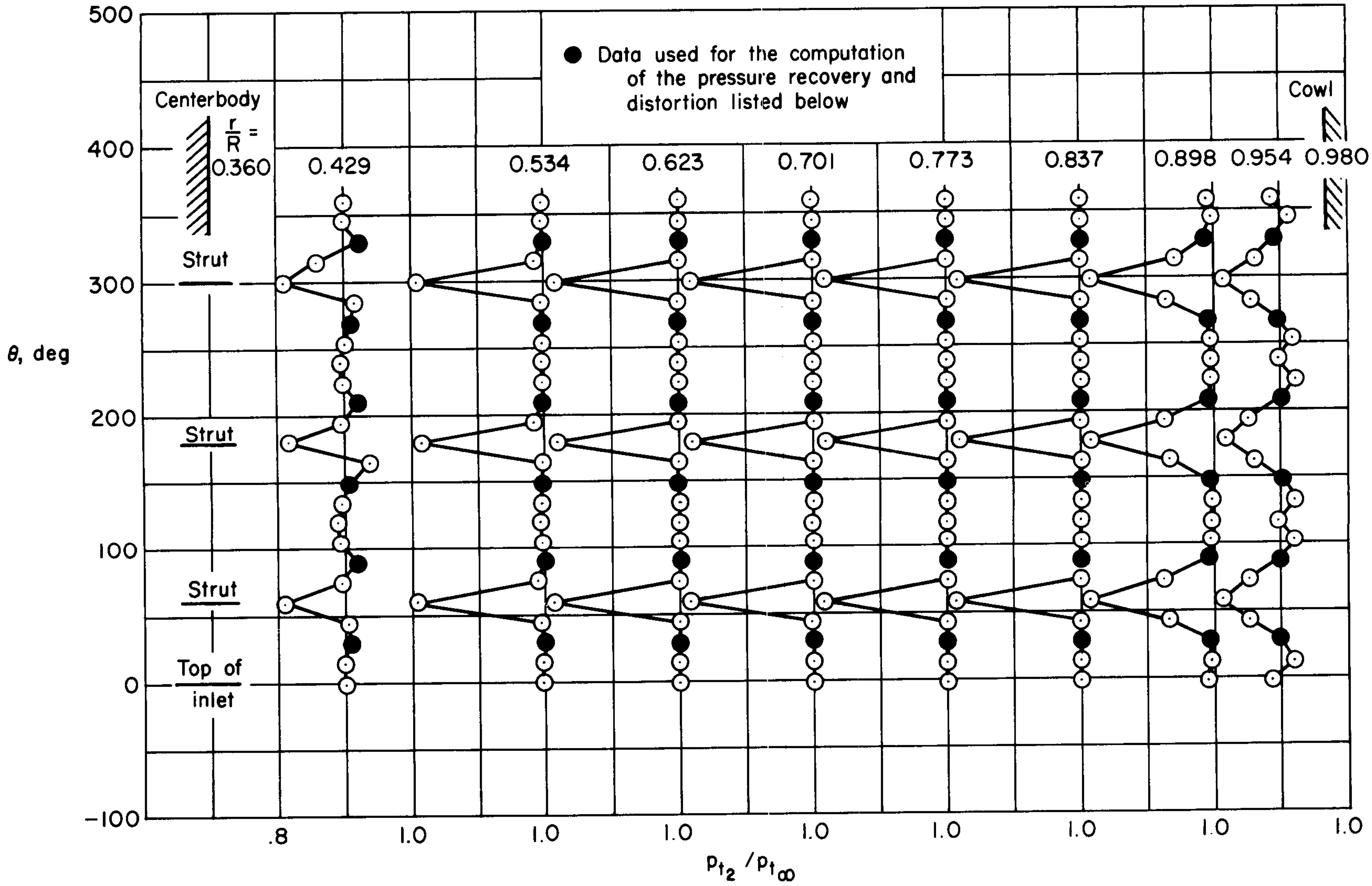

(a) $\alpha = 0°$, $\bar{p}_{t_2}/p_{t_\infty} = 0.975$, $\Delta p_{t_2} = 0.113$

Figure 59. – Circumferential total-pressure profiles at angle of attack; $M_\infty = 0.80$, $m_{bl}/m_\infty = 0$, $m_{bp}/m_\infty = 0$, vortex generator configuration 00, $x_{lip}/R = 3.881$, $m_i/m_\infty = 0.556$.

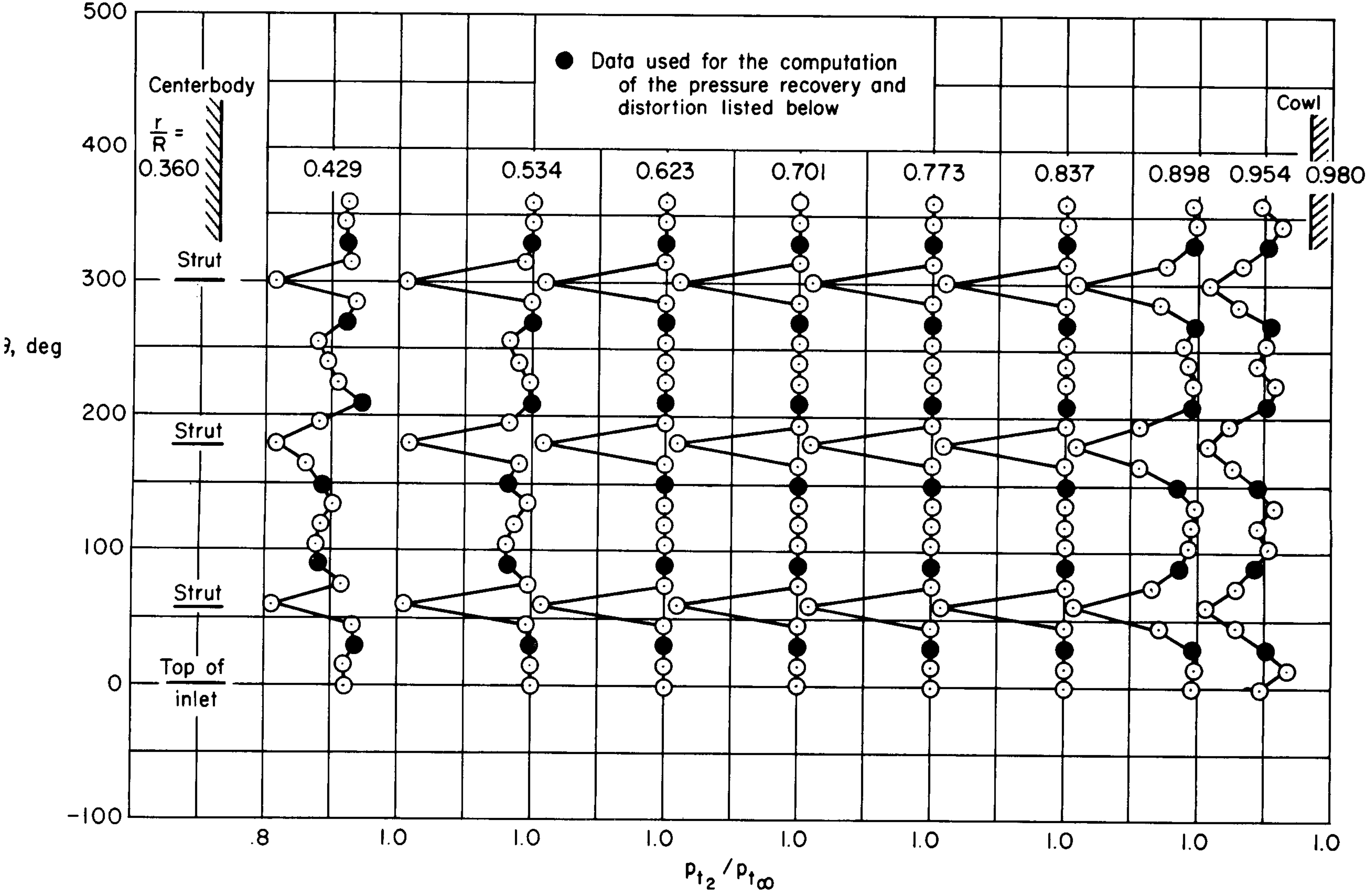

(b) $\alpha = 2.0°$, $\bar{p}_{t_2}/p_{t_\infty} = 0.973$, $\Delta p_{t_2} = 0.123$

Figure 59. – Continued.

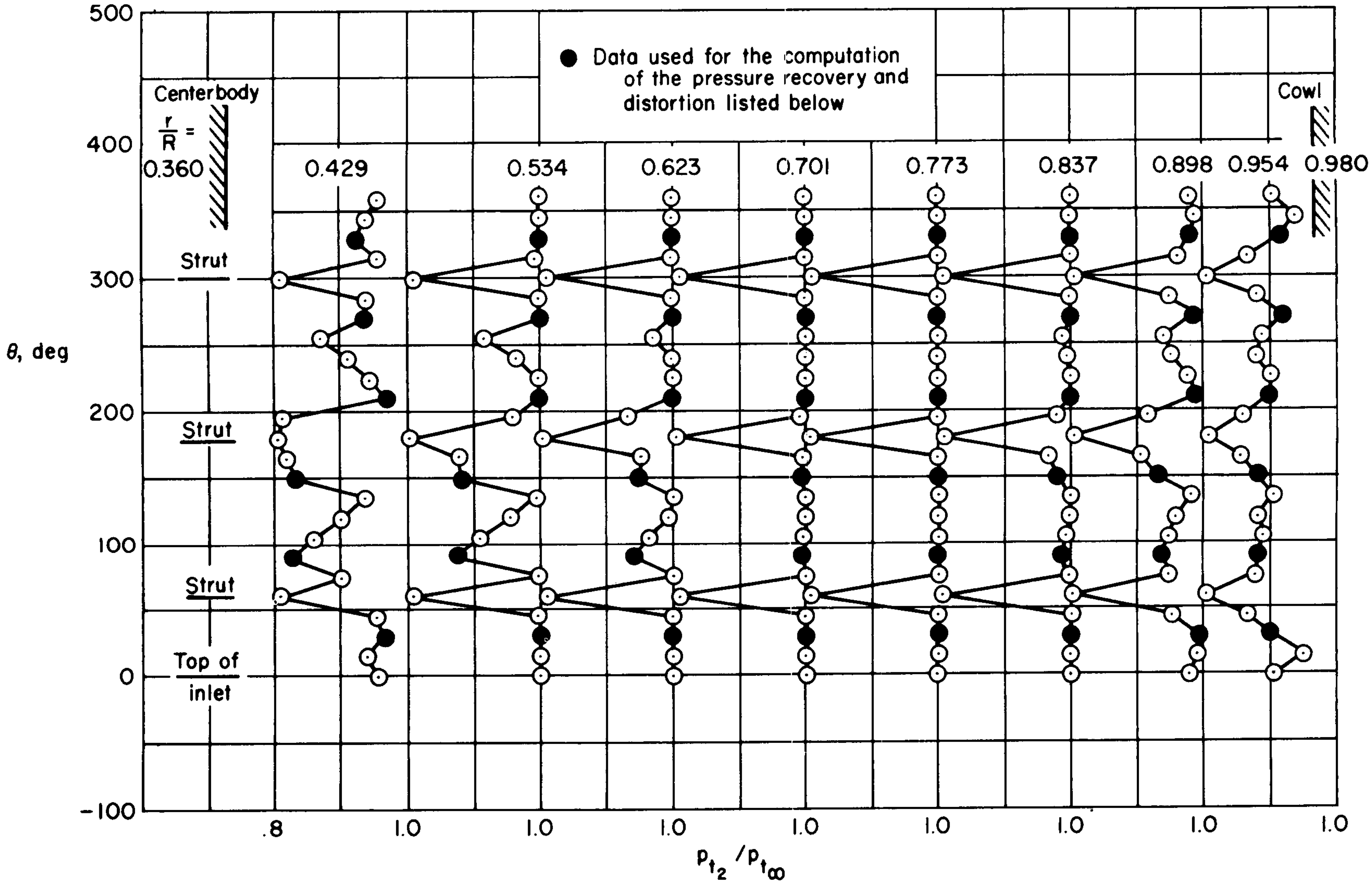

(c) $\alpha = 5.0°$, $\bar{p}_{t_2}/p_{t_\infty} = 0.964$, $\Delta p_{t_2} = 0.181$

Figure 59. – Continued.

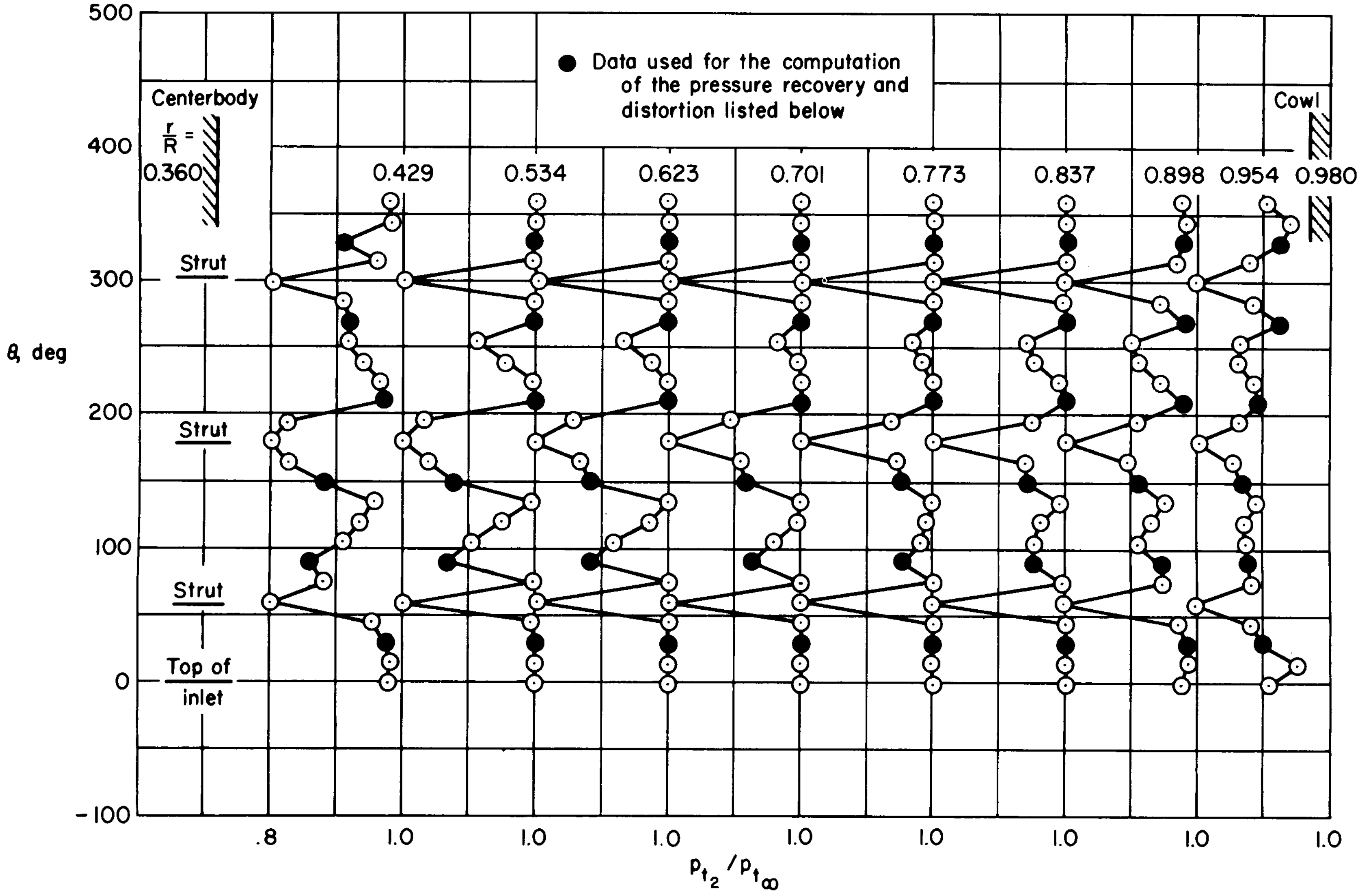

(d) $\alpha = 8.0°$, $\bar{p}_{t_2}/p_{t_\infty} = 0.955$, $\Delta p_{t_2} = 0.149$

Figure 59. – Concluded.

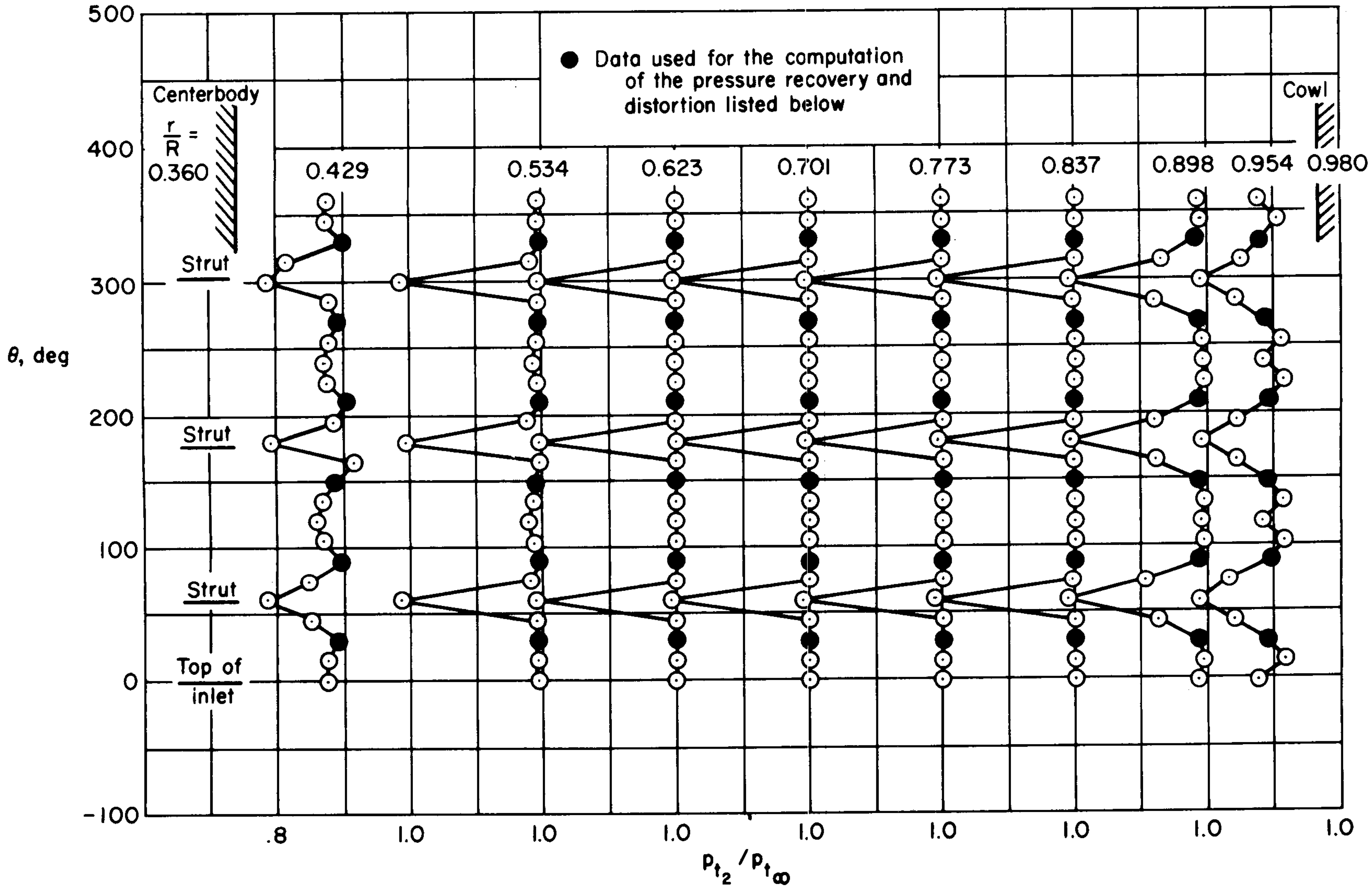

(a) $\alpha = 0°$, $\bar{p}_{t_2}/p_{t_\infty} = 0.969$, $\Delta p_{t_2} = 0.123$

Figure 60. – Circumferential total-pressure profiles at angle of attack; $M_\infty = 1.0$, $m_{bl}/m_\infty = 0$, $m_{bp}/m_\infty = 0$, vortex generator configuration 00, $x_{lip}/R = 3.881$, $m_i/m_\infty = 0.558$.

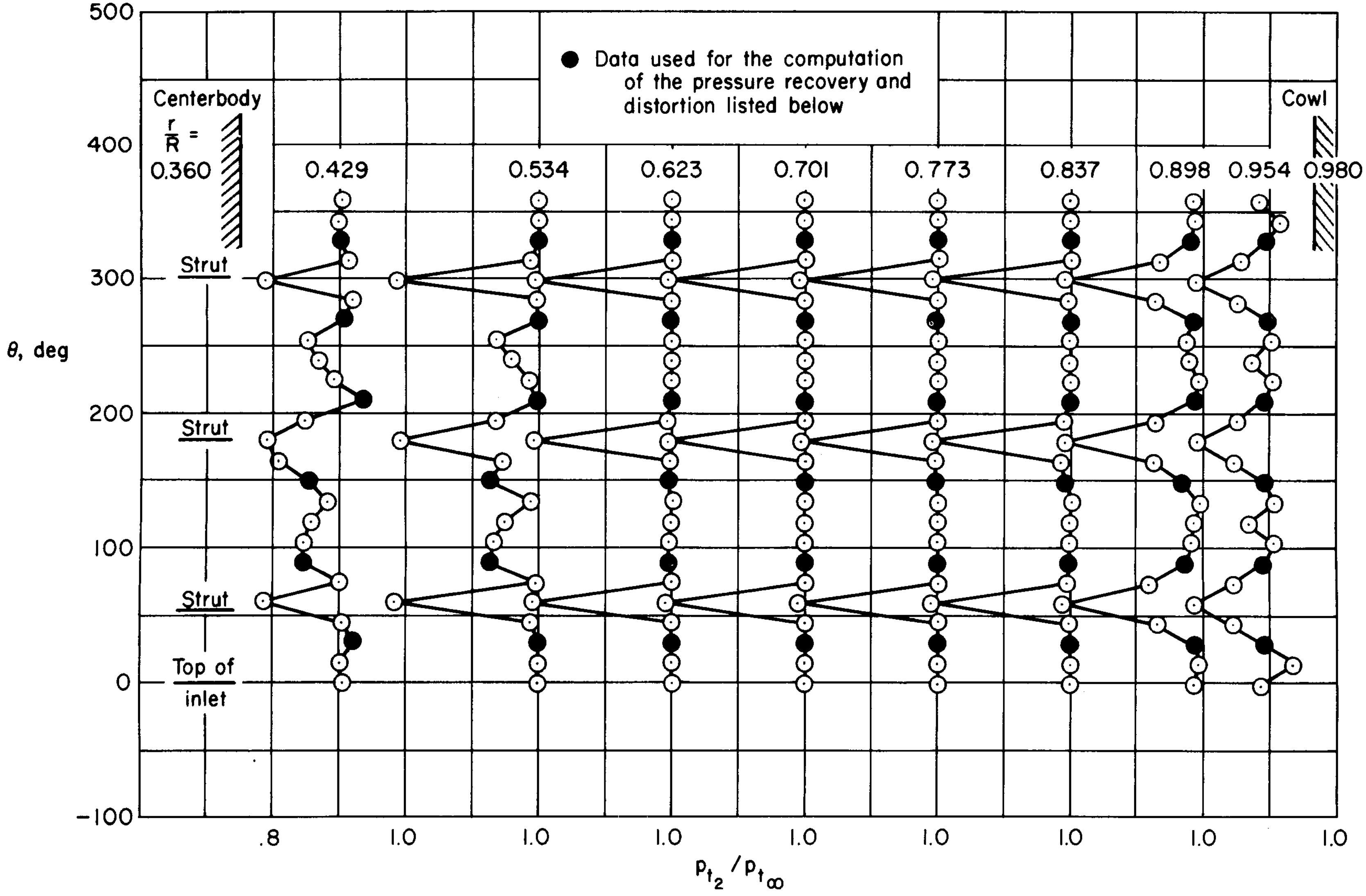

(b) $\alpha = 2.0°$, $\bar{p}_{t_2}/p_{t_\infty} = 0.967$, $\Delta p_{t_2} = 0.160$

Figure 60. – Continued.

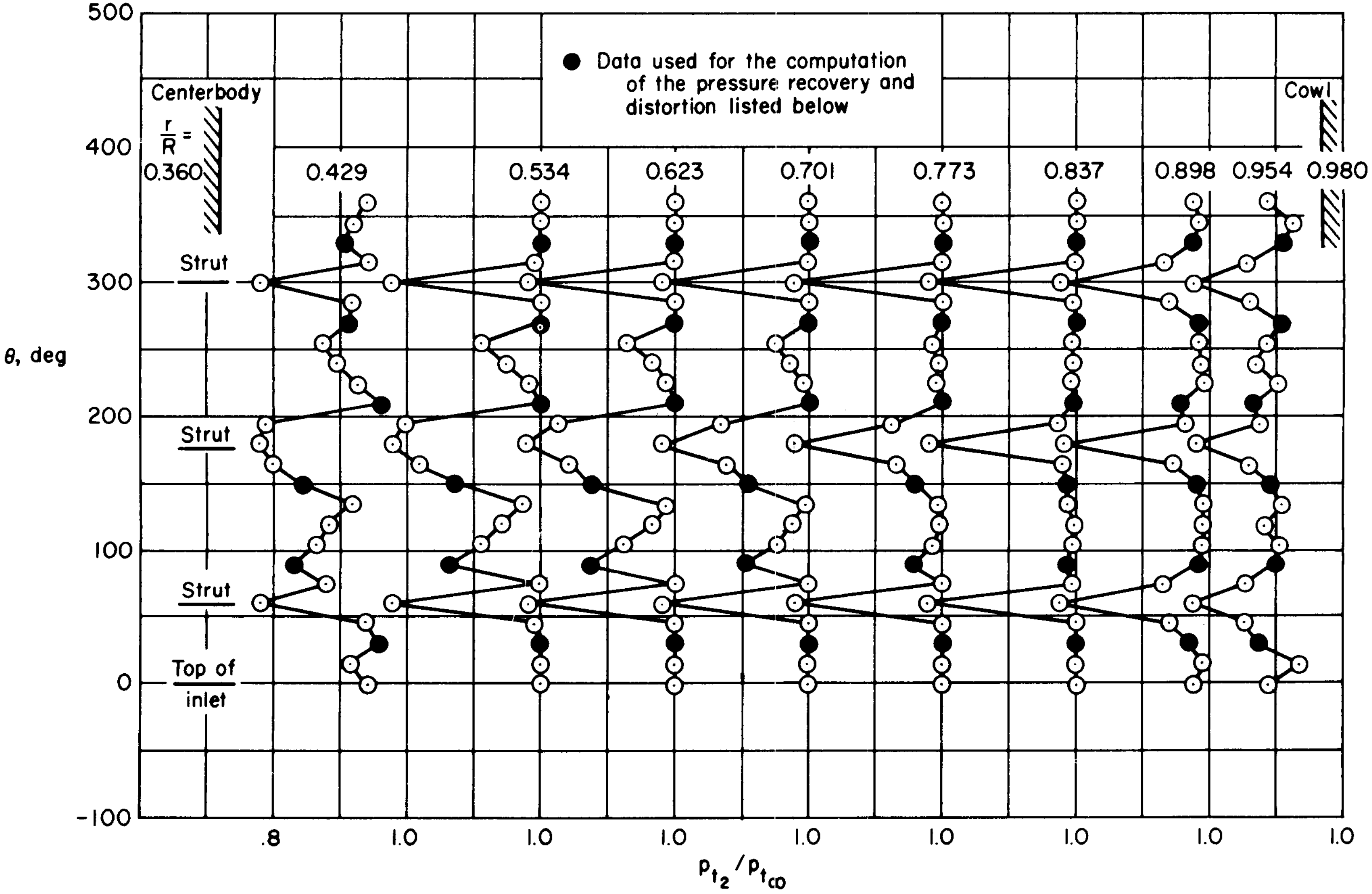

(c) $\alpha = 5.0°$, $\bar{p}_{t_2}/p_{t_\infty} = 0.954$, $\Delta p_{t_2} = 0.177$

Figure 60. – Continued.

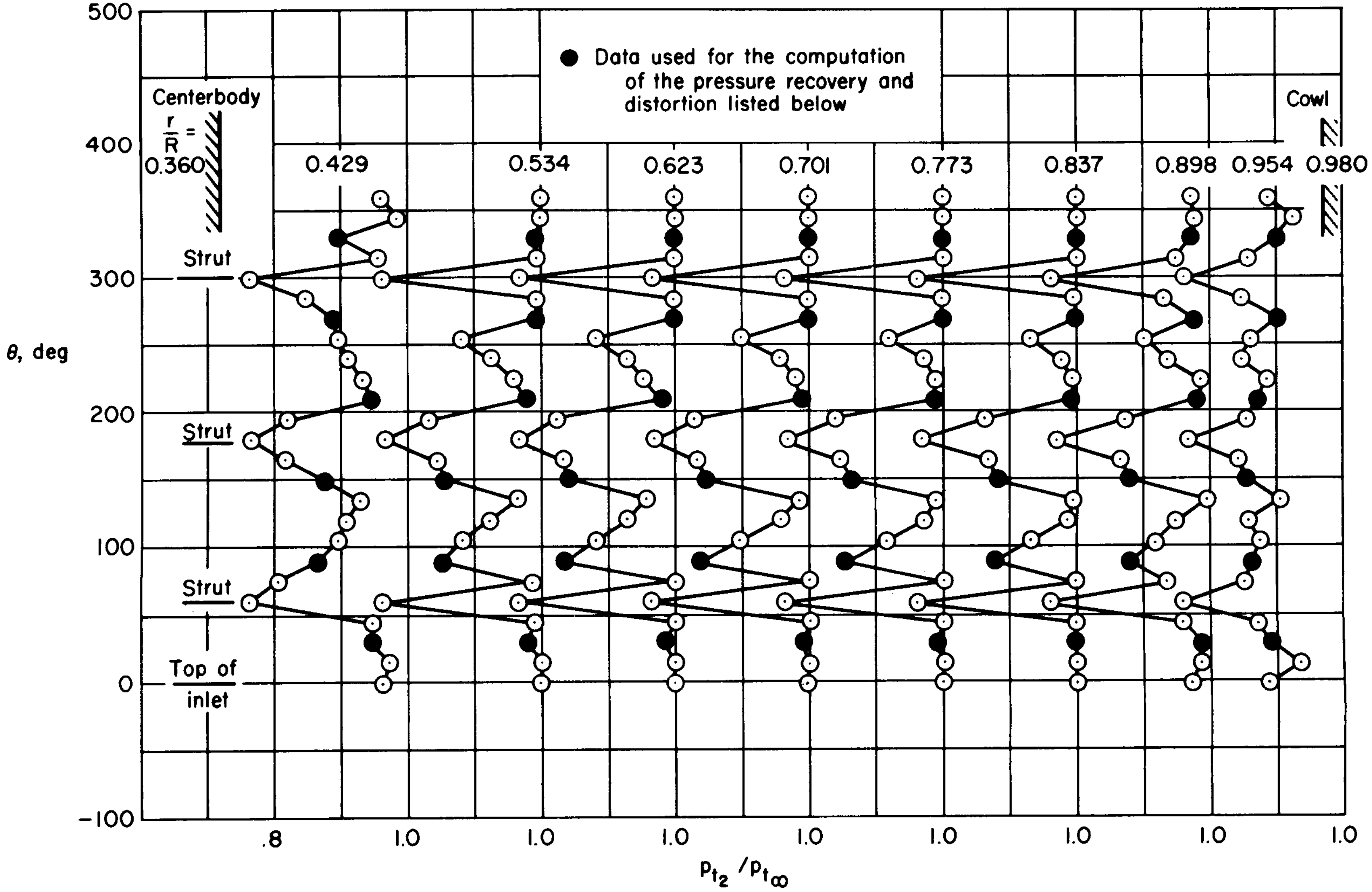

(d) $\alpha = 8.0°$, $\bar{p}_{t_2}/p_{t_\infty} = 0.932$, $\Delta p_{t_2} = 0.176$

Figure 60. – Concluded.

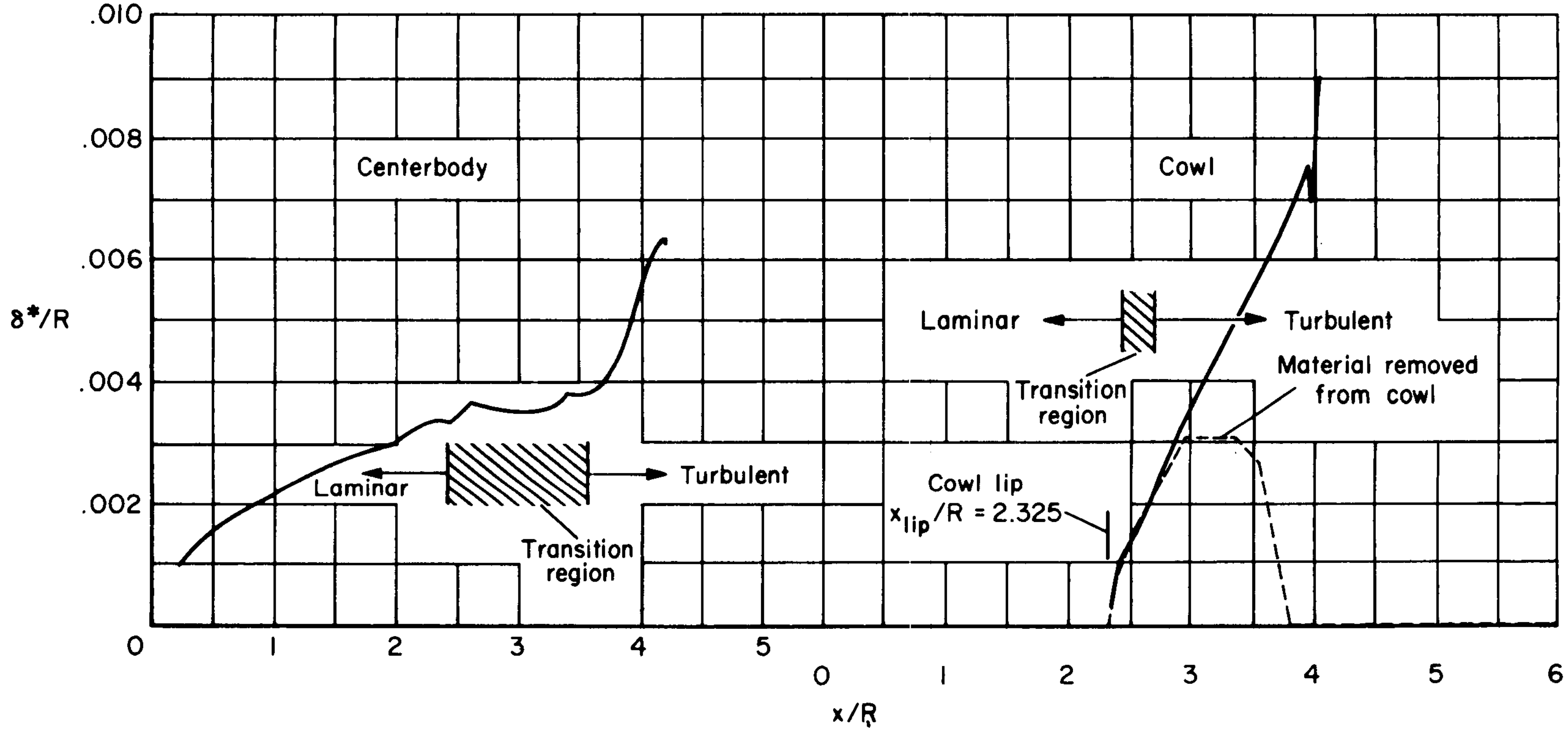

Figure 61. – Theoretical boundary-layer displacement thickness; $M_\infty = 2.65$, $\alpha = 0°$, $x_{lip}/R = 2.325$.

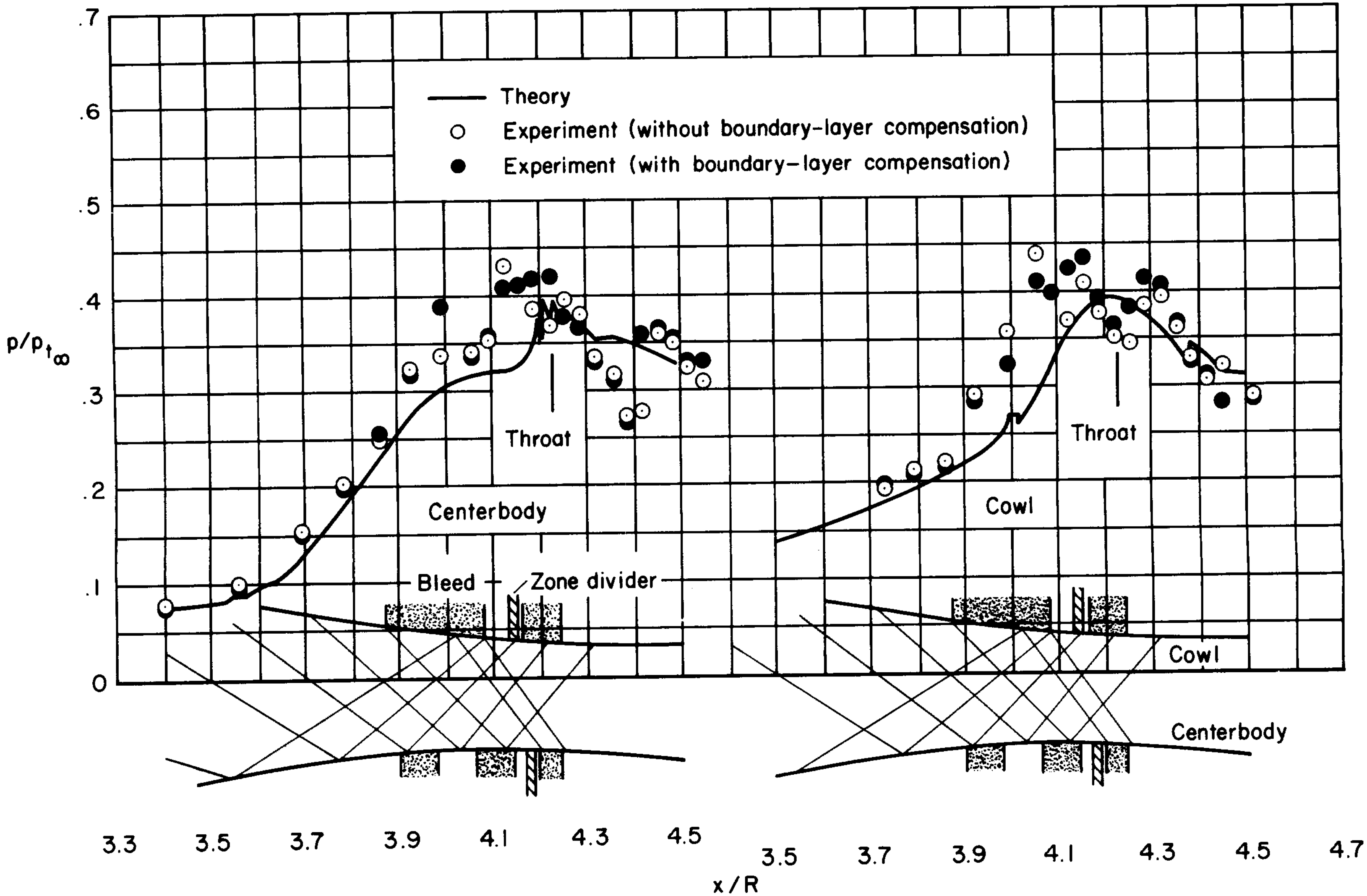

Figure 62. – Static-pressure distributions at the supercritical points with and without boundary-layer compensation; $M_\infty = 2.65$, $\alpha = 0°$, $x_{lip}/R = 2.325$, bleed configuration A.

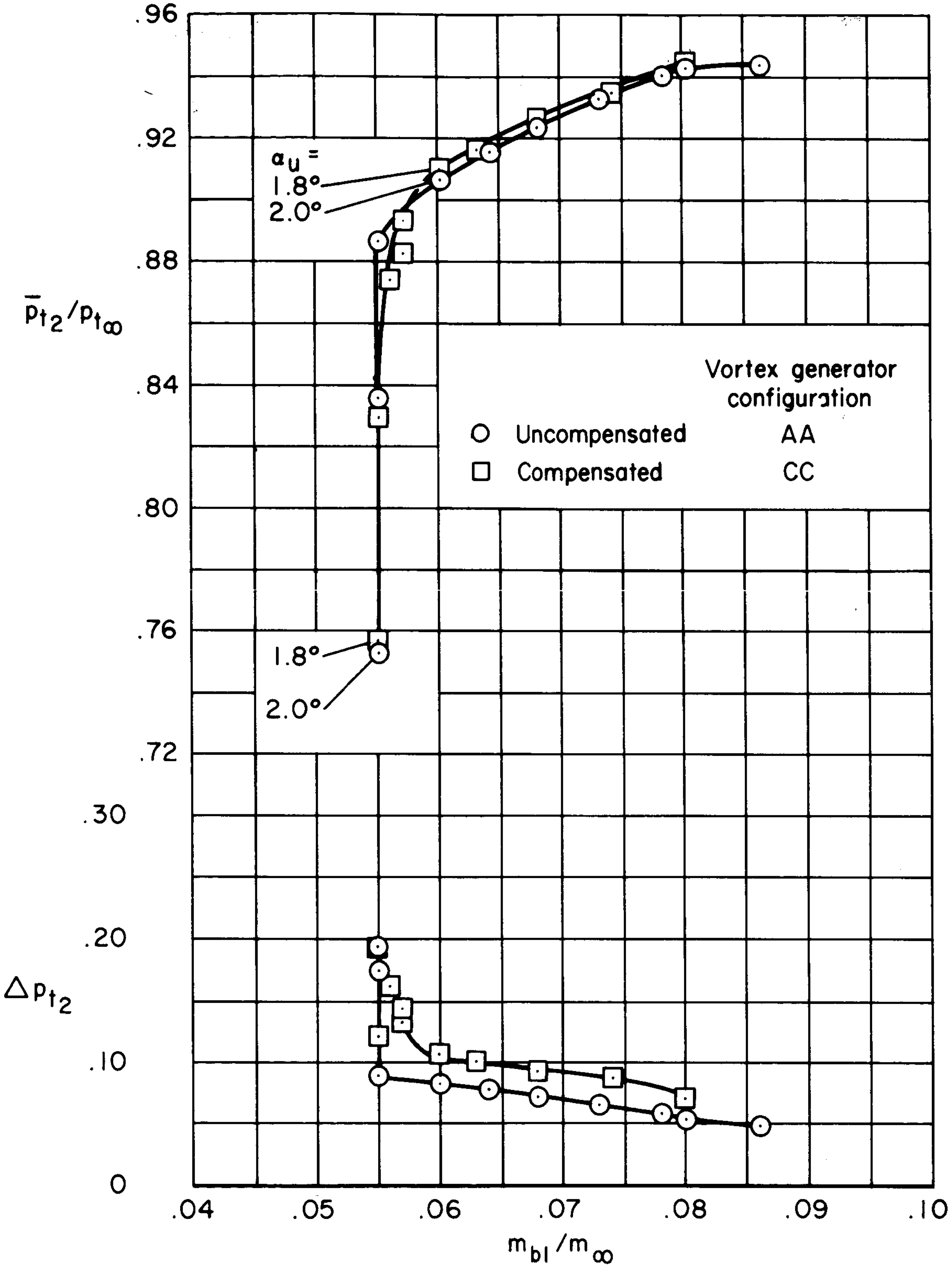

Figure 63. – Performance at the engine face with and without boundary-layer compensation; $M_\infty = 2.65$, $\alpha = 0°$, $x_{lip}/R = 2.325$, bleed configuration A.